Multifaceted Approach in the Photonic and Biological Applications of CdS and Ag Nanoparticles Engineered on DNA and Schiff Base Templates

Thesis submitted to the
University of Calicut for the partial fulfilment of
the requirements for the award of the degree of

DOCTOR OF PHILOSOPHY IN PHYSICS

by

REENA V N

Under the guidance of

Dr. Nithyaja B
Associate Professor of Physics

Research and Post Graduate Department of Physics
Government College Madappally, Vadakara
2024

Department of Physics
Govt. College Madappally, Vadakara

Dr. Nithyaja B
Associate Professor
Department of Physics

5 March 2024

CERTIFICATE

This is to certify that the thesis entitled **"Multifaceted Approach in the Photonic and Biological Applications of CdS and Ag Nanoparticles Engineered on DNA and Schiff Base Templates"** is a report of original work carried out by **Ms. Reena V N**, under my supervision and guidance in the Department of Physics, Govt. College Madappally, Vadakara, Calicut, Kerala and that no part thereof has been presented for the award of any other degree.

Nithyaja

Dr. Nithyaja B
Research Supervisor

P.O. Madappally College, Vatakara, Kerala-673102
Ph: 0496 2512587, Email physicsdeptgcm@gmail.com

DECLARATION

I hereby declare that the work presented in this thesis entitled "**Multifaceted Approach in the Photonic and Biological Applications of CdS and Ag Nanoparticles Engineered on DNA and Schiff Base Templates**", is the original work done by me under the guidance of **Dr. Nithyaja B**, Associate Professor, Department of Physics, Govt. College Madappally, Vadakara, Kerala, and no part thereof has been presented for the award of any other degree.

Madappally
March 2024

Reena V N
Research Scholar (Part-time)
Department of Physics
Govt. College, Madappally, Vadakara Kozhikode, Kerala

ACKNOWLEDGEMENTS

On the occasion of completing my PhD thesis, I am humbled to acknowledge that this accomplishment is the result of the collective support and encouragement of numerous individuals around me. Their guidance, encouragement, and untiring belief in my abilities have been the driving force behind the completion of this thesis. I am immensely grateful for their presence and contributions, which have enriched my academic journey and made this achievement possible.

I am deeply grateful to my research guide, Dr. Nithyaja B, whose guidance and mentorship have been invaluable throughout this research journey. I sincerely appreciate the time and expertise she has generously shared with me, enriching my understanding and molding me into a more conscientious scholar. I fondly recall her unwavering support throughout my years of research, patiently listening to me, forgiving my lapses, and providing immense freedom to work.

I express my thanks to Dr. Preetha B, Principal, as well as all the previous principals during my research period at Govt. College Madappally, Vadakara, Kozhikode, for providing all the facilities in the department to accomplish my research work. I extend my gratitude to Dr. Suneera T P, head of the department of Physics, for understanding the difficulties of a part-time research scholar and for providing ample support for the conduct of my research work. Heartfelt thanks to Dr. Harikrishnan G of the Physics department for consistently enquiring about the progress of my research work and offering valuable suggestions. Thanks to all my colleagues Hameed M, Preetha A U, Sajitha NM, Mubash MCV, and Santhikrishna U of the Physics department, Govt. College Madappally for their constant support and understanding. Thanks to all the non-teaching staffs of the department for their help in various situations. Thanks to Head of Zoology, Chemistry and Botany departments for providing different research facilities essential for the advancement of my work. Sincere thanks to Ms. Bhagyasree G S, the research scholar of the department, for her boundless help and support. It's rare to encounter individuals who offer assistance without seeking personal gain. Your presence in the lab was a great source of relief for me during the challenging times of my research.

Big thanks to Dr. Priya P, Principal of Govt. Arts and Science College Calicut, for placing her trust in me and for temporarily exempting from various responsibilities in the college during the final stages of my research. Thanks to Dr. Binitha M P, head of the department of Physics, Govt. Arts and Science College Calicut for giving enough consideration and support during the crucial period of my research. Thanks to all my colleagues of Physics department for their care and support.

Special thanks to Dr. R. Aswati Nair, Department of Biochemistry and Molecular Biology, Central University of Kerala, for allowing me to conduct the Bioimaging application on my samples. Moreover, she paid close attention to supervising the Bioimaging analysis carried out by her research scholar, Shilpa. Thanks to Shilpa, she dedicated her valuable time sincerely for me.

Dr. S N Potty, a scientist at C-MET Thrissur, my MSc project guide, is a humble and motivating figure who allowed me to conduct some relevant analysis for my research. I am grateful to him. I would like to express my gratitude to Mr. Packia Selvam, a research associate at the same lab, for his help with the analysis. I appreciate Mr. Akhil Raman T, my student at Govt. College Madappally and a research scholar at Central University, Hyderabad, for conducting some research analysis and collecting necessary research papers I required. Thanks to the technicians, SAIF-MG University, CSIF-Calicut University, STIC-CUSAT for various characterizations and analysis for the research work.

I have thoroughly enjoyed the atmosphere at the C H Muhammed Koya Library of the University of Calicut during the writing period of my thesis. I extend my gratitude to each member of the library staff for their exceptional service and the remarkable freedom they provide to academic individuals.

Heartfelt thanks to Linu George, my friend, for all the moral support she gives. She helped lift me up from tough situations, giving me the courage to continue working and shine in my research endeavors.

Amma is the backbone of everything. I dedicate this thesis to my incredibly hardworking mother, whose determined dedication and sacrifices have been my guiding light throughout this journey. Her tireless support has been influential in shaping my academic pursuits and achievements. Big thanks to Achan for always being by my side to help me handle difficult situations. I am also grateful to my sister, Jiji, for her understanding, love, and support. Much love to Anai and Ahin for their affectionate support.

Thanks to Subin, my life partner, whose knowledge of chemistry greatly contributed to my research work and he gave me necessary suggestions, instructions, and corrections during my research period.

A warm embrace to my children Evalin and the little boy, who always seek my company, may have faced inconvenience during the course of my research. Your presence has been a source of comfort, alleviating my stress during the research period. Thanks to all other family members and friends for their support on this endeavor.

Reena V N

Dedicated to Amma

ABSTRACT

Bionanophotonics, a fusion of biology, nanotechnology, and Photonics, fosters the development of devices and tools with dimensions on the nanoscale, facilitating interactions at the level of biomolecular and cellular structures. Nanomaterials are utilized in bionanophotonics to manipulate light-matter interactions at the nanoscale within biological systems, enabling advanced imaging, sensing, and therapeutic applications.

Template synthesis of nanomaterials involves using a pre-formed template to guide the growth and organization of nanoscale structures with precise control over size, shape, and composition. This study employs two templates – DNA and a novel Schiff base ligand – for nanoparticle synthesis. DNA templates excel in generating nanostructured photonic materials and inorganic structures, showcasing potential for highly ordered nanostructures. Schiff base ligands, cost-effective and environmentally friendly, are emerging as templates for nanoparticle synthesis.

Comprehensive studies on DNA-capped CdS and Ag nanoparticles reveal their diverse applications. The CdS nanoparticles demonstrate tunability in the emission properties of rhodamine 6G dye, efficient photodegradation, antibacterial activity, and Bioimaging applications. Silver nanoparticles exhibit larvicidal, antibacterial effects, Bioimaging and fluorescence enhancement in rhodamine 6G dye. Schiff base ligands, important in coordination chemistry, form metal complexes with various biological and catalytic applications. A novel Schiff base ligand and its Ni (II) complex were synthesized. They show semiconductor properties and biological activities. CdS nanoparticles were also synthesized by using the Schiff base as a template. It also shows photocatalytic activity and different biological applications like antibacterial and bioimaging. Both the CdS show green fluorescence in bioimaging of HeLa cells (cervical cancer cells), while the Ag nanoparticles show red fluorescence. Moreover, Schiff base ligands are employed in metal sensors utilizing absorption and fluorescence spectra, offering promising prospects in environmental monitoring and biomedical diagnostics. A solid metal sensing device has also been fabricated using a thin film made of Schiff base, with Raman spectrum assistance. In conclusion, this research opens avenues for advancements across various fields. Nanophotonics and nanomaterials offer solutions for healthcare and biotechnology challenges, using DNA templates and Schiff base ligands in nanoparticle synthesis and metal sensing. Collaborative interdisciplinary efforts are crucial for driving innovation and addressing complex issues in materials science and healthcare.

ഡിഎൻഎ, ഷിഫ് ബേസ് ലിഗാൻഡ് ടെംപ്ലേറ്റുകൾ എന്നിവയിൽ രൂപകൽപ്പന ചെയ്തിട്ടുള്ള കാഡ്മിയം സൾഫൈഡിന്റെയും സിൽവർ നാനോകണങ്ങളുടെയും ഫോട്ടോണിക്, ബയോളജിക്കൽ ആപ്ലിക്കേഷനുകളിലേക്ക് ബഹുമുഖ സമീപനം

സംഗ്രഹം

ബയോളജി, നാനോടെക്നോളജി, ഫോട്ടോണിക്സ് എന്നീ മൂന്ന് ശാസ്ത്രശാഖകളെ ഒരുമിപ്പിച്ചു കൊണ്ട് നിരവധി ആരോഗ്യ സംരക്ഷണ തലങ്ങളിൽ പ്രായോഗികമായ കണ്ടെത്തലുകൾ ഗവേഷണം ചെയ്തുകൊണ്ടിരിക്കുന്ന നൂതനമായ ഒരു മേഖല ആണ് ബയോനാനോഫോട്ടോണിക്സ്. ഇത് നേരത്തെയുള്ള രോഗം കണ്ടെത്തലും, പ്രകാശം അടിസ്ഥാനമാക്കിയുള്ള നവീനമായ ചികിത്സ രീതികളും വാഗ്ദാനം ചെയ്യുന്നു. ഇവിടെ, നൂതനമായ ഇമേജിംഗ്, സെൻസിംഗ്, മറ്റു ചികിത്സാ രീതികൾ എന്നിവ പ്രാപ്തമാക്കാൻ ജീവജാലങ്ങളിലെ ശശീരത്തിനുള്ളിലെ നാനോ സ്കെയിൽ അളവിൽ ഉള്ള മെറ്റീരിയൽസും പ്രകാശവും തമ്മിൽ ഉള്ള പ്രകാശ-ദ്രവ്യ പ്രതിപ്രവർത്തനങ്ങൾ കൈകാര്യം ചെയ്യുന്നതിനായി നാനോ മെറ്റീരിയലുകളെ ഉപയോഗിക്കുന്നു. അത്തരത്തിൽ ചില നാനോകണങ്ങളെ നിർമിക്കുകയും അവയുടെ ചില ബിയോളോജിക്കൽ, ഫോട്ടോണിക് പ്രായോഗികത കണ്ടെത്തുന്നതിന് വേണ്ടി ഉള്ള ഒരു ശ്രമമാണ് ഈ തീസിസിൽ ഉൾക്കൊള്ളിച്ചിരിക്കുന്നത്. നാനോകണങ്ങളുടെ സിന്തെസിസിന് ടെംപ്ലേറ്റ് രീതി ഉപയോഗപ്പെടുത്തുന്നു. വലിപ്പം, ആകൃതി, ഘടന എന്നിവയിൽ കൃത്യമായ നിയന്ത്രണത്തോടെ നാനോ സ്കെയിൽ ഘടനകളുടെ വളർച്ചയും ഓർഗനൈസേഷനും മാർഗ്ഗനിർദ്ദേശം നൽകുന്നതിന് മുൻകൂട്ടി തയ്യാറാക്കിയ ടെംപ്ലേറ്റ് ഉപയോഗിക്കുന്നു. നാനോകണങ്ങളെ സമന്വയിപ്പിക്കാൻ ഈ പഠനത്തിൽ ഉപയോഗിച്ചിരിക്കുന്ന രണ്ട് ടെംപ്ലേറ്റുകൾ ഡിഎൻഎയും ഒരു പുത്തൻ ഷിഫ് ബേസ് ലിഗാൻഡും ആണ്. ഡിഎൻഎ ടെംപ്ലേറ്റുകൾ നാനോ സ്കെച്ചർ ചെയ്ത ഫോട്ടോണിക് മെറ്റീരിയലുകളും അജൈവ ഘടനകളുടെ സമന്വയവും സുഗമമാക്കുന്നു, ഉയർന്ന ക്രമത്തിലുള്ള നാനോ സ്കെച്ചറുകൾക്കുള്ള സാധ്യത കാണിക്കുന്നു. ചെലവ് കുറഞ്ഞതും പരിസ്ഥിതി സൗഹൃദവുമായ ഷിഫ് ബേസ് ലിഗാൻഡുകൾ നാനോകണങ്ങളുടെ സിന്തസിസിന്റെ ക്യാപ്പിംഗ് ഏജന്റായി ഉയർന്നുവരുന്ന ഒരു സംയുക്തമാണ്. ഡിഎൻഎ കൊണ്ട് ക്യാപ് ചെയ്ത കാഡ്മിയം സൾഫൈഡ്, സിൽവർ നാനോകണങ്ങൾ എന്നിവയെക്കുറിച്ചുള്ള സമഗ്രമായ പഠനവും വൈവിധ്യമാർന്ന പ്രയോഗങ്ങളും ഇവിടെ ഗവേഷണം ചെയ്യുന്നു. റോഡാമൈൻ 6 ജി ഡൈയുടെ ഫ്ലൂറസെൻസ് തീവ്രത കൂട്ടാനും എമിഷൻ ട്യൂൺ ചെയ്യാനും കാഡ്മിയം സൾഫൈഡ്, സിൽവർ നാനോപാർട്ടിക്കിളുകൾക്ക് കഴിയുന്നതായി കാണുന്നു. ഇവ രണ്ടും, ഫോട്ടോഡീഗ്രേഡേഷൻ, ആൻറി ബാക്ടീരിയൽ പ്രവർത്തനം, ബയോഇമേജിംഗ് ആപ്ലിക്കേഷനുകൾ എന്നിവയിൽ മികച്ച പ്രവർത്തനം കാഴ്ച വെക്കുന്നു. കൂടാതെ സിൽവർ നല്ല രീതിയിൽ കൊളുകിന്റെ ലാർവയെ നശിപ്പിക്കുന്നതായും കണ്ടെത്താൻ കഴിഞ്ഞു. കോർഡിനേഷൻ രസതന്ത്രത്തിൽ പ്രധാനപ്പെട്ട ഷിഫ് ബേസ് ലിഗാൻഡുകൾ വിവിധ ജൈവ, ഉത്തേജക പ്രയോഗങ്ങളുള്ള ലോഹ സമുച്ചയങ്ങൾ ഉണ്ടാക്കുന്നു. ഈ ഗവേഷണത്തിൽ ഒരു പുതിയ ഷിഫ് ബേസ് ലിഗാൻഡും അതിന്റെ നിക്കൽ കോംപ്ലക്സും ഉണ്ടാക്കിയിട്ടുണ്ട്. ഇവയ്ക്ക് രണ്ടിനും അർദ്ധചാലക ഗുണങ്ങളും ജൈവ പ്രവർത്തനങ്ങളും കാണിക്കുന്നുണ്ട്. ഷിഫ് ബേസ് ടെംപ്ലേറ്റായി ഉപയോഗിച്ച് കാഡ്മിയം സൾഫൈഡ് നാനോ കണങ്ങൾ ഉണ്ടാക്കാൻ നമുക്ക് കഴിഞ്ഞിട്ടുണ്ട്. ഇത് ഫോട്ടോകാറ്റലിറ്റിക് പ്രവർത്തനവും ആൻറി ബാക്ടീരിയൽ, ബയോ ഇമേജിംഗ് പോലുള്ള വ്യത്യസ്ത ജൈവ പ്രയോഗങ്ങളും കാണിക്കുന്നു. ഇത്തരത്തിൽ ഡി എൻ എ ഉപയോഗിച്ചും ഷിഫ് ബേസ് ഉപയോഗിച്ചും ഉണ്ടാക്കിയെടുത്ത കാഡ്മിയം സൾഫൈഡ് നാനോകണങ്ങൾ കൊണ്ട് സെർവിക്സ് കാൻസർ കോശങ്ങൾ ആയ ഹേലാ കോശങ്ങളെ പച്ച ഫ്ലൂറസെൻസോട് കൂടി തെളിമയോടെ ബയോ ഇമേജിംഗിൽ കാണാൻ സാധിക്കുന്നു, അതേസമയം സിൽവർ നാനോകണങ്ങൾ ചുവന്ന ഫ്ലൂറസെൻസോട്ട കൂടി ആണ് ഇവയെ പ്രദർശിപ്പിക്കുന്നത്. കൂടാതെ, അബ്സോർപ്ഷൻ, ഫ്ലൂറസെൻസ് സ്പെക്ട ഉപയോഗിച്ച ചില ലോഹങ്ങളെ ഡിറ്റക്ട് ചെയ്യാൻ നേരത്തെ പറഞ്ഞ ഷിഫ് ബേസിനെ ഉപയോഗപ്പെടുത്തിയിട്ടുണ്ട്. ഇത് പരിസ്ഥിതി നിരീക്ഷണത്തിലും ബയോമെഡിക്കൽ ഡയഗ്നോസ്റ്റിക്സിലും നല്ല സാധ്യതകൾ വാഗ്ദാനം ചെയ്യുന്നു. രാമൻ സ്പെക്ട്രത്തിന്റെ സഹായത്തോടെ, ഷിഫ് ബേസ് കൊണ്ട് നിർമ്മിച്ച നേരിയ ഫിലിം ഉപയോഗിച്ച് ഒരു ഖരാവസ്ഥയിൽ ഉള്ള 'മെറ്റൽ സെൻസിംഗ് ഉപകരണവും പരീക്ഷിച്ചിട്ടുണ്ട്. ഉപസംഹാരമായി, ഈ ഗവേഷണം വിവിധ മേഖലകളിലെ പുരോഗതിക്കുള്ള വഴികൾ തുറക്കുന്നു. നാനോഫോട്ടോണിക്സും നാനോ മെറ്റീരിയലുകളും ആരോഗ്യ സംരക്ഷണത്തിനും ബയോടെക്നോളജി വെല്ലുവിളികൾക്കും പരിഹാരങ്ങൾ വാഗ്ദാനം ചെയ്യുന്നു, ഡിഎൻഎ ടെംപ്ലേറ്റുകളും ഷിഫ് ബേസ് ലിഗാൻഡുകളും നാനോകണങ്ങളുടെ നിർമിതിക്കും, മെറ്റൽ സെൻസിംഗിലും പ്രധാന പങ്ക് വഹിക്കുന്നു. മെറ്റീരിയൽ സയൻസിലും ഹെൽത്ത്കെയറിലെയും സങ്കീർണ്ണമായ പ്രശ്നങ്ങളെ അഭിസംബോധന ചെയ്യുന്നതിനും നവീകരണത്തിന് നേതൃത്വം നൽകുന്നതിനും സഹകരിച്ചുള്ള ഇന്റർ ഡിസിപ്ലിനറി ശ്രമങ്ങൾ നിർണായകമാണ്.

ABBREVIATIONS USED

CdS	-	Cadmium Sulfide
Ag	-	Silver
DNA	-	Deoxyribonucleic acid
NPs	-	Nanoparticles
Rh6G	-	Rhodamine 6G
MB	-	Methylene Blue
STED	-	Stimulated emission depletion
SMLM	-	single-molecule localization microscopy
MRI	-	Magnetic resonance Imaging
CT	-	Computed Tomography
Au	-	Gold
HOMO	-	Highest Occupied Molecular Orbit
LUMO	-	Lowest Unoccupied Molecular Orbital
GaN	-	Gallium nitride
GaP	-	Gallium phosphide
GaAs	-	Gallium Arsenide
InP	-	Indium Phosphide
InAs	-	Indium Arsenide
ZnO	-	Zinc Oxide
ZnS	-	Zinc sulfide
CdSe	-	Cadmium Selenide
CdTe	-	Cadmium Telluride

CTAB	-	Cetyltrimethylammonium Bromide
MSN	-	Mesoporous Silica Nanoparticles
CNT	-	Carbon Nanotubes
AAO	-	Anodized aluminum oxide
TiO2	-	Titania
$Fe3O_4$	-	Iron oxide
OLED	-	Organic LED
CuO	-	Copper oxide
HCl	-	Hydrochloric acid
CCT	-	Correlated colour temperature
DMSO	-	Dimethyl sulfoxide
SEM	-	Scanning Electron microscopy
TEM	-	Transmission electron microscopy
FRET	-	Fluorescence Resonance Energy Transfer
DMF	-	Dimethylformamide
UV	-	Ultraviolet
XRD	-	X-ray Diffraction

Preface

Bionanophotonics, harmoniously blends biology, nanotechnology, and photonics, fostering the development of devices and tools with dimensions on the nanoscale, facilitating interactions at the level of biomolecules and cellular structures. In this interdisciplinary realm, nanomaterials play a pivotal role, manipulating light-matter interactions at the nanoscale within biological systems, enabling advanced imaging, sensing, and therapeutic applications.

Template synthesis of nanomaterials involves using a pre-formed template to guide the growth and organization of nanoscale structures with precise control over size, shape, and composition. This study employs two templates – DNA and a novel Schiff base ligand – for nanoparticle synthesis. DNA templates excel in generating nanostructured photonic materials and inorganic structures, showcasing potential for highly ordered nanostructures. Schiff base ligands, cost-effective and environmentally friendly, are emerging as capping agents for nanoparticle synthesis.

The thesis is divided into nine chapters. **Chapter 1** introduces the thesis work, while **Chapter 2** details the experimental techniques and characterizations used in the research work. **Chapter 3** gives a comprehensive study on DNA-capped CdS and **Chapter 4** explores some photonic and biological applications of Ag nanoparticles synthesized using DNA. Both DNA capped CdS and Ag nanoparticles exhibit tunability in the emission properties of rhodamine 6G dye, efficient photodegradation, antibacterial activity, and bioimaging applications.

Chapter 5 describes the synthesis of a novel Schiff base ligand, serving as a template for synthesising CdS nanoparticles. The synthesis of Ni (II)

complex using this Schiff base ligand is also discussed. They show semiconductor properties and biological activities. **Chapter 6** focuses on the synthesis of CdS nanoparticles by using the Schiff base as template. These CdS nanoparticles show photocatalytic activity and promise for in antibacterial and bioimaging applications.

Chapter 7 confers a Schiff base metal sensor utilizing absorption and fluorescence spectra. It offers promising prospects in environmental monitoring and biomedical diagnostics. A solid metal sensing device is also investigated in this chapter using a thin film made of Schiff base, assisted by Raman spectroscopy. **Chapter 8** presents the general conclusions drawn from all the studies discussed in preceding chapters.

Finally, **chapter 9** outlines the future prospects derived from the results of various works carried out in the thesis. This research opens avenues for advancements across various fields in photonics, nanotechnology and biotechnology.

List of publications

1. Reena V N, Bhagyasree G S, Shilpa T, Aswati Nair R, & Nithyaja B (2024). Multifaceted Applications of DNA-Capped Silver Nanoparticles in Photonics, Photocatalysis, Antibacterial Activity, Cytotoxicity, and Bioimaging. Journal of Fluorescence, 1-15. (Publisher: Springer Nature)

2. Reena V N, Bhagyasree G S, Shilpa T, Aswati Nair R, Misha H, & Nithyaja, B. (2024). Photocatalytic, Antibacterial, Cytotoxic and Bioimaging Applications of Fluorescent CdS Nanoparticles Prepared in DNA Biotemplate. Journal of Fluorescence, 34(1), 437-448. (Publisher: Springer Nature)

3. Reena V N, Kumar K S, Shilpa T, Aswati Nair R, Bhagyasree, G. S., & Nithyaja, B. (2023). Photocatalytic and enhanced biological activities of schiff base capped fluorescent CdS nanoparticles. Journal of Fluorescence, 33(5), 1927-1940. (Publisher: Springer Nature)

4. Reena V N, Misha H, Bhagyasree G S, Nithyaja B. (2022). Enhanced photoluminescence and colour tuning from Rhodamine 6G-doped sol–gel glass matrix via DNA templated CdS nanoparticles. AIP Advances, 12(10), 105217. (Publisher: AIP)

5. Reena V N, Kumar K S, Bhagyasree G S, Nithyaja, B (2022) One-pot synthesis, characterization, optical studies and biological activities of a novel ultrasonically synthesized Schiff base ligand and its Ni (II) complex. Results in Chemistry, 4, 100576. (Publisher: Elsevier)

6. Reena V N, Shanasree M, Kumar S, Bhagyasree G S, Nithyaja B (2022) Mosquito Larvicidal Activity of DNA Capped Colloidal Silver Nanoparticles. IOP Conference Series: Materials Science and Engineering, 1221, 012051. (Publisher: IOP Publishing)

Co-authored publications

1. Subin Kumar K and **Reena V N** (2024). Crystal Structure, Anticancer, and Antimicrobial Evaluation of a Novel Substituted Pyrazole Ligand and Its Co (II), Ni (II), and Zn (II) Complexes. Pharmaceutical Chemistry Journal, 57(8), 1-9. (Publisher: Springer Nature)

2. Subin Kumar K and **Reena V N** (2022) Design, synthesis, crystal structure, antitumour and antimicrobial evaluation of a novel substituted pyrazole and its some metal complexes. Materials Today: Proceedings, 62, 5427-5433. (Publisher: Elsevier)

3. Subin Kumar K, **Reena V N**, Aravindakshan K K (2021) Synthesis, anticancer and larvicidal activities of a novel Schiff base ligand, 3-((2-((1-(4-hydroxyphenyl) ethylidene) amino) ethyl) imino)-N-(p-tolyl) butanamide and its Mn (II), Fe (III), Co (II), Ni (II) and Zn (II) complexes. Results in Chemistry, 3, 100166. (Publisher: Elsevier)

4. Bhagyasree G S, **Reena V N**, Abith M, Sabari Girisun T C, Nithyaja, B (2023) Enhanced adsorption and non-linear optical properties of DNA-CTAB functionalized mesoporous silica nanoparticles and their influence on enhancement of photoluminescence of Rhodamine 6G dye. AIP Advances, 13(5), 055017. (Publisher: AIP)

5. Bhagyasree G S, Sreenilayam S, Brabazon D, **Reena V N**, Nithyaja B (2022) Transmission characteristics of DNA templated 1D photonic crystal system for 3D printing applications: Simulation. *Results in Engineering*, 16, 100750.

Conference Papers

1. Reena V N and Nithyaja B (2021) Mosquito Larvicidal Activity of DNA Capped Colloidal Silver Nanoparticles- Second International Conference on Physics of Materials & Nanotechnology (ICPN 2021) 28-30, October 2021

2. Reena V N and Nithyaja B (2020) Fluorescent Enhancement of Rhodamine 6G dye by colloidal silver nanoparticles Derived from DNA biotemplate-International conference on Theoretical and Experimental Physics (ICTEP-2020 February 5-6 2020 – Organized by Department of Physics, Farook College Kozhikode

3. Reena V N, Jishna N, Nithyaja B (2019) Effect of CdS nanoparticles on fluorescence of Rhodamine 6G dye doped sol-gel derived glasses-International conference of on Energy and Environment (iCEE 2k19) organized by TKM College of Arts and Science, Kollam 12-14 December 2019

CONTENTS

LIST OF TABLES

LIST OF FIGURES

Chapter 1

Template based synthesis of nanomaterials: A Gateway to Photonic and Biological Advancements

This chapter commences by introducing the field of bionanophotonics providing a concise overview. Subsequently, it familiarizes nanoparticles which have emerged as a versatile class of materials with unique properties and a widespread of potential applications in various fields. The chapter discusses the synthesis, characterization, and utilization of CdS and Ag nanoparticles. It highlights the challenges associated with conventional nanoparticle synthesis methods and underscores the advantages of template-based approaches in achieving precise control over nanoparticle size, shape, and composition. The thesis objectives and central themes of photonic and biological applications of nanoparticles were outlined. It emphasizes the potential impact of template-based synthesis of nanoparticles. The subsequent sections provide a review of template-synthesized nanoparticles and offer a detailed overview of DNA, highlighting its advantages as a template for the synthesis of various nanoparticles. Special attention is given to reviewing DNA capped CdS and Ag nanoparticles, since a considerable part of this thesis concentrates on their synthesis. In the coming section, it familiarizes Schiff base ligands and their applications. A detailed description is also given on the template nature of Schiff base and different nanoparticles synthesized with Schiff base ligand.

1.1Introduction

Bionanophotonics is an interdisciplinary field which combines biology, nanotechnology, and photonics. It focuses on the application of nanomaterials and photonic principles to address challenges and unlock opportunities in the biological sciences and healthcare. Biophotonics studies how light interact with living organisms, blending photonics and biology. This exciting field holds promise for detecting diseases early and developing new light-based treatments. Also, biology is advancing photonics since biomaterials are showing promise in the development of new photonic media for technological applications. Optical bioimaging is a method used to examine cell and tissue structures, functions, and diseases at different levels, such as the cellular, tissue, and living specimen levels. New multifunctional materials are crucial for the development of next generation information technology, enabling faster speeds, stronger encryption, terabit data storage, and high-resolution displays [1].

The field of nanophotonics has seen rapid growth in recent years. Nanophotonics opens up exciting opportunities and enables new technologies, though nanotechnology cannot claim to solve every problem. Essentially, nanophotonics considers light-matter interactions on a scale smaller than the wavelength of light. This development has made various applications possible, including microscopy, sensing, imaging, medicine, light sources, and functional devices [1-3].

There are three conceptual divisions in nanophotonics, as shown in the diagram below, Figure. 1.1. The Nanoscale photoprocesses at nanoscale can be used to fabricate nanostructures using nanolithography. These nanostructures can be used to form nanoscale sensors and actuators. A nanoscale optical memory is one of the exciting concepts of nanofabrication. During nanofabrication, the photoprocesses are confined to well-defined nano

regions, allowing structures to be formed in an exact geometry and arrangement [4-5]. The confinement of radiation at the nanoscale occurs in near-field geometry. It enables optical resolution of less than 100 nm by breaking diffraction barriers. A practical method for controlling the electro-optical properties of a material is to manipulate its molecular architecture and morphology at the nanoscale [6-10].

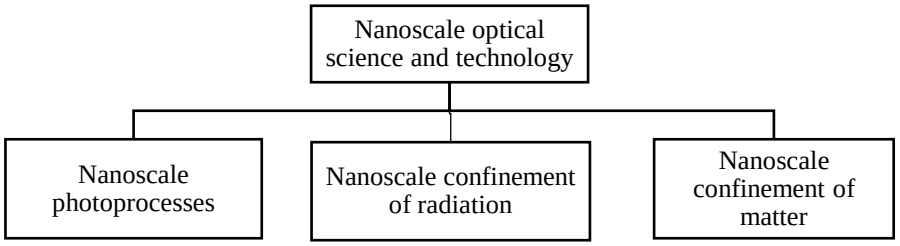

Figure.1.1 Three divisions of nanophotonics

1.2 Research areas in Bionanophotonics

(a) Biomedical Imaging (Bioimaging)

Bioimaging is a multidisciplinary field that encompasses various techniques for visualizing biological structures, functions, and processes at the molecular, cellular, and organismal levels. Bionanophotonics enables advanced imaging techniques with enhanced resolution and contrast. Nanoparticles and nanoscale probes are used as contrast agents in techniques like fluorescence microscopy, enabling the visualization of cellular and molecular processes [11]. These imaging modalities play a key role in both research and clinical settings, providing valuable insights into normal physiology and disease states. Advances in bioimaging technologies have revolutionized medical diagnostics, treatment monitoring, and understanding of complex biological phenomena. Additionally, molecular imaging

approaches enable the visualization of specific molecular targets, allowing for early disease detection and personalized medicine [12-13].

(b) Sensors and Diagnostics

Nanophotonic sensors offer high sensitivity and specificity for detecting biomolecules. These sensors have applications in medical diagnostics, environmental monitoring, and biotechnology, offering the potential for real-time and label-free detection of biomarkers [1]. Research in this field focuses on refining sensor designs, optimizing nanomaterial properties, and expanding the range of applications to advance our understanding of complex biological phenomena and improve healthcare diagnostics [2].

(c) Drug Delivery

Drug delivery refers to the process of administering therapeutic agents, such as medications or pharmaceuticals, to achieve a desired therapeutic effect in the body. The goal of drug delivery systems is to enhance the efficacy, safety, and targeted delivery of drugs while minimizing side effects. Various strategies and technologies are employed to achieve controlled release, improve bioavailability, and optimize the pharmacokinetics of drugs. Nanomaterials play a vital role in targeted drug delivery systems. They can encapsulate therapeutic agents and transport them to specific cells or tissues, improving drug efficacy while minimizing side effects [14-15].

(d) Tissue Engineering

Bionanophotonics contributes to tissue engineering by providing nanoscale scaffolds and platforms for cell growth and tissue regeneration. This technology aims to create functional biological tissues for transplantation and regenerative medicine.

(e) Optogenetics

This is a scientific technique that employs light to control the activity of genetically modified cells, typically neurons. Light-sensitive proteins like opsin, and nanoparticles are used in optogenetics to control and manipulate cellular activity with precision. This method is broadly used in neuroscience to study neural circuits and behaviours, providing valuable insights into brain function. Optogenetics has potential applications beyond neuroscience, but ethical considerations are important, particularly in human studies [16].

(f) Theragnostic

Theragnostic is a treatment strategy that unites therapeutics with diagnostics. Combining therapy and diagnostics, theragnostic approaches influence bionanophotonics to develop multifunctional agents that simultaneously diagnose and treat diseases. This promises personalized medicine solutions. It links both a diagnostic test that identifies patients most likely to be helped or injured by a new medication, and targeted drug therapy based on the test results [17].

Bionanophotonics merges the capabilities of nanomaterials and photonics to explore, manipulates, and advance our understanding of biological systems. Its applications hold significant promise for health care, biotechnology, and fundamental biological research offering innovative solutions to complex challenges in these fields. The merging of nanomaterials, templates, and applications allows the design of multifunctional platforms, integrating photonic properties, drug delivery capacities, and diagnostic functionalities. Interdisciplinary association between nanomaterials, photonics, and biology experts accelerates the transformation of research findings into practical applications.

1.3 Introduction to Nanomaterials

Nanomaterials have emerged as a revolutionary class of materials with properties that often challenge conventional knowledge. Nanoparticles are particles having dimensions at nanoscale, typically in the size range 1- 100 nm. At this scale, these materials exhibit novel and exceptional characteristics that set them apart from their bulk counterparts. [18-22]. Nanomaterials enable the miniaturization of photonic devices, resulting in more compact and portable optical systems. Nanomaterial-based sensors offer supreme sensitivity, making them suitable for sensing low concentrations of analytes which is vital in environmental monitoring, healthcare diagnostics, and industrial quality control. The size, shape, composition, and surface properties of nanomaterials can be accurately tailored to meet specific application requirements [23-24].

Nanomaterials, such as photonic crystals and plasmonic structures, enable the development of nanophotonic waveguides [25]. These tiny structures guide and manipulate light at the nanoscale, facilitating the miniaturization of optical components. Nanophotonic waveguides are subwavelength-scale structures designed to guide and control light at the nanoscale, typically using high-refractive-index materials like silicon or silicon nitride. These waveguides are fundamental building blocks in the field of nanophotonics, allowing for the precise manipulation and confinement of light within tiny dimensions, well below the wavelength of the guided light. They find critical applications in photonic integrated circuits (PICs), optical interconnects, sensors, and on-chip optical communication systems, enabling faster and more compact devices. Nanophotonic waveguides come in various forms, including dielectric waveguides, plasmonic waveguides, photonic crystal waveguides, and slot waveguides, each tailored for specific functionalities, like light routing, splitting, coupling, and filtering. By harnessing the unique

properties of nanoscale waveguides, researchers and engineers are paving the way for next-generation photonic technologies [26-27].

Nanomaterials like semiconductor nanowires or quantum dots can serve as gain media for nanoscale lasers. These miniature lasers find applications in optical communication, on-chip integration, and medical diagnostics [28-31]. Metamaterials, artificial electromagnetic media that are structured on the nanometer scale, were suggested for the negative-refractive index 'superlens'. Later, metamaterials emerged as a paradigm for crafting electromagnetic space and operating the propagation of waves, giving rise to the field of transformation optics [32].

Metallic nanoparticles can support localized surface plasmon resonances, which are extremely sensitive to changes in their local environment. This sensitivity is harnessed in plasmonic sensors for detecting molecules, biomarkers, and pollutants with exceptional precision [33-34].

Semiconductor quantum dots, due to their tunable emission properties, are used as sensitive probes in fluorescence-based sensors for applications like DNA sequencing and cellular imaging [35-36]. Utilizing nanoparticles provides researchers with the ability to finely adjust the physical attributes of the sensing coating, including thickness, roughness, specific area, and refractive index. This adjustment contributes to the development of improved sensors, surpassing traditional sensing coatings in terms of response time and sensitivity. Additionally, the nanometric size of nanoparticles introduces unique properties, further expanding the potential for novel sensing applications. Nanomaterial coatings on optical fibers can improve the sensitivity of sensors for various parameters, including temperature, strain, and chemical concentrations [37-38].

Nanomaterials enable super-resolution microscopy techniques such as stimulated emission depletion microscopy (STED) and Single-molecule localization microscopy (SMLM). STED microscopy is a super-resolution imaging technique that exceeds the diffraction limit, allowing the visualization of fine details in biological samples with extraordinary clarity. This technique is particularly valuable for studying structures at the nanoscale. In STED microscopy, a focused laser beam is employed to excite fluorescent molecules in the sample, but a surrounding donut-shaped depletion laser beam is applied simultaneously. The depletion beam is engineered to de-excite the fluorophores in the outside regions of the excitation spot, leaving only the central region to fluoresce. By carefully manipulating the intensity and shape of the depletion beam, this method effectively narrows down the emitting region, letting for much higher spatial resolution than traditional microscopy [39-40]. In SMLM, computational techniques are used to precisely trace individual fluorescent molecules from sequences of diffraction-limited images. These localized molecules are then utilized to produce a super-resolution image, a series of super-resolution images over time, or to define molecular trajectories [41].

Nanoparticles can serve as contrast agents in medical imaging techniques like MRI [42], CT [43], and photoacoustic imaging [44]. They enhance imaging contrast and improve diagnostic accuracy.

Nanomaterials play a key role in advancing holography, improving recording, modulation, and sensing capabilities. Photopolymer nanocomposites utilize nanoparticles to enhance holographic recording materials, boosting sensitivity and resolution. Metasurfaces, made of nanomaterials like plasmonic or dielectric Nanoparticles, allow ultrathin holographic devices, such as meta-holograms, with subwavelength thickness. Liquid crystal Nanoparticles offer dynamic control for real-time holographic displays. Quantum dots and

plasmonic nanoparticles improve holographic sensing for specific analytes. Metamaterials and nonlinear optical nanomaterials contribute to tailored holographic functionalities, providing unique electromagnetic properties and enabling applications like multi-photon holography [44].

Apart from the applications discussed so far, nanoparticles have been used to enhance the photoluminescence of certain organic dyes. A study focused on monitoring the fluorescence enhancement of pyrromethene laser dyes through their complexation with Ag nanoparticles [45-46]. In another study, Au nanoparticles were used to enhance the fluorescence of Rhodamine B dye incorporated into polyvinyl alcohol film [47-49].

Nanomaterials have revolutionized biological applications by providing tools for precise drug delivery, sensitive diagnostics, tissue engineering, and advanced bioimaging. Their interactions with biological systems are carefully designed to optimize their effectiveness while minimizing potential harm. The interdisciplinary synergy between nanotechnology and biology has opened new avenues for addressing complex challenges in healthcare, biotechnology, and life sciences. The interplay between nanomaterials, template-based synthesis, and photonic-biological applications holds immense potential for driving innovative solutions and advancements in science and technology [50-57].

The fascination with nanomaterials can be attributed to several compelling factors:

(a) Size-Dependent Properties

One of the most intriguing aspects of nanomaterials is their size-dependent behaviour. As the size of a material approaches the nanoscale, quantum effects come into play, leading to unique electrical, optical, magnetic, and mechanical properties. For instance, Au nanoparticles exhibit vibrant colours

due to their size-dependent plasmonic resonances, while carbon nanotubes possess remarkable electrical conductivity and strength [58].

(b) Quantum confinement properties

Quantum confinement is a quantum mechanical phenomenon that happens when the motion of charge carriers, such as electrons and holes, becomes limited in all three dimensions. In nanomaterials, especially nanoparticles or nanocrystals, the confinement of these charge carriers within a small volume leads to quantization of energy levels. These results in discrete electronic states and a bandgap, even in materials that might be conductive in bulk form [59]. Quantum dots and nanowires are examples where quantum confinement effects are pronounced.

These phenomena are mainly evident in semiconductor nanoparticles where the energy levels become discrete, leading to size-dependent electronic and optical properties. For instance, as the size of a semiconductor nanoparticle decreases, the energy gap between the HOMO and the LUMO rises, influencing the electronic and optical characteristics of materials [60]. This has practical implications in fields such as quantum dots for displays, solar cells, and other optoelectronic applications [61].

Understanding and manipulating size-dependent properties and quantum confinement effects enable the design of nanomaterials with tailored functionalities, impacting fields like nanoelectronics, photonics, and quantum computing [59, 62].

(c) Tailored Properties

Researchers have the ability to precisely engineer nanomaterials to exhibit specific properties by controlling their size, shape, composition, and structure. This level of control allows for the design of materials with customized functionalities, making nanomaterials a powerful tool for addressing unique scientific and technological challenges [63-65].

(d)Environmental Benefits

Nanomaterials present promising environmental benefits across various domains. Engineered nanoparticles show potential in water treatment by efficiently removing pollutants and heavy metals through processes like adsorption and catalysis, thereby enhancing water quality and purification. Moreover, in air quality improvement, catalytic nanoparticles play a role in the efficiency of converting harmful emissions from vehicles, contributing to reduced air pollution [66]. Nanoparticles are also essential in soil remediation, aiding in the breakdown or removal of contaminants in polluted soils. Furthermore, they contribute to renewable energy technologies, such as more effective solar cells. Nanoparticles find application in environmental monitoring through the development of sensors with enhanced sensitivity. In waste management, they are incorporated into packaging materials to extend shelf life and reduce food waste. Additionally, nanoparticles support energy efficiency in buildings by enhancing the thermal properties of insulation materials. While these applications hold promise, it is crucial to consider and address potential environmental and health risks associated with nanoparticle use [67].

Exploring nanomaterials extend beyond conventional disciplines uniting chemists, physicists, biologists, engineers, and materials scientists. This interdisciplinary collaboration has led to remarkable discoveries and innovative solutions to complex problems.

1.4 Metal and Semiconductor Nanoparticles

Metal and semiconductor nanoparticles have expanded significant importance in various fields due to their unique properties and potential applications. These nanomaterials can be synthesized and modified with different chemical functional groups, enabling them to bind with antibodies, ligands and drugs. Metallic nanoparticles have exclusive characteristics such as surface plasmon resonance and optical properties. It has extensive applications in therapeutic

areas, biotechnology, and vehicles for gene, optoelectronics, catalysis, and drug delivery. There are several daily life applications for metal nanoparticles: they have attained market acceptance in creams, shampoos, clothing, footwear, and plastic containers after the development of new economically feasible methods for their production [68-78].

Semiconductor nanoparticles, often mentioned to as quantum dots, are tiny crystalline structures with sizes on the nanoscale. Due to their quantum confinement effect, they exhibit unique electronic and optical properties that can be precisely controlled by adjusting their size. Semiconductor nanoparticles play a vital role in many emerging technologies. A semiconductor material's chemical and physical properties will change dramatically when its size is decreased to the nanoscale. Due to their large surface area or quantum size effect, this leads to unique properties. The conductivity of the semiconductor and its optical properties can be transformed. The field of semiconductor nanomaterials and devices is still in its initial stages. Still, they can be used in many applications, including solar cells, LED, nanoscale electronic devices, laser technology, waveguides, chemical and biosensors, super absorbents, packaging films, armour components, automobile parts, and catalysts [79-81].

Among the metallic nanoparticles, Au and Ag are the most preferred due to their unique chemical and physical properties. Au nanoparticles have good colloidal stability and can be used in various biological applications. They are also utilized in biosensors, electronic devices, conducting materials, smart paper, textiles, and surface-enhanced Raman spectroscopy. Au nanoparticles are wine-red and possess antioxidant properties, while Au particles are yellow and inert and come in various sizes and shapes. Au nanoparticles were widely applied in cellular imaging and photodynamic therapy [82-85].

Semiconductor nanocrystals originate from diverse compounds, categorized as II-VI, III-V, or IV-VI semiconductor nanocrystals, reflecting the groups of

elements in the periodic table from which they derive. Notable examples include silicon and germanium from group IV, GaN, GaP, GaAs, InP, and InAs from group III-V, and ZnO, ZnS, CdS, CdSe, and CdTe from group II-VI semiconductors. [86-99].

1.5 Templates in Nanomaterial Synthesis

Templates have emerged as a versatile and powerful method to achieve nanoscale materials. Templates, which can be in the form of porous solids, molecular structures, or even biological entities, serve as moulds or scaffolds for the creation of nanomaterials with tailored characteristics [100-102]. Template synthesis of nanomaterials, a cutting-edge technology forged in the 1990s, has arisen as a highly effective method widely employed in recent years. In 1999, South Korean scientists, led by Kim et al., exploited MCM-48 mesoporous silica as a template to successfully synthesize three-dimensional cubic mesoporous carbon, known as CMK-1 [103]. During same period, Japanese researchers, including Moriguchi et al., employed cationic surfactant CTAB as a template, employing phenolic resin as a carbon source to synthesize disordered carbon materials [104]. The template method verifies to be versatile and easy to implement, offering control over the structure, morphology, and particle size of nanomaterials through the template material. This method is generally categorized into hard and soft template methods. Dong et al. from Fudan University employed the hard template method, using mesoporous carbon pellets as a template to synthesize several non-silicon-based mesoporous materials, including solid or hollow aluminium oxide, titanium oxide, and aluminium phosphate microspheres [105]. Meanwhile, researchers like Firouzi et al. [106-107] from the University of California used the soft template method. The template synthesis method is known for its insensitivity to preparation conditions, simplicity in operation, and its ability to tailor the properties of nanomaterials for a range of applications.

1.5.1 Role of Templates in the synthesis of nanoparticles

(a) Controlling Size

Templates play a vital role in determining the size of nanomaterials. The size of the pores or features within the template dictates the ultimate size of the synthesized nanomaterial. For example, if a nano-porous membrane is used as a template, the size of the pores will dictate the size of the nanoparticles formed within those pores. This control over size is crucial because many properties of nanomaterials, such as their optical, electronic, and catalytic properties, are strongly size-dependent. By adjusting the template's dimensions, researchers can precisely tune the size of the resulting nanomaterials, ensuring they meet specific requirements for a given application [108].

(b) Shaping Nanomaterials

Templates also enable the precise control of nanomaterial shape. The geometry of the template can determine the geometry of the nanomaterial. For instance, the usage of an anisotropic template, such as a nanowire, can lead to the synthesis of one-dimensional nanomaterials like nanorods or nanowires. Meanwhile, isotropic templates can yield spherical or quasi-spherical nanoparticles. The ability to dictate shape is of dominant importance in applications where specific geometries are essential, such as in drug delivery carriers, where nanoparticles with well-defined shapes can improve drug release and targeting [108].

(c) Tailoring Properties

Templates offer a means of tailoring the properties of nanomaterials. By selecting a template material with specific properties, such as surface chemistry or electrical conductivity, these characteristics can be imparted to

the nanomaterial during synthesis. Additionally, the selection of template can influence the crystallographic structure and composition of the nanomaterial. This control allows for the creation of hybrid nanomaterials with a combination of desirable properties from both the template and the synthesized material [109].

(d) Diverse Template Types

Templates come in various forms, including hard templates (e.g., porous membranes or lithographically patterned surfaces) and soft templates (e.g., micelles, polymers, or biomolecules) [110]. Each type offers unique advantages and challenges, allowing for a widespread of nanomaterial synthesis approaches. Moreover, biological templates, such as viral capsids or DNA, have gained attention for their ability to guide the formation of nanomaterials with remarkable precision and complexity [111].

Templates represent a versatile and essential tool in the synthesis of nanomaterials. They empower researchers to engineer nanomaterials with unprecedented control over size, shape, and properties, enabling tailored solutions for a multitude of applications. The investigation into the convergence of nanomaterials, templates, and their applications in photonic and biological sciences, it becomes evident that templates play essential role in harnessing the full potential of nanotechnology in these fields. Precision in nanomaterial synthesis is of supreme importance, predominantly when considering applications in photonics and biology [112].

Tailoring the characteristics of nanomaterials is important in both photonics and biology, where precise control over size, shape, composition, and structure permits for customization to specific application requirements. In photonics, manipulating the shape and size of nanoparticles effect their optical properties, such as absorption and emission. Similarly, in biology,

careful control over the surface chemistry of nanoparticles is vital for applications such as targeted drug delivery and bioimaging. This precision not only improves the efficacy of nanomaterials but also contributes to the development of highly efficient optical devices in photonics, including lasers, photodetectors, and waveguides. Moreover, precision make sure consistency and reproducibility, providing researchers and engineers with reliable material properties for scientific research, medical diagnostics, and manufacturing processes. This consistency reduces variability, leading to more accurate data interpretation and predictable outcomes. Furthermore, the precision accomplished in nanomaterial synthesis plays a role in reducing waste and resource consumption, as it allows the controlled production of nanomaterials with desired properties, thereby reducing environmental impact [111-113].

Templates provide a structured framework that dictates the shape and size of nanomaterials. The dimensions of the template, such as pore size or pattern, directly influence the resulting nanomaterial's size and morphology. This control is crucial in applications where nanoscale dimensions are critical, such as in photonic devices requiring specific wavelengths of light interaction or in biological applications where nanoparticles must fit precisely into cellular structures [114].

The precision in nanomaterial synthesis is an important prerequisite in the fields of photonics and biology. Templates serve as priceless tools that enable this precision by permitting scientists and engineers to control the size, shape, and properties of nanomaterials with unparalleled accuracy. This control not only advances our understanding of fundamental science but also translates into practical benefits by improving the efficiency, reliability, and effectiveness of nanomaterials in widespread applications [114].

The method of template synthesis is exhibited in Figure.1.2. In template synthesis, a controlled framework is established employing a template material, represented as a tubular form. Nanoparticle precursors are introduced into this framework, resulting in the formation of nanoparticles depicted in rod shaped material within the template. Subsequently, the template material is removed, often through extraction, leaving behind the synthesized nanoparticles. This process enables precise control over the size, shape, and properties of the nanoparticles, making template synthesis a versatile method in materials science and nanotechnology [115].

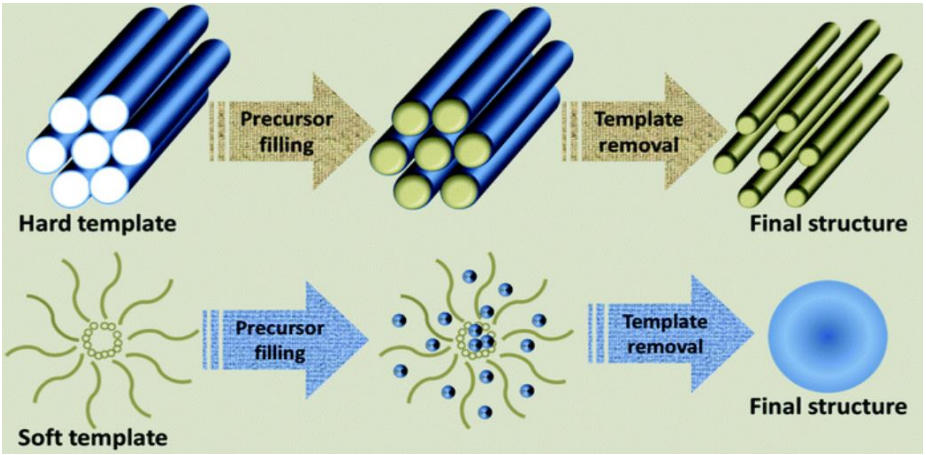

Figure.1.2 schematic representation of template synthesis of nanomaterial. Reproduced from reference [115]

1.5.2 Different nanoparticles synthesized through template methods

Mesoporous silica nanoparticles (MSNs) are synthesized by using surfactant templates like CTAB or Pluronic triblock copolymers [116]. These templates create ordered porous structures within the silica matrix. MSNs have applications in drug delivery, catalysis, and as carriers for various payloads owing to their high surface area and tunable pore sizes. The general process involves mixing a silica precursor, a surfactant template, and a solvent. The surfactant self-assembles to form a template micelle structure, and silica

precursors condense around these micelles. After removal of the surfactant template, mesoporous silica nanoparticles are obtained. These materials are highly ordered and have applications in drug delivery systems and catalysis [117].

Researchers use organic-inorganic hybrid templates like siloxane-organic block copolymers. These templates allow for precise control over pore size and structure. The resulting mesoporous silica nanoparticles can be tailored for specific applications, including in drug delivery and nanocomposites.

Biological molecules, such as DNA or proteins, can also serve as templates for mesoporous silica synthesis. DNA-templated MSNs involve the use of DNA strands as structure-directing agents. The silica precursor binds to the DNA template and forms mesoporous silica structures with a shape and size described by the DNA template. These DNA-templated MSNs are of interest for drug delivery and gene therapy. Another template employed in the preparation of silica nanoparticles are colloidal crystal template, which is formed by closely packed spherical particles. The silica precursor is then infiltrated into the voids of this crystal, and upon calcination, the template is removed, leaving behind an ordered array of mesopores. This method can produce 2D or 3D ordered mesoporous structures, which are beneficial for photonics and sensors. Multi-walled carbon nanotubes can turn as sacrificial templates for mesoporous silica nanoparticles. The carbon nanotubes are coated with a silica layer, and after removal of the carbon core, mesoporous silica nanotubes are obtained. These materials are used in applications such as drug delivery and catalysis [118]. Inverse Opals are another option for the synthesis of silica nanoparticles. Inverse opals are created by infiltrating a three-dimensional, ordered array of spherical particles, polystyrene beads, with a silica precursor. After the template is removed, the resulting material is a mesoporous silica inverse opal with an interconnected porous structure.

These materials have unique optical properties and are used in photonic devices [119].

Template synthesis can yield Au nanoparticles with controlled sizes and shapes. For instance, using DNA templates, Au nanoparticles with well-defined geometries can be produced. Au precursors bind to the DNA sequences and are subsequently reduced to form nanoparticles [120-121]. Block copolymers, such as *polystyrene-b-poly(2-vinylpyridine)* (PS-b-P2VP), are used to create micellar structures that serve as templates for Au nanoparticle formation. The Au precursors are reduced within these micelles [122-123]. Biomolecules, such as peptides and proteins, can guide the synthesis of Au nanoparticles by reducing Au ions and directing their assembly [124-125]. Colloidal crystal templates involve the self-assembly of colloidal particles into ordered arrays. These templates guide the infiltration of Au precursors, resulting in ordered Au nanoparticles. Silica spheres can be used as templates for the deposition of Au, resulting in the formation of hollow Au nanoparticles [126]. Similar to Au, Ag nanoparticles can be synthesized with specific shapes and sizes using templates. They are utilized in antimicrobial coatings, catalysis, and as optical materials. Surfactants like CTAB or sodium dodecyl sulfate (SDS) acted as templates for the synthesis of Ag nanoparticles [127-128]. They form micellar structures in which Ag ions are reduced to form Nanoparticles. Biological molecules such as proteins, peptides, and DNA can serve as templates for the synthesis of Ag nanoparticles. These biomolecules reduce Ag ions and control nanoparticle formation [129-130]. One research paper reports the preparation of Ag Nanoparticles using amphiphilic tri-block copolymer poly (ethylene oxide)-block-poly (propylene oxide)-block-poly (ethylene oxide) as a template [131]. Carbon nanotubes or graphene can serve as templates for the synthesis of Ag nanoparticles. Silver ions are adsorbed onto the carbon structures and reduced to form nanoparticles [132].

Magnetic nanoparticles such as iron oxide, nickel, cobalt, manganese ferrate can be synthesized by templating within a host matrix, such as polymers, biological molecules, viruses, or mesoporous materials. These nanoparticles have applications in MRI, targeted drug delivery, and magnetic hyperthermia for cancer treatment [133]. Polymer nanoparticles can be synthesized using block copolymers as templates. These nanoparticles can serve as drug delivery carriers, nano-reactors, or support structures for catalytic materials. CNT with defined diameters and chirality are another class of nanoparticles can be synthesized using templates. CNTs can be synthesized within porous templates, such as AAO. Titania nanoparticles can be synthesized via template method and many templates like mesoporous silica, block copolymer Pluronic 10R5, AAO, DNA, and protein [134].

Quantum dots like CdS, CdSe and CdTe can be synthesized using templates like DNA, to control their size and composition [135-137]. These nanoparticles are essential in applications such as fluorescent labeling, photovoltaics, and bioimaging. Template methods can also be employed to synthesize ceramic nanoparticles like ZnO, Fe_3O_4 and TiO_2 [138-140]. These materials find applications in various fields, including electronics, catalysis, and environmental remediation.

In template synthesis, the choice of template, precursor materials, and synthesis conditions can be tailored to synthesize nanoparticles with specific characteristics, making this a valuable technique for several scientific and industrial applications. Researchers continue to explore and refine template methods to create nanoparticles with enhanced properties and novel functionalities, leading to a broad spectrum of applications in various fields.

From the literature review it was found that DNA is a perfect biotemplate for the synthesis of metal as well as semiconductor nanoparticles.

1.6 DNA as a biotemplate

It's widely recognized that DNA is the most vital biomaterial for all living organisms as it carries their genetic code. Over the past 20 years, DNA, known as “the molecule of life”, has significantly interested researchers in various fields of science and technology. The DNA molecule is characterized by its helical structure, as proposed by Watson and Crick. It consists of two polynucleotide strands wrapped around each other, with a diameter of approximately 2 nm. The fundamental building block, or 'monomer', of DNA comprises a base covalently bonded to a sugar molecule, which, in turn, is covalently bonded to a phosphate group forming the backbone of the DNA polymer. There are four distinct base molecules in DNA: adenine (A), thymine (T), guanine (G), and cytosine (C), each featuring a conjugated ring structure, as depicted in Figure. 1.3. [70, 133, 141].

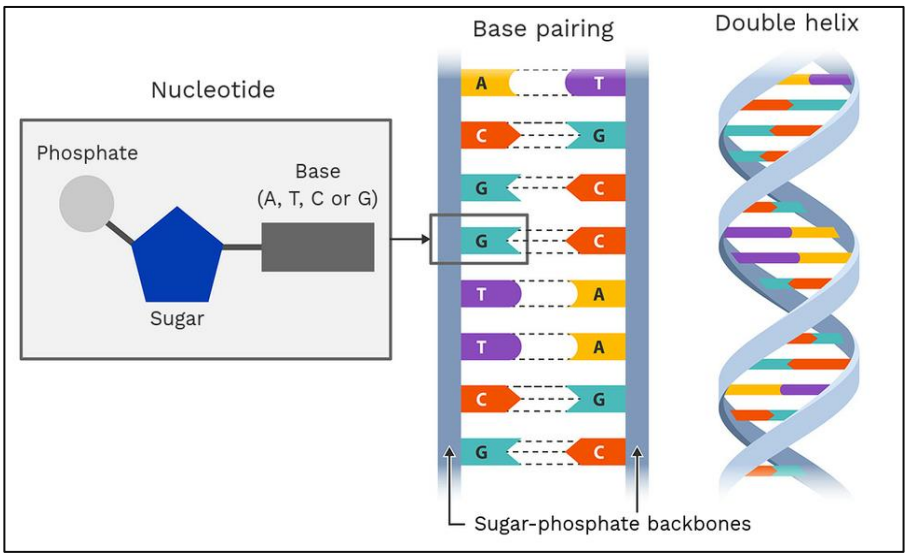

Figure.1.3 Double helix structure of DNA. Reproduced from the reference [133]

The double helix chains of DNA are negatively charged due to the presence of phosphate groups that are regularly arranged in the two backbones. Over

the past two decades, more experimental reports have been published on DNA research, indicating its growing popularity among scientists and engineers. DNA has many applications, including electronics, optics, biochemistry, and environmental protection. The biopolymer made from DNA is plentiful, cost-effective, renewable, and made from eco-friendly materials. As these biopolymers can be prepared by recycling the waste products from agriculture and fishing sectors, the usage will not lead to the depletion of resources or cause harm to the environment. DNA-based biopolymers display minimal optical loss, typically ranging from 0.1 to 1.2 dB/cm, across a wide spectrum of wavelengths spanning from 600 to 1700 nm [142-143]. These films also exhibit superior third harmonic generation susceptibility compared to silica due to the highly portable conjugated π electrons of DNA. By incorporating DNA into CTMA films and polymers with substantial nonlinear optical coefficients, the efficiency of poling is significantly enhanced, rendering them well-suited for the fabrication of nonlinear optical devices [144-149].

Another potential application of DNA is that it can be used as biotemplate for the synthesis of inorganic quantum-confined structures such as quantum dots, metal nanoparticles and quantum wires [150]. The biotemplate method uses DNA templates as "smart glue" to assemble nanoscale building blocks, resulting in a top-down approach for building nanostructured photonic materials. After being stretched and positioned, DNA molecules are typically treated with metal ions to bind the ions to the DNA [151]. Metal ions have the ability to undergo reduction, leading to the formation of metal clusters facilitated by metal seeds present on DNA templates. These seeds function as catalysts for further reduction, allowing the groups to grow till the reaction is complete [152]. This procedure has been used to create a range of metallic nanowires, including those made from Ag, palladium, platinum, nickel, copper, and cobalt metal ions deposited on DNA. Additionally, Coffer and

colleagues were the pioneers in using DNA as a template for CdS nanoparticles [153].

DNA can also be used as a supervisory template for polymerizing conducting polymers. For example, polypyrrole and polyaniline are prepared on the DNA template by cationic monomers' interaction with the backbone of DNA immobilized on a Si surface. This approach can potentially fabricate high-density conducting polymer nanowires with a fixed position and alignment on a Si surface [154].

The practice of DNA in electronic, optical, biomaterials, catalysts, and environmental protection separation depend on its fundamental properties associated to the double helical structure. The highly charged double helix shows local stiffness within a range of approximately 50 nm but long-range flexibility in water. Consequently, DNA serves as an excellent template for fabricating highly ordered nanostructures by binding cationic agents like metal ions, cationic surfactants, and polycationic agents. When DNA is in a dilute solution, it takes on a wormlike shape [70]. However, these molecules can be easily stretched and turned into linear templates, forming ordered nanostructures. Scientists believe that DNA condensation occurs through a process of nucleation and growth. This means that a single DNA molecule comprises a proto-toroid, which then collects other DNA molecules and grows into a highly organized toroidal structure. The DNA structures that are arranged in a specific order have the potential to be used in the creation of nanostructures. When DNA interacts with cationic surfactants, like hexadecyl trimethyl ammonium chloride, it forms a precipitate that produces a complex that can dissolve in common organic solvents. This allows for easy casting into thin films. The shape of the surfactant complex can be controlled and is often arranged in a local order [133].

The Figure. 1.4 shows the bases are stacked at regular intervals along the helix axis, 0.34 nm apart [133]. The helix has a wide major groove and a narrow minor groove, both of roughly the same depth. B-DNA structure of DNA allows small molecules to fit between stacked bases or bind in the grooves between the two backbones. These interactions are selective and specific, making DNA useful for removing pollutants or arranging functional molecules as a template. DNA is biocompatible and found in almost all living organisms, making it an excellent biomaterial. Figure.1.5 represents the scheme for the production of a nanoparticle from two salt solutions A^+ and B^- [133].

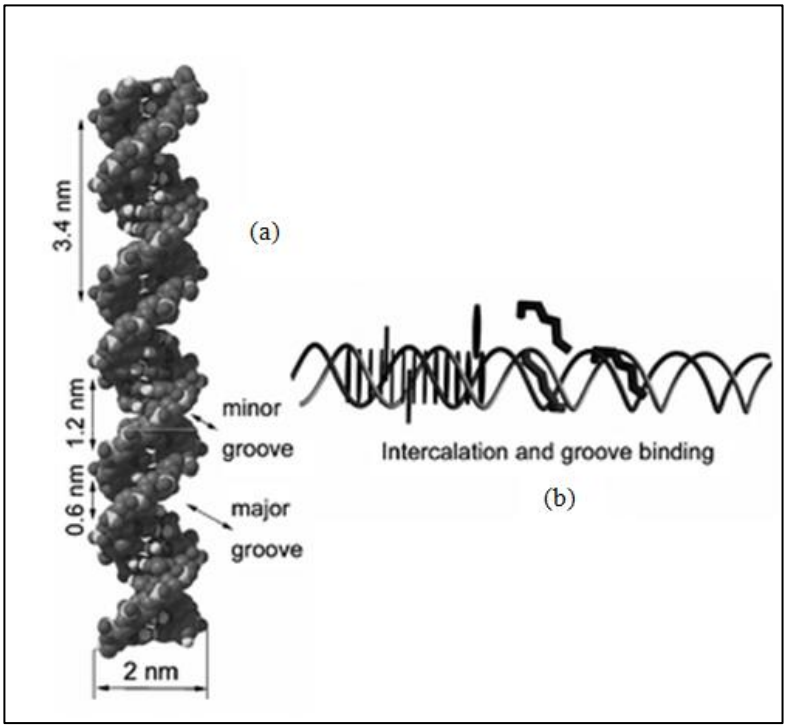

Figure.1.4 (a) Different grooves present in DNA and (b) intercalation and groove binding of DNA. Reproduced from the reference [133].

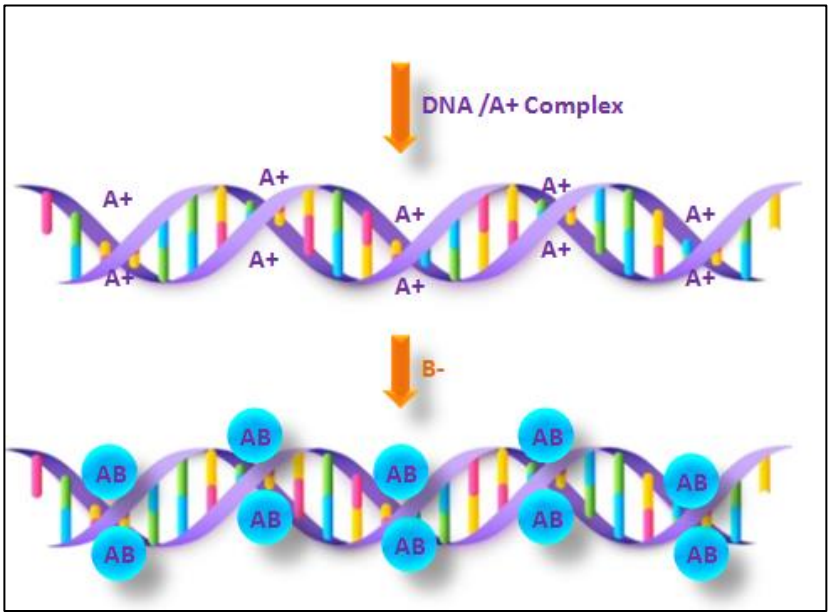

Figure.1.5 Scheme for the production of AB nanoparticle in DNA template. Reproduced from the reference [220]

In 2005, Kulkarni S K et al. reported a DNA-capped CdS nanoparticle in which they studied the interaction of Histone protein with CdS nanoparticles and investigated the photoluminescence variation [155]. DNA has been mixed during the preparation of the nanoparticles, which results into cadmium-rich nanoparticles producing a stable complex with DNA. These particles show strong fluorescence, spectral nature of which depends upon the medium in which the particles are synthesized. When interacted with proteins, fluorescence peak intensity of CdS nanoparticles increased significantly. In the work by Ma N et al., CdS nanocrystals with monomeric and oligomeric nucleic acid ligands are synthesized, and their properties are monitored as a function of the length and sequence of the passivating ligand [156]. Monomeric nucleic acids such as ATP, GTP, CTP, UTP, and oligomeric nucleic acid of 18-mer DNA were used as ligands to synthesize CdS nanocrystals. They used double-stranded DNA obtained from herring

sperm. Yao Y et al., in 2008, CdS nanoparticles on DNA templates were synthesized by heating the DNA networks with Cd^{2+} in thiourea [157]. In 2012, Nithyaja B et al. followed the same procedure to synthesize CdS nanoparticles and studied the bandgap tunability, photoluminescence, and excitation wavelength dependency on fluorescence emission [158].

Lan lan Sun et.al reported the synthesis of Ag nanoparticles ring on DNA template. The Ag nanoparticles ring which was about 1.5 μm in length and about 2.2 nm in height can be obtained by adjusting the reaction time [159]. In 2012, Zon et al. reported photo-induced nucleation and growth of Ag nanoparticles with DNA as capping agent [160]. Nithyaja et.al synthesized Ag nanoparticles in DNA template and studied nonlinear optical properties [70]. In 2017, Eden et al., reported Ag nanoparticles capped with DNA and citrate that are investigated electrochemically using stripping voltammetry and nano-impacts [161]. Chumpol J et al., in 2018, reported the synthesis of Ag nanoparticles using bacterial genomic DNA as a stabilizing agent and suggested they were good antibacterial agent [124]. Again in 2020, they investigate the use of small size DNA, a plasmid DNA, for aiding a green production of non-spherical Ag nanoparticles via the LED-irradiation activation [219]. A report was published on the sensing of H_2S in live cells at different phases of cell division. This was achieved by developing a fluorescent nanosensor with double-strand DNA-stabilized Ag nanoflakes in 2019 by Sitao Xie et al [162].

Utilizing the double helical structure of DNA, DNA serves both as a capping agent and a template for nanoparticles. Within each turn of the DNA helix, a major groove and a minor groove are formed. Leveraging this structural arrangement, the major groove provides ample space for nanoparticle growth, making it an ideal location. Nucleation initiates with the binding of Ag^{+} ions to either the DNA bases or phosphate groups, followed by gradual reduction

of Ag ions to metallic Ag at the nucleation site. Ultimately, the growth of Ag nanoparticles is constrained by the major groove of DNA [70].

Synthesizing nanoparticles in Schiff -base ligand template is an establishing technique, where few works have been carried out successfully. Schiff base ligand can be act as a template, very similar to biomolecule structure. Schiff bases have been used extensively in coordination chemistry because of their coordination behaviour, and they can easily be synthesized and coordinated with metals. They have been studied widely due to their effortless preparation and capability to fetch structural and electronical modifications. They could coordinate metal ions in a monodentate as well as polydentate manner to produce variety advantageous metal complexes. They possess many excellent physical, chemical and biological properties, which make them applicable in biological, inorganic, catalytic, pharmaceutical, and analytical fields [163-171]. The imine group present in the Schiff base plays an essential role in their biological activity [172]. They own structural similitude with natural biological molecules. Biological activities like antimicrobial, antidyslipidemic, antihelmintic, antitubercular, antidepressant, anticonvulsant, anti-inflammatory, analgesic, non-ulcerogenic, antitumor, antioxidant, antiviral, antihypertensive, antidiabetic, and antiglycation were reported recently for different Schiff bases and proved that they were potentially bioactive cores [173]. In addition to the biological activities of Schiff base, they possess applications in multiple fields like laser technology, light emitting diodes, sensors, solar cells and photochemical catalysis [174]. The chemical structural and other fundamental details of Schiff base ligands are explained in the next section.

1.7 Schiff base ligand

Schiff bases were first discovered by Hugo Schiff in 1864 when he synthesized and reported on the product of primary amines reacting with carbonyl compounds [175]. This reaction forms a compound with an azomethine group (-CH=N), which is commonly known as a Schiff base. This base is easily made by condensing a primary amine with a carbonyl compound (aldehyde or ketone). Schiff bases of aliphatic aldehydes are not very stable and tend to polymerize [218], whereas those of aromatic aldehydes, which have an effective conjugation system, are more stable. Some people use the term Schiff base only for secondary aldimine (azomethine where the carbon is connected to a hydrogen atom), with a general formula of RCH=NR'. The nitrogen chain makes the Schiff base into a stable imine. A Schiff base resulting from aniline, where R3 is a phenyl- or substituted phenyl radical, can be called an anil (Figure.1.6). Schiff base's chelating ability is high due to the lone pair of electrons on the sp^2 hybridized nitrogen atom of the azomethine group. These compounds are considered "Privileged ligands" due to their versatility and ease of preparation, which benefits various scientific fields such as biological, pharmacological, clinical, and analytical [175].

Schiff bases are molecules that can act as ligands with coordination sites ranging from one to seven. They can be monodentate, bidentate (with N-N or N-O donors), tridentate, or polydentate ligands. In a monodentate Schiff base, the basic strength of the (C-N) group is not strong enough to form a stable complex by the coordination of the imino nitrogen atom to a metal ion. To stabilize the metal-nitrogen bond, at least one additional donor atom should be present, suitably oriented near the N, and can form a five- or six-membered chelate ring [176].

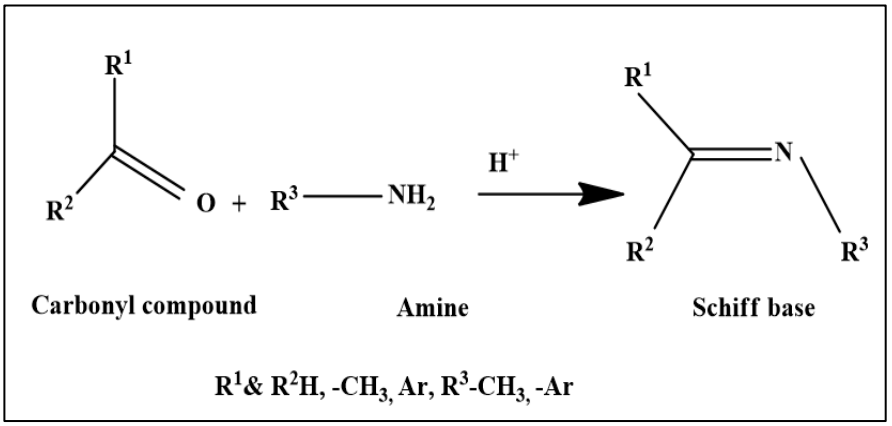

Figure.1. 6 Scheme for the preparation of Schiff bases

These days, mixed ligands and their complexes garner increased attention due to their useful properties. The mixed ligand contains at least two different functional groups that can bind to the metal atom. As their donor atoms provide unique reactivity to metal complexes, these ligands have become increasingly popular today [177]. Mixed Schiff bases and metal complexes have been applied as optical, chemical and biological sensors. The chemical and optical sensing method utilized the fluorescence behaviour of these materials. This fluorescence sensing technique has fascinated great attention for the detection of significant metal ions and anions in a living cell due to their quick response, high sensitivity, and immediate visual analysis [178-179]. Schiff bases are used in sensing applications for metallic cations and anions in different kind of environmental and biological media. There is a growing need for accurate identification of harmful pollutants like toxins and metal ions, especially in health and environmental applications. The release of these pollutants from industrial and farming practices poses a threat to human health and the environment. Current methods like flame atomic absorption spectroscopy and inductively coupled plasma mass spectrometry are expensive, time-consuming, and not very sensitive. Further, Schiff bases and their metal complexes serve as fluorescent probes for bioimaging that can

differentiate cancerous cells from normal cells using fluorescent imaging in cellular biology [180-181].

1.7.1 Photonic Applications of Schiff base ligand

The fluorescent properties of Schiff base ligands find applications in non-linear optics, optical sensing, bioimaging, dye industry, optoelectronics etc.

Organic materials with nonlinear optical properties are typically created by bonding electron-donating and withdrawing groups using a large D-π-A conjugated system. This formation called a push-pull system, enhances molecular polarizability and increases the nonlinear optical response. The bridge groups commonly used for this system are carbon-carbon double bonds (-C=C-) and carbon–nitrogen double bonds (-C=N-) or nitrogen-nitrogen double bonds (-N=N-). Aromatic and heteroaromatic rings are excellent choices for constructing third-order NLO materials for the electron-donating component in the push-pull system. Among such materials, Schiff bases are of particular interest. Large number of works have been done so far and found that Schiff bases are important nonlinear optical materials [182-187].

Chemical sensing using Schiff bases has been extensively studied, particularly in the selective response of different compounds to specific analytes. Schiff bases are a crucial class of compounds that exhibit interesting sensing behavior toward various analytes. Optical chemosensors, particularly those based on Schiff base structures, have shown great potential in detecting metal ions like Al^{3+}, Fe^{3+}, $Cr^{3+,}$ Cu^{2+}, Hg^{2+}, Co^{2+}, Zn^{2+}, Ni^{2+}, Pb^{2+}, Pd^{2+}, Cd^{2+}, Mn^{2+}, Mg^{2+} [188-193]. These compounds effectively detect anions such as CN^-, F^-, $H_2PO_4^-$, and iodide. Anions like CN^- and F^- pose a significant risk to humans and the environment. The Schiff base skeleton contains H-bond donors and acceptors that interact with anions. These interactions serve as an

effective signaling mechanism for detecting different analytes in various scenarios. The receptor's selectivity towards a specific target depends on factors such as the electronic structures of both the receptor and target, the size of the target, and the nature of the solvent used [194-195].

The use of fluorescent measurements to detect analytes is highly effective due to its convenience, low cost, ability to detect low level substances, quick photoluminescence response and usefulness in bioimaging. Biomolecules within living systems can be monitored with fluorescence imaging (bioimaging). Fluorescent probes that use Schiff base have been created to detect harmful substances and visualize different analytes within biological systems in the last few years. Few examples are given here. The Schiff base, reported by Bhuvanesh N et al. in 2018 by the condensation reaction between methyl carbazate and 5-nitro-2-thiophenecarboxaldehyde in ethanol/acetic acid, detects Ag^{+} in live cell imaging [196]. Liu et al. in 2018 reports, Picolinohydraxide coupled 4-(diethylamino) salicylaldehyde-based Schiff base could detect Al^{3+} and Zn^{2+} in Hela cells when treated Al^{3+} and Zn^{2+} [197]. Schiff base based on pyrene and triphenylmethylamine were used for screening Hg^{2+} in live HeLa cells, reports by Wu Y et al [198-199].

Organic LEDs are p-n junction semiconductor materials with various supporting layers that yield electroluminescence. They are commonly used in displays and light sources because they save energy and don't require a backlight for displays. Metal-organic compounds have distinct optical and electronic properties because of the interactions between metal and organic ligands. Schiff bases and their complexes are widely used in the construction of OLEDs to adjust the emission colour and enhance device efficiency. To create high-performance OLEDs, two important factors are necessary: high carrier mobility and intense luminescence. These qualities can be achieved through the use of planar molecules with an extended π-conjugated system.

The process of creating high-performance OLEDs involves utilizing various phosphorescent d^6 and d^8 metal complexes, which are associated with nitrogen and carbon as donor atoms. A few examples are noted here. Zhang and colleagues, in 2017, created Schiff base compounds through the combination of substituted salicylaldehydes and aniline complexes with Pt [200]. These compounds were then utilized in the development of phosphorescent blue light-emitting diodes. Lepnev and colleagues, in 2009, created green emitting OLED using Zn complexes of tetradentate Schiff bases made from derivatives of salicylaldehyde and o-vanillin [201].

Transition metal complexes of numerous Schiff bases, such as Aluminum (III), Iron (III), Cobalt (II), Nickel (II) and Copper (II), have been used as a mordant in dyeing techniques. The concept of complexation and mordanting is similar in coordination applications. An electron-withdrawing group is the basis of the chromophore theory. In autochromes, electrons are released and linked through conjugated systems. The idea of the donor-acceptor chromogen was created. Additionally, it has been noticed that the absorption band of the colour can shift to a longer wavelength, known as a bathochromic shift. It can be achieved by increasing the chromophore's electron-withdrawing power, enhancing the auxochromes' electron-releasing power, and extending the conjugation length. While lacking rigorous theoretical support, the chromophore and autochrome theory is proposed to explain the origin of colour in dye molecules. Chromophores of this type include carbonyl (C=O), diazo (-N=N-), azomethine (-CH=N-) and nitro (NO_2). A hydroxyl group (OH) and an amino group (NR_2) increase the intensity of the colour and shift the absorption to longer wavelengths of light. In addition to azo dyes, carbonyl dyes, azomethine dyes, and nitro dyes, the concept applies to chemical dye classes. For example, in 2012, Tao T and colleagues created three pairs of high-performance Disperse Red dyes by combining substituted *2-aminobenzothiazoles with 3-(diethylamino) phenol* or *3,5-dichloro-2-*

hydroxybenzaldehyde through diazotization and Schiff-base condensation reactions [202]. This allowed them to compare the structural and spectral differences between the resulting heterocyclic azo dyes and Schiff bases. In 2014, Abuamer K. M and his colleagues studied the usefulness of Schiff base in dyeing techniques [203]. Metal complexes of the prepared Schiff base derived from salicylaldehyde (or salicylaldehyde derivatives) and 2-aminophenol or 2-aminobenzyl alcohol were considered [204].

1.7.2 Biological applications of Schiff base ligand

Schiff bases hold great significance in the field of biology, owing to their similarity in structure to naturally occurring biological molecules. A (C=N) bond in a ligand is essential for biological activities. The sp^2 hybridized nitrogen atom in the azomethine linkage contains a lone pair that plays a critical role in exhibiting these activities. These types of compounds have gained attention for their role in metalloenzymes and as biomimetic models. It has been observed that the N atom plays a crucial role in coordinating metals as the active site in many metallobiomolecules. Ligands with hetero atoms such as oxygen, nitrogen, and sulphur donors, when paired with transition metal complexes, exhibit anticancer, anti-tumour, antiviral, antifungal, analgesic, antidiabetic, antipyretic activities and antibacterial properties [205]. Few examples showing the different biological activities are addressed here. The Schiff base, *(E)-4-((benzo[d]thiazol-2- ylimino) methyl)-2-methoxyphenol*, and their metal complexes exhibit antimicrobial activity towards *S. aureus*, *Bacilus subtilis*, and *E. coli* [206]. 1-((pyridine-2-ylimino) methyl) napthalen-2-ol named ligand and its metal complexes show anticancer properties in the cancer cell line MCF-7, SkBr-3 [153]. Schiff base, *(E) -3-chloro-4-fluoro-N-(4-fluorobenzylidene)aniline* and their metal complexes possess antioxidant activity [212]. The Schiff base, *2-benzyl-4-{(E)-[(3,4-dihydroxyphenyl)methylidene]amino}-1,5-dimethyl-1,2-dihydro-*

3H-pyrazol-3-one has activity against LPS-stimulated COX-2 mRNA levels [207]. *N'-[(1E)-1-(5-bromo-2-hydroxyphenyl)ethylidene]-3,4,5-trihydroxy benzohydrazide* inhibits human acetylcholinesterase enzyme which was used to treat against Alzheimer disease [208]. *2- {(2E)-2-[(4-bromophenyl) methylidene]hydrazinyl}-N-{4-[(7-chloroquinolin-4-yl)amino]phenyl}-2-oxoacetamide* were used against a malarial infectious strain of 3D-7 P. falciparum [209].

1.7.3 Schiff base ligand as a template

The increasing popularity of nanoparticles emanating from Schiff bases in nanotechnology is due to their novelty, effortlessness, cost-effectiveness, and eco-friendliness in preparation. The critical task to obtain the nanoparticles of precise properties is the selection of a suitable capping agent. The Schiff bases hold a functional head group and one or more hydrocarbon tails that handle quantum dots' nucleation and maturation [163]. In the case of the extinction of medicinal plants, Schiff bases would vie with natural extracts as capping agents. In addition, the Schiff base ligand's cytotoxicity studies show above 90 per cent cell viability below 20 µg/ml concentrations which is an indeed intention in choosing a capping agent. Both these properties of the Schiff base ligand expose themselves as an acceptable capping agent for the synthesis of nanoparticles [210]. Nanoparticles derived from Schiff bases are found to be less reported and must be included in future researches. Schiff base-derived nanoparticles appropriate for various photonic and biological applications were reported in recent research reports. They are metal nanoparticles like Au, Ag, nickel, and copper and nonconducting nanoparticles like Ag_2S and silica nanoparticles and semiconductor nanoparticles like CdS, ZnS, CdTe, ZnSe, CuO, ZnO [163-166, 168]. Figure.1.7 shown below gives the schematic

representation of the synthesis of nanoparticles where Schiff base was used as template.

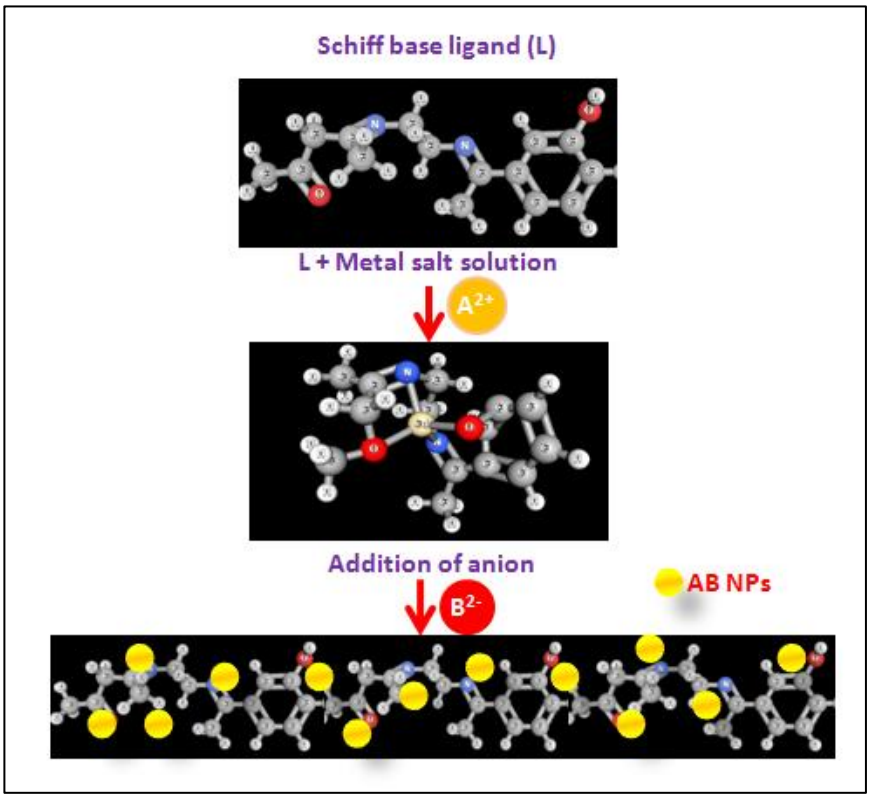

Figure.1.7 Schematic representation of formation of nanoparticles in Schiff base template.

The Schiff base-derived CdS was reported in 2013 by Shakouri-Arani M et al., utilizing the Schiff base as the sulfuring agent [211]. Schiff base ligand by coated Au nanoparticles through replacing citrate as a stabilizing agent was synthesized in 2015 and it was found to be a Fe (III) sensor [166]. Again in 2015, Zinc oxide nanoparticles were prepared by decomposing a Zn (II) Schiff-base complex created from alanine and salicylaldehyde-5-sulfonate, then coordinated with zinc acetate [212]. 2015, CuO nanoparticles were prepared using Cu (II) Schiff base complex and studied their photocatalytic activity [213]. Schiff-base, *(2-[(4-methoxy-phenylimino)-methyl]-4-nitro*

phenol) was used as a complexing agent to prepare CdS nanoparticles using the sonochemical method. The Ni (II) Schiff base complexes were thermally decomposed at 450^0C for three hours to produce pure NiO nanoparticles with an average size of 10-15 nm in 2014 [214]. In 2019, Ayodhya, D et. al, Zinc ZnS nanoparticles were synthesized through a co-precipitation method that involves using Schiff base *(2-[(4-methoxy-phenylimino)-methyl]-4-nitrophenol)* as a capping agent [164]. It has been discovered that ZnS has the potential to act as a selective photocatalyst for breaking down harmful pollutants, as well as a selective sensor for detecting heavy metal ions. F.A. Almashal et.al, synthesized Ag nanoparticles employing Schiff base, of *4-((2-hydroxybenzylidene) amino) benzoic acid*, as a capping agent and their antibacterial activities have been evaluated [215]. Omar, M.S et al, in 2020, ZnS nanoparticles were encapsulated using the co-precipitation method with the Schiff bases, *salicylaldehyde 2-methyl-3-thiosemicarbazone*, and *salicylaldehyde triazole*. They found that these ZnS nanoparticles were inactive against bacteria [165-167]. The Schiff base ligand *((1-((E)-(4-(trifluoromethoxy) phenylimino) methyl) naphthalen-2-ol))* was used for the synthesis of Au nanoparticles by chemical reduction method, reported in 2023 by G. Suneetha et.al [216]. A report in 2023 on capping of Ag nanoparticles via Schiff base ligand *N-(diphenylmethylene)-6-nitrobenzo[d]thiazol-2-amine* to form Schiff base stabilized Ag nanoparticles by co-precipitation method using $NaBH_4$ and methanol solvent [217]. These Ag nanoparticles have antibacterial properties that are related to their morphology. After reviewing the literature, it was found that limited research has been done on using Schiff base to synthesize nanoparticles. Therefore, exploiting Schiff base for the synthesizing of nanoparticles is relevant recent research fields.

1.8 Objectives of this Thesis

- Synthesis of DNA-capped CdS and Ag nanoparticles.
- Study the photonic and biological applications of DNA capped CdS and Ag NPs.
- Investigation into photocatalytic activity and fluorescence enhancement in Rh6G dye-doped sol-gel glasses of these nanoparticles.
- Also, exploration of antibacterial, larvicidal, cytotoxic effects, and bioimaging applications.
- Synthesis and study of properties of a novel Schiff base ligand.
- Examination of applications of Ni (II) metal complex of the Schiff base ligand.
- Utilization of Schiff base ligand as a template for synthesizing CdS nanoparticles
- Research on photonic and biological applications of Schiff base capped CdS nanoparticles.
- Designing a chemical sensor using the Schiff base ligand.

1.9 Relevance of this Study

This research is relevant because it integrates multiple disciplines such as nanotechnology, coordination chemistry and biology. By doing so, it opens up new possibilities for creating advanced materials that have diverse functionalities. These materials have the potential to be applied in various fields, including photonics and medicine, promising significant advancements in technology and healthcare. This interdisciplinary approach not only

expands our understanding of fundamental science but also paves the way for practical innovations that can address complex challenges in different industries.

1.10 Conclusions

This chapter offers a comprehensive introduction to the thesis. It starts with a concise overview of the topic of bionanophotonics, delving into various photonic and biological applications of nanoparticles. The importance of template synthesis is emphasized, along with a discussion on different templated nanoparticles. Special attention is given to the importance of DNA biotemplates, and a thorough literature review is presented, concentrating particularly on DNA templated nanoparticles, with a detailed examination of Ag and cadmium sulfide nanoparticles. Additionally, the introduction of the Schiff base, a biomimetic molecule, is explored, and the potential role of Schiff base templates is considered.

References

[1] Prasad P N, Introduction to biophotonics (2004) John Wiley & Sons.

[2] Chai Yeh, Applied Photonics (2012) Elsevier.

[3] Richard S Quimby, Photonics and Lasers (2006) John Wiley & Sons.

[4] Kwang-Sup Lee, Marek Samoc, Paras N Prasad, Polymers for Photonic Applications (1989) Comprehensive Polymer Science and Supplements 407.

[5] Aavishkar Katti and Yogesh Sharma, Photonic Materials: Recent Advances and Emerging Applications (2023) Bentham Science Publishers.

[6] Mool C Gupta (1997) A Handbook of Photonics 5, CRC-Press

[7] F Duport et al., Scientific Rep., 6 (2016) 22381.

[8] V Bangari et al., IEEE, 26(1) (2016) 1.

[9] P N Prasad and D J Williams, Introduction to nonlinear optical effects in molecules and polymers (1991) (Vol. 1) Wiley, New York.

[10] B E Saleh & M C Teich, Fundamentals of photonics (2019) John Wiley & sons.

[11] P Sharma et al., Adv. Colloid Interface Sci., 123 (2006) 471.

[12] Y Yang et al., Chem. Rev., 113(1) (2013) 192.

[13] S T Selvan et al., Langmuir, 26(14) (2010) 11631.

[14] R Langer, Science, 249(4976) (1990) 1527.

[15] K K Jain, Drug delivery systems (2008) (Vol. 251) Totowa, NJ, USA: Humana press.

[16] G P Dugué et al., Prog. Brain Res., 196 (2012) 1.

[17] F Pene et al., Crit. Care Med., 37(1) (2009) S50.

[18] T S Srivatsan, AS Edelstein and RC Cammarata, Nanomaterials: Synthesis, Properties, and Applications, Editors: Institute of Physics, London, 1996 (2012) 596.

[19] A S Edelstein and R C Cammaratra, (Eds.). Nanomaterials: synthesis, properties and applications. CRC press (1998).

[20] D Vollath & W V V G C KGaA, Nanomaterials an introduction to synthesis, properties and application (2008) Management 7(6), 865-870.

[21] Q Zhanget al., Chem Soc Rev, 42(7) (2013) 3127.

[22] S K Murthy, Int J Nanomedicine, 2(2) (2007) 129.

[23] J Zhou et al., Small, 14(40) (2018) 1801882.

[24] H Kim et al., Adv. Mater., 30(10) (2018) 1701460.

[25] D E Chang et al., Phys. Rev. Lett., 110(11) (2013), 113606.

[26] W Bogaerts et al., J. Light. Technol., 23(1) (2005) 401.

[27] R Thomson & S Milson, Nanostructures for Advanced Electromagnetic and Photonic Devices (2023) 11141, EasyChair,

[28] A Costela et al., Adv. Mater., 21(41) (2009) 4163.

[29] N Y Khudair and M K Dhahir, Opt. Laser Technol., 169 (2024) 110185.

[30] K Dolgaleva and R W Boyd. JOSA B, (2007) 24(10) A19-A25.

[31] N Padiyakkuth etal., Mater. Adv., (2022) 3(17), 6687-6706.

[32] Y Chen et al., Acs Photonics, 4 (4) (2017) 852.

[33] M E Stewart et al., Chem. Rev., 108(2) (2008) 494.

[34] J P Camden et al., Acc. Chem. Res., 41(12) (2008) 1653.

[35] G W Walker et al., Appl. Phys. Lett., 83(17) (2003) 3555.

[36] L Chen and H Han. Microchimica Acta, 181 (2014) 1485.

[37] D Pawar and S N Kale Microchimica Acta, 186 (2019) 1.

[38] A Urrutia et al., J. Sens., 2016 (2016).

[39] Y Xu et al., Chem. Soc. Rev., 50(1) (2021) 667.

[40] G Vicidomini et al., Nat. Methods, 15(3) (2018) 173.

[41] M Lelek et al., Nat. Rev. Methods Primers, 1(1) (2021) 39.

[42] H Na et al., Adv. Mater., 21(21) (2009) 2133.

[43] M Shilo et al., Nanomedicine, 7(2) (2012) 257.

[44] X Liu et al., Aggregate, 2(1) (2021) 4.

[45] C L Hsieh et al., Opt. Express, 17(4) (2009) 2880.

[46] M E Sakr et al., Luminescence, 29(7) (2014) 938.

[47] V Levchenko et al., Opt. Mater., 34(2) (2011) 360.

[48] B M Mastiholi et al., IOSR j. appl. phys., 6(6), 43.

[49] El-Molla et al., J. Nanomater., 28(1-A) (2017) 43-50.

[50] M M Mecheril and J Philip, AIP Conference Proceedings, 2263 (1) (2020) AIP Publishing.

[51] M Rahmandoust and M R Ayatollahi (2019) Nanomaterials for advanced biological applications, Springer (104)

[52] M I Majeed et al., J. Integrating green Chem. Sustain. Eng., (2019) 581.

[53] De Jong et al., Int J Nanomedicine, 3(2) (2008) 133.

[54] I Katouzian and S M Jafari, Trends Food Sci., 53 (2016) 34.

[55] C Jianrong et al., Biotechnol. Adv., 22(7) (2004) 505.

[56] L A Smith and P X Ma, Colloids Surf. B, 39(3) (2004)125-131.

[57] F Villanueva-Flores et al., Nanotechnology 31(13) (2020) 132002.

[58] L Pokrajac et al., ACS Nano, 15(12) (2021) 18608.

[59] E Roduner, Chem. Soc. Rev., 35(7) (2006) 583.

[60] U Manzoor et al., Phys. E: Low-Dimens. Syst. Nanostructures, 41(9) (2009) 1669.

[61] D P Hagberg et al., J. Org. Chem., 72(25) (2007) 9550.

[62] A Bayat and E Saievar-Iranizad, J. Lumin., 192 (2017) 180.

[63] M Q He et al., Nano Today, 35 (2020) 101005.

[64] R Prasad et al. Wiley Interdiscip. Rev. Nanomed. Nanobiotechnol., 8(2) (2016) 316.

[65] A Stangl et al., J. Mater. Chem., A10(5) (2022) 2528.

[66] S M Taghavi et al., Electron. Physician, 5(4) (2013) 706.

[67] S S Patil et al., Environ. Technol. Innov., 5 (2016)10.

[68] V V Mody et al., J. Pharm. Bioallied Sci., 2(4) (2010) 282.

[69] A R Sharma et al., J. Nanobiotechnology, 20(1) (2022) 1.

[70] B Nithyaja et al., Nanosci Nanotechnol, 2(4) (2012) 99.

[71] L Zhang et al., Biosens. Bioelectron., 165 (2020) 112370.

[72] S L Capehart et al., Bioconjug. Chem., 25(10) (2014) 1888.

[73] J Jana et al., RSC advances, 6(89) (2016) 86174.

[74] S Chupradit et al., Adv. Mater. Sci. Eng. 31(1) (2022) 016401.

[75] U Y Qazi and R Javaid, Advances in Nanoparticles, 5 (1) (2016) 27.

[76] O Smriti et al., Lett. Drug Design & Disc. 20 (10) (2023) 1437.

[77] S Said et al., Mater Sci Energy Technol., 3 (2020) 344.

[78] B N Nunes et al., Catalysts, 10 (1) (2020) 126.

[79] A M Smith and S Nie, Acc. Chem. Res., 43(2) (2010) 190.

[80] S Suresh, J. Nanosci. Nanotechnol., 3(3) (2013) 62.

[81] M K Sahu, Int. J. Appl. Eng. Res., 14(2) (2019) 491.

[82] B N Nunes et al., Catalysts, 10 (1) (2020)126.

[83] X Niu et al., Sens. Actuators B Chem., 255 (2018)1577.

[84] I Hammami and N M Alabdallah, J. King Saud Univ. Sci., 33(7) (2021) 101560.

[85] S J Amina and B Guo, Int J Nanomedicine,15 (2020) 9823.

[86] S Conesa-Boj et al., Nano letters, 17(4) (2017) 2259.

[87] A Mangababu et al., Appl. Surf. Sci., 589 (2022) 152802.

[88] E V Melik-Gaykazyan et al., JETP Letters, 109 (2019) 131.

[89] P K Khanna et al., Mater. Lett., 57(30) (2003) 4617.

[90] L Shang et al., Nanoscale Res. Lett., 13 (2018) 1.

[91] H F Gaiser et al., ChemComm, 56(15) (2020) 2312.

[92] C G Tu et al., Nanotechnology, 30(27) (2019) 275201.

[93] Y Wang et al., Ceram. Int., 48(7) (2022) 8882.

[94] N Dengo et al., J. Phys. Chem., C, 124(14) (2020) 7777.

[95] A Salem et al., Results Phys., 7 (2017) 1175.

[96] E Nogueira et al., Microelectron. Reliab., 52(9-10) (2012) 1853.

[97] P Chopade et al., Woodhead Publishing, (2022) 105.

[98] H Dabhane et al., J. Environ. Chem. Ecotoxicol., 3 (2021) 209.

[99] J Balakrishnan et al., Nano express, 1(2) (2020) 020015.

[100] Y Liu et al., Chem. Soc. Rev., 42(7) (2013) 2610.

[101] M R Jones et al., Chem. Soc. Rev., 111(6) (2011) 3736.

[102] H Hsueh et al., Chem. Soc. Rev., 44(7) (2015) 1974.

[103] T W Kim et al., J. Am. Chem. Soc., 127 (20) (2005) 7601.

[104] I Moriguchi et al., Chem. Lett., 11 (1999) 1171.

[105] A Dong et al., J. Am. Chem. Soc., 125 (17) (2003) 4976.

[106] A Firouzi et al., Science, 267 (5201) (1995)1138.

[107] Q Huo et al., Nature, 368 (1994) 317.

[108] M P Pileni, Nat. Mater., 2(3) (2003) 145.

[109] D C Leitao et al., Nanotechnology, 23(42) (2012) 425701.

[110] B R Thompson et al., J. Mater. Chem. A, 7(14) (2019) 8030.

[111] D Gupta et al., Environ. Res., (2023) 116316.

[112] J C Hulteen and C R Martin, Mater. Chem., 7(7) (1997) 1075.

[113] Y Xie et al., J. Nanomater., 2016 (2016).

[114] D Liu et al., Adv. Mater., 30(48) (2018) 1802104.

[115] R R Poolakkandy and M M Menamparambath, Nanoscale Adv., 2(11) (2020) 5015.

[116] T H Tsoi et al., ChemPlusChem, 82(5) (2017) 802.

[117] B J Kim et al., Langmuir, 23(25) (2007) 12693.

[118] J Lee et al., Macromolecules, 50(23) (2017) 9373.

[119] K Bolaños et al., Int J Nanomed., 14 (2019) 6387.

[120] L Rastogi et al., Mater. Sci. Eng. C., 32(6) (2012) 1571.

[121] L Lu et al., Langmuir, 19(7) (2003) 3074.

[122] Z Sui et al., Phys. E: Low-Dimens. Syst. Nanostructures.33(2) (2006) 308.

[123] U Y Qazi et al., Chem. Lett., 43(11) (2014) 1693.

[124] J Chumpol & S Siri, Artif. Cells Nanomed. Biotechnol, 46(3) (2018) 619-625.

[125] L Fageriaet al., ACS omega, 2(4) (2017), 1489.

[126] L Wang et al., Colloids Surf. A Physicochem., 257(2005). 231.

[127] J W Lee et al., Sci. Rep., 11(1) (2021) 5140.

[128] J Maityet al., Polym. Bull., 80(2) (2023) 1997.

[129] J C Ramos et al., J. Alloys Compd., 643(2015) S84.

[130] H Song et al., Nano Res., 7, (2014) 104.

[131] R Rekha et al., J. Photochem. Photobiol. B: Biol., 199 (2019)111620.

[132] A J Steckl, Nat. Photon., 1 (3) (2007).

[133] D L Xiang et al., Chem. Soc. Rev., 37, (2008) 2745.

[134] B B Lakshmi, Chem. Mater., 9(11) (1997) 2544.

[135] D Xu and G Guo, Nanowires and Nanobelts: Materials, Properties and Devices, (1) (2003) 317.

[136] S N Sarangiet al., Phys. E: Low-Dimens. Syst. Nanostructures., 42(5) (2010) 1670-1674.

[137] G R Bardajee et al., Spectrochim. Acta A Mol. Biomol. Spectrosc., 269 (2022) 120702.

[138] N Li et al., J. Phys. Chem., C115(51) (2011) 25266.

[139] D Nyamjav and A Ivanisevic. Biomater., 26(15) (2005) 2749.

[140] M M Viana et al., Ceram. Int., 36 (7) (2010) 2047.

[141] Travers et al., The FEBS journal, 282 (12) (2015) 2279.

[142] E. Heckman et al., Appl. Phys. Lett., 87 (2005) 211115.

[143] T Kentaro and O A Yoshio, J. Am. Chem. Soc., 118 (1996) 10679.

[144] L Wang et al., Chem. Mater., 13 (2001) 1273.

[145] J Hagen et al., Appl. Phys. Lett., 88 (2006) 171109.

[146] B Singh et al., J. Appl. Phys., 100 (2006) 24514.

[147] J Grote et al., Proc. SPIE, 6117, (2006) 0J1.

[148] E Heckman, Proc. SPIE, 6117(2006) 59.

[149] L Zhiguo et al., Mater. Lett., 62 (2008) 2315.

[150] Y Yong, Nanotechnology, 19 (2008) 405601.

[151] W Gang, J Phys Chem. B., 109(2005) 23941.

[152] J J Storhoff and C A Mirkin, Chem. Rev., 99 (1999) 1849.

[153] J L Coffer, et al., Nanotechnology, 3(2) (1992) 69.

[154] Y Ma et al., J. Am. Chem. Soc., 126(22) (2004) 7097.

[155] S K Kulkarni et al., Biosens. Bioelectron., 21(1) (2005) 95.

[156] N Ma et al., Langmuir, 23(26) (2007) 12783.

[157] Y Yao et al., Nanotechnology, 19 (2008) 405601.

[158] B Nithyaja et al., J. Appl. Phys., (112) (2012) 064704.

[159] L Sun et al., Appl. Surf. Sci., 252(14) (2006) 4969.

[160] V B Zon et al., Nanotechnology, 23(11) (2012), 115607.

[161] E E Tanner et al., Phys. Chem. Chem. Phys., 19(15) (2017), 9733.

[162] S Xie et al., Anal. Chem., 91(24) (2019) 1540.

[163] D Ayodhya et al., J. Fluoresc., 25(5) (2015) 1481.

[164] D Ayodhya and G Veerabhadram., J Mater., 5 (2019) 446.

[165] M S Omar et al., Synthesis, 11 (2020) 1309-1318.

[166] A A Jimoh et al., J. Nanomater., 16(1) (2015) 190.

[167] M Masjedi et al., Superlattices Microstruct., 62 (2013) 30.

[168] N N M Shahri et al., RSC Adv., 12 (2022) 3136.

[169] K Subin Kumar and K K Aravindakshan K K, Results Chem., 3(2021) 100129.

[170] N Dhar Do and C L Taploo, J. Sci. Ind. Res., 41 (1982) 501.

[171] P Przybylski et al., Curr Org Chem., 13 (2009) 124

[172] S Cleiton M Da et al., J. Adv. Res., 2 (1) (2011) 1.

[173] A Kajal et al., J. Catal., 2013 (2013).

[174] K Sneha and Dhanya, J. Electron. Mater., (2021) 1.

[175] K Subin Kumar, J Coord Chem., 74(16) (2021) 2798.

[176] K Subin Kumar, Results Chem., 4 (2022) 100463.

[177] P Espinet and K Soulantica, Coord. Chem. Rev., 193(1999) 499.

[178] Berhanu et al., Trends in Anal. Chem., 116 (2019) 74.

[179] L Fan et al., Sens. Actuators B Chem., 203 (2014) 550.

[180] L Fan et al., J. Lumin., 155 (2014) 84.

[181] B Derkowska-Zielinska et al., Opt. Laser Technol., 124 (2020) 105968.

[182] K N Bhat et al., Mater. Chem. Phys., 44 (1996) 261.

[183] J P Costes eta l., Inorg. Chem., 44 (2005) 1973.

[184] N Ananthi et al., Opt. Photon. J., 2 (2012) 40.

[185] SBonhommeau et al., J. Phys. Chem. C, 116 (2012)11251.

[186] V M Herrera-Ambriz et al., J. Phys. Chem. C, 115 (2011) 23955.

[187] H J Jung et al., Tetrahedron Lett., 51 (30) (2010) 3962.

[188] Ghorai et al., New J.Chem., 40(9) (2016) 7821.

[189] Abou-Omar et al., ACS omega, 6(32) (2021) 20812.

[190] L Hou, et al., J. Mater. Chem., B, 5(45) (2017) 8957.

[191] K P Carter et al., Chem. Rev., 114(8) (2014) 4564.

[192] Y Jeong et al., Inorganica Chim. Acta, 381 (2012) 2.

[193] P B Tchounwou et al., J Mol Clin Environ Toxicol, 101 (2012) 133.

[194] S Y Lee et al., Tetrahedron, 72 (2016) 5563.

[195] N Bhuvanesh et al., J. Photochem. Photobiol. A, 360(2018) 6.

[196] D Udhayakumari and V A Inbaraj, J Fluoresc., 30(5) (2020)1203.

[197] Y Wu et al., Spectrochim Acta A, 223 (2019)117315.

[198] S Kagatikar and D Sunil, Electron. Mater., (2021) 1.

[199] J Zhang et al., Org. Electron., 42 (2017) 153.

[200] L Lepnev et al., Synth. Met., 159 (2009) 625.

[201] K Sneha and S Dhanya, J. Elec. Mater. (2021) 1.

[202] T Tao et al., Dyes Pigm., 92(3) (2012) 916.

[203] D Maity, Int. J. Res. Anal. Rev., 6(2) (2019) 471.

[204] M A Ashraj et al., International Proceedings of Chemical, Biological and Environmental Engineering, 10 (2011) 1.

[205] M Sadia et al., J. King Saud Univ. Sci., 33 (2020)101331.

[206] A Mermer et al., J. Mol. Struct., 1181 (2019) 412.

[207] N S Asfandiyarova and E V Philippov, Terapevticheskii arkhiv., 92 (1) (2020) 82.

[208] JO Adebayo et al., Parasitol. Res., 119 (2020) 2749.

[209] T Senasu and S Nanan, J. Mater. Sci. Mater., 28(23) (2017) 17421.

[210] S A Osman et al., J. Serb. Chem. Soc., 79 (2014) 953.

[211] M Shakouri-Arani and M Salavati-Niasari, New J Chem., 38 (2014) 1179.

[212] M Gharagozlou eta l., Ceram. Int., 41(7) (2015) 8382.

[213] E M M Ibrahim et al., Mater. Res. Bull., 107 (2018) 492.

[214] A D Khalaji and D Das, Int. Nano Lett., 4 (2014) 1.

[215] F A Almashal et al., Egypt. J. Chem., 63(3) (2020) 813.

[216] G Suneetha et al., Results Chem., 5 (2023) 100688.

[217] K Kumar et al., J. Indian Chem. Soc., 100(4) (2023) 100965.

[218] T A Nibila et al., Res. in Chem., 2 (2020) 100062.

[219] J Chumpol & S Siri, J. Nanosci. Nanotech., 20(3) (2020)1678-1684.

[220] A S Zhuk et al., Int. J. Mol. Sci., 24(15) (2023) 12163

Chapter 2

Synthesis Methods and Characterization Techniques

This chapter describes various procedures used for the preparation and characterization of nanoparticles. The ultrasonic irradiation method was well utilized while synthesizing nanoparticles. Incorporation of nanoparticles into silica glass matrix and related studies are a part of this thesis. Therefore, the experimental details related to this are also incorporated here. A detailed description of different characterization techniques and essential information on different biological applications and photocatalytic activity are also accommodated in this chapter.

2.1 Introduction

This chapter provides a complete overview of different procedures employed in the preparation and characterization of nanoparticles. A particular attention is given to the effective utilization of the ultrasonic irradiation method during the synthesis of nanoparticles. Furthermore, the chapter investigates into the incorporation of nanoparticles into a silica glass matrix, offering insights into the related studies explored within this thesis. Detailed experimental procedures associated with these processes are also included.

In addition to the synthesis and incorporation aspects, the chapter furnishes an in-depth exploration of various characterization techniques essential for analysing nanoparticles. Furthermore, it incorporates valuable information on diverse biological applications and the photocatalytic activity of the synthesized nanoparticles. However, detailed descriptions of specific synthesis procedures and experimental setups can be found in the relevant chapters.

The literature survey revealed different synthesis methods for the preparation of nanoparticles. A chemical co-precipitation method is adopted to synthesize CdS nanoparticles and chemical reduction method for synthesizing Ag nanoparticles. These reactions were accomplished through the ultrasonic irradiation method.

Several techniques were employed to characterize the synthesized samples. The optical studies conducted through UV-visible absorption spectra and photoluminescence spectra. The absorption spectra were obtained using Shimadzu UV-1800 UV-vis Spectrophotometer. Fluorescence spectra were attained using the Horiba Fluorolog 3 Fluorescence Spectrometer. The crystallinity of the samples was accomplished through X-ray diffraction

studies. Powder XRD patterns of the synthesized samples were recorded at room temperature conditions by Rigaku Ultima IV, Japan, X-ray diffractometer utilizing Cu Kα radiation (λ = 1.54182 Å) operating at 35 kV and 25 mA. The surface morphology of the samples was obtained using SEM (Jeol 6390LA/OXFORD XMX N) and TEM (Joel/JEM 2100). A Floid Evos imaging system was used to visualize the cellular imaging at 20X magnification.

2.2 Experimental Techniques

Chemical co-precipitation method was used for the preparation of CdS nanoparticles and chemical reduction scheme was used via ultrasonic irradiation for the preparation of Ag nanoparticles.

2.2.1 Chemical coprecipitation method

The co-precipitation technique is popular in the delivery of materials and precursors required for a reaction to produce a desired product. Its main objective is to create multi-component materials by forming intermediate precipitates, usually in the hydrous oxides or oxalates forms. This technique ensures that the components are thoroughly mixed during precipitation, and chemical homogeneity is maintained upon calcination. In the coprecipitation process, aqueous metal salts are combined with a base at high temperatures for acting as precipitating agent. This method is basically used for synthesis, and on occasion, it is carried out under an inert atmosphere.

When using the coprecipitation method for synthesis, one of its advantages is that it can create a crystalline size within a specific range liable on the chosen precipitating agent. Moreover, by adding capping agents, the shape as well as size of the crystals can be altered. On the other hand, this method requires multiple rounds of washing, drying, and calcination to achieve a pure

phosphor phase, which is a disadvantage [1]. Figure. 2.1 shows the schematic representation of synthesis of nanoparticles in coprecipitation method.

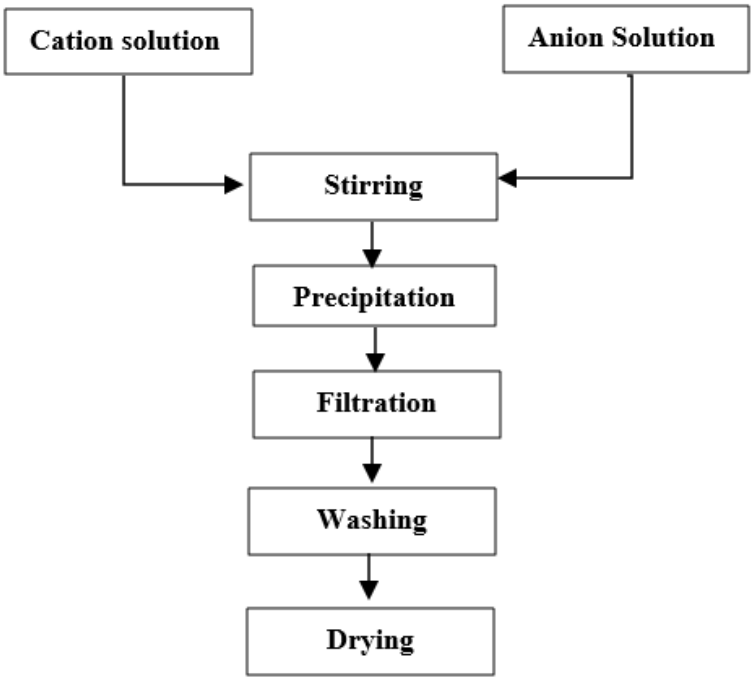

Figure.2.1 Typical coprecipitation method for the synthesis of nanoparticles.

2.2.2 Chemical-reduction method

Metallic nanoparticle synthesis through chemical-reduction method involves three stages. These are the reduction of metal salts using reducing agents, the stabilization of ionic complexes, and the size control with a capping agent. This method has been used to create various types of metallic nanoparticles. Sodium borohydride is a strong reductant while citrate is a weak reductant. Smaller nanoparticles are produced by stronger reducing agents. Figure.2.2 gives the schematic representation of chemical reduction method for synthesizing nanoparticles [2].

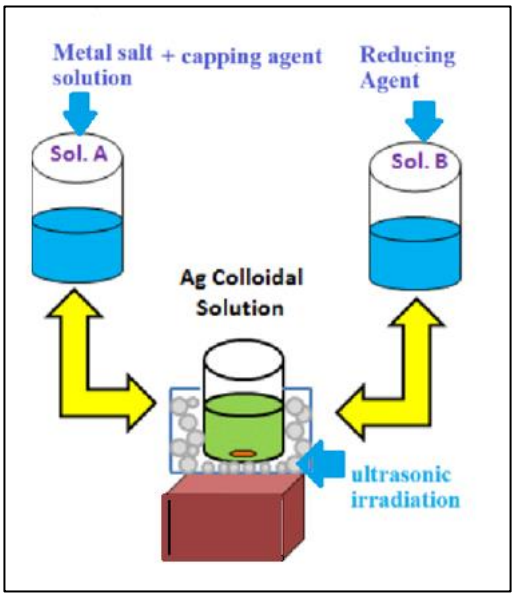

Figure.2.2 Schematic representation of chemical reduction method for the synthesis of nanoparticles.

2.2.3 Ultrasonic irradiation method

The ultrasonic irradiation method is exploited for all synthesis parts. The CdS and Ag nanoparticles were synthesized using template directed synthesis by ultrasonic irradiation. DNA and a novel mixed Schiff base ligand were used as templates for synthesizing of CdS nanoparticles. Ag nanoparticles were prepared using DNA template as followed by earlier literatures [3]. The Schiff base template synthesis did not result in the nanoparticle formation in the case of Ag. Dark brown precipitate was formed which indicate the formation of bulk Ag. The prepared CdS and Ag nanoparticles were used for different photonic and biological applications.

The sonochemical (ultrasonic irradiation) method is a simple and efficient technique for the preparation of nanoparticles. When ultrasonic waves pass through liquids and a large number of micro bubbles form, grow, and collapse within a few microseconds called ultrasonic cavitation. According to the

sonochemical theory calculations, a rigorous environment can be created by ultrasonic cavitation with temperatures and pressures approaching 5000 K and 500 atm, respectively, with heating and cooling process are exceeding at the rates 109 K/s. Therefore, ultrasound has been extensively applied in particles' blending, grinding, dispersion and activation. By taking advantage of the multiple effects of ultrasound, one can break down the aggregates of nanoparticles [3-4].

The ultrasonic irradiation of liquids induces ultrasonic cavitation, which creates various chemical and physical effects that facilitate chemical reactions. The method is quick, simple, and allows for the synthesis of nanoparticles with controllable morphologies, various shapes, and assemblies such as nanobelts, nano rings, core-in-shell, and cluster-in-cluster bimetallic nanoparticles. However, it is not suitable for heat-sensitive materials, is an energy-intensive process, and has difficulty with scale-up [5].

DNA capped CdS and Ag nanoparticles were used to study the fluorescence variations in rhodamine 6G doped sol-gel derived glasses. They were also used to study the photocatalytic activity of rhodamine 6G and methylene blue dyes.

2.3 Preparation of Rh6G doped sol-gel derived glasses

The Rh6G doped sol-gel glasses were prepared by the following method. A 5 ml ethanolic solution of 0.01 mM Rh6G is added to 5 ml ethanol and kept under stirring for 10 minutes. A 10 ml of TEOS is added to this mixture and stirred well. One or two drops of acid like HCl were dropped to the reaction mixture to fasten the sol-gel process. The stirring continued for another 30 minutes, 10 ml of the clear solution was poured into petri dish of diameter 10 cm and kept undisturbed for one week. The coloured sol-gel glass obtained

was transparent and the average thickness and diameter of the derived glasses are 1±0.25 mm and 7±0.5 cm respectively.

2.4 Characterization Techniques

2.4.1 Structural and morphological characterizations

Structural and morphological characterizations are important in understanding and optimizing the applications of nanoparticles, which exhibit unique properties due to their dimensions (1-100 nm). Detailed analyses, including X-ray diffraction, electron microscopy, and spectroscopy will reveal factors like size, shape, crystal structure, and composition. These insights inform the design of nanoparticles tailored for diverse fields, such as medicine, electronics, catalysis, and materials science. Comprehending nanoparticle intricacies is vital for unleashing their full potential in developing innovative technologies.

(a) X-ray diffraction studies

The XRD enables both quantitative and qualitative analysis of crystals. The three-dimensional array of oscillators in crystals can be probed at various angles using monochromatic X-rays, giving information on nanomaterial phase and unit cell dimensions. The XRD procedure comprises high-energy particles colliding with matter, ejecting electrons and producing characteristic X-rays. Specifically, Kα radiations, such as the doublet Kα1 and Kα2 from copper, are generally used in diffractometers for crystal diffraction, with the powder diffraction method applying Bragg's law for structural and phase identification. The interaction with lattice planes results in radiated light experiencing constructive or destructive interferences, aiding in crystal analysis [6].

A diffractometer contains of a radiation source, sample, and detector, like a photographic plate or a sophisticated counter. In the Debye-Scherrer process, finely grounded powder is exposed to monochromatic X-rays, and diffracted beam intensity is estimated as the detector collects reflections from various nanocrystal planes. Peak positions are compared for phase and plane identification, giving crystal structure and quantitative phase analysis. X-rays cause electron vibrations through elastic or inelastic collisions. Coherent scattering results from elastic collisions, whereas inelastic collisions cause Compton scattering. The total scattering intensity, summing powers from each electron, is estimated. A convergent X-ray beam improves sensitivity and resolution when the source and detector align on the same circle. In Bragg's condition, diffraction happen precisely one wavelength behind the previous plane due to constructive interference. The diffraction peak width reflects the number of planes in the crystallites. Finally, the Scherrer formula is employed to compute the size of the crystallites [7].

$$d = \frac{0.9\lambda}{\beta\cos\theta}$$

Where d and λ are respectively the crystallite size and the wavelength of the X-rays used, 1.5406 Å, β is the full width at half maximum, and θ is the diffraction peak angle.

As crystallite size decreases, the diffracted lines show increased broadening. This broadening, observable in XRD patterns can be applied to estimate particle sizes up to 200 nm using the given equation. Additionally, non-uniform stress within the crystallites contributes to pattern broadening. XRD serves as a valuable technique, offering crucial insights such as compound phase identification i.e., whether it is amorphous or crystalline, measurement of degrees of crystallinity, determination of crystal structures, assessment of crystallite sizes, orientation analysis of single crystals, quantitative phase

analysis, and determination of residual stress in crystals [6-7]. Powder XRD patterns of the synthesized samples were recorded at room temperature conditions by Rigaku Ultima IV, Japan, X-ray diffractometer utilizing Cu Kα radiation (λ = 1.54182 Å) operating at 35 kV and 25 mA, at CMET, Thrissur.

(b) SEM

The SEM utilizes a focused electron beam to scan a sample, generating images by detecting signals resulting from electron interactions with the sample atoms. This approach provides valued information about both the surface topography and composition of the sample. The components of the SEM instrument are Electron source, Anode, Condenser lens, Scanning coils, Objective lens.

The electron source of the microscope is responsible for producing electrons at the top of its column. Then these electrons are attracted to the anode plate, and form a beam. The beam size is estimated by the condenser lens, which can control the number of electrons in it. This size determines the image's resolution. Apertures control beam size. The scanning coils deflect the beam along the X and Y axes to ensure that it properly scans the surface of the sample. Finally, the objective lens, last in the lens sequences, focuses the beam onto a small spot on the sample. As SEM lenses are electromagnetic, they are made up of a coil of wires inside metal poles. These coils generate a magnetic field when a current passes through it. The electrons are affected by it, allowing the microscope to control them [8-9].

The sample preparation for SEM imaging includes sample size, shape, state, and conductivity. Non-conductive samples necessitate coating with materials like Au, Ag, platinum, or chromium to improve conductivity and prevent electron beam damage. Confirming sample cleanliness is crucial for clear imaging. Preserve structural integrity with a fixative or alcohol dehydration.

Before vacuum exposure, make sure complete sample dryness to prevent water vaporization interference with the electron beam and keep image clarity [10].

(c) TEM

Transmission electron microscopy involves passing beams of electrons through a biological specimen or sample to generate high-resolution, magnified images revealing surface topology. The TEM is a particularly designed tool used for analysing and visualizing samples within a specified range of dimensions from 1 µm to 1 nm. It can reveal highly detailed information that is not accessible by traditional light microscopes.

The transmission electron microscope contains an electron source, commonly referred to as a gun or electron canon. The gun is typically made of either lanthanum hexaboride or tungsten and has a V-shaped filament. An electric potential is applied to the anode, which causes the filament (cathode) to warm up and produce an electron current. The De Broglie equation determines the wavelength of the electron [11].

$$\lambda = \frac{h}{[2m_0 eV(1 + \frac{eV}{2m_0 c^2})]^{1/2}}$$

Where λ is the wavelength, h is the Planck constant, m_0 is the residual mass of the electron, e is the charge of the electron, V is the potential difference, and c is the speed of light.

After this, the electron beam hits the sample where several processes are experienced in which the electrons that affect the sample are dispersed avoiding the loss of energy (elastic) and other processes in which electrons

hand over part of their energy to internal electrons of the sample (inelastic). Next, there is the objective lens which has the function of focusing the scattered beams to form the first image thanks to a diffraction process performed by the projection lens which expands the electron beam and reflecting in the phosphor screen [12-13].

During the sample preparation for TEM imaging, critical consideration is ensuring the technique employed does not affect the observed sample. Two key sample types are self-supported and supported. Self-supported samples undergo thinning processes to attain 100-200 nm sheets, followed by cutting into 3 mm diameter discs and polishing via different methods. Supported samples are deposited onto copper grids by fragmenting the material in an agate mortar, disintegrating it in a solvent such as ethanol or acetone, depositing drops on the grid, allowing solvent evaporation, and introducing the sample under the microscope [14].

2.4.2 Optical Studies

(a) UV – visible absorption spectroscopy

UV-visible absorption spectroscopy is a method that uses electromagnetic radiation with wavelengths between 190 nm and 800 nm. It is employed for analyzing how a substance absorbs and transmits ultraviolet and visible light, offering insights into its electronic structure and concentration. The overall energy of a molecule comprises electronic, vibrational, and rotational energy components. When UV rays are directed to the molecule, it causes a shift in the electronic energy levels. The spectrometer then records the wavelengths at which the absorption of UV occurs in the material, resulting in a graph of absorption versus wavelength. The basic principle behind the operation of the UV-Vis spectrometer is Beer Lambert's law. The equation governing it is given by [15],

$$A = \varepsilon l c$$

Where A is the absorption (arb. units), ε is the molar absorptivity (M^{-1} cm^{-1}), l is the length of the cuvette or sample holder and c is the molar concentration of the solution [16]. Furthermore, the Beer-Lambert law can be employed for quantitative analysis, finding the concentration of a solution based on the extinction coefficient, absorbance, and path length of light.

The band gap energy (E_g) is a crucial factor in determining a material's optical properties and can be estimated through the absorption coefficient and photon energy relationship. Both direct and indirect electronic transitions can occur, with the latter involving both photons and phonons. The equation $\alpha h\upsilon = (h\upsilon - E)^n$ relates the absorption coefficient and photon energy (hν), the exponent n indicates the type of electronic transition that causes absorption [17].

To determine the band gap energy of materials, scientists use a Tauc plot which graphs ($\alpha h\upsilon$) against hυ and extrapolates to the X-axis. This plot takes into account both the absorption data and the sample thickness. For powder samples, scientists disperse the powder in solvents such as water and ethanol to conduct UV-visible absorption spectroscopy analysis. However, this method is limited for powder samples as the chance for precipitation increases as particle size decreases [16].

UV-visible spectrometer includes essential components like a light source, monochromator, sample holder, detector, and signal processor. Deuterium discharge lamps are used for UV measurements, while tungsten-halogen lamps are employed for visible and near-infrared measurements. The monochromator disperses incoming light into components, allowing a known wavelength to pass through. A quartz cuvette holds the sample and reference, and a photomultiplier tube acts as the detector for computer output. UV-

visible spectroscopy is valuable for impurity detection, structural elucidation, and certain quantitative analyses. Furthermore, the Beer-Lambert law can be employed for quantitative analysis, finding the concentration of a solution based on the extinction coefficient, absorbance, and path length of light. The UV-visible absorption spectra of the samples were obtained using the Shimadzu UV-1800 UV-vis Spectrophotometer.

(b) Photoluminescence Spectroscopy

Photoluminescence (Fluorescence) spectroscopy is an analytical technique that comprises the absorption of photons by a molecule in its ground state, followed by the emission of longer-wavelength photons upon relaxation to the ground state. This emitted fluorescence gives valuable information about the molecular structure, concentration, and environment of the fluorescent species. Its sensitivity, non-invasiveness, and capability to provide real-time information make fluorescence spectroscopy an indispensable tool in modern scientific research and diagnostics [18-19]. The photoluminescent experiments studied in this thesis were conducted using the Horiba Fluorolog 3 Fluorescence Spectrometer.

2.4.3 Chromaticity Studies and CCT

Chromaticity studies comprise the examination and analysis of colours, specifically their characteristics and relationships. Chromaticity is a concept in colour science that focuses on the quality of colour, independent of its brightness, and is often represented as a point in a colour space. One commonly used colour space is the Commission International d'Eclairge (CIE)1931 XY chromaticity diagram, where chromaticity coordinates (x, y) describe the hue and saturation of colour. Chromaticity studies are essential in various fields, including lighting, imaging, and displays as they provide a systematic approach to understanding and reproducing colours accurately.

These studies help to define colour gamuts, analyze colour rendering properties, and optimize colour reproduction in diverse applications, contributing to advancements in industries such as design, photography, and technology. This colour space can be employed to compute different parameters like dominant wavelength, colour purity, and CCT. The colour purity of the prepared samples can be estimated according to the formula [20-21],

$$\frac{\sqrt{(x-x_n)^2+(y-y_n)^2}}{\sqrt{(x_i-x_n)^2+(y_i-y_n)^2}} \times 100\%$$

Where (x, y) are the CIE chromaticity coordinates; (x_n, y_n) refers to CIE chromaticity coordinates for the white point and (x_i, y_i) are the coordinates of the dominating wavelength. These investigations were carried out using an OHSP350 spectrometer with a wavelength range of 380-780 nm.

2.5 Photonic Applications

Nanoparticles are best suitable photocatalyst for photocatalytic activity which initiate under the light and catalyst. Semiconductors are the most efficient photocatalyst due to their remarkable photocatalytic activity and wide band gap in visible region.

Nanoparticles embedded in dye-doped sol-gel glasses have garnered significant attention for their applications in photonic technologies. Additionally, the incorporation of nanoparticles into dye-doped sol-gel glasses enhances the fluorescence properties of the system. This collaborative effect results in improved light emission characteristics, finding applications in advanced sensors, imaging technologies, and optoelectronic devices.

Industrial waste in wastewater treatment has evolved into a serious health problem in recent decades due to the growth of industries. Consequently,

wastewater treatment methodology has been the subject of intense research in recent years. Dye-containing wastewater demands highly effective treatment due to its acute toxicity. Several dyes are potentially canned annually from textile, ink, paper, pharmaceutical, cosmetic, and other industries [22-26]. Based on reduced time and energy efficiency procedures, photocatalysis was an adequate alternative approach in comparison with other methods. Recent research ascertained that semiconductor nanoparticles are good alternatives for photocatalyst [27-28].

The photodegradation of organic dye solutions by CdS and Ag nanoparticles was studied. To do this, chose two organic dyes; Rh6G and MB. In this particular procedure, 10 mg of CdS or 10 ml of Ag nanoparticles is added to 100 ml of 10^{-5} M aqueous dye solutions and stirred under a dark environment for 30 minutes in an ultrasonicator, which ensure the adsorption-desorption equilibrium among the nanoparticles. A UV light of wavelength 254 nm irradiation with continuous stirring was provided to the reaction mixture. In a study, it is exhibited that the rate of degradation of pollutants was faster using UV than solar light. It is shown that shorter wavelengths have a greater chance of trapping electron-hole pairs than long wavelengths of visible light. Furthermore, only 5% of the solar spectrum contains UV light, limiting the potential for very good results [29]. The degradation of the dye solutions was monitored at regular intervals (0, 25, 50, 75, 100, and 120 minutes) using a UV-Vis spectrophotometer. The procedure is repeated without nanoparticles to study the photocatalytic efficiency of L-CdS. The formula can find the photodegradation [30],

$$\%\ of\ degradation = \frac{A_0 - A_T}{A_0} \times 100$$

Where, A_0 is the initial absorbance of dye and A_T is the absorbance of the dye after irradiation in a particular time interval.

The procedure for the fluorescence enhancement of Rh6G doped sol-gel glasses in the presence of CdS and Ag nanoparticles are described in the concerned chapters.

2.6 Biological Applications

In this thesis, it has been included four different biological applications of nanoparticles and other exclusive biological applications like antioxidant activity of Schiff base ligand and its complex was incorporated in the respective chapter.

2.6.1 Antibacterial activity

The antibacterials present in the samples can diffuse into the medium and interact in a plate freshly seeded with the test organisms. The resulting inhibition zones will be uniformly circular as there will be a confluent lawn of growth. Three microbes were taken in this procedure: two Gram positive, *Staphylococcus aureus* and *Streptococcus mutans*, and one Gram negative, *Pseudomonas aeruginosa*. These organisms were cultured on 20 ml Muller Hinton agar plates. Wells of approximately 10 mm were bored using a cutter. 1000 µg/ml of sample was taken. After 24 hours of incubation at 37^0C, the plates were removed. The antibacterial activity was examined by measuring the diameter in millimeters of the inhibition zone formed around the well [31]. In this study, streptomycin was used as a standard antibacterial agent.

2.6.2 Cytotoxicity Assay: MTT Assay

In MTT assays, the reductase enzyme within the mitochondria of living cells reduces the MTT mixture into purple formazan crystals, which are subsequently soluble in DMSO. The absorbance of the coloured solution is assessed at 595 nm, using 655 nm as the reference wavelength. This reduction process occurs exclusively when

mitochondrial reductase enzymes are active, permitting the conversion rate to be directly correlated with the number of viable (living) cells. Evaluating cytotoxicity includes comparing the purple formazan production of cells treated with a drug to untreated control cells, where a decrease in purple indicates potential effects on cancer cells. Conversely, if the drug does not induce cytotoxicity, live cells' mitochondrial reductase enzymes will convert MTT to purple formazan, resulting in a more intense purple colour.

For the cytotoxicity test, HeLa cells, a human cell line, were utilized. These cells were cultured in a T-25 flask with complete minimum essential medium (DMEM) supplemented with 1% antibiotic solution (1X) and 10% FBS for 2-3 passages to maintain exponential growth. The culture took place in a CO_2 incubator with 5% CO_2, 37^0C, and a humidified atmosphere. Upon reaching confluence, the medium was carefully removed, the flask was washed with 1X phosphate-buffered saline (1XPBS), and 1.5 mL trypsin was added. After a 2-minutes incubation at 37^0C, a 1.5 mL complete DMEM solution was added to neutralize the trypsin. After, the cells were centrifuged at 2000 rpm for 5 minutes, and the pellet was resuspended in 1 mL of complete DMEM. For the assay, 10,000 cells per well were seeded in 96-well plates and incubated for 24 hours in a CO_2 incubator.

The next day the depleted media was aspirated, and required amounts of samples were added in triplicates for the treatment. Cells without drug were kept as control, and media without cells were kept blank. The plate was then incubated in a CO_2 incubator for 24 hours. 10µL of MTT reagent was discharged to each well and covered with aluminium foil (as MTT is light sensitive), followed by 3 hrs incubation at 37^0C. After the incubation period, the media was removed carefully, and 100 µLof DMSO was poured to each well. The plates were then kept for 10-15 minutes on a platform shaker so that the formazan crystals get dissolved. The absorbance reading was

assessed at 595 nm and 655 nm as reference wavelengths using iMark Microplate Reader S/N 21988 [32]. The equation calculates survivability percentage [33],

$$Survivability\ \% = \frac{sample\ average}{control\ average} \times 100$$

Where sample average and control average mean that the blank corrected average value of difference of absorption value at 655 nm and 595 nm.

2.6.3 *In-vitro* Bioimaging

For bioimaging studies, HeLa cells, 1×10^4 cells per well, were cultured in a 96-well plate with coverslips and incubated overnight at 37^0C so that the cells were attached to the surface of the cell-cultured plate. A required amount of the samples was added to the HeLa cells and incubated for 24 hours. Cells without drug were kept as control, and media without cells were kept blank. The plate was then incubated in a CO_2 incubator for 24 hours. After 24 hours of treatment, cells were viewed under a fluorescence microscope. The Floid Evos imaging system was used to visualize the cellular imaging at 20X magnification.

The Floid Evos imaging system is a useful platform intended for fluorescence and transmitted light imaging in biological applications. The fluorescence mode uses specific excitation and emission filters to illuminate and capture fluorescently labelled samples, providing comprehensive insights into cellular components. Furthermore, the system offers brightfield imaging for unstained samples, allowing for the observation of cell morphology [34].

2.7 Conclusions

This chapter provides a comprehensive overview of various synthesis methods and techniques employed for the preparation and characterization of nanoparticles. Additionally, the chapter goes beyond synthesis and extends its scope to encompass the characterization it explains the techniques crucial for understanding the properties of the prepared nanomaterial samples. Furthermore, expands to comprise detailed procedures for diverse photonic and biological applications of these nanomaterials.

References

[1] W S Peternele et al., J. Nanomater., 2014, (2014) 94.

[2] O Mustapha et al., In Functionalized graphene nanocomposites and their derivatives Elsevier (2019) 21.

[3] H Xia and Q Wang, Chem. Mater., 14(5), (2002) 2158.

[4] R Mahdavi, and S S A Talesh, Ultrasonics Sonochemistry, (39) (2017) 504.

[5] J A Fuentes-García, Ultrasonics Sonochemistry, 70 (2021) 105274.

[6] D D Le Pevelen, Small molecule X-ray crystallography, theory and workflow (2010) 2559.

[7] H H Perkampus, UV-VIS Spectroscopy and its Applications. Springer Science & Business Media (2013).

[8] K D Vernon-Parry, Scanning electron microscopy: an introduction. III-Vs review, 13(4) (2000) 40.

[9] A Mohammed and A Abdullah, International Conference on Hydraulics and Pneumatics-HERVEX, Băile Govora, Romania, (2018) 7.

[10] P Echlin, Handbook of sample preparation for scanning electron microscopy and X-ray microanalysis. Springer Science & Business Media (2011).

[11] E J S Fonseca et al., Phy. Rev. Lett., 82(14) (1999) 2868.

[12] M Winey et al., Conventional transmission electron microscopy. Molecular biology of the cell, 25(3) (2014) 319.

[13] C F Escalante, Fundamentals of transmission electron microscopy, the technique with the best resolution in the world (2019).

[14] D S Rao et al., TEM specimen preparation techniques. Microscopy: science, technology, applications and education, 2 (2010) 1232.

[15] Pfeiffer et al., J Chem. Edn 28 (3) 1951 123.

[16] H Förster, UV/vis spectroscopy Characterization, Springer I (2004) 337.

[17] S Usharani & V Rajendran. Journal of Science: Advanced Materials and Devices, 2(3) (2017) 333-339.

[18] CA Royer, Fluorescence spectroscopy, (1995) 65.

[19] A Sharma and S G Schulman, Introduction to fluorescence spectroscopy New York: Wiley (13) (1999).

[20] Y Shi et al., Dalton Trans., 43(6) (2014) 2418.

[21] B Das et al., Results Opt., (2020) 100013.

[22] Gamal El-Din, Sci. Total Environ., 809 (2020) 151120.

[23] Z Charikleia J. Environ. Manag., 297 (2021) 113301.

[24] W Long et al., Colloids Surf. A Physicochem., 650 (2022) 129468.

[25] P Fatemeh et al., Sustain. Chem. Pharm., 23 (2021)100501.

[26] A Bahadoran et al., J. Photochem. Photobiol. B, Biol., 228 (2022) 112393.

[27] Y Zahraa et al., Dyes Pigm.,159 (2018) 49.

[28] W Guo et al., Tetrahedron Lett., 57 (2016) 3801.

[29] B Xu et al., Chemosphere, 243 (2020) 125366.

[30] D Ayodhya and G Veerabhadram, J. Materiomics, 5 (2019) 446.

[31] S Naranthatta et al., ACS omega, 6 (2021) 8646.

[32] National Committee for Clinical Laboratory Standards Fifth Edition Approved Standard M2–A5 NCCLS, Villanova, PA (1993)

[33] D Henry et al., X-ray reflection in accordance with Bragg's Law. Integrating Research and Education (2012).

[34] H S Lahoti et al., Cureus., 14(9) (2022).

Chapter 3

Photonic and Biological Applications of DNA-capped CdS Nanoparticles

This chapter is dedicated to the comprehensive investigation of DNA-capped CdS (D-CdS) nanoparticles, covering their synthesis, characterizations, and various applications. The synthesis of CdS NPs is achieved through the application of ultrasonic irradiation, with DNA serving as a biotemplate. The synthesized nanoparticles are characterized through UV-visible absorption spectrum and XRD. Their morphology and dimensions were assessed using SEM and TEM. Furthermore, photoluminescence experiments are conducted to determine the emission wavelengths of the samples. The first section of the chapter explores the influence of D-CdS nanoparticles on the photoluminescence of Rh6G doped sol-gel derived glasses. The results obtained indicate that D-CdS NPs have a pronounced effect on the photoluminescence of Rh6G doped sol-gel glasses. Not only do they enhance the photoluminescence, but they also demonstrate the capability to tune the emission peak of the Rh6G doped glasses. This tuning effect is achieved by adjusting the concentration of D-CdS nanoparticles in the composite material. Additionally, the chapter explores the photocatalytic properties of D-CdS nanoparticles, the results shows that they are potential photocatalysts for Rh6G and MB. This part provides insights into the potential applications of D-CdS in areas related to optics and catalysis. The second part focuses on biological applications. The biological relevance of D-CdS nanoparticles is examined in terms of their antibacterial activity, cytotoxicity, and bioimaging capabilities. This section sheds light on the potential use of D-CdS in biomedicine, particularly for applications related to antibacterial agents, cell toxicity assessment, and imaging.

The results of this chapter are published as:

1. Reena V N, Misha H, Bhagyasree G S, Nithyaja B. (2022). Enhanced photoluminescence and colour tuning from Rhodamine 6G-doped sol–gel glass matrix via DNA templated CdS nanoparticles. *AIP Advances*, 12(10) 105217. (Publisher: AIP)
2. Reena V N, Bhagyasree G S, Shilpa T, Aswati Nair R, Misha H, Nithyaja B. (2024). Photocatalytic, Antibacterial, Cytotoxic and Bioimaging Applications of Fluorescent CdS Nanoparticles Prepared in DNA Biotemplate. *Journal of Fluorescence*, 34(1) 437. (Publisher: Springer Nature)

3.1 Introduction

Deoxyribonucleic acid (DNA), a bio-organic polymer, is an important biotemplate for the synthesis of inorganic nanomaterials due to its well-defined sequence of DNA base and a variety of super helix structures. Investigations on the preparation of nanomaterials discovered that DNA can act as "smart glue" for gathering nanoparticles (NPs) [1-5]. The development of functionalized nanomaterials using proteins, peptides, nucleic acids is the current advances in biotechnology. Many metal nanoparticles (NPs), semiconductor NPs were effectively prepared using DNA biotemplate. Metal NPs of gold, silver, nickel, palladium, copper, and platinum and semiconductor NPs of cerium oxide, CdS were synthesized using DNA template [6-12].

In this chapter, the synthesis, characterization and different photonic and biological applications of DNA templated CdS (D-CdS) NPs are discussed. A co-precipitation method along with an ultrasonic irradiation is implemented here. The capping agents are crucial in synthesizing highly mono-dispersed CdS NPs by growth restriction methods. Several biocompatible capping agents are exploited to achieve growth restriction in preparation for CdS NPs [13-16]. Their chemical and physical properties strongly depend on size [17-19]. Their excellent properties have been exploited in applications like LEDs, lasers, sensors, solar cells, photocatalysis, photocells, display devices, invertors, waveguides, and bioimaging [20-28].

A few research works have been carried out to exploit the properties of CdS NPs for enhancing the fluorescence properties of rare-earth-doped sol-gel glass. One of the recent works in this direction is the effect of CdS NPs on the emission of Eu^{3+} ions implanted in a silicophosphate glass fabricated by the sol-gel method and they found that CdS can enhance the PL of Eu^{3+} ions [29-31]. It is also reported that CdS is utilized in many ways to get low-

threshold optical gain [32-34]. Shoujun LAI *et. al*. studied the changes in FRET that occurred during the incorporation of functionalized CdS NPs into different organic dyes. They found that the relative fluorescence intensity is increased in the CdS-Rh6G system due to the FRET between donor of CdS NPs and acceptor of rhodamine dyes [35]. Recently CdS quantum dots have been incorporated with Rh6G aqueous solution and studied and verified the improvement in PL intensity [36]. As Rh6G is dissolved in an aqueous solution, there is a greater chance for photobleaching than that in a solid matrix. The CdS NPs can act as a photocatalyst on irradiation to the light of energy equal to or greater than its bandgap energy and can produce an oxidative and reductive unit. The photogenerated charge carriers formed in valance and conduction bands react with water or dissolved oxygen to produce reactive oxidizing agents like $OH^{\cdot}$ and $O_2^{\cdot-}$. They can decompose dye molecules into smaller molecules. While dispersing CdS in Rh6G aqueous solution, there may be a chance of degrading the dye [37]. However, Rh6G is carcinogenic for living organisms and corrosive to metals; aqueous Rh6G cannot be handled safely [38-40]. When Rh6G is doped in a solid matrix such as sol-gel glasses, it will be inactive with water and hence the above-mentioned risk may reduce. According to Ali et al., a hole in the photocatalyst can react with a hydroxide ion and water molecule to create a stronger oxidizing agent $OH^{\cdot}$ radicals that can aid in the degradation of dye [41]. Even though, CdS NP is a photodegrading agent, once we incorporate CdS NPs in solid sol-gel glass matrix, the photodegradation of Rh6G can be reduced due to lack of water content in the matrix.

Industrial waste in wastewater treatment has evolved into a serious health problem in recent decades due to the development of industries. Consequently, wastewater treatment methodology has been the subject of intense research in recent years. Dye-containing wastewater demands highly effective treatment due to its acute toxicity. Several dyes are

potentially canned annually from textile, ink, paper, pharmaceutical, cosmetic, and other industries [42-46]. Based on reduced time and energy efficiency procedures, photocatalysis is an adequate alternative approach compared to other methods [47-48]. Recent research studies ascertained that CdS NPs are good alternatives as photocatalysts [49].

The fluorescent behaviour of CdS NPs has been taken advantage of in biomedical applications, and they have more advantages over conventional organic dyes, especially in bioimaging applications. CdS is a promising candidate for *in-vivo* and *in-vitro* imaging of normal and cancerous cells [50-52]. Incorporating NPs into biological systems necessitates biocompatibility. To achieve biocompatibility, NPs must be capped with natural or organic structures, it may reduce the toxicity of CdS. Therefore, they may possess potential applications in bioimaging and associated applications. Here, the CdS NPs prepared on DNA template which acts as a biological over-coating to CdS. This coating will reduce the effect of surface charges around CdS NPs and also reduce toxicity [50].

This chapter discusses the synthesis and characterization of DNA capped CdS NPs. The photocatalytic activity of D-CdS NPs on Rh6G and MB and the effect of D-CdS on the photoluminescence of Rh6G doped sol-gel derived glasses. In the proceeding part, the biological applications such as antibacterial activity, cytotoxicity and bioimaging of D-CdS NPs were screened.

3.2 Materials and Methods

All chemicals cadmium nitrate, sodium sulfide, double-stranded DNA sodium salt derived from herring sperm, tetraethyl orthosilicate (TEOS), ethanol, Rh6G dye and MB dye were obtained from Sigma Aldrich.

3.2.1 Synthesis of D-CdS NPs

The CdS NPs were synthesized by the co-precipitation method [53]. Here DNA is used as a capping agent and it serves as a template for NPs due to the

presence of a double helix structure containing one major and one minor groove [54-56]. The melting temperature (t_m) of double stranded DNA (dsDNA) is in the range of 52–58 ^{0}C. In this range, 50% of the dsDNA will unwind to single-stranded DNA. At approximately 95 ^{0}C, complete denaturation of DNA occurs. [57].

For the synthesis of CdS NPs, 50 mM Cadmium nitrate hexahydrate ($Cd(NO_3)_2.6H_2O$) was dissolved in 0.5 wt% (of cadmium nitrate) of DNA aqueous solution. While stirring continuously, 50 mM Sodium sulfide (Na_2S) solution was added to this solution. A yellow-coloured precipitate was obtained indicating the formation of CdS NPs. The precipitate was filtered, washed with de-ionized water and dried at 45^{0}C for further investigation.

The possible capping mechanism of the dsDNA is explained as follows: Sulfide ions in sodium sulfide will bind to Cd^{2+} ions bound on the phosphate groups of DNAs and the CdS nucleus is formed in the DNA network. DNA prevents the agglomeration and aggregation of CdS NPs. As the formation of CdS NPs took place at room temperature, DNA retains its double stranded structure, hence acts a strong capping agent. In a previous report [58-59], CdS was synthesized using DNA with aqueous solution of Cadmium acetate and Thiourea at 70^{0}C for 100 minutes. Heating can indeed have a damaging effect on DNA, as it can cause the denaturation of the DNA molecule. DNA denaturation involves the separation of the double-stranded DNA into two single strands due to the disruption of hydrogen bonds between the complementary bases. This process typically occurs at high temperatures, as DNA molecules are more stable in their double-stranded, helical form at lower temperatures. The denaturation of DNA can have significant implications in the framework of DNA capped CdS NPs. Since DNA serves as a capping agent in the synthesis and stabilization of these NPs, any significant denaturation of the DNA molecules can weaken or disrupt their

capping action. This, in turn, can affect the overall properties and behavior of the NPs. To maintain the integrity of the DNA capping in D-CdS NPs, it is important to carefully control the temperature during synthesis and subsequent handling to prevent excessive denaturation. Additionally, other methods, such as using stabilizing agents or optimizing reaction conditions, may be employed to lessen the potential adverse effects of heating on the DNA capping action and the properties of the NPs.

3.2.2 Fabrication of CdS incorporated Rh6G-doped sol-gel glass

The CdS NPs incorporated Rh6G doped sol-gel glasses were prepared by the following method as shown in the schematic Figure.3.1. A 5 ml ethanolic solution of 0.01 mM Rh6G is added to 5 ml ethanolic solution of CdS and kept under stirring for 10 minutes. A 10 ml of TEOS was added to this mixture and stirred well. One or two drops of 0.1 M HCl were added to the reaction mixture to fasten the sol-gel process. The stirring continued for another 30 minutes. Took 10 ml of the clear solution and poured into petri dish of diameter 10 cm and kept undisturbed for one week. The coloured sol-gel glass obtained was transparent and the average thickness and diameter of the derived glasses are 1±0.25 mm and 7±0.5 cm respectively. A couple of similar samples were prepared with different concentrations of CdS (0 ppm, 1 ppm, 5 ppm, 10 ppm, 15 ppm, and 20 ppm).

The photoluminescence measurements, chromaticity studies and CIE coordinates (1931 colour space) of Rh6G doped sol-gel glasses were carried out. These investigations were carried out by using an OHSP350 spectrometer. The samples were placed in a sample holder within a dark environment. The excitation light source was the frequency doubled generated laser at 532 nm using Nd: YVO_4 laser, which was directed onto the sample. A polymer optical fiber cable was used to carry the collected light

from the sample to the spectrophotometer, which is kept at 90 degrees from the sample. The emitted fluorescence is measured by the sensitive detector and it records the spectra.

The Figure.3.2 shows the schematic of the synthesized Rh6G doped glasses before and after incorporating with CdS. There is variation in colour of Rh6G doped glasses with that of Rh6G incorporated CdS NPs. The PL spectrum is also shown in this picture, where also one can observe the colour difference.

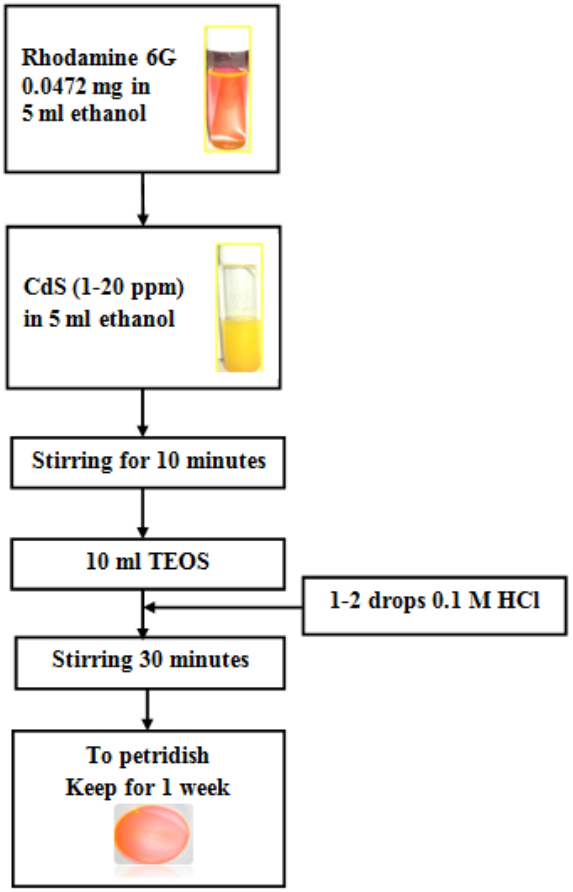

Figure.3.1 Schematic diagram of preparation of D-CdS NPs incorporated Rh6G-doped sol-gel glass

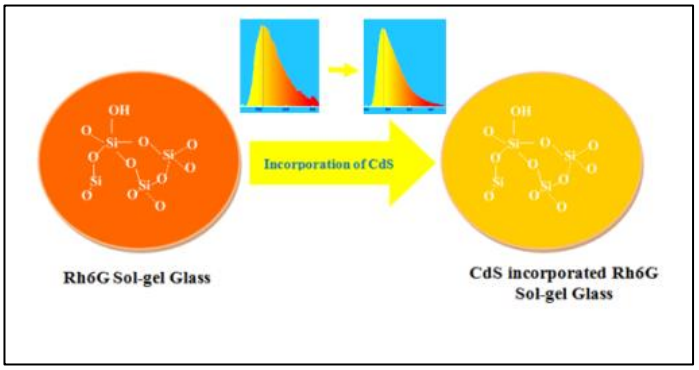

Figure.3.2 The Representation of Rh6G glass and D-CdS NPs incorporated Rh6G glass and their graphical variations of PL spectra

3.2.3 Photocatalytic Activity

The surge in industrial waste in recent decades, driven by industrial growth, has escalated wastewater treatment concerns, leading to intense research. Dye-laden wastewater poses a particularly acute toxicity challenge due to the discharge of numerous dyes from industries like textiles, inks, papers, pharmaceuticals, and cosmetics [43-46, 60]. Photocatalysis has emerged as an efficient method for treating such wastewater, offering reduced time and energy consumption. Recent studies support the use of semiconductor NPs as effective photocatalysts [47-48].

The photodegradation of organic dye solutions by D-CdS was studied. The procedure for the investigations on photocatalytic activity of NPs has been explained in chapter 2.

The procedure for doing antibacterial activity, cytotoxicity, In-vitro bioimaging of HeLa cells have been discussed in chapter 2.

3.2.4 Characterization of D-CdS

The D-CdS NPs were characterized by using different Physico-chemical techniques. The formation of D-CdS was confirmed from their characterization data, including, UV-visible absorption, PL, XRD, SEM, and

TEM imaging. Chromaticity studies were done for the sol-gel glass samples to find the CIE coordinates (1931 colour space) using OHSP 350 spectrophotometer.

3.3 Results and discussions

The characterization results and different applications are discussed in this section.

3.3.1 UV-visible absorption spectra

The UV–visible absorption spectra of uncapped CdS and D-CdS are shown in Figure.3.3. The absorption band of the CdS NPs is observed in the wavelength range 425 nm-515 nm with a well-defined maximum at 480 nm is attributed to the optical transition of the first excitonic state. The band gap energy (E_g) of CdS can be obtained by using the formula: $E_g=1240/\lambda$, where λ is the wavelength of the absorption edge. The calculated bandgap energy of CdS from the absorption edge is 2.58 eV. The maximum absorption peak of uncapped CdS is at 499 nm with bandgap energy of 2.48eV. Comparing this maximum excitonic wavelength with the absorption peak of bulk CdS, a blue shift in maximum absorption is observed which is due to the particle size reduction as a result of quantum confinement of the photo-generated electron-hole pairs [35, 49]. It is also noted that CdS has non-zero absorption in the wavelength range from 350 nm to 700 nm. The particle size R can be obtained from Brus formula [36],

$$E_g(R) = E_g(\text{Bulk}) + \frac{\hbar^2\pi^2}{2R^2}\left[\frac{1}{m_e} + \frac{1}{m_h}\right] - \frac{1.786e^2}{\varepsilon R}$$

Where $E_g(R)$ is the bandgap energy of the quantum dot, E_g (Bulk) is the bandgap energy of bulk material R is the size of the quantum dot, and h is Plank's constant. m_e and m_h are the effective masses of the electron and hole

respectively. e is the electron charge, ε is the relative dielectric constant of CdS (ε=8.9). The calculated particle size is around 3.5 nm, which is a little smaller than that of the particle size observed by the SEM image; it may be due to the aggregation of particles while drying the samples.

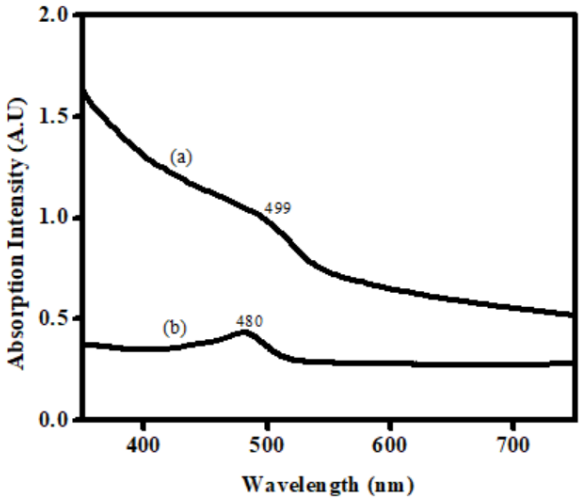

Figure.3. 3 UV-visible absorption spectra of (a) uncapped and (b) D-CdS

3.3.2 XRD

The structural properties of CdS NPs have been investigated by X-ray diffraction technique as shown in Figure.3.4. The XRD pattern gives information about the crystalline phase and crystalline size. The XRD pattern of CdS offers three prominent peaks at 2θ values of 26.70^0, 44.20^0, and 52.2^0; the corresponding indexations could be at (111), (220), and, (311) which are evident for the cubic crystal structure (JCPDS file (10-454)). The broadened peaks show that the sizes of the particles are in the nanometer range [61-64].

The crystallite size of D-CdS NPs can be obtained from Scherrer's formula [65-66]. The formula is given by

$$d = \frac{0.9\lambda}{\beta\cos\theta}$$

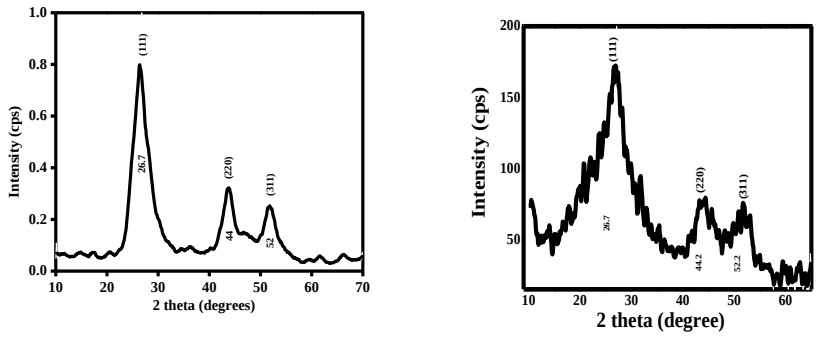

(a) (b)

Figure.3.4 XRD pattern of uncapped CdS (a) and D-CdS (b)

Where d is the crystallite size in nm, λ is the wavelength of the X-rays used, 1.5406 Å, β is the full width at half maximum, and θ is the diffraction peak angle. The average crystalline size is obtained to be 2 nm.

3.3.3 SEM

In Figure 3.5, the SEM image shows a detailed view of the structural characteristics of D-CdS. The material's morphology is prominently spherical, as obvious from the image analysis. Each individual CdS particle displays a uniform and compact spherical shape. Notably, the size distribution of these spherical particles is confined to dimensions below 10 nm. This nanoscale size is revealing a finely tuned and controlled synthesis process, contributing to the precise formation of CdS NPs within the desired size range. The spherical morphology observed in the SEM image is an important aspect of the material's nanostructure, and understanding such features are vital in the unique properties and potential applications of D-CdS in various scientific and technological domains.

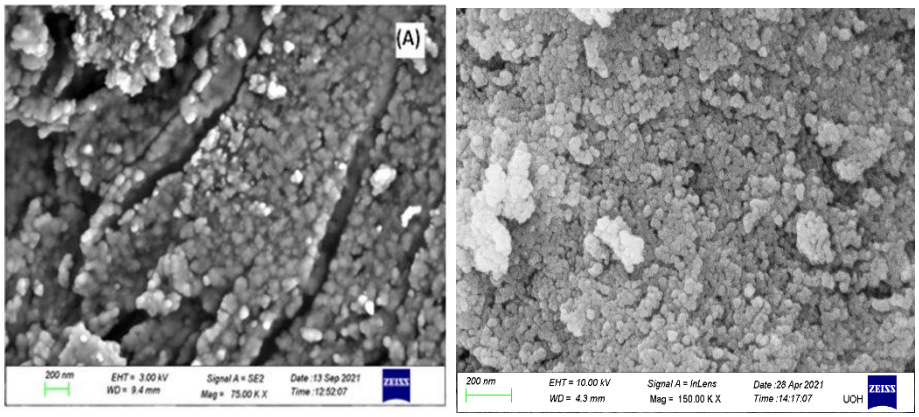

(a) (b)

Figure.3.5 SEM image of (a) uncapped CdS (b) D-CdS NPs

3.3.4 TEM

The TEM image of D-CdS is shown in Figure.3.6. It exhibits monodispersed particles with an average size of 10 nm. Some NPs get aggregated due to large specific surface area and high surface energy. When DNA molecules are introduced to the surface of CdS NPs, they can form a coating around the NPs through interactions such as electrostatic attraction or chemical bonding. The spherical behaviour of DNA-capped CdS NPs is likely due to the arrangement of DNA molecules around the NPs, which can influence their overall shape and structure.

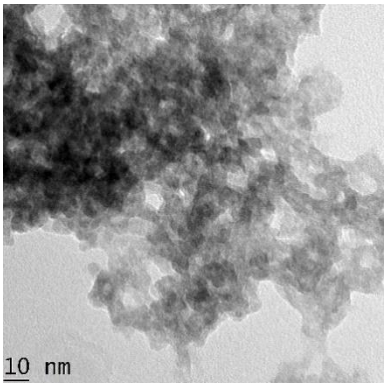

Figure.3.6 TEM image of D-CdS

3.3.5 Photoluminescence

The photoluminescence spectra of uncapped CdS and D-CdS are demonstrated in Figure.3.7. The PL spectrum of D-CdS, shows two peaks in the range of 450 nm to 600 nm for an excitation wavelength of 400 nm. The first higher peak was centred at 486 nm and the second lower peak was centred at 541 nm. The peak at 486 nm is attributed to the emission from the absorption edge. The peak at 541 nm corresponds to emission due to surface states or traps associated crystalline defects. Here, in the CdS NPs, this emission is linked to cadmium and sulfur atom vacancies [67-68, 70]. The uncapped CdS has also two peaks, one is at 491 nm and the second one is at 549 nm. The peaks of D-CdS are blue-shifted as compared to uncapped CdS. This blue shifting is due to the quantum confinement effect of D-CdS. A considerable amount of enhancement in the fluorescence intensity of D-CdS was noted. This may be due to the presence of Schiff base ligand which is highly fluorescent around the wavelength of 500 nm, which matches the emission wavelength of CdS NPs.

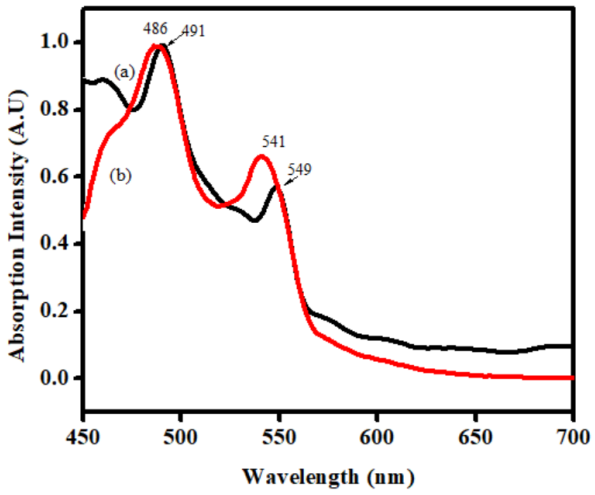

Figure.3.7 PL spectra of Uncapped CdS (a) and (b) D-CdS

As the synthesized D-CdS possess emission wavelength in visible region and considering the biocompatibility, fluorescence cell imaging

may be a key application. Also, due to the multiple emission wavelengths, D-CdS can be employed for the production of multicoloured light emitting diodes [34].

3.4 Photonic applications

D-CdS NPs have emerged as versatile and promising materials in a numerous of photonic applications, leveraging their unique properties at the nanoscale. The precise control over the size and morphology of these NPs plays a title role in enhancing the quantum efficiency and colour purity of the emitted light, making them ideal candidates for advanced lighting technologies. The application of D-CdS NPs in photonic technologies spans a wide range, encompassing optoelectronics, photovoltaics, nonlinear optics, and sensing devices. Their tailored properties at the nanoscale open up avenues for innovation and advancement in various photonics-related fields, contributing to the progress of cutting-edge technologies with enhanced performance and efficiency.

The effect of D-CdS NPs on the photoluminescence of Rh6G doped sol-gel derived glasses are investigated here and studied their chromaticity. Additionally photocatalytic studies of D-CdS NPs were done using Rh6G and MB dyes.

3.4.1 Effect of D-CdS on the photoluminescence of Rh6G doped sol-gel derived glass

This study investigates the influence of synthesized D-CdS NPs on the photoluminescent properties of Rh6G-doped sol-gel derived glass. The incorporation of D-CdS NPs into the glass matrix introduces a different dimension to the photoluminescence behavior, showcasing potential enhancements or modifications in the emission characteristics. The investigation aims to untie the synergistic effects between D-CdS NPs and Rh6G dye, shedding light on their combined impact on the optical properties of the sol-gel glass system. To characterize the sol-gel glass samples, absorption spectrum and XRD analysis were done.

Figure 3.8 (a) displays the absorption spectrum of sol-gel-derived glasses and Rh6G doped sol-gel glass. While the sol-gel glasses do exhibit finite absorption in the UV region, they demonstrate minimal absorption in the visible region, allowing for high optical transmittance in this range. The absorption in the range of Rh6G-doped sol-gel is found to be in between 450 nm to 570 nm with a maximum of 525 nm. This can be assigned to the monomeric state of Rh6G equivalent to S0→S1 transitions [69-70]. A dimeric peak of Rh6G was also found on the left of the major peak which is around 480 nm. Figure.3.8 (b) represents the absorption spectrum of Rh6G doped sol-gel glasses with varying concentrations of D-CdS. The absorption in the range of 400 nm to 650 nm has been considered here. At lower concentration of CdS NPs, the absorption intensity of Rh6G reduced drastically with a blue shift. On increasing the concentration of CdS NPs, the absorption intensity increased gradually with successive blue shifts from 523 nm to 514 nm. The reduction in intensity at lower CdS NPs concentrations may be attributed to the adsorption of dye molecules onto the surface of CdS NPs [36]. The absorption peak of CdS could not be differentiated from the spectrum because the dimeric peak of Rh6G coincides with the absorption peak of CdS.

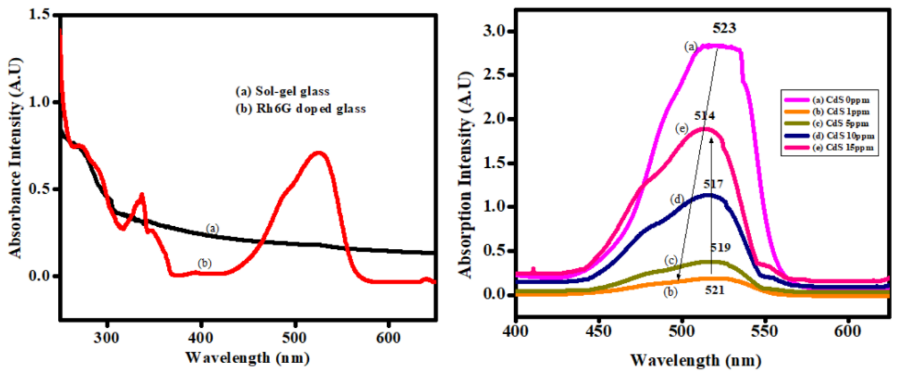

Figure.3. 8 Absorption Spectra of (a) Sol-gel glass and Rh6G doped sol-gel glass (b) CdS incorporated Rh6G-doped sol-gel glass

The XRD pattern presented in Figure.3.9 for the CdS-incorporated Rh6G glass reveals a distinctive feature, a broad peak centered at 23.5 degrees. Notably, the absence of characteristic diffraction peaks associated with crystalline CdS approves the amorphous nature of the material. This observation indicates that the CdS NPs are successfully embedded in the glass matrix, providing valuable insights into the structural characteristics and phase composition of the CdS-incorporated Rh6G glass [71].

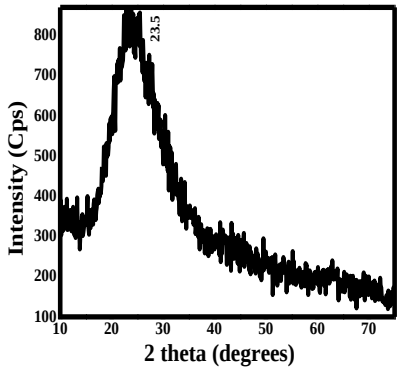

Figure.3.9 XRD pattern of CdS incorporated Rh6G doped sol-gel glass

(a) Photoluminescence of Rh6G doped sol-gel glass

The photoluminescence spectrum of Rh6G glass is studied with an excitation wavelength of 532 nm for the concentrations $1x10^{-7}$, $1x10^{-6}$, $1x10^{-5}$, $1x10^{-4}$, $1x10^{-3}$and $1x10^{-2}$ M. The luminous intensity of each concentration is carried out at room temperature. Figure.3.10 shows the effect of the concentration of the Rh6G molecule on the PL of Rh6G-doped glasses. In the inset, the histogram of the maximum intensity peak of each concentration along with the corresponding maximum emission wavelength is shown. As the concentration of dye increases, the PL is also increased. After$1x10^{-5}$ M, there is a tendency for fluorescence quenching due to the phenomenon of

concentration quenching [70]. On an increase in the concentration from $1x10^{-7}$M to $1x10^{-2}$ M, the maximum emission wavelength is shifted from 570 nm to 601 nm. This red shift is due to the increase in the concentration of Rh6G molecules.

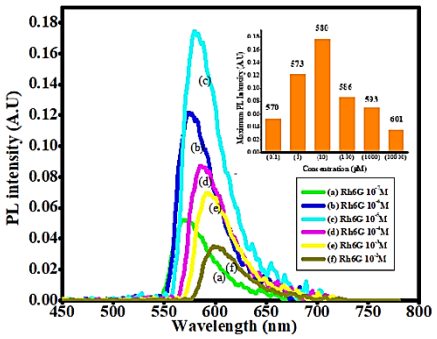

Figure.3.10 PL spectra of Rh6G glass at different concentrations

To investigate how CdS NPs affect the PL of Rh6G, a concentration within the quenching region ($1x10^{-4}$ M) was chosen. Figure.3.11 exhibits the emission spectra of Rh6G-doped sol-gel glass with an excitation wavelength of 532 nm. The spectrum specifies a gradual blue shift from 586 nm to 573 nm and the enhancement occurred in the emission intensity by varying the concentration of CdS from 0 ppm to 15 ppm. After 15 ppm of CdS concentration, the intensity is reduced to less than that of the intensity of Rh6G sol-gel glass with blue shift to 567 nm. The enhancement of PL intensity in the presence of CdS may be due to the radiative energy transfer (ET) from the semiconductor quantum dot to Rh6G dye molecules. In the energy transfer process, CdS quantum dots operate as donors to the accepter Rh6G. This process happens only when the gap between CdS and Rh6G becomes adequately short. This is efficiently achieved by the presence of abundant defect states in the CdS NPs. These defect states induce trap levels within the bandgap of CdS; their corresponding emission overlaps finely with Rh6G. This provides an easy energy transfer from CdS to Rh6G and causes

the enhancement in the luminous intensity. The emission peak around 480 nm can be attributed to the radiative transition between the conduction band and cadmium vacancy level. The pictorial representation of this energy transfer is shown in Figure.3.12. The blue shift in the emission peak can be illustrated as a result of the coalition of two possibilities. When CdS is incorporated into the Rh6G sol-gel matrix, it may defend against the dye-dye interaction and lessen the self-quenching. On increasing the concentration of CdS this effect will be pronounced; this leads to gradual blue shifting of emission peak intensity. Another possible mechanism is that when CdS emits a wavelength of 546 nm in the visible region, there may be a chance to absorb and re-emit this radiation by the excited Rh6G molecules. This may lead to an enhancement and blue shifting in the emission peak intensity. The decrease in PL intensity with the excessive addition of CdS can be attributed to quenching caused by the surplus CdS. Indeed, as the concentration of CdS exceeds a certain threshold, Rh6G molecules are adsorbed onto the CdS surface, forming a non-fluorescent complex. This complex absorbs excitation wave intensity and undergoes non-radiative de-excitation. [29-30, 72]. Tunability of emission wavelength can be achieved from 586 nm to 567 nm by changing the concentration of CdS.

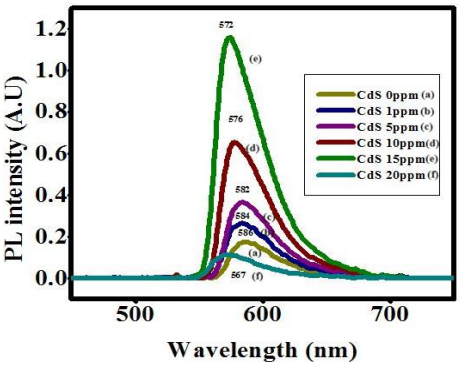

Figure.3. 11 Photoluminescence curve of D-CdS incorporated Rh6G doped sol-gel glass

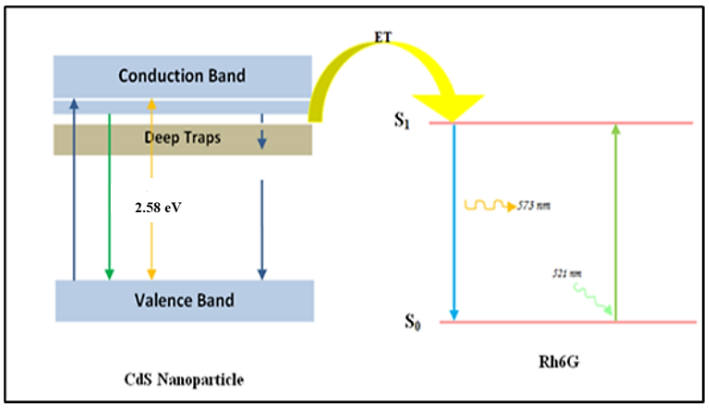

Figure.3. 12 Energy level diagram showing the radiative transfer from CdS to Rh6G

(b) Annealing temperature effect on photoluminescence

To examine the annealing temperature effect on the PL of the samples, PL spectra for annealed Rh6G sol-gel glass with 15 ppm CdS were taken at the same excitation wavelength, 532 nm. In Figure.3.13, the annealing temperature effect on PL at 60^0C, 100^0C, 150^0C, and 250^0C of Rh6G is shown. At 60^0C, it is found that the PL is enhanced by 2.5-fold associated with a right shift of peak from 573 nm to 577 nm. A maximum PL intensity enhancement by 4.5-fold is observed at 100^0C, and the corresponding peak shift is from 573 to 581 nm. The main luminous quenchers, hydroxyl groups, present in the sol-gel glass may reduce their density upon increasing annealing temperature. This will lead to enhancement in the PL intensity. At 150^0C, the PL intensity is reduced more than that of PL intensity at 60^0C and 100^0C, and a 1.5-fold enhancement in the PL intensity than that of the Rh6G at room temperature with a peak shift from 573 to 584 nm. At 250^0C, the intensity of luminescence reduced drastically to a value less than that of intensity at room temperature with a peak shift from 571 to 593 nm. The reduction of PL intensities in high annealing temperature may due to the following reasons. The structural modifications of sol-gel-derived glasses may have significant consequences on the emission of Rh6G molecules on

heat treatment. Though, at sufficiently high temperatures about 250^0C, there is a reduction in the number of defects in the sol-gel matrix which slow down the energy transfer. Furthermore, there occurs shrinkage in the sol-gel network which leads to the aggregation of CdS NPs and causes an energy migration amongst CdS. It also observed the bleaching of Rh6G molecules on Rh6G glass at high temperatures. This will also lead to a reduction in intensity at 250^0C [73-74]. The annealing temperature studies on the sample reveal that an increment in temperature can also tune the emission wavelength from 571 nm to 593 nm.

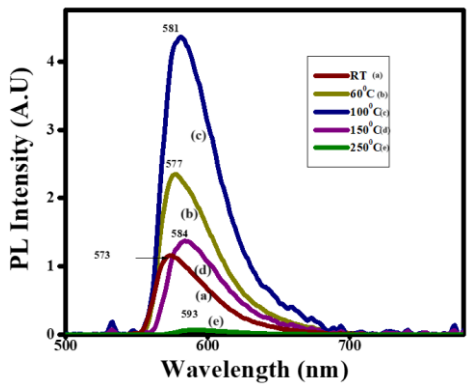

Figure.3.13 Photoluminescence curve of Rh6G glass with different annealing temperatures

(c) Chromaticity studies and CCT

The emitted colours of Rh6G sol-gel glass with and without CdS are plotted as (x, y) coordinates in two-dimensional colour space defined CIE 1931 diagram. The location of the colour coordinates for Rh6G sol-gel glass with and without CdS NPs in the CIE chromaticity diagram is shown in Figure.3.14. From this figure, one can see that the colour of the prepared sample is located in the orange region and the CIE coordinates vary from (x=0.5842, y=0.4106 to x=0.5296, y=0.4692) in accordance with varying concentration of CdS NPs.

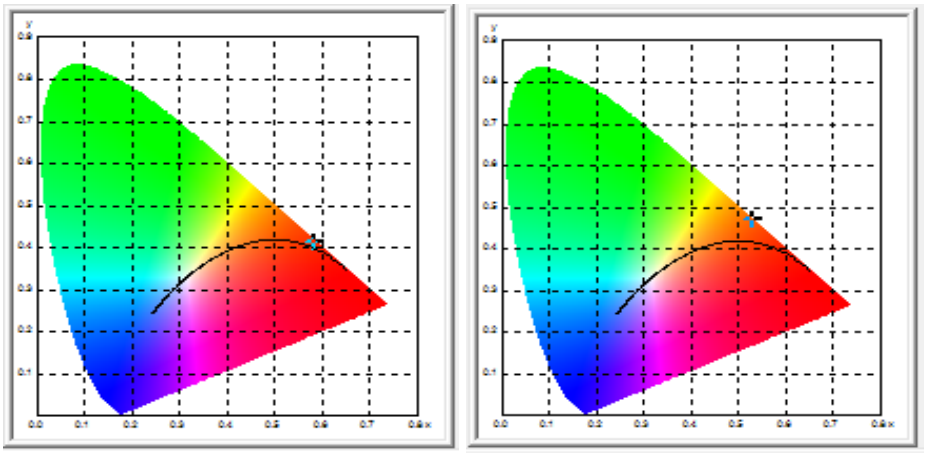

(a) (b)

Figure.3. 14 (a) Chromaticity diagram of Rh6G glass (b) CdS incorporated Rh6G glass

To facilitate the quality of light, CCT values have been calculated by using McCamy empirical formula [54];

$$CCT = -437n^3 + 3601n^2 - 6861n + 5514.31$$

Where $n = \frac{(x-x_e)}{(y-y_e)}$ and the x_e and y_e are the chromaticity epicenter, whose value is x_e=0.3320 and y_e =0.1858

The CCT values lie between 1595 K and 2316 K when the concentration of CdS varies between 0 ppm and 15 ppm. CCT values between 2000-3000K are referred to as warm white light and appear as orange to yellow-white in colour. The CCT values in this range usually are used for household lighting [75-77]. The colour purity values for both samples are found to be above 99.5%. The presence of CdS may affect the CIE coordinates and CCT values of Rh6G sol-gel glass.

(d) Photoluminescence dynamics

The time-resolved fluorescence spectroscopy gives information on the decay dynamics of excited states of Rh6G doped sol-gel glasses. In Figure.3.15, it is

shown that the fluorescence lifetime decay curves of both Rh6G glass and CdS incorporated Rh6G glass at room temperature. For this, 15 ppm CdS incorporated Rh6G glass was taken because it showed maximum emission intensity. The fluorescence lifetime decay curves were fitted with exponential decaying function as below [78],

$$I(t) = \sum_{j=1}^{m} \alpha_j \exp\left(-\frac{t}{\tau_j}\right)$$

Where α_j is the weighing factor, τ_j is the fluorescence lifetime associated with j^{th} component, m is the number of discrete decay component. The fluorescence decay curves were fitted with triple exponential function of the following form

$$I(t) = \alpha_1 \exp\left(-\frac{t}{\tau_1}\right) + \alpha_2 \exp\left(-\frac{t}{\tau_2}\right) + \alpha_3 \exp\left(-\frac{t}{\tau_{31}}\right)$$

And the average lifetime can be determined from the formula [79],

$$< \tau > = \sum_{j=1}^{j=m} \frac{\alpha_i \tau_i}{\sum_{j=1}^{m} \alpha_i}$$

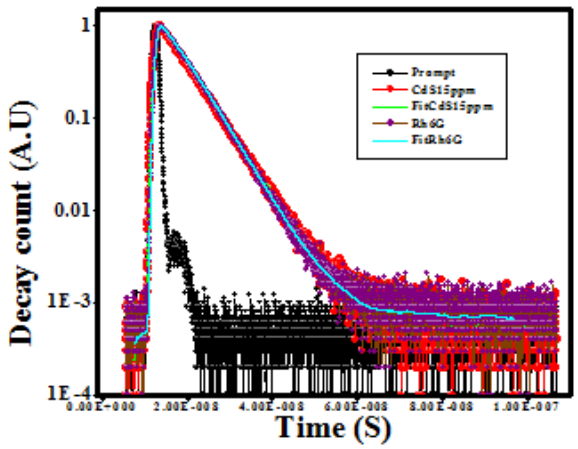

Figure.3.15 Fluorescence lifetime decay of Rh6G-doped sol-gel glass with and without CdS

The goodness of the fit can be evaluated from the value χ^2. For Rh6G and CdS incorporated Rh6G, the fluorescence lifetime decay curves were fitted with third order exponential decaying functions with χ^2value around 1.35. The average decay lifetime of Rh6G-doped sol-gel glass is in the nanosecond range, 1.5 ns and that of CdS incorporated Rh6G glass is also found to be 1.5 ns. It is clear that the incorporation of CdS has minimal effect on the fluorescence lifetime of Rh6G. On increasing the concentration of CdS, the presence of defect states in the CdS NPs may also increase. These defect states induce trap levels within the bandgap of CdS and boost the rate of energy transfer to Rh6G. Even though the concentration of CdS can enhance the rate of energy transfer; it does not control the emission probability to ground state. It can be concluded from the fluorescence lifetime, CdS can tune the emission wavelength and intensity of Rh6G without altering its emission lifetime.

3.4.2 Photocatalytic activity of D-CdS

The photocatalytic degradation of Rh6G and MB was studied in the presence and absence of D-CdS under UV irradiation, for a period of 120 minutes. For this, 10 mg of CdS was taken. The absorption peak of Rh6G at 520 nm and absorption peak of MB at 665 nm were considered to demonstrate the photocatalytic activity. Figure.3.16(a) shows the absorption spectra of R6G in the absence of D-CdS. The peak corresponding to 520 m is due to the transition between S0 to S1 [70]. Figure.3.16(b) shows the absorption spectra of Rh6G in the presence of photocatalyst. It was observed that decrement in the intensity of maximum absorption was very less in the absence of D-CdS after 120 minutes UV irradiation. It is observed that the percentage of degradation (Figure.3.16 (c)) of Rh6G increased in the presence of the

photocatalyst; 64% degradation occurred within 120 minutes. At the same time, only 7 % of degradation happened without a photocatalyst.

Figure.3.17 (a) and (b) demonstrate the absorption spectra of MB in the absence and presence of D-CdS respectively. The maximum absorbance takes place in the range of 550 nm to 700 nm with a pair of characteristic peaks at 612 nm and 665 nm. The peak at 665 nm is due to π-π* transition associated with the resonance of the π electrons from sulphur resonating with those from carbons in thiazinic center. The peak at 612 nm corresponds to π-π* transition of benzene rings [80]. According to Figure.3.17 (c), in the absence of catalyst, 12% degradation occurred for both peaks within 120 minutes. In the presence of a photocatalyst, within 120 minutes, 91 % of degradation occurred for the peak at 612 nm whereas, 98.9% degradation occurred for the peak at 665 nm.

D-CdS is found to be a potential photocatalyst for MB. The photodegradation of MB is greater than that of Rh6G, possibly due to Rh6G's higher photostability. Photocatalytic mechanism of D-CdS is instigated by irradiation by UV light. Excitation of electrons from the valence band to the conduction band of CdS, results in the production of electron-hole pairs [34, 35]. In addition to longer charge carrier lifetimes, CdS NPs show better redox properties because the photo-generated electrons and holes are inhibited under UV irradiation. The OH radicals are formed when the holes in CdS react with water molecules or hydroxide ions. The OH radicals are effective oxidizing agents, and attack organic pollutants present at the surface of CdS. The possible mechanism of photocatalytic reactions of Rh6G and MB as follows:

$$CdS + h\upsilon \rightarrow CdS + h^+ + e^-$$

$$h^+ + H_2O \rightarrow OH^- + H^+$$

$$h^+ + OH^- \rightarrow OH^{\cdot}$$

$$O_2 + e^- \rightarrow O_2^-$$

$$2H_2O + O_2^- + e^- \rightarrow 2OH + 2OH^-$$

$$OH^{\cdot} + Dye(RhG + MB) \rightarrow Degradedproducts$$

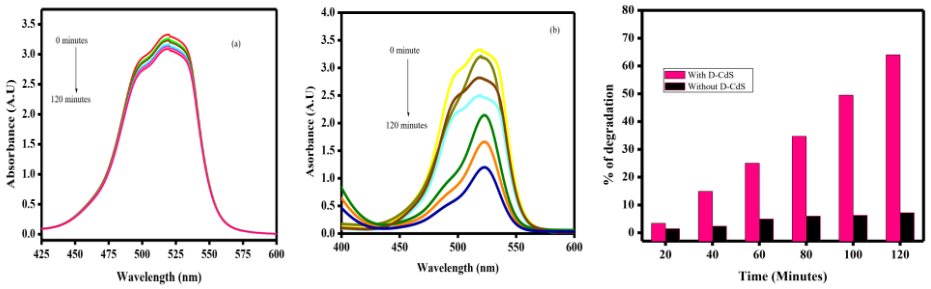

(a) (b) (c)

Figure.3.16 Photocatalytic degradation of Rh6G in the (a) absence and (b) presence of catalyst under UV irradiation (c) percentage of degradation with and without catalyst

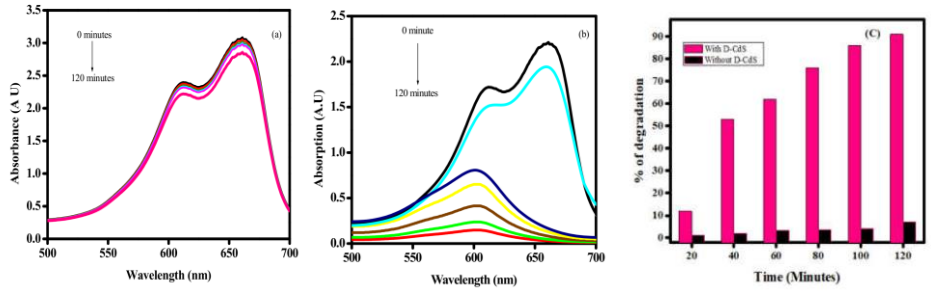

(a) (b) (c)

Figure.3.17 Photocatalytic degradation of MB in the (a) absence and (b) presence of catalyst under UV irradiation (c) percentage of degradation with and without catalyst

In Figure.3.18, the showed diagram explains the mechanism underlying the photocatalytic behaviour of D-CdS when interacting with various dyes. The illustration likely outlines the series of steps involved in the photodegradation of the dyes facilitated by D-CdS under light irradiation. Understanding this photocatalytic mechanism is vital for separating the efficiency and selectivity of D-CdS in degrading different dye molecules, finding its potential applications in wastewater treatment or environmental remediation.

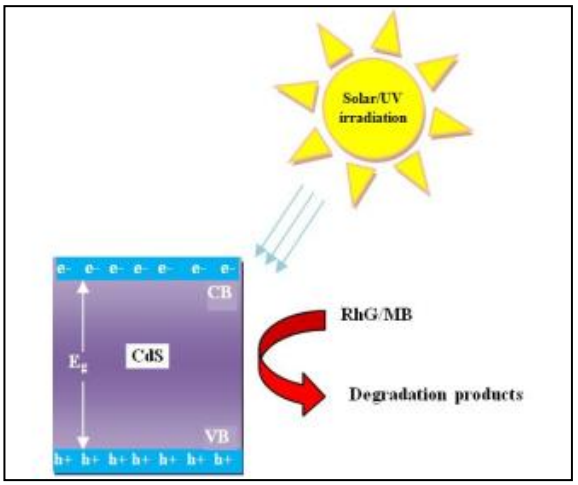

Figure. 3.18 Mechanism of photocatalytic behaviour of D-CdS

3.5 Biological applications of D-CdS

The synthesized D-CdS NPs analysed a comprehensive examination for different biological applications, including antibacterial studies, cytotoxicity studies, and bioimaging investigations. This multifaceted approach in the study aimed to explore the potential of D-CdS NPs across various biological contexts. Antibacterial studies were conducted to assess the nanoparticles' efficacy in inhibiting bacterial growth, while cytotoxicity studies focused on understanding their impact on cell viability. Moreover, bioimaging studies were employed to assess the

nanoparticles' suitability for imaging biological structures, demonstrating the versatility of D-CdS NPs in different biological applications.

3.5.1 Antibacterial Activities

The experimental details for the antimicrobial studies were presented in the experimental section. The antimicrobial activities of the prepared samples, D-CdS and uncapped CdS were investigated by disc diffusion method using Pseudomonas aeruginosa (Gram-negative), *Staphylococcus aureus,* and *Streptococcus mutans* (Gram-positive) The D-CdS and uncapped CdS are exhibiting inhibition to both Gram - positive and Gram-negative pathogenic bacteria. The diameter of inhibition zone was measured for1mg/ml concentration. Table.3.1 shows the inhibition zone diameter for the samples at 1 mg/ml concentration. D-CdS shows better activity towards Gram-negative bacteria, *Pseudomonas aeruginosa*. Gram - positive bacteria consists of a thick peptidoglycan cell wall (monoderms). Gram negative bacteria have much thinner peptidoglycan cell wall and in addition they have an outer membrane containing lipopolysaccharides surrounding the cell wall (diderms). Lipopolysaccharides consist of lipids and polysaccharides. Polysaccharides are polymeric carbohydrates composed of long chains of monosaccharide units joined by glycosidic linkages. Lucas R et. al explained the interaction between carbohydrates and DNA [81]. Here in our work, the antibacterial sample consists of DNA capped CdS NPs. Once the D-CdS introduced into the bacteria, it can interact with the outer layer, lipopolysaccharides, of Gram-negative bacteria much faster than in Gram-positive bacteria. The particle size reduction and DNA biotemplate effect make the D-CdS more active than uncapped CdS.

Table.3.1 Antibacterial activity of D-CdS and uncapped CdS

Species	Zone diameter (mm) Concentration (1mg/ml)		
	D-CdS	Uncapped CdS	Standard (Streptomycin) (100 µg/ml)
Pseudomonas aeruginosa	24	13	29
Staphylococcus aureus	20	12	27
Streptococcus mutans	17	11	25

3.5.2 Cytotoxicity analysis: MTT Assay

The cytotoxic impact of both D-CdS NPs and uncapped CdS on HeLa cell lines was assessed over a 24-hour period. Figure.3.19 illustrates the results of the MTT assay, depicting the relationship between concentration and cell survival rate. D-CdS NPs shows considerable toxicity towards HeLa cells. In Figure.3.20 (a) and (b), the cell viabilities of the D-CdS, and uncapped CdS respectively for different concentrations are shown. Figure.3.20 (a) implies that inhibition of HeLa cells is steadily enhanced with D-CdS nanoparticle concentration i.e, it showed a dose-dependent toxicity. At a concentration 2.5 µg/ml, it shows 84% cell viability and 43% viability 12.5µg/ml. The calculated LC_{50} value is equal to 8µg/ml.

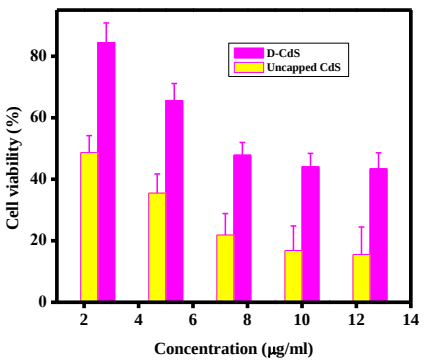

Figure.3.19 Histogram - cell viability of D-CdS and Uncapped CdS

The LC_{50} value of uncapped CdS is found to be 2.4µg/ml. The LC_{50} value of uncapped CdS on HeLa cells reported by Susha Naranthatta is 7 µg/ml [51]. In another report, SkTofajjen Hossain, LC_{50} value of uncapped CdS is observed to be 4 µg/ml [82]. Reyes-Esparza reported an improved biocompatibility in dextrin-capped CdS NPs than uncapped CdS [83]. According to them, a concentration less than 1 µg/mL is not at all toxic to HeLa cells. The concentrations taken in this work is much higher than this. Therefore, DNA, the capping agent to CdS can improve biocompatibility by reducing the toxicity of unmodified CdS. Here the LC_{50} value of D-CdS is much greater than that of uncapped CdS, which indicates that toxicity reduced considerably for D-CdS. Toxicity and LC_{50} value are inversely proportional.

As CdS NPs possess photoluminescence in the visible range of wavelength, the biocompatible D-CdS can effectively be used as potential candidate for in vitro cellular imaging (bioimaging).

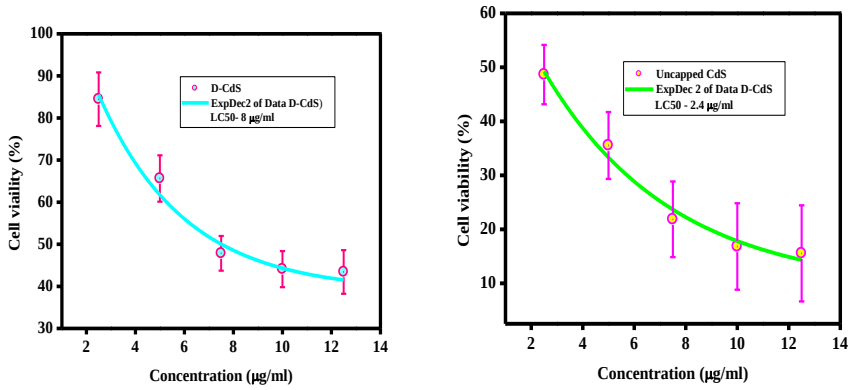

(a) (b)

Figure.3.20 The Cell viability (a) exponential fit D-CdS (b) uncapped CdS

3.5.3 Bioimaging

Bioimaging is an important aspect of this study, focusing on D-CdS NPs. HeLa cells were subjected to treatments with 2.5 µg/ml of D-CdS NPs and uncapped CdS, a concentration lower than the LC_{50} of D-CdS. After 24 hours of treatment, the cells were observed under a fluorescence microscope, allowing for visualization of the cell membrane, a double-layered lipid structure that separates the cytoplasm from the external environment. Figure.3.21 (a) and (b) shows the bright field images of the HeLa cells treated with 2.5µg/ml of uncapped CdS and D-CdS respectively. For a concentration study of D-CdS, 5µg/ml was also taken in to consideration. Figure.3.21 (c) shows the bright field image of HeLa cells treated with 5 µg/ml D-CdS.

The cells are clearly seen from the bright-field images. Cells with round shape represent cell death. It is obvious from the Figure.3.21 (a) that more cells were destroyed in the presence of uncapped CdS which due to its high toxicity. Image is very unclear due to the presence of bigger sized CdS NPs. This uncapped CdS were not much soluble in any solvents. Therefore, it is not a desirable candidate for bioimaging. In Figure.3.21 (b), cells are destroyed in the presence of D-CdS (2.5 µg/ml). Even though the cell death rate is lesser than that of uncapped CdS, cells are very clearly seen. It proves that D-CdS is a promising candidate for bioimaging. It is obvious from the Figure.3.21 (b) and (c) that D-CdS shows a dose-dependent toxicity as seen from MTT assay. Higher number of cell death happened for a higher concentration.

The cellular imaging capability of the biocompatible D-CdS is definitively proven by the bright green fluorescence showcased in Figure.3.22.

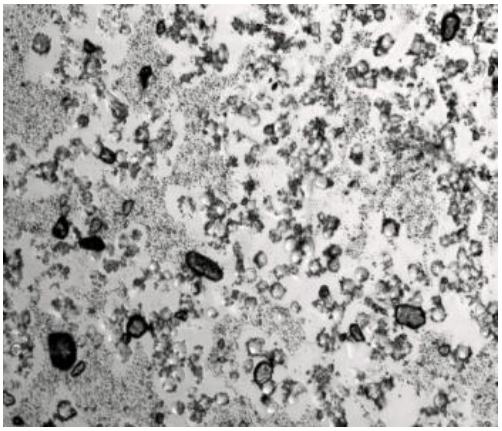

(a)

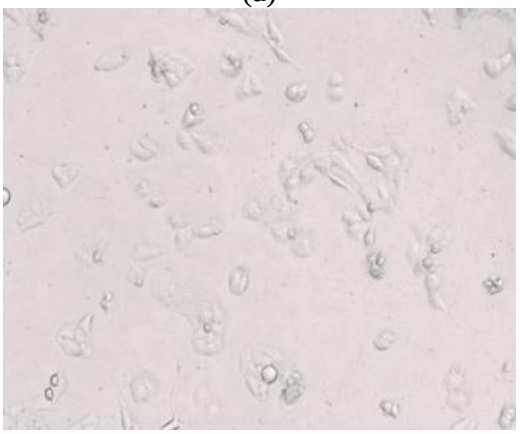

(b)

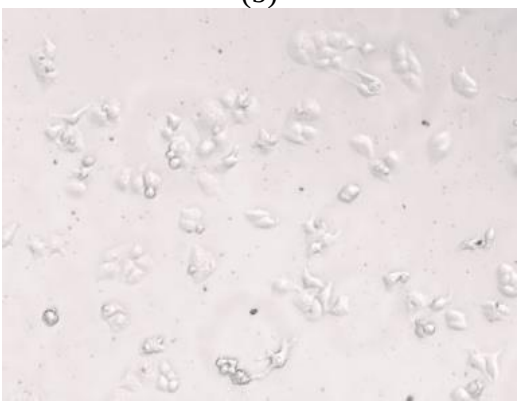

(c)

Figure.3. 21 Bright-field images of HeLa cells in the presence of (a) Uncapped CdS 2.5 µg/ml (b) D-CdS 2.5 and (c) D-CdS 5µg/ml. Cell death is visible by the round shape of the cell.

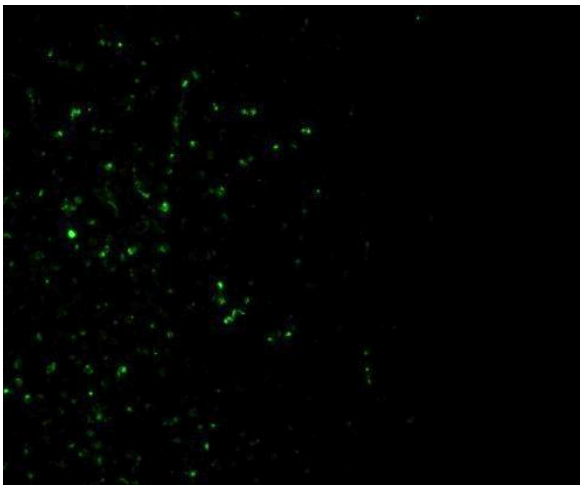

Figure.3. 22 Fluorescent image of the cells in the presence of D-CdS NPs showing green fluorescence

3.6 Conclusions

In this study, the effect of CdS NPs on the PL of Rh6G-doped sol-gel glass is investigated. It has been shown that CdS NPs can significantly affect the emission of Rh6G from 586 nm to 572 nm. The annealing temperature has a considerable effect on the PL of Rh6G-doped glasses from 573 nm to 584 nm. The presence of CdS changed the CIE coordinates and enhanced the CCT values according to chromaticity studies. Based on this study, the samples fall into the category of warm light and could be used for household lighting. The addition of CdS does not significantly alter the fluorescence lifetime decay of Rh6G. As a result of the studies done in this work, new possibilities can be explored for modifying the emission properties of Rh6G thereby can utilize in the design of solid-state lasers with wavelength tunability. The high photodegradation percentage of Rh6G (70%) and MB (98%) was observed in the presence of 10mg of CdS NPs in 120 minutes of UV irradiation. The CdS NPs were screened for their antibacterial activity and the results showed that they are biologically active. The

cytotoxicity of the CdS NPs were assessed via the MTT assay, proved that the D-CdS is less toxic than uncapped CdS. In vitro cellular imaging applications of prepared D-CdS are also investigated and demonstrated.

References

[1] E Braun et al., Nature, 391 (1998) 775.

[2] L Zhiguo et al., Mater. Lett., 62 (2008) 2315.

[3] Y Yong Yao et al., Nanotechnology, 19 (2008) 405601.

[4] W Gang et al., J. Phys. Chem. B, 109 (2005) 23941.

[5] J Zhu et al., Mat. Res. Bull., 36 (2001) 1687.

[6] N K Radhika et al., IEEE Sens. J., 20 (16) (2020) 9179.

[7] E Braun et al., Nature, 391 (1998) 775.

[8] L Zhiguo et al., Mater. Lett., 62 (2008) 2315.

[9] Y Yong et al., Nanotechnology, 19 (2008) 405601.

[10] Gang Wei et al., J. Phys. Chem. B, 109 (2005) 23941.

[11] S J Tan et al., Angew. Chem., 126(5) (2014) 1340.

[12] P P Jyothi et al., Bull. Mater. Sci., 43 (2020) 1.

[13] B S GoudA et al., Mater. Today: Proc., 3(10) (2016) 4003.

[14] K Prasad and A K Jha, J. Colloid Interface Sci., 342(1) (2010), 68-72.

[15] M D Rao and G Pennathur, Mat. Res. Bull., 85, (2017) 64.

[16] P Bansal, N Jaggi, S K Rohilla, Res. j. chem. sci., 2(8) (2012) 69.

[17] R Banerjee et al., J. Phys. Condens. Matter., 12 (2000) 10647.

[18] E Braun et al., Nature, 391 (1998) 775.

[19] A M Smith and S Nie, Acc. Chem. Res., 43(2) (2010) 190.

[20] J Jasieniak et al., ACS nano, 5(7) (2011) 5888.

[21] X L Liu and Y J Zhu, Mater. Lett., 63 (2009) 1085.

[22] D S Chuu and C M Dai, Phy. Rev., B45(20) (1992) 11805.

[23] J S Jie et al., Nano Lett., 6 (2006) 1887.

[24] S Yong et al., J. Appl. Phys., 128 (7) (2020) 075303.

[25] J W Stouwdam and R A Janssen, Adv. Mater., 21(28) (2009) 2916.

[26] Z F Liu et al., J. Mater. Chem., 20(3) (2010) 492.

[27] R M Ma., Nanotechnology, 18 (2007) 205605.

[28] N Pradhan et al., Nano Lett., 14 (2007)312.

[29] B Ghosh et al., Sol. Energy Mater. Sol. Cells., 92 (2008)1099.

[30] F B Slimen et al., RSC adv., 7(24) (2017)14552.

[31] S Rai and L Bokatial, Bull. Mat. Sci., 34(2) (2011) 227.

[32] L Bokatial and S Rai, J. Lumin.,130(10) (2010) 1857.

[33] Q Zhang et al., Nano Energy, 30 (2016) 481.

[34] B Guzelturk et al., Adv. Mater., 27(17) (2015) 2741.

[35] M A Sakr et al., Res. J. Nano. Eng., 3(2) (2019) 1.

[36] L Shoujun, Rev Roum Chim., 54(10) (2009) 815.

[37] M M Mecheril and J Philip, AIP Conference Proceedings, 2263(1) (2020) 060011.

[38] C Regmi et al., Front. Chem., 6 (33) (2018).

[39] Z Kang et al., Nano Res., 8 (2015) 2004.

[40] E R Nestmann et al., Cancer Res., 39 (1979) 4412.

[41] S Thaler et al., Investig. Ophthalmol. Vis. Sci., 49 (2008) 2120.

[42] H Ali, E Khan and M A Sajad, Chemosphere, 91(7) (2013) 869.

[43] Gamal El-Din, Sci.Total Environ., 809(2020) 151120.

[44] Z Charikleia et al., J. Environ. Manag., 297 (2021) 113301.

[45] W Long, Colloids Surf. A Physicochem. Eng. Asp., 650 (2022) 129468.

[46] P Fatemeh et al., Chem. Pharm., 23 (2021)100501.

[47] A Bahadoran, J. Photochem. Photobiol. B, Biol., 228 (2022) 112393.

[48] Y Zahraa et al., Dye. Pig., 159 (2018) 49.

[49] Guo Wei et al., Tetrahedron Lett., 57 (2016) 3801.

[50] Z H Jabbar and S E Ebrahim, Environ. Nanotechnol. Monit. Manag., 17 (2022): 100666

[51] S Naranthatta et al., ACS omega, 6 (2021) 8646.

[52] K Shivaji et al., ACS Appl. Nano Mater., 1 (2018) 1683.

[53] L Hong et al., RSC adv., 7 (2017) 36819.

[54] V N Reena et al., AIP Adv., 12 (10) (2022) 105217.

[55] C Abbasian et al., J. Appl. Phys., 131(15) (2022) 150902.

[56] Pandey et al., J. Appl. Phys., 131(7) (2022) 074901.

[57] J D Watson and F HC Crick, Nature, 171(4356) (1953) 737.

[58] X Wang et al., Environmental health and toxicology, 29(1) (2014) 2014007.

[59] Y Yao et al., Nanotechnology, 19 (2008) 405601.

[60] B Nithyaja et al., J. Appl. Phys., (112), (2012) 064704.

[61] L E Brus, J. Chem. Phys., 80 (1984) 4403.112

[62] R Maddalena et al., Thermochimica Acta, 672 (2019) 142.

[63] W Wang, et al., Chem. Mater., 14 (2002) 3028.

[64] R Devi et al., Bull. Mater. Sci., 30 (2007) 123.

[65] S Aneeqa et al., World Academy of Science, 4(9) (2010) 532.

[66] K S Rathore et al., J. Ovonic Res., 5(6) (2009) 175.

[67] T Meron and G Markovich, J. Phys. Chem. B, 109 (2005) 20232.

[68] López-Cabaña, Nanoscale Res. Lett., 6 (2011) 1.

[69] H Cao et al., Inorg Chem., 45 (2006) 5103.

[70] J C Wu et al., J. Phy. Chem. C, 115 (2011) 5675.

[71] J Guthmuller and B Champagne, J. Phy. Chem., A112 (14) (2008) 3215.

[72] A Penzkofer and W Leupacher, J. Lumin., 37(2) (1987)61.

[73] C András et al., J. Appl. Phys., 131(7) (2022) 071102.

[74] F Higuchi and J I Muto, Phy. Lett. A, 81(1) (1981) 95.

[75] B Das B et al., Res. Opt., 1 (2020) 100013.

[76] M Nandimath et al., J. Lumin., 207 (2019) 571.

[77] Graf R F (1999) Modern Dictionary of Electronics, Boston, MA.

[78] J Shakya et al., AIP Conference Proceedings, 1942 (2018) 050119.

[79] J Shakya, H Sahoo, and T Mohanty, J. Mater. Sci., 52(7) (2017) 3831.

[80] A Khan et al., Inorg. Chem. Commun., 72 (2016) 33.

[81] R Lucas et al., J. Org. Chem., 79(6) (2014), 2419.

[82] H Sk Tofajjen, and S K Mukherjee, J. Hazard. Mater., 260 (2013) 1073.

[83] Reyes-Esparza et al., J. Nanobiotechnology, 13 (2015) 1.

Chapter 4

Photonic and Biological Applications of DNA capped Ag Nanoparticles

This Chapter covers the synthesis, characterization, and the diverse applications of DNA-capped silver nanoparticles (Ag NPs). Characterizations of the Ag nanoparticles were done using absorption spectra and SEM. Spectra shows a predominant peak at 425 nm and the SEM image shows the particles size is about 45 nm. The investigation demonstrates substantial photocatalytic efficacy, photodegradation of MB is higher than Rh6G. The effect of Ag nanoparticles enhances the fluorescence of Rh6G doped sol-gel glasses. Furthermore, the findings illustrate significant mosquito larvicidal effects and antibacterial effects for both Gram-positive and Gram-negative bacteria, with DNA-capped Ag nanoparticles. Cytotoxicity assessments on HeLa cells reveal concentration-dependent effects, with an LC50 value of 47 µl/ml. Additionally, in-vitro experiments with HeLa cells suggest the promising utility of DNA-capped silver nanoparticles for bioimaging applications. This comprehensive analysis highlights the multifunctionality and potential of DNA-capped silver nanoparticles, offering promising avenues for further exploration and innovation within various scientific domains, particularly in the realm of nanomaterial research.

The results of this chapter are published as:

1. Reena V N, Shanasree M, Kumar S, Bhagyasree G S, Nithyaja B, Mosquito Larvicidal Activity of DNA Capped Colloidal Silver Nanoparticles. IOP Conference Series: Materials Science and Engineering 1221 (2022) 012051 (Publisher: IOP Publishing)
2. Reena V N, Bhagyasree G S, Shilpa T, Aswati Nair R, Nithyaja B, Multifaceted Applications of DNA-Capped Silver Nanoparticles in Photonics, Photocatalysis, Antibacterial Activity, Cytotoxicity, and Bioimaging. Journal of Fluorescence (2024) 1. (Publisher: Springer Nature)

4.1 Introduction

DNA-capped silver nanoparticles (Ag NPs) have emerged as a fascinating class of nanomaterials due to their exceptional properties and versatility in both scientific and industrial applications [1]. The synthesis of these nanoparticles involves the use of DNA as a capping agent, which imparts stability, control over size and shape, and biocompatibility. This paper aims to investigate some photonic and biological applications of DNA-capped Ag NPs [2-5]. The synthesis of DNA-capped Ag NPs is a well-established process. It often involves incubating DNA-coated with metal ions in a reducing agent solution. DNA serves as a stabilizing agent, preventing the uncontrolled growth of Ag NPs and ensuring the formation of well-defined structures. The resulting DNA-Ag NPs exhibit uniform size and shape, making them highly suitable for various applications [6-10].

DNA-capped Ag NPs have garnered significant attention in the field of optics and medical applications. Their unique optical, electrical, thermal properties and chemical stability make them ideal for enhancing the photoluminescence of dyes, such as Rh6G. The photoluminescence of dye can be enhanced using metal nanoparticles due their surface plasmon effect [11, 12]. These improved phenomena can be applied in optical technology industry. This property has significant implications in the development of dye lasers and fluorescence-based technologies. The Ag NPs have demonstrated the capability to enhance the PL intensity of Rh6G when dissolved in aqueous solutions [13-15]. The dissolution of Rh6G in water, however, is often associated with a higher possibility of photobleaching. To lessen this effect, incorporating Rh6G into a sol-gel derived matrix has been explored as an effective strategy. The sol-gel matrix serves to reduce the occurrence of photobleaching, providing a more stable environment for Rh6G molecules. Nevertheless, Rh6G poses risks to living organisms as it is carcinogenic and

corrosive to metals, making the handling of aqueous Rh6G unsafe [16]. However, when Rh6G is incorporated into a solid matrix like sol-gel glass, its interaction with water is minimized, thereby reducing the associated risks mentioned above. This approach enhances safety by qualifying the potential harm associated with direct exposure to aqueous Rh6G, making the use of Rh6G in a solid matrix, such as sol-gel glass, a safer alternative. Even though, Ag NPs are photodegrading agent, once we incorporate Ag NPs in solid sol-gel glass matrix, the photodegradation of Rh6G can be reduced due to lack of water content in the matrix.

The Ag NPs find applications in medical imaging, where their optical properties enhance contrast and sensitivity. DNA-capped Ag NPs show promise in lasing applications due to their ability to enable precise control over lasing wavelengths and intensities by modifying DNA sequences. The DNA capping enhances nanoparticle stability and facilitates controlled self-assembly, promoting conditions for efficient lasing. This technology has potential implications for compact, tunable, and highly customizable laser sources in fields like sensing, imaging, and communications [17-18].

One of the most fascinating aspects of DNA-capped Ag NPs is their potential in eco-friendly larvicidal activities [19-21]. The green synthesis of Ag NPs using plant extracts with insecticidal properties has shown exceptional promise. These nanoparticles are highly efficient against mosquitoes, even at low concentrations. Furthermore, the synthesis of DNA-capped Ag NPs is environmentally friendly, cost-effective, and less energy-intensive, making it a sustainable approach to pest control and insect-borne disease prevention [22-26].

The antibacterial properties of Ag NPs, including DNA-capped ones, have substantial implications in various medical and environmental applications. Ag NPs have demonstrated effectiveness in wound treatment, catheter

coatings, textile fabrics, and water disinfection [2,7, 27]. Their cytotoxicity, a subject of ongoing research, is attributed to factors like the presence of dissolved Ag^+ ions and nanoparticle size. Understanding these effects is crucial for safe and effective application [28-31]. While a previous study explored the antibacterial activity of bacterial genomic DNA-stabilized Ag NPs under light activation, our investigation employed herring sperm derived DNA as a stabilizing agent, and notably, light activation was not required in our study [32]. Ag NPs have become promising candidates for bioimaging applications, particularly in fluorescence imaging. The unique optical properties of these NPs enhance imaging sensitivity and contrast. In fields like medical diagnostics and fluorescence microscopy, Ag NPs offer exciting possibilities for enhancing image quality and accuracy [33].

Previous work has reported the synthesis method and explored the nonlinear properties of DNA-capped Ag NPs [5]. The photonic applications of these nanoparticles, including their photocatalytic activity and their impact on the PL of Rh6G-doped sol-gel derived glasses, have not been investigated before. Additionally, this study presents novel findings in the realm of biological applications, including larvicidal activity, antibacterial activity, cytotoxicity, and bioimaging.

This chapter discusses the photocatalytic activity of DNA capped Ag NPs on Rh6G and MB and the effect of Ag NPs on the photoluminescence of Rh6G doped sol-gel derived glasses. In the proceeding part, the biological applications such as larvicidal activity, antibacterial activity, cytotoxicity and bioimaging of Ag NPs were screened.

4.2 Materials and Methods

All the chemicals utilized were procured from Sigma-Aldrich. The synthesis of Ag NPs was accomplished through a chemical reduction method. This

approach involves the reduction of silver ions in a solution to form nanoscale silver particles via DNA template, and its successful implementation underscores the controlled and tailored synthesis of Ag NPs suitable for different applications in the research [5,8].

4.2.1 Synthesis of Ag NPs

The procedure previously performed by Nithyaja et al. was repeated in the synthesis of Ag NPs [5]. Utilizing a conventional reduction technique, Ag NPs were synthesized within an aqueous solution containing DNA extracted from Herring sperm. A 0.25 mM of $AgNO_3$ dissolved in a 20 ml aqueous solution containing 20 weights % DNA and allowed to ultrasonicate for 10 minutes. While stirring, 0.6 ml of 10 mM sodium Borohydride ($NaBH_4$) was added and stirring continued for 30 s. Deep golden yellow coloured solution of Ag NPs was obtained [8]. The absorption spectrum of the synthesized Ag NPs was analyzed and the surface topology was observed by SEM.

4.2.2 Preparation of Ag incorporated Rh6G doped sol-gel glass

The Ag NPs incorporated Rh6G doped sol-gel glasses were prepared by the following method as shown in the schematic Figure.4.1. A 0.5 ml of Ag NPs was added to 10 ml ethanolic solution of 0.01 mM Rh6G and kept under stirring for 10 minutes. 10 ml of TEOS is added to this mixture and stirred well. Required amount of de-ionized water also added to equalize the water content in each sample. One or two drops of HCL were added to the reaction mixture to fasten the sol-gel process. The stirring continued for another 30 minutes and the clear solution was poured into petri dish of diameter 10cm and kept undisturbed for one week. The coloured sol-gel glass obtained was transparent and the average thickness and diameter of the derived glasses are 1±0.25 mm and 7±0.5 cm respectively. A couple of similar samples were

prepared with varying concentrations of Ag NPs (0 ml, 0.5 ml,1 ml, 2.5 ml and 5 ml).

The photoluminescence measurements, chromaticity studies and CIE coordinates (1931 colour space) of Rh6G doped sol-gel glasses were investigated. These investigations were carried out both in the presence and absence of Ag NPs using an OHSP350 spectrometer. The samples were placed in a sample holder within a dark environment. The excitation light source was the frequency generated laser at 532 nm using Nd: YVO_4 laser, which was directed onto the sample. A polymer optical fiber cable was used to carry the collected light from the sample to the spectrometer, which is kept at 90 degrees from the sample. The emitted fluorescence is measured by the sensitive detector and it records the spectra.

The schematic presented in Figure 4.2 depicts the synthesis process of Rh6G doped glasses before and after incorporation with Ag NPs. The visual representation highlights a noticeable shift in colour between the Rh6G doped glasses and the Rh6G doped sol-gel glasses post-incorporation with Ag NPs. This colour variation is visually evident, underscoring the impact of the nanoparticle integration on the optical properties of the material. The accompanying PL spectrum further highlights this difference, illustrating a distinct change in the emission characteristics. The observed colour discrepancy in both the schematic and PL spectrum signifies the successful incorporation of Ag NPs, suggesting potential alterations in the optical and photoluminescent behaviour of the Rh6G doped sol-gel glasses.

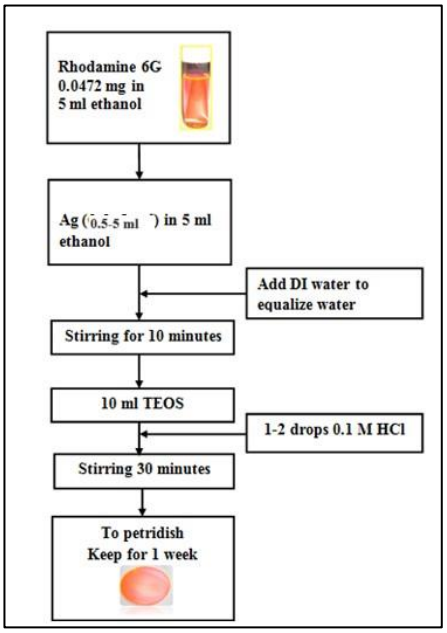

Figure.4.1 Schematic diagram of preparation of Ag incorporated Rh6G-doped sol-gel glass

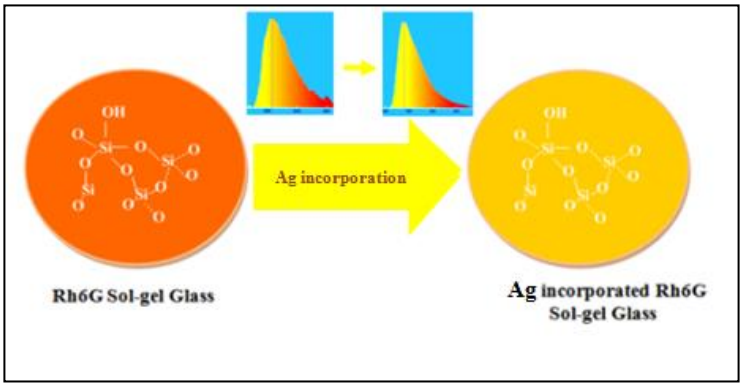

Figure.4.2 Representation of Rh6G glass and Ag incorporated Rh6G glass and their graphical variations of PL spectra

4.2.3 Photocatalytic activity of Ag NPs

Photocatalytic activity of the synthesized Ag NPs was done as in the previous chapter. Here 5 ml of Ag NPs were added to Rh6G and MB as photocatalyst

before irradiation. Absorption spectra of each sample were taken for 120 minutes of irradiation [34].

4.2.4 Larvicidal activity studies of Ag NPs

The larvicidal activity of Ag NPs was estimated against mosquito larvae, demonstrating significant efficacy in larval mortality. The nanoscale dimensions and inherent antimicrobial properties of Ag NPs likely contributed to their potent larvicidal effects, suggesting their potential as an environmentally friendly and effective solution for controlling mosquito populations in aquatic environments. The observed larvicidal activity underscores the promising role of silver nanoparticles in the development of sustainable and targeted approaches for vector control. Mosquito larvae were collected from Kannur district, Kerala (11°54'30.2"N 75°19'3.0"E). Healthy third instar larvae were cultured in tap water at a temperature of 30°C± 2°C. The larvicidal studies followed World Health Organization (WHO) guidelines [35]. Various concentrations of Ag NPs (0.5 ml, 1 ml, 2.5 ml, and 5 ml) were tested in 200 ml of distilled water, each with 25 larvae. A control group with 200 ml water was also used. Five trials were conducted for each concentration. Larval mortality rates after 24 hours were determined, and the average mortality rate was calculated using the Abbott formula. Mosquitoes lay eggs in water therefore to destroy mosquitoes at their larval stage, it is necessary to apply the larvicidal agent directly to water containing larva. The larvicidal agent is more effective when it is miscible in water. Since Ag NPs has colloidal nature in water, they can be more effective than D-CdS NPs. The mortality rate in accordance with concentration of Ag NPs was calculated by using Abbott's formula. The mortality data were subjected to probit analysis for finding LC_{50}, LC_{90}. LC_{50} is the lethal concentration of the sample for 50% mortality ad LC_{90} is that for 90% mortality.

4.2.5 Colour analysis of the microscopic image of larva

The Ag NPs treated and non-treated larvae were viewed under Olympus CX43 bio-microscope and taken photographs were analyzed with RGB and HSV colour analysis by Python Programming (Version-Python 3.8) to visualize the image in another colour space. By doing this, one can visibly recognize the changes in a treated and non-treated larva.

The method of representing the contained colours in digitally is generally referred to as colour space models. Each colour spaces describes the colour information in special ways which makes certain computations more beneficial and also contribute a way to find colours that is more perspective. The colour spaces in this study used are RGB and HSV [36]. A brief description of each is shown below.

4.2.6 RGB colour space

RGB colour space is the base model which is derived from three orthogonal additives red, green and blue chromaticity commonly known as primary colours. All the other colour spaces are obtained by mathematical transformation of RGB colour space.

4.2.7 HSV colour space

HSV colour space is a cylindrical coordinate representation of RGB colour space formulated through non-linear transformation. HSV colour space is closer to the way human perceive a colour. Hue (H) represents the dominant wavelength present in a mixture of colour. Saturation (S) gives the measure of pure colour diluted by white light. The Value (V) component provides the gray value from negative value (blue colour) to positive value (yellow). It encodes the perceptual difference in colours when viewed by human.

Antibacterial activity, cytotoxicity and bioimaging applications of Ag NPs were done as in the procedure described in the experimental section of chapter 2. Three microbes were taken for investigation; two gram-positive, *Staphylococcus aureus* and *Streptococcus mutans*, and one gram-negative, *Pseudomonas aeruginosa.*

4.3 Result and Discussions

The confirmation of Ag NPs formation was verified through their characterization data. UV-visible absorption spectroscopy provided valuable insights into the optical properties of the synthesized nanoparticles, offering information on their size, shape, and concentration by analyzing the absorption peaks in the UV-visible range. Additionally, SEM was employed to visualize and analyze the surface morphology and structure of the Ag NPs. Together, these characterization techniques, providing a thorough understanding of the key attributes and confirmatory the successful synthesis of silver nanoparticles in the study.

4.3.1 Characterizations of Ag NPs

The Figure 4.3. represents the UV-visible spectrum of Ag NPs and the absorption peak was observed around 425 nm. The SPR peak of Ag NPs mentioned in many other previous reports is matches with this value [5,8]. The emission wavelength of Ag NPs is usually situated in region 400-600 nm. The luminescence of Ag metal is generally attributed to electronic transitions between the upper d band and conduction sp band [5, 8]. As the Ag NPs possess emission wavelength in visible region and considering the biocompatibility, these NPs can be greatly recommended to fluorescence imaging of cells.

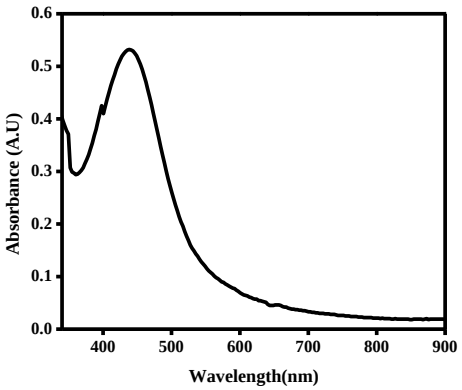

Figure.4. 3 Absorption spectra of Ag NPs

The SEM image shown in Figure 4.4 provides valuable insights into the characteristics of Ag NPs. The NPs exhibit a typical spherical morphology, suggesting a uniform and well-defined three-dimensional structure at the nanoscale. The significance of this spherical shape lies in its potential influence on the nanoparticles' reactivity, stability, and interactions with their surroundings. The associated information indicates an average nanoparticle size of 45 nm, referring to the diameter of these spherical structures. Nanoparticle size is a critical parameter as it plays a crucial role in determining various material properties. In this context, the 45 nm average size holds importance for understanding and manipulating the behaviour of these Ag NPs in applications ranging from catalysis to biomedical fields, where nanoscale dimensions can significantly impact performance and functionality.

The emission wavelength of Ag NPs is usually situated in region 400-600 nm. The luminescence of Ag metal is generally attributed to electronic transitions between the upper *d* band and conduction *sp* band [5, 8]. As the Ag NPs possess emission wavelength in visible region and considering the biocompatibility, these NPs can be greatly recommended to fluorescence imaging of cells.

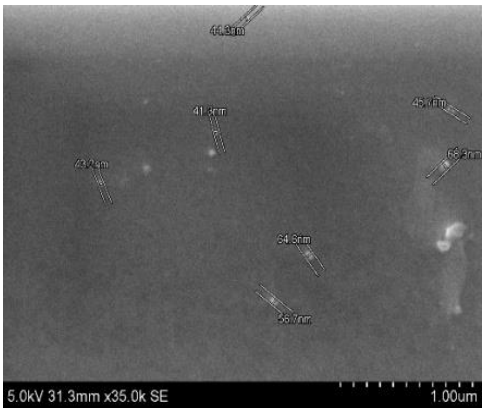

Figure.4. 4 SEM image of Ag NPs

4.4 Photonic applications of Ag NPs

The experimental exploration of Ag NPs encompasses two fundamental photonic applications. Firstly, Ag NPs are examined for their photocatalytic activity, exploiting on their unique catalytic properties under light exposure. This study aims to assess their efficacy in promoting chemical reactions, potentially for applications in environmental remediation. Additionally, the impact of Ag NPs on the photoluminescence of Rh6G doped sol-gel derived glasses is investigated. By introducing Ag NPs into these glasses, the study aims to understand how the nanoparticles influence the emission properties of Rh6G doped sol-gel glasses. This dual investigation into photocatalytic activity and photoluminescence modulation not only broadens our understanding of Ag NPs' applications but also provides insights into their potential roles in diverse photonic technologies, spanning environmental remediation to optoelectronic devices.

4.4.1 Effect of Ag NPs on the photoluminescence of Rh6G doped sol-gel derived glass

The investigation focused on the photoluminescence of sol-gel derived glasses doped with Rh6G under two conditions: with and without the presence of Ag NPs. This comparative study aimed to discern the influence of Ag NPs on the photoluminescent properties of Rh6G within the glass matrix. Additionally, the research investigated into the temperature dependence of photoluminescence in glasses incorporating Ag NPs and Rh6G. This aspect of the study sought to explain how variations in temperature impact the luminescent behavior of the glasses. By examining these dual factors, the presence of Ag NPs and the temperature conditions, the research contributes valuable insights into the complex interaction between nanoparticle incorporation and environmental factors on the photoluminescence of doped sol-gel derived glasses, thereby enhancing our understanding of their potential applications in optoelectronics and related technologies. The characterizations of the Ag NPs incorporated Rh6G doped glasses were done using absorption spectra and XRD.

The absorption spectrum exhibited by sol-gel-derived glasses, Rh6G doped glasses, and also Ag NPs incorporated Rh6G glasses are shown in Figure. 4.5. Even though the sol-gel derived glasses have finite absorption in the UV region, no considerable absorption is observed in the visible region and they exhibit high optical transmittance in this region. The absorption in the range of Rh6G-doped sol-gel is found to be in between 450 nm to 570 nm with a maximum of 537 nm. This can be assigned to the monomeric state of Rh6G equivalent to S0→S1 transitions [37-38]. A dimeric peak of Rh6G was also found on the left of the major peak which is around 480 nm. On increasing concentration of Ag NPs, the absorption intensity is also increased with a notable blue shift. The Rh6G peak blue shifted from 537 nm to 507 nm.

Unlike D-CdS, here an enhancement in absorption intensity is noted. This is because that the absorption range of Ag NPs is in the range of 400-550 with a maximum at 425nm. This region overlaps with the absorption spectra of Rh6G. The overlapping of the curves is the evidence of conditions of plasmon resonance. On increase in concentration of Ag NPs, there is a tendency to left shift also.

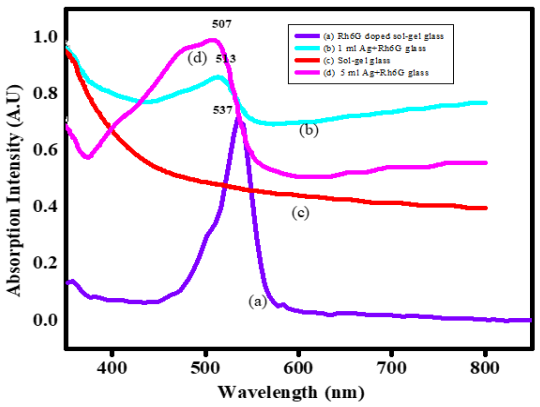

Figure.4. 5 Absorption Spectra of Sol-gel glass and Ag NPs incorporated Rh6G-doped sol-gel glass

The XRD pattern represented in Figure 4.6, corresponding to the Rh6G glass incorporating Ag NPs, reveals significant information about the structural characteristics of the material. The existence of a broad peak centered at 23.5^0 is particularly noteworthy, as it indicates the amorphous nature of the material. In XRD patterns, sharp peaks typically signify crystalline structures, whereas broad peaks are revealing of an amorphous or disordered arrangement of atoms. The broad peak observed at 23.5^0 suggests that the structure of the Rh6G glass, with the incorporation of Ag NPs, lacks long-range order and exhibits an amorphous behavior. This finding holds relevance in materials science, as the amorphous state can influence various properties such as optical transparency, mechanical flexibility, and electrical conductivity.

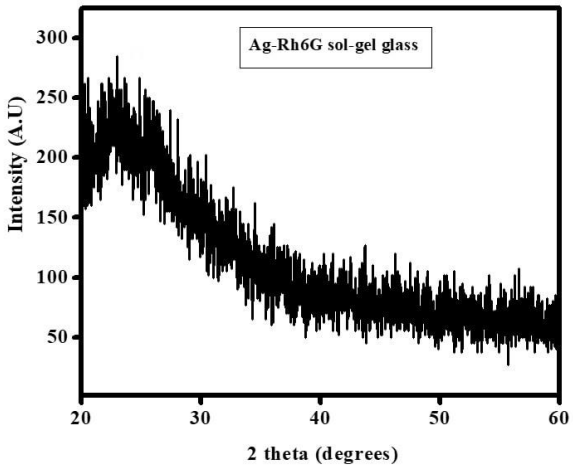

Figure.4.6 XRD pattern of Ag incorporated Rh6G doped sol-gel glasses

(a) Photoluminescence of Rh6G doped sol-gel glass

The PL of Rh6G glass is studied with an excitation wavelength of 532 nm for different concentrations are shown Figure.3.9 of chapter 3.

In order to study the effect of Ag NPs on the PL of Rh6G, a concentration in the quenching region ($1x10^{-4}$ M) is selected. Figure.4.7 exhibit the emission spectra of Rh6G-doped sol-gel glass and its fluorescence emission variation upon the addition of varying concentration of Ag NPs (0 mL, 0.5 mL, 1 mL, 2 mL, and 5 mL); excitation wavelength was 532 nm. As increase in concentration of Ag NPs, the intensity of emission of Rh6G doped glass is significantly increased. The spectrum specifies a red shift from 582 nm to 596 nm upon the addition of 0.5 mL of Ag NPs. Moreover, on increasing the concentration of Ag NPs, a gradual blue shift (from 596 to 590 nm) in the peak is also observed. The presence of Ag NPs leads to a phenomenon called plasmonic enhancement. Plasmons are collective oscillations of electrons in metal NPs. They can interact strongly with nearby fluorophores, thereby modifying their emission properties. Here the plasmonic interaction between the dye molecule and the Ag NPs causes increased fluorescence emission.

When evaluating the fluorescence intensity of a dye absorbed into Ag NPs, it's crucial to take into account the spectral overlap between the dye's properties and the localized surface plasmon resonance (LSPR) of the nanoparticles. The Ag NPs show fluorescence peak in the range of 400-600 nm [5, 8]. Therefore, there may be a chance to absorb and re-emit this radiation by the excited Rh6G molecules. This may lead to an intensified radiative decay process. The blue shifting of the emission wavelength may be due to the presence of coupled emission of Ag NPs along with Rh6G. Tunability of emission wavelength can be achieved from 580 nm to 590 nm by changing the concentration of Ag NPs. The drop in the PL intensity upon the excess addition of Ag NPs can be explained by the quenching due to the excess Ag NPs. As the concentration of Ag NPs surpasses a certain threshold, Rh6G molecules undergo adsorption onto the Ag NPs' surface, forming non-fluorescent complexes. These complexes not only absorb the intensity of the excitation wave but also dissipate this energy non-radiatively [39-40]. The photobleaching of the samples for is negligible under room temperature conditions.

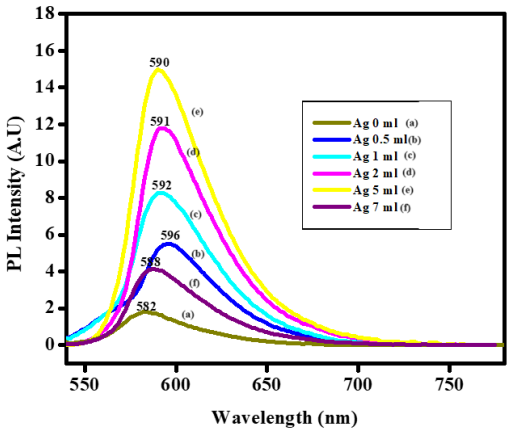

Figure.4.7 Photoluminescence curve of Ag NPs incorporated Rh6G doped sol-gel glass

(b) Annealing temperature effect on photoluminescence

To examine the annealing temperature effect on the PL of the samples, PL spectra for annealed Rh6G sol-gel glass with 2 ml Ag NPs were taken at the same excitation wavelength, 532 nm. In Figure.4.8, the annealing temperature effect on PL at 60^0C, 100^0C, 150^0C, and 250^0C of Rh6G is shown. At 60^0C, it is found that the PL is enhanced by approximately by 2-fold associated with a right shift of peak from 590 nm to 596 nm. A maximum PL intensity enhancement by approximately by 3-fold is observed at 100^0C, and the corresponding peak shift is from 590 to 601 nm. The main luminous quenchers, hydroxyl groups, present in the sol-gel glass may reduce their density upon increasing annealing temperature. This will lead to enhancement in the PL intensity. At 150^0C, the PL intensity is reduced than that of PL intensity at Rh6G at room temperature with a peak shift from 590 to 604 nm. At 200^0C, the intensity of luminescence reduced drastically to a value less than half of its intensity at room temperature with a peak shift from 590 to 606 nm. The reduction of PL intensities in high annealing temperature may be due to the following reasons. Structural modifications of sol-gel-derived glasses may have significant consequences on the emission of Rh6G molecules on heat treatment. Though, at sufficiently high temperatures about 200^0C, there is a reduction in the number of defects in the sol-gel matrix which slow down the energy transfer. Furthermore, there occurs shrinkage in the sol-gel network which leads to the aggregation of Ag NPs nanoparticles and causes an energy migration amongst Ag NPs. It also observed the bleaching of Rh6G molecules on Rh6G glass at high temperatures. This will also lead to a reduction in intensity above 150^0C [41-43]. The annealing temperature studies on the sample reveal that an increment in temperature can also tune the emission wavelength from 590 nm to 604 nm.

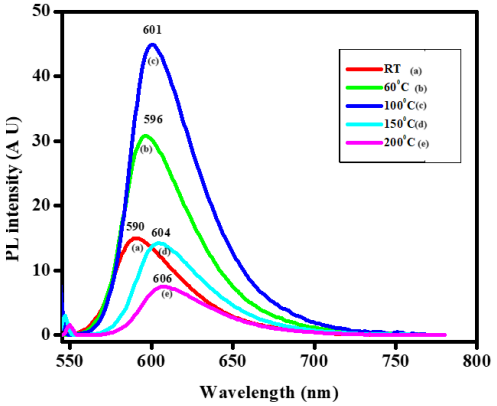

Figure.4.8 PL spectra of Ag NPs incorporated Rh6G doped sol-gel glass with annealing temperatures

(c) Chromaticity studies and CCT

The location of the colour coordinates for Rh6G sol-gel glass with and without Ag NPs nanoparticles in the CIE chromaticity diagram is shown in Figure.4.9. From this figure, one can see that the colour of the prepared sample is located in the orange region and the CIE coordinates vary from (x=0.5842, y=0.4106 to x=0.5981, y=0.4008) in accordance with varying concentration of Ag NPs (0 ml to 5 ml).

The CCT values lie between 1595 K and 1473 K when the concentration of Ag NPs varies between 0 ml and 5 ml. The colour purity values for both samples are found to be above 99.5%. The presence of Ag NPs affects the CIE coordinates and CCT values of Rh6G sol-gel glass [44].

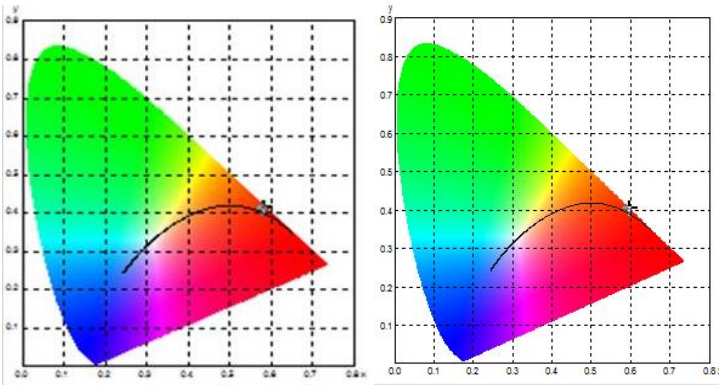

Figure.4.9 Chromaticity diagram of (a) Rh6G glass (b) Ag NPs incorporated Rh6G glass

(d) Photoluminescence dynamics

The time-resolved fluorescence spectroscopy gives information on the decay dynamics of excited states of Rh6G doped sol-gel glasses. In Figure 4.10, it is shown that the fluorescence lifetime decay curves of both Rh6G glass and Ag NPs incorporated Rh6G glass at room temperature. For this, 2 mL Ag incorporated Rh6G glass was taken because it showed maximum emission intensity. It is clear that the incorporation of Ag NPs has no effect on the fluorescence lifetime of Rh6G. Even though the concentration of Ag NPs can enhance the rate of energy transfer; it does not control the emission probability to ground state. It can be concluded from the fluorescence lifetime; Ag NPs can tune the emission wavelength and intensity of Rh6G.

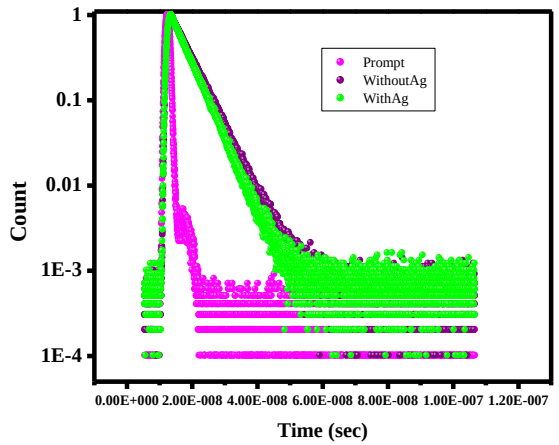

Figure.4.10 Fluorescence lifetime decay of Rh6G-doped sol-gel glass with and without Ag NPs

4.4.2 Photocatalytic activity

The Ag NPs are also useful in the field of photocatalytic degradation, which is becoming increasingly eco-friendly and less costly with a low environmental impact. The photocatalytic activity of Ag NPs was investigated by photodegradation of Rh6G and MB under UV irradiation. Photocatalytic activity of Ag NPs on Rh6G was evaluated for a period of 120 minutes. For this 10 ml of Ag NPs were taken. The activity of Ag NPs is negligible for Rh6G; this can be seen from the Figure.4.11. This may be due to the overlapping of emission wavelength of Rh6G and Ag NPs. Emission wavelength region of Ag NPs is between 400-600 nm and that of Rh6G is 532 nm. The corresponding photodegradation of Rh6G is less than 10% for a period of 120 minutes. In the case of MB dye, there is noticeable activity found for MB, which is shown in Figure. 4.12. The graph represents the absorption spectra of the dye solution irradiated by UV radiation at different time (0 min, 5 min, 10 min, and 20 min). The peak at 425 nm may be due to the presence of Ag NPs; its intensity has enhanced on addition of Ag NPs.

The peaks corresponding to MB dye lies between 600 and 670 nm. The intensities of the absorption peaks of MB are enhanced in the presence of Ag NPs except the peak at 665 nm. From the graph we can observe the absorption peak of methylene blue dye was decreased and the absorption peak of the silver nano is enhanced. The percentage of photodegradation of MB dye is about 34% in 20 minutes. Even if the photocatalytic degradation value is 34%, from 20 minutes onwards no specific peak at 665 (characteristic peak of MB) is not found. This indicates that, in the presence of Ag NPs, a complete degradation has occurred to MB. The absorbance value in the region 600- 700 nm may be absorption value of Ag NPs.

It is known that Ag NPs have high surface area to volume ratio due to their small size. The high surface area provides numerous active sites for the adsorption of methylene blue dye molecule. The adsorption of the dye on to the Ag NP's surface is the first step in the degradation process. The Ag NPs can act as electron donors and acceptors during catalytic reactions. When Ag NPs are irradiated with light, they can absorb photons and generate electron-hole pairs. This photo generated electron can be transferred to the adsorbed methylene dye molecule, initiating redox reactions. The transfer of electron between Ag NPs and MB dye molecule results in the degradation of the molecule [45].

The catalytic degradation of MB using Ag NPs also depends on several factors, including concentration of the dye, size of the nanoparticle, and reaction condition (pH). Optimizing these parameters can enhance the catalytic efficiency [46].

During the catalytic degradation of methylene blue there is an enhancement in the absorption spectra of Ag NPs. Since the solution is irradiated by the UV radiation the size of the Ag NPs reduces which leads to the increment in the number of Ag NPs in the solution of methylene blue. This causes the

enhancement in the absorbance of the Ag NPs. This also speeds up the process of dye degradation. The catalytic degradation of MB has huge applications in waste water treatment and environmental remediation. Methylene blue is a synthetic dye used in industries such as textiles printing and dying but it is also an environmental pollutant due to its toxic and carcinogenic properties. In waste water treatment Ag NPs can act as a catalyst to degrade the dye molecule in to harmless products. It helps in reducing the colour and toxicity of the waste water before its discharge in to natural water bodies. Ag NPs can also use for water purification. During the dye degradation it also prevents the growth of microorganisms in water that may arise due to the decomposition of dyes. These are some of the applications of Ag NPs in dye degradation. Figure.4.13 represents the percentage of degradation of MB in the presence of Ag NPs.

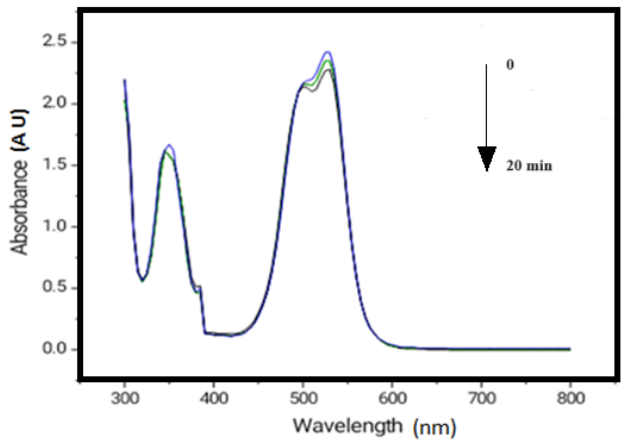

Figure.4. 11 Absorption spectra (Photocatalytic degradation) of Rh6G in the presence of Ag NPs

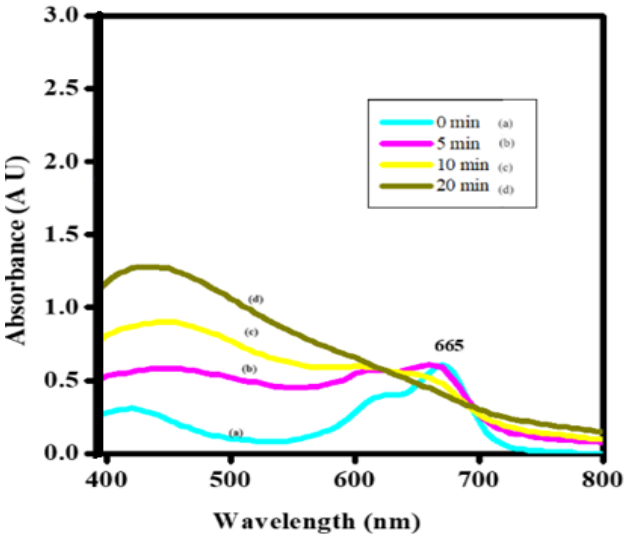

Figure.4.12 Absorption spectra (Photocatalytic degradation) of MB in the presence of Ag NPs

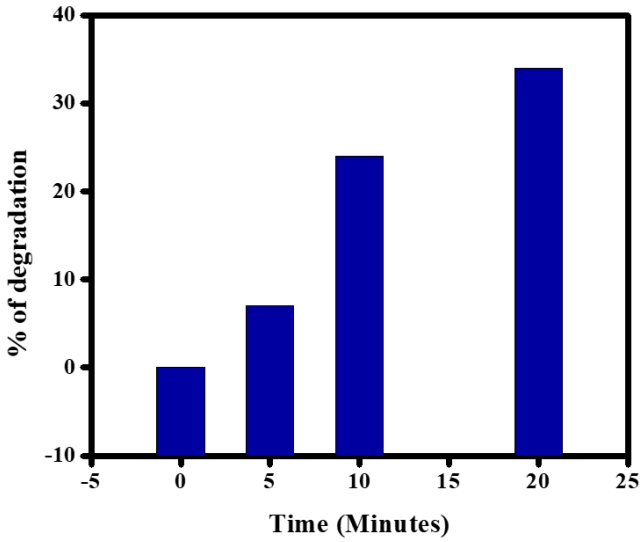

Figure.4.13 Photocatalytic degradations of MB in the presence of Ag NPs

4.5 Biological Applications of Ag NPs

4.5.1 Larvicidal Activity of Ag NPs

The mortality data attained from bioassays conducted for a duration of 24 hours is visually presented in Figure 4.14, while Table.4.1 provides a comprehensive overview of the mortality values observed at the 24 hours mark. Notably, the impact of Ag NPs is striking, revealing a 100% mortality rate at a concentration of 5 ml. In contrast, both the control group and the capping agent, DNA, exhibited negligible mortality. Figure 4.15 demonstrates a probit analysis. The calculated LC_{50} (lethal concentration for 50% mortality) and LC_{90} (lethal concentration for 90% mortality) values for Ag NPs are determined to be 0.55445 and 2.8305, correspondingly. Additionally, 95% confidence interval for these values was calculated. These findings underscore the potent bioactivity of Ag NPs, particularly at higher concentrations, as evidenced by the considerable mortality rates and the precise quantification provided by the probit analysis.

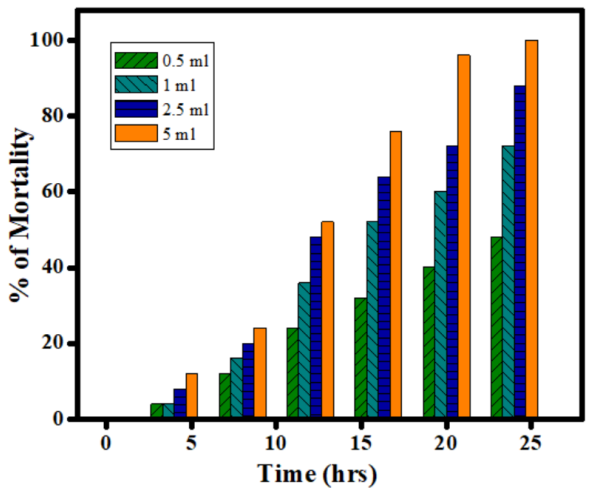

Figure.4.14 Percentage of Larvae dead Vs time of exposure

To determine the toxicity of Ag NPs, a non-target organism *P.recticulata* (Guppy) of 1 g±0.25 g were collected and 30 healthy P.*recticulata*were placed in 400 ml water solution with three replicates. Each group was exposed to Ag NPs (5 ml) with one control group where 30 *P.recticulata* were placed in unchlorinated water and observed for duration of 3 days with 24 hours periods. It is found that no *P.recticulata*were died in the presence of Ag NPs. This indicates that larvicidal activity of DNA capped colloidal Ag NPs are targeted to larva only.

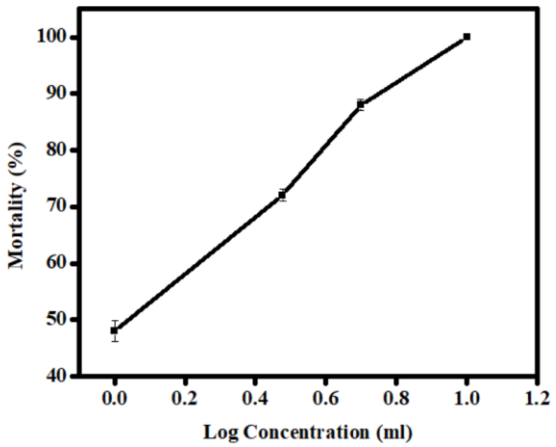

Figure.4.15 Probit Analysis

Table.4. 1 Larvicidal activity of Ag NPs against Culex third instars larvae

Mosquito larva	Concentration of Ag NPs (ml)	24 hrs mortality (%) ± SD	LC_{50} (ml) (LCL-UCL)	LC_{90} (ml) (LCL-UCL)
Culex	Control (Water)	0.0±0.0	0.55445 (0.335 – 0.775)	2.8305 (2.61 – 3.05)
	DNA (1 mg)	0.0±0.0		
	0.5	48±1.79		
	1	72±1.06		
	2.5	88±0.97		
	5	100±0.0		

Figure.4.16 represents different colour models of dead larva treated in 5 ml, in which the mortality is 100% in 24 hours. The light microscopic image of

this larva shows yellowish shade as seen in Figure.4.16 (a). It indicates that the Ag NPs were covered all over the body of larva. The microscopic image of the treated larva in RGB colour space was converted into HSV colour, which is shown in Figure 4.16 (b). The fluorescent green colour indicates the dark shades of Figure.4.16 (a). It could not clearly differentiate between fluorescent green and yellow colour from the HSV colour image, masking is done for Figure.4.16 (b) for all the colours other than the colour of Ag NPs and it is shown in Figure.4.16 (c). Since head, thorax and tail already have dark shade, it is difficult to differentiate Ag NPs colour from the microscopic image. To emphasize the colour of the Ag NPs on the larva's head, thorax, and tail in Figure 4.16 (d), all other sections were masked.

From all these analyses it is clearly observed that the Ag NPs were deposited on the surface of the body, the skin, of each larva. The size of pores in the skin may be comparable to the size of the Ag NPs. The pores on the skin of larva may be blocked. It leads to the death of the larva very fast. The number of Ag NPs increases it takes less time to block the pores so that the mortality rate is directly proportional to the number of Ag NPs and time.

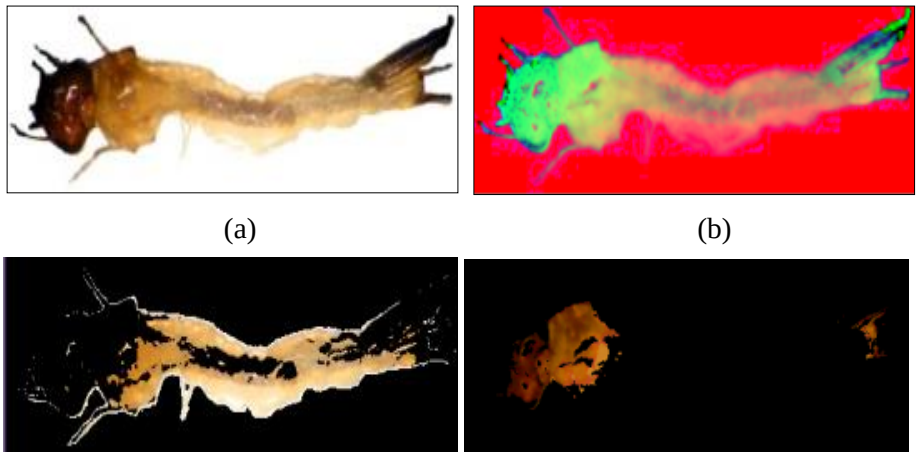

Figure.4.16 Colour analysis of treated larva

Figure.4.17. shows the colour analysis of the larva immersed in distilled water. All the colour analysis done for the treated larva was again done for this non treated larva. In Figure.4.17 (b), 4.17 (c) and 4.17(d) it could not observe any colour other than the original.

The colour analysis reveals that Ag NPs is deposited all over the body. Even if the mosquito swallows the particles, the main reason for death is the deposition of Ag NPs on the surface of the body. From RGB colour analysis, it is found that the nanoparticles were deposited wholly on the skin of the mosquito.

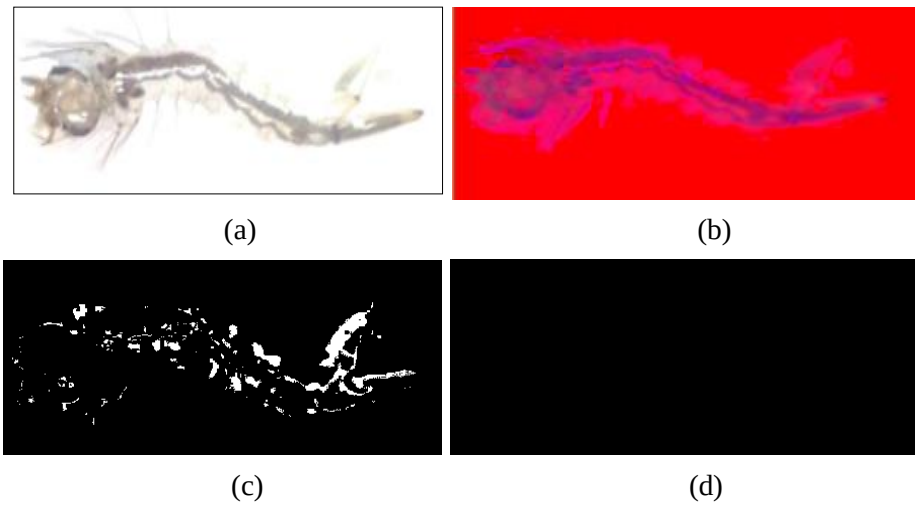

Figure.4.17 Colour analysis of non-treated larva

The sample, treated larva is prepared for SEM analysis as per protocol. Initially treated larvae were fixed with formaldehyde followed by dehydration using acetone after that the sample were dried in air. Figure.4.18 is the SEM image of treated larva, it could be clearly seen the Ag NPs are deposited all over the skin as primarily confirmed in colour analysis.

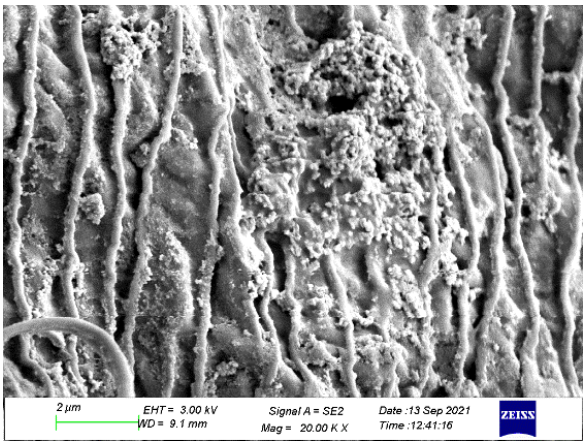

Figure.4.18 SEM image of the fixed treated larva

4.5.2 Antibacterial activity

The antimicrobial activity of the Ag NPs was investigated by disc diffusion method using *Pseudomonas aeruginosa, Staphylococcus aureus*, (Gram-positive) and *Streptococcus mutans* (Gram-negative). It exhibits inhibition to both gram positive and gram-negative pathogenic bacteria. The diameter of inhibition zone was measured for1mg/ml concentration. Table.4.2. shows the inhibition zone diameter for the samples at 1 mg/ml concentration. Ag NPs show better activity towards gram-negative bacteria, *Pseudomonas aeruginosa*.

Table.4. 2 Antibacterial activity of Ag NPs

Species	Zone diameter (mm) Concentration (1mg/ml)	
	Ag NPs	Standard (Streptomycin) (100µg/ml)
Pseudomonas aeruginosa	28	29
Staphylococcus aureus	25	27
Streptococcus mutans	24	25

4.5.3 Cytotoxicity analysis: MTT Assay

Cytotoxic effect of Ag NPs against HeLa cell lines was examined within 24 hours. Figure.4.19. shows the MTT assay results with concentration versus cell survival rate. Ag NPs shows considerable toxicity towards HeLa cells. Figure.4.20 (a) implies that inhibition of HeLa cells is steadily enhanced with Ag NPs concentration i.e., it showed a dose-dependent toxicity. At a concentration 20 µl/ml, it shows 96% cell viability. Cytotoxicity has pronounced from 25 µl/ml and at a concentration of 100 µl/ml, it shows 34% viability. The calculated LC_{50} value is equal to 47 µl/ml.

As Ag NPs possess photoluminescence in the visible range of wavelength, the biocompatible Ag NPs can effectively be used as potential candidate for in-vitro cellular imaging.

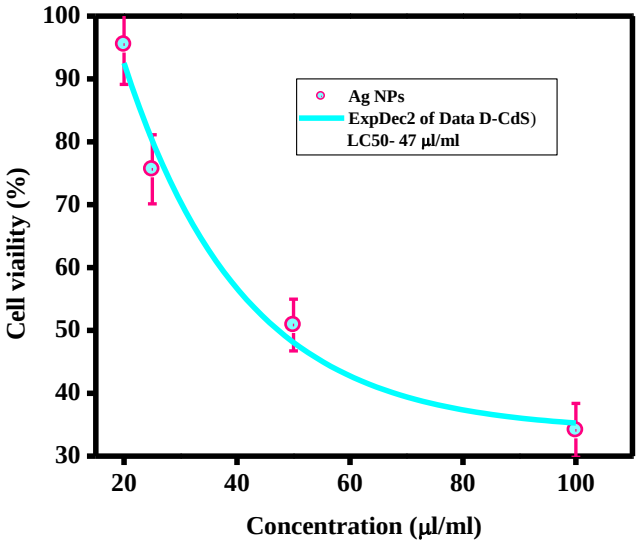

Figure.4. 19 Cell viability and exponential fit of Ag NPs

4.5.4 Bioimaging

HeLa cells were treated with Ag NPs for different concentrations for a period of 24 hours. After 24 hours of treatment, cells were viewed under a fluorescence microscope. The cell membrane, a double-layered lipid, detaches the cytoplasm from the surroundings. Figure.4.20 (a), (b), (c) and (d) shows the bright field images of the HeLa cells treated varying concentration of Ag NPs (0µl/ml, 25µl/ml, 50 µl/ml, 100µl/ml). Figure.4.20 (a) represents the HeLa cell images without any treatment after 24 hours.

The cells are clearly seen from the bright-field images. Cells with round shape represent cell death. Deaths were not observed up to a concentration of 20 µl/ml. Ag NPs are not toxic to cells up to 20 µl/ml. From 25 µl/ml onwards cell death was observed and the rate of cell death increased. It proves that Ag NPs are promising candidates for bioimaging. It is obvious from the Figure.4.20 (b), (c) and (d) that Ag NPs shows a dose-dependent toxicity as seen from MTT assay. Higher number of cell death happened for a higher concentration.

The cellular imaging capability of the biocompatible Ag NPs is definitively proven by the bright red fluorescence showcased in Figure.4.21.

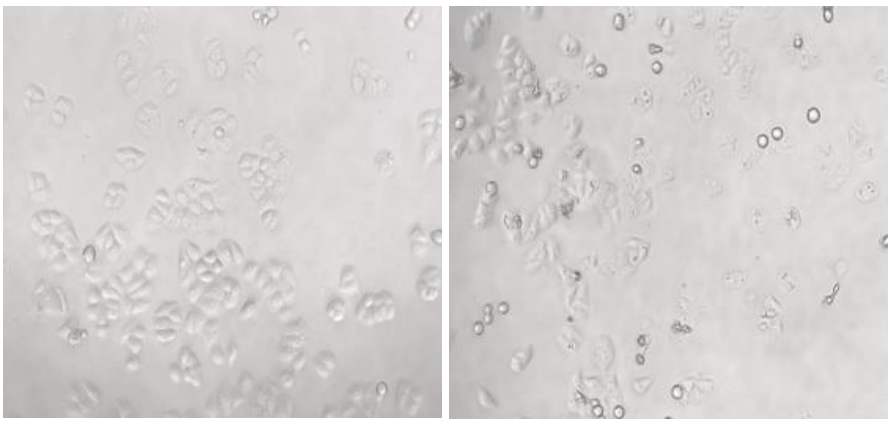

(a) (b)

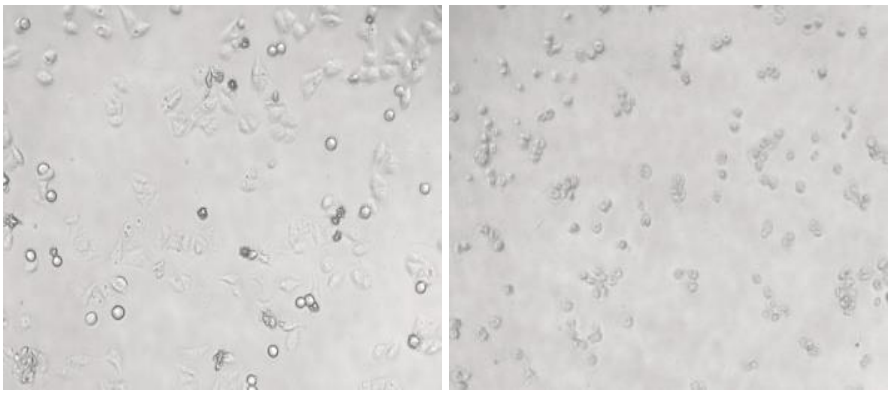

(c) (d)

Figure.4.20 Bright field images of HeLa cells (a) without Ag NPs (b) 25 µl/ml, (c) 50 µl/ml, (d) 100 µl/ml

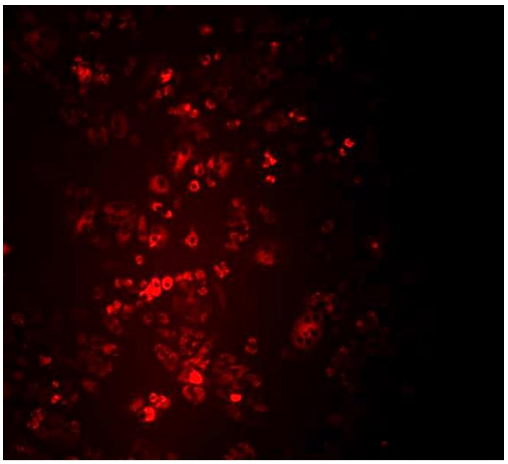

Figure.4.21 Fluorescent image of the cells in the presence of Ag NPs showing red fluorescence

4.6 Conclusions

This chapter delivers a comprehensive summary of diverse applications associated with DNA-capped colloidal Ag NPs. Notably, these nanoparticles exhibit larvicidal and antibacterial activities. Their larvicidal properties are highlighted by the significant mortality observed in bioassays, particularly evident at a concentration of 5 ml. In addition to their bioactivity, DNA-capped Ag NPs demonstrate versatility in enhancing fluorescence and tuning

the emission wavelength in Rh6G doped sol-gel derived glasses. The investigation into their photocatalytic activity reveals a noticeable capacity, although it is established that they may not serve as optimal photocatalysts. Moreover, the cytotoxicity assessment places DNA-capped Ag NPs as suitable candidates for fluorescence imaging applications, showcasing dose-dependent cell death toward HeLa cells. The multifaceted properties exhibited by DNA-capped Ag NPs highlight their potential in diverse fields, positioning them as promising materials for larvicidal, antibacterial, fluorescence enhancement, and bioimaging applications.

References

[1] V Chandrakala et al., Emergent mater., 5(6) (2022) 1593.

[2] J Chumpol and S Siri, J. Nanosci. Nanotechnol., 20(3) (2020) 1678.

[3] S Xie et al., Anal. Chem., 91(24) (2019) 15404.

[4] V B Zon, G A Burley and U Rant, Nanotechnology, 23(11) (2012) 115607.

[5] B Nithyaja, H Misha and V P N Nampoori, Nanosci. Nanotechnol., *2*(4) (2012) 99.

[6] Q Sun et al., Biomater. Res., 26(1) (2022) 1.

[7] L Danai et al., Nanomedicine, 18(9) (2023) 769.

[8] B Nithyaja, et al., J. Nonlinear Opt. Phys. Mater., 20(01) (2011) 75.

[9] E E Tanner et al., Phys. Chem. Chem. Phys., 19(15) (2017) 9733.

[10] G Wei et al., Appl. Surf. Sci., 252(5) (2005) 1189.

[11] Hu et al., Protein J., 29(4) (2010) 234.

[12] J Homola et al., Sens. Actuators B Chem., 54(1-2) (1999) 3.

[13] R F Oulton et al., Nature, 461(7264) (2009) 629.

[14] G Liu et al., J. Nanosci. Nanotechnol., 11(11) (2011) 9523.

[15] R F Kubin and A N Fletcher, J. Lumin., 27(4) (1982) 455.

[16] D S Chuu and C M Dai, Phy. Rev., B45(20) (1992)11805

[17] A M Asiri et al., J. Saudi Chem. Soc., 15(2) (2011) 121.

[18] S H Jeong et al., Part. Part. Syst. Charact., 32(2) (2015) 164.

[19] A Hajra, S Dutta and N K Mondal, J Parasit Dis., 40(4) (2016) 1519.

[20] S S Cheng et al., J. Agric. Food Chem., 52(14) (2004) 4395.

[21] G Rajagopal et al., Heliyon 7(6) (2021) 07360.

[22] V N Reena et al., IOP Conference Series: Materials Science and Engineering, 1221(1) (2022) 012051.

[23] N Sutthanont et al., Insects, 10(1) (2019) 27.

[24] B Morejon et al., J. Nanotech.,2018 (2018)

[25] D Kalaimurugan et al., J. Clust. Sci., 30 (2019) 225.

[26] L D Amarasinghe et al., Heliyon, 6(6) (2020) 04322

[27] M Morais et al., J. Med. Chem., 63(23) (2020) 14308.

[28] S Devanesan et al., Int. J. Nanomed., 16 (2021) 3343.

[29] P Manivasagan et al., BioMed. Res. Int., 2013(2013).

[30] R Verkhovskii et al., Heliyon, *5*(3) (2019).

[31] N Yan, Hong Kong University of Science and Technology, (2020).

[32] P Tan et al., Biotech. App. Biochem., 68(6) (2021) 1236.

[33] V Kravets et al., Nanosc. Res. Lett., 11 (2016) 1.

[34] B Xu et al., Chemosphere, 243 (2020) 125366.

[35] WHO 2006 Guidelines for testing mosquito adulticides intended for Indoor Residual Spraying (IRS) and Insecticide Treated Nets (ITNs)

[36] Menesatti P et al., Sensors, 12(6) (2012) 7063.

[37] Guthmuller J et al., J. Phys. Chem., 112(14) (2008) 3215.

[38] A Penzkofer and W Leupacher et al., J. Lumin., 37(2) (1987) 61.

[39] C András et al., J. App. Phy., 131(7) (2022) 071102.

[40] A V Deshpande and U Kumar, J. Lumin.,128 (2008) 1121.

[41] X L Liu and Y J Zhu., Mater. Lett., 63 (2009) 1085.

[42] Y Ghasemi et al., Acta Biomed., 80 (2009) 156.

[43] V N Reena et al., AIP Adv., 12(10) (2022).

[44] D Latha et al., Mater. Sci. Eng., 9 (1) (2017).

[45] V Balamurugan et al., Mater. Today: Proc., 62 (2022) 5365.

Chapter 5

Synthesis, Characterization and Applications of Schiff base Ligand and Its Ni (II) Complex

Schiff base ligands are essential in coordination chemistry, where they form coordination complexes with metal ions, leading to various applications in catalysis and materials science. They also have biological relevance, appearing in biomolecules and demonstrating potential in medicinal chemistry for their role in anticancer and antibacterial compounds. Schiff bases are commonly used as templates for the synthesis of NPs. These organic compounds play a crucial role in controlling the nucleation, growth, and stabilization of NPs, enabling precise control over their size, shape, and properties. This templating approach is valuable in various fields, including materials science, catalysis, and nanotechnology. This chapter discusses the synthesis and characterization and some applications of Schiff base ligand and one of its metal complexes. Here, a novel tetradentate Schiff base ligand, *3-((2-(-(1-(2-hydroxyphenyl) ethylidene) amino) ethyl) imino)-2-pentone* and its Ni (II) complex have been synthesized by green chemical, ultrasonication method. The optical bandgap energy, fluorescence spectrum lifetime analyses and chromaticity studies were accomplished to encounter the possibilities of optical applications. The fluorescence nature of both ligand and complex was found to be in the visible range. Optical bandgap energy values fall in the range of semiconductor materials. The chromaticity studies give the CIE 1931 coordinates and colour correlation temperature values of the samples. The ligand and the Ni (II) complex were screened for biological activities such as antimicrobial, antioxidant, and larvicidal activities.

Results of this chapter are published as:

Reena V N, Kumar K S, Bhagyasree G S, Nithyaja, B (2022). One-pot synthesis, characterization, optical studies and biological activities of a novel ultrasonically synthesized Schiff base ligand and its Ni (II) complex. *Results in Chemistry*, *4*, 100576. (Publisher: Elsevier)

5.1 Introduction

Schiff bases have been used extensively in coordination chemistry because of their coordination behaviour, and they can easily be synthesized and coordinated with metals. They have been studied widely due to their effortless preparation and capability to fetch structural, electronic and behaviour modifications. They could coordinate metal ions in a monodentate as well as polydentate manner to produce various advantageous metal complexes. Both Schiff and its coordination compounds have a broad range of multidisciplinary applications like catalysts, pharmaceutics, the food industry, and the dye industry. Schiff bases have been found to possess a wide range of biological activities, including antifungal, antibacterial, larvicidal, antimalarial, antiproliferative, anti-inflammatory, antiviral, and antipyretic activities. [1-4]. In spite of the ease of preparation and cost-effectiveness of Schiff base ligands, biological investigations remain relevant. These days, mixed ligands and their complexes are garnering increased attention due to their useful properties. The mixed ligand contains at least two different functional groups that can bind to the metal atom. As their donor atoms provide unique reactivity to metal complexes, these ligands have become increasingly popular today [5].

Recently, mixed Schiff bases and their metal complexes have been applied as optical, chemical and biological sensors. The chemical and optical sensing method utilized the fluorescence behaviour of these materials. This fluorescence sensing technique has fascinated great attention for the detection of significant metal ions and anions in a living cell due to their quick response, high sensitivity, and immediate visual analysis [6-15]. Further, Schiff bases and their metal complexes serve as fluorescent probes for bioimaging that can differentiate cancerous cells from normal cells using fluorescent imaging in cellular biology [16, 17].

The structural resemblances of Schiff base molecules to biological molecules contribute to their biological relevance and activity. Schiff bases typically consist of a carbon-nitrogen double bond (C=N) formed by the condensation of a primary amine with a carbonyl group from an aldehyde or a ketone [1]. This structure imparts several characteristics that enhance their interaction with biological molecules. The (C=N) functional group in Schiff bases is similar to the peptide bond in proteins, providing a structural resemblance to key components of biological macromolecules. The electron-rich nature of the (C=N) bond enables Schiff bases to participate in various interactions, such as coordination with metal ions and hydrogen bonding with biological molecules. The flexible nature of Schiff bases permits them to adopt different conformations, facilitating their binding to diverse biological targets. This flexibility is crucial for their ability to interact with specific binding sites on proteins or enzymes. The polar nature of the (C=N) bond and other functional groups present in Schiff bases allows for hydrogen bonding interactions with biological molecules, influencing their pharmacological and biochemical activities. Schiff bases can coordinate with metal ions, resembling the coordination sites found in metalloenzymes and other metal-containing biological structures. These structural features enable Schiff bases to mimic and interact with components of biological systems, making them versatile molecules in the design of biologically active compounds. Researchers exploit these structural similarities to tailor Schiff bases for the synthesis of NPs and specific biological applications, ranging from enzyme mimics to drug candidates with diverse pharmacological properties.

Schiff base complexes, formed by coordinating Schiff base ligands with metal ions, perform a potential role across scientific and technological domains. Their versatility is evident in catalysis, where they act as efficient catalysts by influencing the reactivity of metal centers. In medicinal chemistry, these complexes exhibit numerous biological activities, such as

antimicrobial, anticancer, and anti-inflammatory properties. The metal-binding capabilities of Schiff base complexes are appreciated for metalloenzyme mimicking and as contrast agents in medical imaging. In materials science, they contribute to emerging functional materials like luminescent compounds and metal-organic frameworks. The flexibility of Schiff base complexes makes them essential in designing materials and molecules for applications spanning catalysis, medicine, and materials science [18].

The synthesis of luminescent metallic complexes drew a lot of attention in recent years; because of their significance in photonics, particularly in optoelectronics, and in the design of sensors, bioimaging applications, and optical materials. Their significant electrical conductivity is a crucial feature in finding applications in optoelectronics [19, 20]. Several recent papers reported studies on organic light-emitting diodes (OLEDs) using Schiff base transition metal complexes [21]. Low cost, intense luminescence efficiency and the ability to customize emission colours make this technology suitable for various digital displays [22-27]. As a quick overview, mixed ligands and their metal complexes can be exploited as a source for new materials with photoluminescence properties, nonlinear optical characteristics, electrical conductivity, magnetic exchange properties, and biological activities [28-32].

Nickel (II) complex is an important transition metal complexes because, they exhibit antibacterial, antifungal, antiproliferative, and anticancer properties [33-36]. As a trace element, nickel plays a vital role in hydrogenases and carbon monoxide dehydrogenases [37-40]. Researchers have recently found that Ni (II) complexes are suitable for optoelectronic applications like OLEDs [41, 42]. In this chapter, we discuss the synthesis a mixed Schiff base, *3-((2-(-(1-(2-hydroxyphenyl) ethylidene) amino) ethyl) imino)-2-pentone* and its Ni (II) complex of by green chemical ultrasonic reflux method.

Characterizations of Schiff base ligand and Ni (II) complex were achieved by various physicochemical, analytical, and spectral methods. Microscopic techniques like SEM and TEM are used to examine surface morphology. The antibacterial, antioxidant, and larvicidal activities of the Schiff base ligand and its Ni (II) complex were studied. Optical bandgap studies and photoluminescence studies were conducted for both the ligand and the complex. Chromaticity studies of both ligand and complex were executed, which provide information on CIE coordinates and CCT.

5.2 Materials and Methods

Chemical reagents, o-hydroxyacetophenone, acetylacetone, 1, 2-ethylenediamine, and solvents, DMSO, DMF, methanol, and ethanol were procured from Sigma-Aldrich and were used as such without further purification. The metal salt, $NiCl_2.2H_2O$ was purchased from Merck and were used without further purification.

Reactions were assessed and monitored by thin layer chromatography by TLC technique on pre-coated silica gel F_{254} plates purchased from Merck and the final product was visualized by exposure to the UV light and kept in an iodine chamber. The melting point of the ligand and the Ni (II) complex was determined using the Fischer-Johns apparatus and remained uncorrected. Elemental analyses for C, H, and N were estimated by making use of the Vario-EL III CHNS analyzer. The instrument used for HRMS is XEVO G2-XS QTOF, which gives the correct *m/z* value. The conductivity of 10^{-3} M solutions of the complex was measured in DMF at 25^0C using a Conductivity Hand-Held Meter LF 330. Magnetic moments were measured on a Sherwood Scientific magnetic moment balance (Model MK1) at room temperature (25^0C) using Hg [Co $(SCN)_4$] as a calibrant, and diamagnetic corrections were calculated from Pascal's constants. The UV-visible spectra of the ligand and the metal complex in the UV-visible region were recorded in DMF

solution. The IR spectra were obtained at room temperature using a Perkin Elmer infrared spectrometer by using a KBr pellet. ^{1}H NMR spectrum recorded using Brucker AV 500 FT NMR spectrometer in DMSO- d6 as the solvent. Powder XRD is a potent technique to explain the structural information of materials of organic and inorganic compounds if single crystal XRD data is not obtained. Powder XRD patterns of the ligand and Ni (II) complex were recorded at room temperature.

5.2.1 Synthesis of the Schiff base ligand

Equimolar amount of acetylacetone (0.025 mol) and o-hydroxyacetophenone (0.025 mol) in a minimum amount of ethanol were mixed thoroughly and added to the ethanolic solution of 1,2-ethylenediamine (0.025 mol) in a 250 ml round bottom refluxing flask and shaken well. The mixture was allowed to reflux for 30 minutes at 70^{0} C on an ultrasonicator with constant stirring (Figure 5.1). The mixture was taken from the ultrasonic apparatus after completion of the reaction and switched off the ultrasonic irradiation. Completion of the reaction was confirmed and monitored by thin-layer chromatographic (TLC) by spotting the reaction mixture on a pre-coated silica gel F_{254} plate purchased from E. Merck. The light yellow coloured crystalline product (Figure 5.1) was filtered slowly by Whatman filter paper, washed several times with ethanol, and dried over anhydrous $CaCl_2$. IUPAC name of the ligand, *3-((2-(-(1-(2-hydroxyphenyl)ethylidene) amino) ethyl)imino)-2-pentone*, is complicated, therefore for the sake of simplicity, it is given a name, **L**.

Yield: 2.01 gram, 55.9 %; **M.p**- 122 ^{0}C. **Colour**: Glittering yellow; ***Anal***. for $C_{15}H_{20}N_2O_2$: ***Calcd*** (%) C, 69.25; H, 7.70; N, 10.79. $C_{15}H_{20}N_2O_2$; ***found.*** (%) C, 69.20; H, 7.74; N, 10.76; **UV/vis**; λ_{max} (ε): 315 nm, 396 nm; **FT-IR** (KBr, ν_{max}/cm^{-1}): 1493 (Ar-C=C), 3445 (-OH), 1231(=N-C-), 1639 (>C=O), 1250 (N-N), 1625 (-N=C), 1644 (N-CH), 3065 (=C-H), 2921 (C-H asym.);**^{1}H**

NMR spectrum (500 MHz, DMSO-d_6; δ; ppm): 7.45-6.85 (4H, m, Ar-H), 5.05 (1H, s, -OH), 0.91 (3H, s, -CH_3 near)**,** 3.59 (2H, t, -CH_2), 1.69 (2H, t, -CH_2), 0.90 (3H, s, -CH_3), 3.47 (2H, s, -CH_2), 2.08 (3H, s, -CH_3); **^{13}C NMR** (75 MHz, DMSO-d_6), δ (ppm): 132.5, 116.0, 121.5, 130.5, 124.0, 161.1, 164.5, 16.7, 62.6, 62.7, 16.6, 164.5, 48.7, 202.9, 31.0; **HRMS (FAB$^+$)** *m/z* = 260.30, ***Cacld*** for $C_{15}H_{20}N_2O_2$= 260.33.

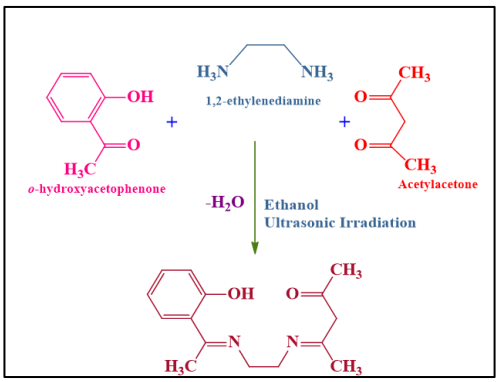

Figure.5.1 Synthesis of the Schiff base ligand, **L**.

5.2.2 Synthesis of Ni (II) complex

The ligand, 0.005 mol, was dissolved in 25 ml of DMSO taken in a round bottom 250 ml refluxing flask. Added 0.005 mol of $NiCl_2.2H_2O$ dissolved in 25 ml ethanol to the above round bottom flask with continuous shaking. The mixture was allowed to reflux for two hours at 70^0C on an ultrasonic apparatus with constant stirring (Figure.5.2). After completion of the reaction, the mixture was taken from ultrasonic apparatus and completion of the reaction was confirmed and monitored by thin-layer chromatographic (TLC) by spotting the reaction mixture on a pre-coated silica gel F_{254} plate purchased from Merck. The product was filtered slowly by Whatman filter paper, washed several times with ethanol and dried over anhydrous $CaCl_2$. Brownish-orange coloured precipitate was obtained.

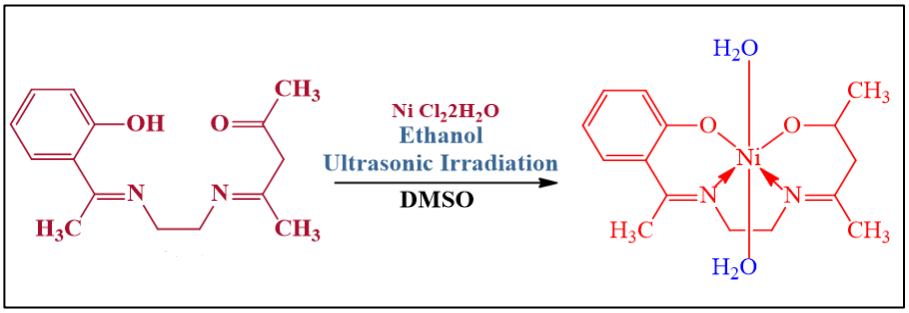

Figure.5.2 Synthesis of Schiff base Ni (II) complex

Yield: 55 %; **Colour:** Brownish-orange; **M.p:** 283-291^{0}C; **Anal.** for $NiC_{15}H_{22}N_2O_4$: ***Calcd***. (%) C, 51.03; H, 6.28; N, 7.93, Ni, 16.63; ***found***(%) C, 51.11; H, 6.22; N, 7.88, Ni, 16.60; $\mathbf{\Omega_m}$: 9 $\Omega^{-1}mol^{-1}cm^2$; μ_{eff}: 3.39 B.M; **FT-IR** (KBr, ν_{max}/cm^{-1}): 3550-3505 (-OH), 1493 (Ar-C=C), 1231(=N-C-), 1205 (>C-O), 1250 (N-N), 1618 (-N=C), 3065 (=C-H), 2921 (C-H asym.), 510 (M-N), 415 (M-O); **UV-Vis** (λ_{max}): 406 nm, 441 nm, and 550 nm; **HRMS** (FAB^+) ***m/z*** = 353.11, ***Calcd*** for $NiC_{15}H_{22}N_2O_4$= 353.04.

5.2.3 Antibacterial Screening

The antimicrobial test was conducted with four microbes: two G-positives (*Streptococcus aureus* and *Streptococcus mutans*) and two G-negatives (*Pseudomonas aeruginosa* and *Escherichia coli*). The procedure for doing antibacterial screening was done as procedure explained in chapter 2. Wells of approximately 10 mm was bored using a good cutter and a concentration of 100 µg/ml of samples was added. The plates were then incubated at 37^{0}C for 24 hours. The antibacterial activity was assayed by measuring the diameter of the inhibition zone formed around the well [43]. In this study, streptomycin was employed as a standard antimicrobial agent.

5.2.4 Antioxidant Activity

The antioxidant capability of both **L** and the Ni (II) complex was tested and compared to standard scavengers such as H_2O_2, superoxide, and nitric oxide. The method developed by Ruch et al. in 1989 was adopted here [44]. The percentage of inhibition can be found by the equation,

$$\% \text{ inhibition} = \frac{control-test}{control} X100$$

5.2.5 H_2O_2 Assay

A solution of H_2O_2 (40 mM) was prepared in phosphate buffer (pH 7.4). Different concentrations of the sample (125 – 2000 µg/ml) from a stock concentration of 10 mg/ml were added to the H_2O_2 solution (0.6 ml). An equivalent amount of distilled water was taken as control which is not containing the test compound. Absorbance of UV-visible spectrometer was read at 230 nm at 0 minutes and after 10 minutes of incubation.

5.2.6 Nitric Oxide Assay

Sodium nitroprusside (5 mmol L^{-1}) in phosphate-buffered saline pH 7.4, was mixed with different concentrations of the sample (125 µg/mL-2000 µg/mL) and incubated at 25°C for 30 minutes. An equivalent amount of distilled water without test compound was taken as control. After 30 minutes, 1.5 ml of the incubated solution was removed and diluted with 1.5 mL of Griess reagent (1% sulphanilamide, 2% phosphoric acid, and 0.1% N-1-naphthyl ethylene diamine dihydrochloride). The absorbance of the chromophore formed during diazotization of the nitrate with sulphanilamide and subsequent coupling with N-1 naphthyl ethylene diamine dihydrochloride was measured at 546 nm and the percentage scavenging activity was measured regarding the standard.

5.2.7 Super oxide Assay

Samples of 125 - 2000 µg/ml from a stock solution of 10 mg/ml, 0.05 ml of Riboflavin (0.12 mM), 0.2 ml of EDTA solution (0.1 M) and 0.1 ml of NBT solution (1.5 mM) were added to the test tube, and this reaction mixture was diluted with phosphate buffer (0.067 M) to reach 2.64 ml. An equivalent amount of distilled water was taken as control which is not containing the test compound. The absorbance of the solution was measured at 560 nm after illumination for 5 minutes incubation in fluorescent light and also measured after illumination for 30 minutes at 560 nm on UV visible spectrophotometer.

5.2.8 Larvicidal Activity

Mosquito larvicidal activity of both **L** and Ni (II) complex was investigated. The procedure for doing larvicidal activity is described in chapter 2. The larvicidal studies were initiated using standard rules described by WHO [45]. Different concentrations of **L** and Ni (II) complex (1-10 µg/ml) were dissolved separately in DMSO and transferred separately to beakers containing 200 ml of distilled water. For performing the larvicidal activities, 25 larvae were introduced to a beaker containing samples. One beaker containing 200 ml water and another containing 200 ml DMSO were taken as controls. For each concentration under observation, five trials were constituted. The larval mortality rates were analyzed and found the mosquito larvae's acute toxicity levels after 24 hours. Dead larvae were identified by snooping in the siphon or cervical region with a fine needle and removed the unmoved larvae from the beaker. The mortality rates of larvae calculated for five replicates. The mortality rate was calculated using the Abbott formula [46].

5.2.9 Chromaticity Studies

Commission International deI'Eclairage (CIE) 1931 chromatic colour coordinates represents the visual system of the human using the primary

colours. The detailed procedure for finding CIE coordinates and CCT are explained in chapter 2. To facilitate the quality of light, CCT values have been calculated by using McCamy empirical formula [47]. The chromaticity studies of **L** and Ni (II) complex were studied under UV irradiation.

5.3 Results and Discussions

5.3.1 Characterization of the Schiff base ligand, L

The Schiff base ligand *3-((2-(-(1-(2-hydroxyphenyl)ethylidene)amino)ethyl) imino)-2-pentone* derived from o-hydroxyacetophenone, acetylacetone and 1,2-ethylenediamine was a glittering yellow crystalline powder, soluble in polar aprotic solvents like DMSO and DMF. The homogeneity and purity of the ligand were tested by the TLC technique. The melting point of the ligand was determined using a Fisher Johns apparatus.

(a) UV-visible absorption spectrum

The UV-visible spectrum of **L** in DMSO was recorded at room temperature. The presence of a λ_{max}, peak at 234 nm was attributed to the $\pi \rightarrow \pi^*$ transition might be due to an aromatic ring or double bond present in the ligand. A peak at 315 nm was due to the $n \rightarrow \pi^*$ transition of the non-bonding electrons presents in the oxygen of the keto (>C=O) and nitrogen of the azomethine (>C=N) groups present in the ligand.

(b) ^{1}H NMR spectrum

The ^{1}H NMR spectrum of the ligand, **L** in DMSO-d6 was recorded. The spectrum showed several peaks that were characteristic of the compound. A sharp singlet observed at 5.05 ppm may be assigned to the -OH proton of o-hydroxyacetophenone moiety. The multiplet observed in the range 7.45 - 6.85 ppm may be attributed to the different aromatic protons of the ligand. There

was a singlet at 3.47 ppm, which may be attributed to the active methylene protons of acetylacetone moiety. Two triplets observed at 3.59 and 1.69 ppm may be attributed to the $-CH_2$ protons of ethylenediamine near o-hydroxyacetophonene and acetylacetone moiety respectively. A singlet signal at 0.91 ppm is due to the $-CH_3$ protons of the o-hydroxyacetophenone moiety. A singlet at 0.90 ppm and another one at 2.08 ppm may be assigned to $-CH_3$ protons of acetylacetone moiety near azomethine N and keto oxygen group respectively.

(c) IR Spectrum

An irreplaceable analytical tool to find out organic and inorganic structures or different bonds interpretation and confirmation involve the class of electromagnetic radiation with frequencies between 4000 - 400 cm^{-1}. The category of this radiation is named infrared radiation, and its analytical application in inorganic and organic chemistry is known as IR spectroscopy. Because interatomic bonds in organic compounds absorb radiation in this region, it can be utilized to determine the structure. Different chemical bonds will absorb varying intensities at varying frequencies. Thus, infrared spectroscopy involves collecting absorption information and analyzing it in the form of an absorption spectrum. The frequencies at which there are absorptions of infrared radiation can be correlated directly to bonds within the compound in question.

IR spectrum of the ligand, **L** demonstrated a medium intensity band at 1639 cm^{-1} is the characteristic band of $\nu_{-C=O}$. The bands present at 1625 and 1231 cm^{-1} were assigned to $\nu_{-C=N}$ and $\nu_{=N-C-}$ respectively. A band at 3065 cm^{-1} may be assigned to the aromatic ν_{-CH2} and another one at 2905 cm^{-1} to the ν_{-CH} of the methylene group. Broadband at 3445 cm^{-1} may be assigned to the phenolic ν_{-OH} of the o-hydroxyacetophenone moiety. The band at 2995 cm^{-1} may be attributed to the $-CH_3$ group present in the ligand.

(d) XRD

The powder XRD study is a key technique to spot the lattice parameters and crystallinity of materials. Figure.5.3 showed the powder XRD pattern of L. Diffraction patterns were recorded in a range of 10-50^0. The sharp peaks in the pattern indicate the crystalline nature of L. A prominent peak observed at 17.2^0 (2θ) with an interplanar spacing of 5.16Å. The average crystalline size can be found out and calculated by using a simple equation, Scherrer's formula [48],

$$D = 0.9\lambda/(\beta \cos\theta)$$

D is the crystallite size, λ is the wavelength of Cu Kα radiation (1.54 Å), β is the corrected half-width of the diffraction peak and θ is the diffraction angle. The crystallite size calculated at 17.2^0 of ligand is found to be below 10 μm. The SEM image (Figure.5.4) is consistent with this result.

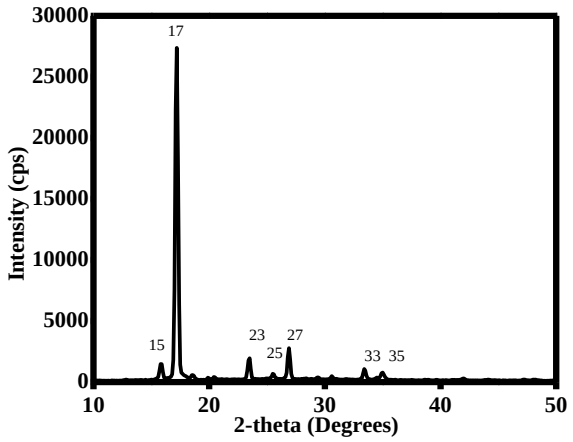

Figure.5. 3 XRD pattern of L

(e) SEM and TEM

The Scanning Electron Microscopic analysis was conducted to observe the surface morphology and the dimension of the ligand, **L**. Figure.5.4 (a) showed that the synthesized Schiff base ligands are of almost rectangular, slices structure with different sizes (an average of few microns). However, particles with a size of few nanometers are also seen from the SEM image, which clustered to form larger-sized agglomerates. Figure.5.4 (b) shows the TEM image of **L**. Both SEM images and TEM images inform exactly the same crystal nature with an average size of 1µm and therefore it is difficult to find the interplanar spacing of **L** from TEM techniques.

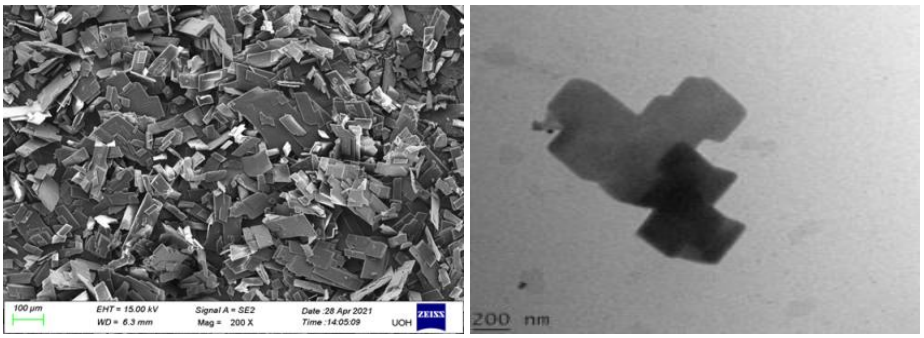

(a) (b)

Figure.5.4 SEM (a) and TEM (b) image of the ligand, **L**

5.3.2 Characterization of Ni (II) complex

The complex, [Ni ($C_{15}H_{18}N_2O_2$) (H_2O)$_2$] was found to be coloured, photo-stable and non-hygroscopic in nature. Solubility was determined and was found to be soluble in polar aprotic solvents like, DMF and DMSO. The information from analytical and molar conductance studies in DMSO exposed that the complex has the formulae as shown given below in Table.5.1.

Table.5. 1 Analytical data of the metal complexes

Compound. Emp. Formula	Mol.Wt. (HRMS (FAB^+) *m/z)*	Molar conductance Ω_m ($\Omega^{-1}mol^{-1}cm^2$)	μ_{eff}^* (B.M)
L (LH_2)	260.30	--	--
[$NiL(H_2O)_2$]	353.11	9	3.20
L= $C_{15}H_{18}N_2O_2$			

(a) Molar conductance

The molar conductance at room temperature was measured using a 10^{-3} M solution of the complexes in DMSO. Ni (II) complex exhibited a lower molar conductivity value, 9 Ω^{-1} $mol^{-1}cm^2$ indicating its very weak-electrolytic nature in DMSO solvent. It was concluded from molar conductance measurement data that it performs as a neutral complex with a non-ionic shape with a mole ratio is 1:1 (M:L). These outcomes are like to the results of the solubility experiment, which showed this complex has neutral and non-ionic form and non-ionic properties. Analytical data and spectral studies also supported the ligand, **L** participated in the complex formation of Ni (II) by neutral coordination, and the suggested molecular formula is [$NiL(H_2O)_2$].

(b) Magnetic susceptibility measurement

Magnetic moments are often used in combination with electronic spectrum to gain the information about oxidation state and stereochemistry of the central metal ion in almost all coordination complexes. The capacity of transition metals to create magnets is a notable property; coordination compound complexes show magnetic properties. Unpaired electrons in coordination metal complexes make them magnetic. Due to the outer electrons being in the *d* orbital, there must be unpaired *d* electrons causing this magnetism. In a molecule, the number of unpaired electrons determines its magnetic properties, which are generated by an electron spin. A common laboratory

practice for determining the magnetic moment for a complex is the Gouy balance method which comprises weighing a sample of the complex in the presence and absence of a magnetic field and detecting its weight difference. The magnetic susceptibility measurements constitute one of the most important experimental routes by which chemists can easily obtain information about magnetic properties, the number of unpaired electrons, and the characteristic geometry of transition metal complexes.

Tetrahedral Ni (II) complexes exhibit high magnetic moment values in the range of 3.62 to 4.01 B.M. which is due to the substantial orbital contribution of the T ground state towards the spin-only value of 2.83 B.M., corresponding to the two unpaired electrons. Large distortions and inequalities in the fields of coordinated ligands are found to result in magnetic moments with small orbital contribution and the magnetic moment values are observed as low as 3.22 B.M. Square-planar Ni (II) complexes have spin-singlet ground state and are diamagnetic. Five coordinated high-spin complexes are known to have magnetic moments in the range of 3.0 to 3.4 B.M. Octahedral Ni (II) complexes ought to register magnetic moments almost equal to the spin-only value, as the ground state 'A' lacks orbital contribution. However, the observed magnetic moment values fall in the range, of 2.60 to 3.30 B.M., due to spin-orbit coupling. In the present investigation, [Ni $(C_{15}H_{18}N_2O_2)(H_2O)_2$] registered a magnetic moment value of 3.20 B.M. indicating its octahedral geometry.

(c) Electronic spectra

The study of electron absorption spectra, especially crystal field spectra of coordination complexes, provides important information on magnitude of energy gaps between the ground and the excited electronic energy states of the metal ions in the complexes, colours of the complexes, the extend of covalent character in metal-ligand bonds, the geometry of the complexes and

the position of metals and the ligands in the spectrochemical and nephelauxetic series.

In the present investigation, electronic spectra of Ni (II) complex exhibited three absorption (λ_{max}) bands in the range of 8,647 cm^{-1}, 13,774 cm^{-1}, and 24,389 cm^{-1}showed in Table.5.2. The ground state Ni (II) in an octahedral coordination is $^3A_{2g}$. Thus, these bands may be assigned to three spin-allowed transition $^3A_{2g} \rightarrow {}^3T_{2g}$ (ν_1), $^3A_{2g} \rightarrow {}^3T_{1g}$ (ν_2) and $^3A_{2g} \rightarrow {}^3T_{1g}(P)$ (ν_3) respectively. The position of bands suggests mostly of octahedral geometry. The ratio of wave numbers of the transitions assigned as $^3A_{2g} \rightarrow {}^3T_{2g}$ (F) and $^3A_{2g} \rightarrow {}^3T_{1g}(F)$ was approximately found to be 1.6 confirming its octahedral geometry.

Table.5. 2 Electronic spectra of complex and its assignment.

Complex	Bands (cm^{-1})	Assignments	Geometry
$[NiL(H_2O)_2]$	8,647	$^3A_{2g} \rightarrow {}^3T_{2g}(\nu_1)$	Octahedral
	13,774	$^3A_{2g} \rightarrow {}^3T_{1g}(\nu_2)$	
	24,389	$^3A_{2g} \rightarrow {}^3T_{1g}(P)$ (ν_3)	

(d) IR Spectra

A band at 3065 cm^{-1} may be assigned to the aromatic $\boldsymbol{\nu_{-CH2}}$ and another one at 2905 cm^{-1} to the $\boldsymbol{\nu_{-CH}}$ of the methylene group. Broadband observed at 3445 cm^{-1} in the spectrum of ligand may be assigned to the phenolic $\boldsymbol{\nu_{-OH}}$ of o-hydroxyacetophenone moiety, but this band is absent in the spectrum of ligand indicating that the coordination of phenolic oxygen after deprotonation. Another broadband present at 3501 cm^{-1} may be assigned to the hydroxyl stretching band of coordinated H_2O as ligands.

Bands at 1639 cm^{-1} present in the spectrum of ligand, **L** assigned to carbonyl stretching, >C=O. But this band is absent in the spectra of complex, Ni (II),

indicated that the >C=O moiety of acetylacetone has undergone enolization from $-CH_2-C=O$ to $-CH=C-OH$ and the deprotonated oxygen atom coordinated to the central metal Ni (II) ion. This was confirmed by the appearance of new bands around 1205 cm^{-1} due to ν_{C-O} in the spectra of the complex. A band of medium intensity at 1625 cm^{-1} in the spectrum of ligand may be assigned to $\nu_{C=N}$. However, in the spectrum of the complex, this band is shifted to a lower frequency by 10 cm^{-1}, indicating the participation of azomethine nitrogens in coordination.

Broad band at 3505 cm^{-1} in the spectrum of the complex were attributed to the hydroxyl stretching modes of water molecules. In addition, strong band at 870 cm^{-1} suggested that the water molecule was coordinated. Medium bands around 510 cm^{-1} and 415 cm^{-1} in the spectra of all the complex may be assigned to ν_{M-N} and ν_{M-O}, respectively. Figure.5.5 represents the structure of the Ni (II) complex.

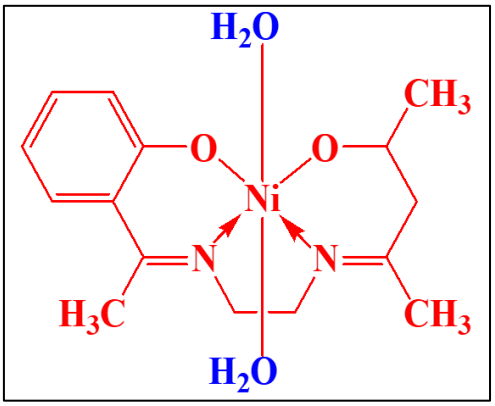

Figure.5. 5 Structure of the Ni (II) complex

(e) XRD

Figure.5.6 shows the powder XRD pattern of the Ni (II) complex. Diffraction patterns were recorded in a range of 10 - 40^0. The sharp peaks in the pattern indicated the crystalline nature of the Ni (II) complex. Powder XRD exhibits a prominent peak at 10.5^0. The average crystalline size of the Ni (II) complex can be found by using Scherrer's formula [46]. The calculated crystallite size at 10.5^0 of the Ni (II) complex is found to be below 5 μm.

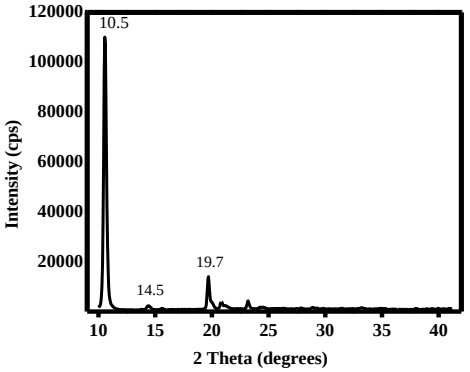

Figure.5. 6 XRD pattern of Ni (II) complex

(f) SEM and TEM

Figure.5.7 shows the SEM image of Ni (II) complex which depicts the shape as a rod-like structure, non-uniform size distribution, with an average diameter, of 50 nm and length wise a few micrometers. The dimension calculated from XRD is consistent with this dimension. This confirms that the rectangular-shaped, micro-sized ligand transformed into a rod-shaped, nano-sized nickel complex. Figure.5.8(a), (b), and (c) are the TEM image of Ni (II)complex, lattice spacing, and electron diffraction pattern of Ni (II) complex respectively. The rod shape of Ni (II) complex is clearly seen from

the TEM image and has a diameter of 50 nm and has a lattice spacing of 0.37 nm.

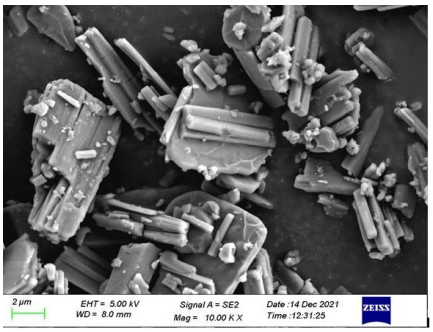

Figure.5.7 SEM image of Ni (II) complex

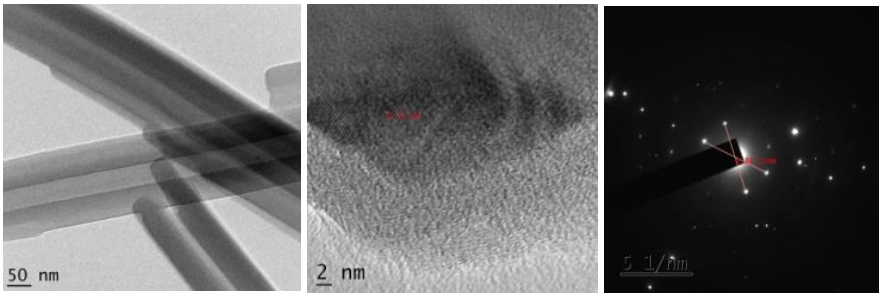

(a) (b) (c)

Figure.5.8 TEM image of (a) Ni (II) complex (b) Lattice spacing and (c) Selected area diffraction (SAED) pattern of Ni (II) complex

5.3.3 Bandgap Energy of L and Ni (II) complex

From the electronic spectrum (UV-visible Absorption spectra), the bandgap energy of both **L** and the Ni (II) complex can be determined accurately. In the process of absorption, an electron will absorb a photon of finite energy and be excited to a higher energy state from a lower energy state. The transmitted radiation can give information about the type of possible electron transitions. The fundamental band-to-band transition shows a sudden rise in

the absorption, the absorption peak, which determines the optical bandgap from the equation,

$$E_g = \frac{hc}{\lambda}$$

The relation between the absorption coefficient (α) and optical bandgap (E_g) is expressed to calculate the band gap of the compound by the following relation [49],

$$\alpha h\nu = A\left(h\nu - E_g\right)^m$$

Where m is equal to 2 for direct transition or $\frac{1}{2}$ for indirect transition. A is an energy independent constant. Plot $(\alpha h\nu)^2$ *Vs*. hν; from which a direct band gap energy was found by extrapolating the linear portion of the curve to $(\alpha h\nu)^2 = 0$. Photophysical and photochemical properties of semiconductors can be predicted by accurate determination of the band gap energy.

From the bandgap energy curve, Figure.5.9, it is clear that the values of the direct bandgap are equal to 2.62 and 2.85 eV for **L** and Ni (II) complex, respectively. The bandgap value proposes that both **L** and Ni (II) complex fall under the category of wide bandgap semiconductors. The bandgap energy of a semiconductor describes the energy needed to excite an electron from the valence band to the conduction band. Since wide bandgap semiconductors have many potential applications in solar cells, optoelectronics, power electronics, and sensors [50], the bandgap energy values of ligand and complex propose that they can be considered appropriate materials for these applications.

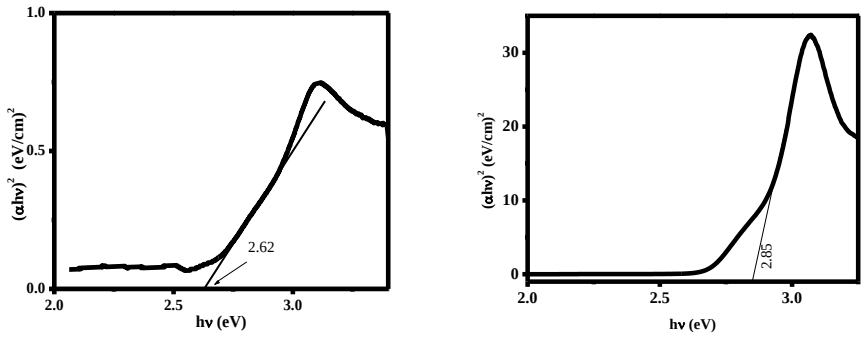

(a) (b)

Figure.5.9 Bandgap energy of (a) L and (b) Ni (II) complex

5.3.4 Photoluminescence of L and Ni (II) complex

The normalized PL spectra of **L** and Ni (II) complex were studied at room temperature with DMSO solvent and which are shown in Figure.5.10 (a) and (b). The excitation wavelength used for PL spectra of **L** and Ni (II) complex is 350 nm. The ligand, **L** shows a strong peak at 500 nm. SEM and TEM images of **L** showed the uniform shape of the ligand, this fact is reflected in the Photoluminescence spectrum where one can observe a perfect-shaped peak with a maximum at 500 nm.

The PL spectra of Ni (II) complex showed one peak at 482 nm with two small shoulder peaks; one is at 437 nm and the other peak is at 528 nm. Multiple peaks in PL spectra for a single excitation wavelength may be due to the non-uniform size and shape of Ni (II) complex as seen from the SEM image which leads to multiple peaks in the photoluminescence spectrum. The peaks confirm that both ligand and Ni (II) complex emit wavelength in the green region as revealed in bandgap energy values. These two materials may be exploited for green-emitting OLEDs.

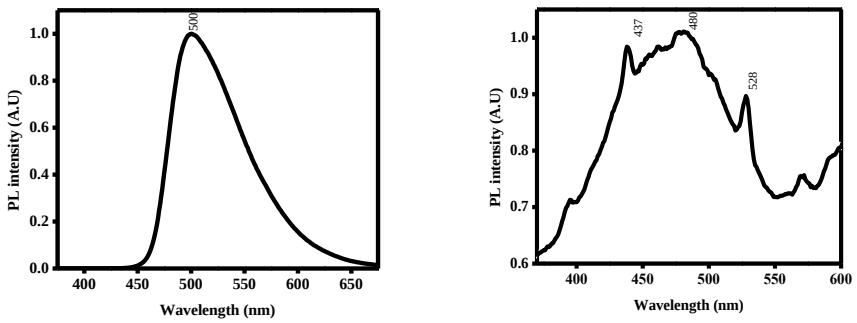

(a) (b)

Figure.5.10 PL Spectra of (a) L and (b) Ni (II) complex

The photograph of **L** in visible light and the presence of UV light irradiation is shown in Figure. 5.11 (a) which visibly shows, **L** absorbs energy in the UV wavelength and there is a change in the emission colour from yellow to light green upon UV irradiation. In Figure.5.11 (b), it is seen that brownish coloured Ni (II) complex turned to light green colour with UV light absorption.

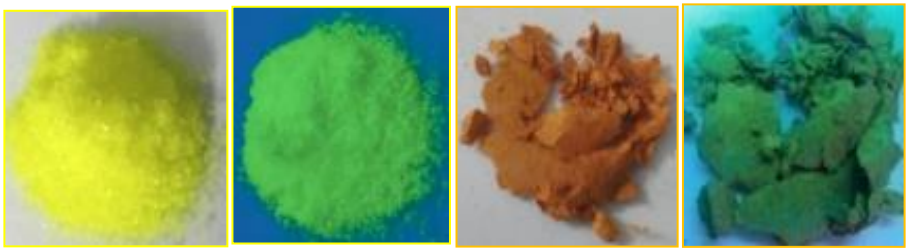

(a) (b)

Figure.5.11 Photograph of (a) L in Visible (left) and in UV light (right) (b) Ni (II) complex in Visible (left) and in UV light (right)

5.3.5 Chromaticity Studies of L and Ni (II) complex

The CIE 1931 chromaticity diagram is shown in Figure.5.12. From this figure, it is seen that, the colour of **L** is located in green region with CIE coordinates (x=0.2849, y=0.5462). The colour of Ni (II) complex is also located in green region with coordinates (x=0.2997, y=0.4582). The corresponding CCT values are 6462 K and 6363 K respectively for **L** and Ni (II) complex. It is noted that, CCT value greater than 5000 K indicates that the light source is a cold light source, which is usually used in commercial lighting. From CIE coordinates and CCT values it is confirmed that both **L** and Ni (II) complex can be used for green emitting LEDs.

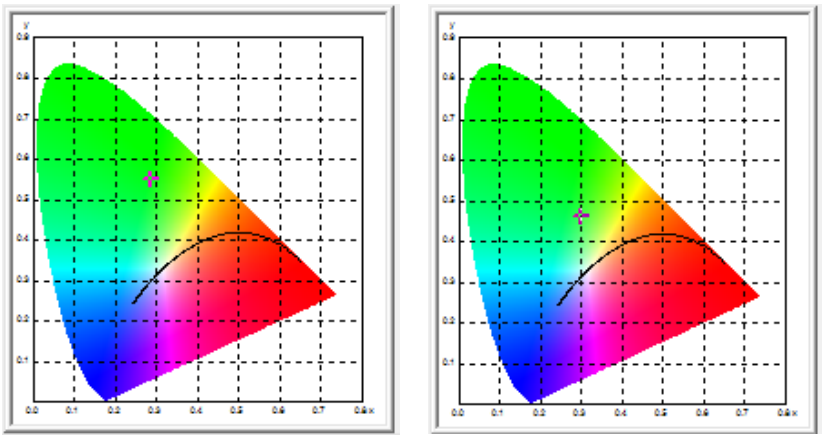

(a) (b)

Figure.5.12 CIE 1930 diagram of (a) L and (b) Ni (II) complex

5.3.6 Fluorescence lifetime decay studies of L and Ni (II) complex

Fluorescence lifetime is related to the time the fluorophore remains average in the excited state before emission takes place. This study provides a deep insight into the photophysical nature and excited state interactions of a fluorophore [51, 52]. Analysis of lifetime measurements can reveal the

dynamic nature of the molecule in the nanosecond timescale. In general fluorescence lifetime is very sensitive to a great variety of internal factors of the fluorophore structure and external factors that include the presence of fluorescence quenchers, temperature, and polarity. Time-resolved fluorescence decay for **L** and Ni (II) complex were measured upon excitation LED of 330 nm and detected at a wavelength of 500 nm which is shown in Figure.5.13. The lifetime of **L** was found to be at 17 ns and upon the formation of the Nickel complex, the fluorescence lifetime is reduced to 13.5 ns which give a clear idea that Ni (II) complex quenches the exciting lifetime of the fluorophore. Here the ligand **L** absorbs the energy of the excitation photon and transfers it to Ni (II) complex. In many cases, the energy gained as a result of photon absorption is lost by nonradiative processes from an excited state generally called quenching and leads to the decrease of the fluorescence lifetime. The energy lost by the nonradiative process is responsible for the excitation of more rotational and vibrational levels.

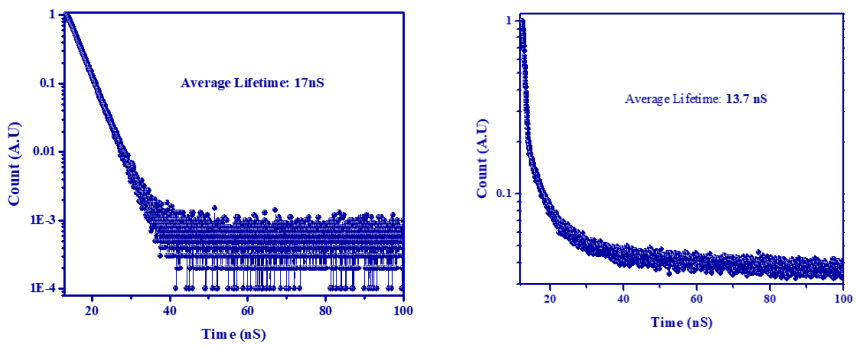

(a) (b)

Figure.5.13 Time resolved fluorescence decay measurements of (a) **L** and (b) Ni (II) complex

5.3.7 Antibacterial Studies of L and Ni (II) complex

The Schiff base ligand, **L** and its Ni (II) complex were investigated for their *in-vitro* antimicrobial activity against two Gram-positive bacteria (*Staphylococcus aureus and Streptococcus mutans)* and two Gram-negative

bacteria (*Pseudomonas aeruginosa* and *Escherichia coli*). The bacterial screening results disclose that the free **L** and its Ni (II) complex are active against the bacterial strain. The inhibition zone diameters of the investigated compounds are summarized in Table.5.3. A comparative study of inhibition zone diameter values of the Schiff base ligand and Ni (II) complex indicated that the metal complexes exhibited higher antibacterial activity than the free Schiff base ligand. This is due to the chelation of metal ions with ligand, which can improve the biological activity of the parent organic compounds. Both ligand and Ni (II) complex show higher activity against the gram-negative bacteria, *Escherichia coli.* Based on Overtone's concept and Tweedy's chelation theory, metal complexes have higher biological activity than their ligands. As metal ions undergo chelation, their polarity is reduced due to the overlap of their orbitals with the ligand and the partial sharing of their positive charge with donor groups. Further, the delocalization of the π-electrons is increased over the whole chelate sphere and enhances the lipophilicity of the complex. Upon chelation, the central metal atom becomes more lipophilic, which in turn makes it easier for it to penetrate the lipid layer of the cell membrane [53, 54]. It was found that both free ligand and their complexes were active against bacteria and the zone inhibition values are found to be similar in comparison with previous studies [55-60].

Table.5. 3 Antibacterial activity of L and Ni (II) complex

Species	Zone diameter (mm) Concentration (100µ/ml)		
	L	Ni (II) complex	Standard (Streptomycin) (100µg/ml)
Staphylococcus aureus	11	15	27
Streptococcus mutans	12	16	25
Pseudomonas aeruginosa	16	22	29
Escherichia coli	17	24	28

5.3.8 Antioxidant Activity of L and Ni (II) complex

Compounds that restrain oxidation inhibit free radical production and chain reactions that can damage cells of organisms are called antioxidants. It is well known that reactive oxygen species (ROS) created during biochemical processes in the body system, such as superoxide anion, nitric oxide, and hydrogen peroxide, are very much reactive and highly destructive transient chemical species. The oxidative damages caused by ROS on lipids, proteins, and nucleic acids may generate various chronic diseases, such as coronary heart disease, atherosclerosis, cancer, and aging [61]. Hence, to prevent free radical damage in the body, it is very significant to govern drugs that may be rich in antioxidants. They help to neutralize harmful free radicals. The antioxidant assay study was performed using different concentrations of **L** and its Ni (II) complex with H_2O_2, Nitric Oxide, and Superoxide, while ascorbic acid (vitamin C) and Gallic acid were used as standards.

(a) H_2O_2 Scavenging activity

The H_2O_2 can pierce into biological membranes systems, but it cannot react with the biological cell membrane. However, H_2O_2 may be toxic to cells because it gives rise to hydroxyl radicals ($OH^{\cdot}$) in the cells. Scavenging of H_2O_2 by samples may be attributed to their donation capacity of electrons to H_2O_2 and in that way neutralizing it to water. The table contains the percentage of inhibition with varying concentrations and IC_{50} of the standard; Ascorbic acid, ligand; **L**, and Ni (II) complex. Table 5. 4 and Figure.5.14 showed that both ligand **L** and Ni (II) complex exhibit H_2O_2 scavenging activity where, Ni (II) complex shows better activity than the ligand, **L**. This may be due to its potent antioxidant activity. At lower concentrations, Ni (II) complex shows higher activity than the standard, Ascorbic acid. As the antioxidant components present in the nano-sized Schiff base metal complex

of Ni (II) is good electron donor, this may accelerate the conversion of H_2O_2 to H_2O. The IC_{50} value of each assay is also shown in the Table.5.4 and which illustrates that IC_{50} of Ascorbic acid <Ni (II) complex < **L**

Table.5. 4 H_2O_2 scavenging activity of **L** and Ni (II) complex with Ascorbic acid as standard

Assay: H_2O_2	**Percentage of inhibition**					**IC_{50}(mg/mL)**
Concentration (mg/mL)	**0.125**	**0.25**	**0.5**	**1**	**2**	
Ascorbic acid	17.01	35.57	54.59	68.97	87.07	0.450
L	11.03	26.67	32.91	45.93	62.83	1.246
Ni (II) complex	18.57	36.81	46.36	62.72	76.36	0.615

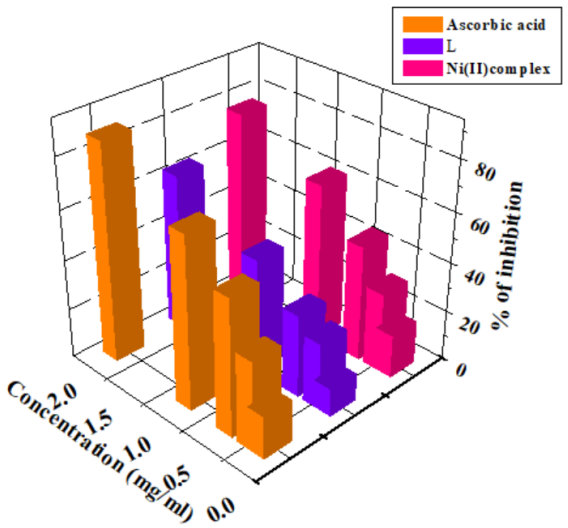

Figure.5.14 H_2O_2 scavenging activities of **L** and Ni (II) complex

(b) Nitric Oxide Scavenging activity

Aqueous sodium nitroprusside solution at physiological pH instinctively generates nitric oxide and which interacts with oxygen to produce nitrite ions that can be estimated using the Griess reagent. Nitric oxide scavengers

compete with oxygen and suppress the production of nitrite ions, a large amount of which may lead to tissue damage. Table.5.5 and Figure.5.15 showed that both **L** and Ni (II) complex exhibit nitric oxide scavenging activity whereas Ni (II) complex shows better activity than **L**. At lower concentrations, Ni (II) complex shows higher activity than the standard, Gallic acid. As the antioxidant components present in the nano-sized Schiff base metal complex of Ni (II) is good electron donor, this may accelerate the conversion of nitric oxide to nitrite ions. The IC_{50} value of each assay is also shown in the table and which illustrates that IC_{50} of Gallic acid <Ni (II) complex < **L**

Table.5. 5 Nitric Oxide scavenging activity of **L** and Ni (II) complex with Gallic acid as standard

Assay: Nitric Oxide	**Percentage of inhibition**					**IC_{50} (mg/mL)**
Concentration (mg/mL)	**0.125**	**0.25**	**0.5**	**1**	**2**	
Gallic acid	20.55	42.23	68.67	80.02	93.97	0.447
L	11.09	26.71	38.99	48.41	65.29	1.090
Ni (II) complex	21.04	28.70	41.85	56.31	69.65	0.790

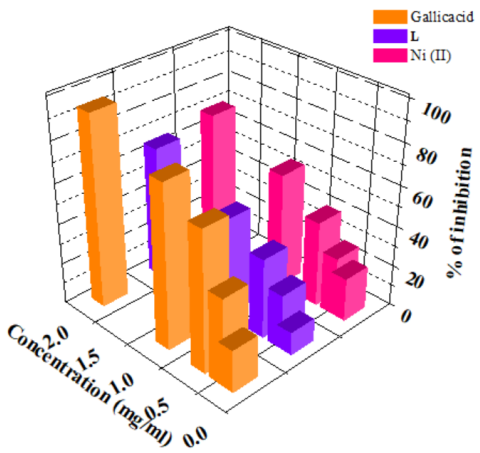

Figure.5. 15 Nitric oxide scavenging activities of **L** and Ni (II) complex

(c) Superoxide scavenging activity

Superoxide is biologically significant because it can produce singlet oxygen and hydroxyl radicals. Overproduction of superoxide anion radical leads to redox which will cause harmful physiological consequences. Table.5.6 and Figure.5.16 shows that both **L** and Ni (II) complex exhibited nitric oxide scavenging activity whereas Ni (II) complex showed better activity than **L**. At lower concentrations, Ni (II) complex shows higher activity than the standard, ascorbic acid. As the antioxidant components present in the Schiff base metal complex of Ni (II) is good electron donor, this may accelerate the conversion of nitric oxide to nitrite ions. The IC_{50} value of each assay is also shown in the table and which illustrates that IC_{50} of ascorbic acid <Ni (II) complex < **L**

Table.5. 6 Super Oxide scavenging activity of **L** and Ni (II) complex with Ascorbic acid as standard

Assay: Super Oxide	**Percentage of inhibition**					**IC_{50} (mg/mL)**
Concentration (mg/mL)	**0.125**	**0.25**	**0.5**	**1**	**2**	
Ascorbic acid	21.18	39.02	53.68	71.65	89.63	0.429
L	11.85	29.54	43.78	58.83	68.23	0.700
Ni (II) complex	22.38	32.86	46.69	64.12	72.21	0.589

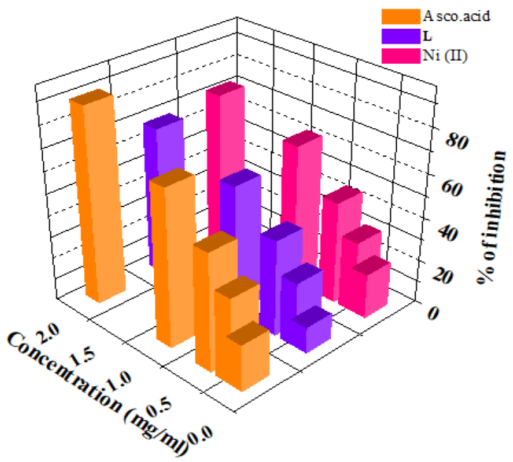

Figure.5. 16 Antioxidant scavenging activities of **L** and Ni (II) complex

Analyzing antioxidant activities upon three different ROS, both ligand and Ni (II) complex exhibit antioxidant activity. There is, however, more antioxidant activity in Ni (II) complex than free ligand. It shows better activity in H_2O_2 than Nitric oxide and superoxide. Moreover, Ni (II) complex shows higher antioxidant activities than the standard at lower concentrations. Based on the results, it can be concluded that the complexes have higher antioxidant activity than free ligands since metal ions may significantly alter their chemical properties. The IC_{50} value of Ni (II) complex appears to be as follows. IC_{50} (Nitric Oxide) > IC_{50} (H_2O_2) > IC_{50} (Super oxide). The antioxidant scavenging activities of **L** and Ni (II) complex were compared with previous reported data and found it is comparable with our results [62-65].

5.3.9 Larvicidal Activity of L and Ni (II) complex

Table.5.7 stands for the mortality rate with standard deviation for a period of 24 hours. The ligand, **L** showed 100% mortality for a concentration 70 µg/ml. At the same time, the control groups water and solvent DMSO showed no mortality. Ni (II) complex showed 100% mortality for a concentration of 50 µg/ml. This shows the mortality rate is faster in complex than the ligand. Chelation increases the lipophilic behavior of the central metal atom, which equips the molecules in crossing the cell membrane of the larva and boosting the larvicidal activity of the complex. Also, since Ni (II) complex could penetrate more easily inside the body of the larva and interrupt the metabolic activities rapidly [66]. Figure.5.17 shows the probit analysis of the mortality; the LC_{50} value is 27.99 and 22.26 µg/ml for ligand and Ni (II) complex respectively. The LC_{90} values are 59.8 and 48.43 µg/ml respectively for **L** and Ni (II) complex. Their confidence interval of 95% is also found and marked in the table. Both **L** and Ni (II) complex show similar larvicidal activity when compared with previous results [19, 67-70].

Table.5. 7 Larvicidal activities of **L** and Ni (II) complex

Mosquito larva	Concentration in DMSO (µg/ml)	24 hrs mortality (%) ± SD	
	Control (Water)	0.0±0.0	
	DMSO	0.0±0.0	
	L/ Ni (II) complex	**L**	Ni (II) complex
Culex	10	18.4±1.959	25.2±1.6
	20	34.4±1.959	45.4±1.959
	30	56.8±2.99	61.2±1.6
	40	66.4±1.959	77.8±2.99
	50	79.2±1.6	100±0
	60	89.2±2.4	100±0
	70	100±0	100±0
	LC_{50}(µg/ml) (LCL-UCL)	27.99 (26.3 - 29.7)	22.26 (21.2-23.3)
	LC_{90}(µg/ml) (LCL-UCL)	59.8 (58.4 - 61.2)	48.43 (47.3-49.6)

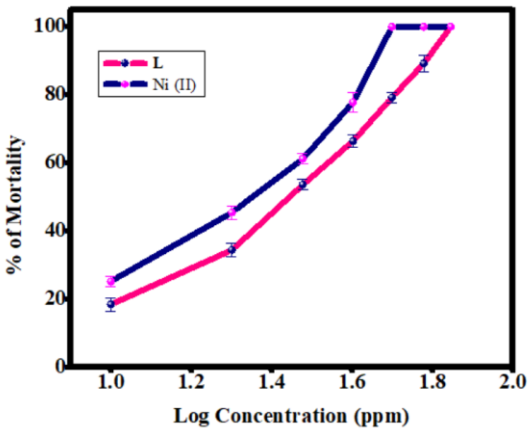

Figure.5.17 Probit analysis of mosquito larva mortality rate in the presence of **L** and Ni (II) complex

5.4 Conclusions

Synthesis of a novel fluorescent, bioactive Schiff base ligand, *3-((2-(-(1-(2-hydroxyphenyl) ethylidene) amino) ethyl) imino)-2-pentone* and its Ni (II) complex using ultrasonic irradiation is reported here. The synthesized ligand and metal complex are characterized analytically and through various spectral techniques such as UV-Vis, IR, NMR and ^{13}C NMR HRMS, XRD, TEM, SEM, molar conductance and magnetic moment data. XRD data confirms the crystalline nature of both ligand and complex. SEM and TEM images showed that the ligand has rectangular morphology and Ni (II) complex has rod shaped surface morphology. Based on the various analytical, spectral and magnetic moment data, Ni (II) complex is assigned to octahedral geometry. The bandgap energy calculation of ligand and Ni (II) complex proposes that they can be considered as a semiconductor material. Based on the photoluminescence spectrum and chromaticity studies, it can be applied in green emitting OLED. Both ligand and Ni (II) complex show biological activities like antibacterial, antioxidant and larvicidal activities. It is observed that Ni (II) complex shows better antibacterial, antioxidant and larvicidal activities than ligand.

References

[1] K Subin Kumar and K K Aravindakshan, Results Chem., 3 (2021) 100129.

[2] N Dhar Do and C L Taploo, J Sci Ind Res., 41(8) (1982) 501.

[3] P Przybylski et al., Curr Org Chem., 13 (2) (2009) 124.

[4] Da Silva et al., J. Adv. Res., 2(1) (2011) 1.

[5] P Espinet and Soulantica. K, Coord. Chem. Rev., 193(1999) 499.

[6] Berhanu et al., Tren. Anal. Chem., 116 (2019) 74.

[7] L Fan et al., Sens. Actuators B Chem., 203 (2014) 550.

[8] L Fan et al., J. Lumin., 155 (2014) 84.

[9] H J Jung, N Singh, D Y Lee, DO Jang, Tetrahedron Lett., 51 (30) (2010) 3962.

[10] Ghorai et al., New J Chem., 40(9) (2016) 7821.

[11] Abou-Omar et al., ACS omega, 6(32) (2021) 20812.

[12] Hou et al., J. Mater. Chem. B, 5(45) (2017) 8957.

[13] Carter et al., Chem. Rev., 114(8) (2014) 4564.

[14] Jeong, Yongsuk, Juyoung Yoon, Inorganica Chim. Acta., 381 (2012) 2.

[15] Liu Haiyang et al., J. Mater. Chem. B, 6(34) 5435.

[16] P B Tchounwou et al., J Mol Clin Environ Toxicol., 101 (2012) 133.

[17] S Y Lee et al., Tetrahedron, 72 (2016) 5563.

[18] A M Abu-Dief and I M Mohamed, J. basic appl. sci., 4(2) (2015) 119.

[19] K Subin Kumar et al., Results Chem., 3 (2021) 100166

[20] J Saranya and S L Santha, J. Chem. Pharm. Res., 7 (4) (2015) 180.

[21] Joseyphus et al., Mycobiology, 36(2) (2008) 93.

[22] H Yersin et al., Coord. Chem. Rev., 255(21) (2011).

[23] G Yu et al., Synth. Met., 117 (1) (2001) 211.

[24] M Srinivas et al., J. Sci.: Adv. Mater. Devices, 1(3) (2016) 324.

[25] A N Gusev et al., J. Phy. Chem. C, 123(18) (2019) 11850.

[26] N K Gondia et al., AIP Conference Proceedings, 1953 (1) (2018) 130018.

[27] Kagatikar et al., J. Elect. Mater., 50(12) (2021) 6708.

[28] Y T Li et al., Synth. react. inorg. met.-org. chem., 34(7) (2004)1165.

[29] Y Aydogdu et al., Mater. Lett., 57(24-25) (2003) 3755.

[30] H Y Bie et al J. Mol. Struct., 660 (1-3) (2003) 107.

[31] S H Rahaman et al., Polyhedron, 24(18) (2005) 3091.

[32] X Y Xu et al., Inorg. Nano-Met. Chem., (9) (2006) 681.

[33] A Pfaltz et al., The Bioinorganic Chemistry of Nickel, VCH: New York, NY, USA, 1988.

[34] R Y Kurtaran et al., J. Inorg. Biochem., 99 (2005)1937.

[35] P Raj, ACS Sustain. Chem. Eng., 5 (2017) 6070.

[36] M Alexiou, J. Inorg. Biochem., 93 (2003) 256.

[37] Z Afrasiabi. J. Inorg. Biochem., 99 (2005) 1526–1531.

[38] W Luo et al., Inorg. Chem. Commun., 10 (2007) 1351.

[39] Buschini A et al., J. Inorg. Biochem., 103 (2009) 666.

[40] P Kalaivani et al., Eur. J. Med. Chem., 82 (2014), 584.

[41] P H Amith Nayak, Mol. Cry. Liq. Cryst., 722(1) (2021) 67.

[42] B R Kirthan, Inorg. Chem.Comm., 135 (2022)109109.

[43] National Committee for Clinical Laboratory Standards Fifth Edition (1993a) Approved Standard M2-A5. NCCLS, Villanova, PA.

[44] R J Ruch, Carcinogenesis., 10 (1989) 1003.

[45] Guidelines for laboratory and field testing of mosquito larvicides (World Health Organization) (2005)

[46] Abbott, S A Walter, J. econ. Entomol., 18(2) (1925) 265.

[47] H Zhang H, Q Zhu, Z Xie, Mater Res Bull., 40(8) (2005)1326.

[48] B D Cullity, Elements of X-ray Diffraction 2nd edn (Addison-Wesley, Philippines, 1978)

[49] F Karipcin et al., Opt. Comm., 272(1) (2007) 131.

[50] T S Liao et al., J. Nanomater., 17 (2015) 1.

[51] J R Lakowicz, Principles of Fluorescence Spectroscopy, 3rd Edn. (Springer, New York, 2006)

[52] Kundu P et al., Journal of fluoresce., 26(3) (2016) 845.

[53] B G Tweedy, Phytopathology, 55 (1964) 910.

[54] T D Thangadurai and K Natarajan, Transit. Met. Chem., 26(4-5) (2001) 500.

[55] J Devi, N Batra, Spectrochim. Acta A Mol. Biomol. Spectrosc., 135 (2015) 710.

[56] M J Barnabas et al., Heliyon, 5(4) (2019) 01521.

[57] A K Mapari, et al., E-Journal of Chem., 8(3) (2011) 1258.

[58] B Nazirkar et al., J. Tai. Uni for Sci., 13(1) (2019) 440.

[59] K Subin Kumar, Res. Chem., 4 (2022) 100463.

[60] K Subin Kumar and V N Reena, Mater. Today: Proceedings, 62 (2022).

[61] B Uttara et al., Curr. Neuropharmacol., 7(1) (2009) 65.

[62] M BHM et al., Der Pharma Chemica, 7 (10) (2015) 556.

[63] Y Harinath Y et al., Spectrochim. Acta A Mol. Biomol. Spectrosc.,101 (2013) 264.

[64] S N Shukla et al., J. Serb. Chem. Soc., 86(10) (2021) 941.

[65] M Yadav et al., J. Chem. Sci.,133(1) (2021) 1.

[66] V N Reena et al., IOP Conference Series: Materials Science and Engineering, 1221 (1) (2022) 012051.

[67] S S Lakshmi et al., J. Chem. Sci.,128(7) (2016) 1113.

[68] M V Joice and P Metilda, J. Co. Chem., 74(14) (2021) 2395.

[69] T J Saritha, and P Metilda, Int. j. adv. sci. res. Manag.,4(4) (2018) 1.

[70] Saranya J, Sundaramurthy Santha Lakshmi, J. Chem. Pharm. Res., 7(4) (2015) 180.

Chapter 6

Photonic and Biological Applications of Schiff base Capped CdS Nanoparticles

This chapter encompasses the synthesis and explores the photonic and biological applications of Schiff base capped CdS NPs. This study utilizes Schiff base ligands as capping agents for the synthesis of biocompatible CdS NPs. The research encompasses the synthesis of CdS NPs and comprehensive analysis of their structural, morphological, and optical properties using techniques such as XRD, SEM, TEM, UV-visible absorption, and PL spectra. The quantum confinement effect, evident in the UV-visible and PL spectrum analysis, showcases the unique characteristics of Schiff base-capped CdS NPs. The CdS NPs are evaluated as efficient photocatalysts for degrading dyes like rhodamine 6G and methylene blue. It demonstrates superior inhibition for both Gram-positive and Gram-negative bacteria. The potential of Schiff base-capped CdS NPs as optical probes in biological applications is illustrated through *in-vitro* bioimaging experiments with HeLa cells, observed under a fluorescence microscope. Furthermore, MTT cell viability assays conducted over 24 hours reveal insights into cytotoxicity, and a comparison between Schiff base-capped CdS and uncapped CdS NPs suggests the former's potential in various biological applications.

The results of this chapter are published as:

Reena V N, Kumar K S, Shilpa T, Aswati Nair R., Bhagyasree G S, Nithyaja, B. (2023). Photocatalytic and Enhanced Biological Activities of Schiff base Capped Fluorescent CdS Nanoparticles. *Journal of Fluorescence*, 33 (5) 1927. (Publisher: Springer Nature)

6.1 Introduction

The increasing popularity of NPs emanating from Schiff bases in nanotechnology is due to their novelty, effortlessness, cost-effectiveness, and eco-friendliness in preparation. The critical task to obtain the NPs of precise properties is the selection of a suitable capping agent. The Schiff bases hold a functional head group and one or more hydrocarbon tails that handle quantum dots' nucleation and maturation [1]. In the case of the extinction of medicinal plants, Schiff bases would vie with natural extracts as capping agents. In addition, the Schiff base ligand's cytotoxicity studies show above 90 percent cell viability below 20 µg/ml concentrations which is an indeed intention in choosing a capping agent. Both these properties of the Schiff base ligand expose themselves as an acceptable capping agent for the synthesis of NPs [2]. Nanoparticles derived from Schiff bases are found to be less reported and must be included in future researches. Recent research reports have highlighted the suitability of Schiff base-derived NPs for a wide range of photonic and biological applications. They are metal NPs like Au, Ag, Ni, and Cu and nonconducting NPs like Ag_2S and silica NPs and semiconductor NPs like CdS, ZnS, CdTe, ZnSe, CuO, ZnO etc. [3-6, 7].

The capping agents are crucial in synthesizing highly mono-dispersed CdS NPs by growth restriction methods. Several biocompatible capping agents are exploited to achieve growth restriction in preparation for CdS NPs [8-11]. Their chemical and physical properties strongly depend on size [12-14]. Their excellent properties have been exploited in applications like light-emitting diodes, lasers, sensors, solar cells, photocatalysis, photocells, display devices, invertors, waveguides, and bioimaging [15-23].

The fluorescent behaviour of CdS NPs has been taken advantage of in biomedical applications, and they have more advantages over conventional organic dyes, especially in bioimaging applications. CdS is a promising candidate for *in-vivo* and *in-vitro* imaging of normal and cancerous cells [24-26]. Incorporating NPs into biological systems necessitates biocompatibility. To achieve biocompatibility, NPs must be capped with natural or organic structures. Since the Schiff base ligand has a biological molecule-like structure, it may reduce the toxicity of CdS. Therefore, they may possess potential applications in bioimaging and associated applications. Here, the CdS NPs will be coordinated into the Schiff base ligand, acting as a biological over-coating to CdS. This coating will reduce the effect of surface charges around CdS and may also reduce toxicity [4, 27].

The Schiff base-derived CdS was reported in 2013 by Shakouri-Arani M et al., utilizing the Schiff base as the sulfuring agent [28]. CdS NPs were prepared in 2015, employing Schiff base as a complexing agent [3]. The synthesis of Schiff-base capped CdS NPs by Kakanejadifard et al. found that these NPs show antimicrobial activities [11].

The synthesis, characterization, and biological activities of this novel Schiff base **L** is explained in the previous chapter. The ligand exhibits antimicrobial, antioxidant and larvicidal activities. The Schiff base is highly fluorescent around the wavelength of 500 nm, which matches the emission wavelength of CdS NPs [29]. It would enhance fluorescent emission intensity in CdS NPs capped with this Schiff base ligand. Therefore, this Schiff base capped CdS NPs are potential fluorescent probe for bioimaging applications.

Taking all the observations mentioned above into consideration, here we report the ultrasonic method of synthesis of CdS NPs using the

Schiff base, **L**, as a capping agent. In the preparation method, non-toxic solvents were utilized. The structural, morphological, and optical properties were studied using XRD, SEM, TEM, UV-visible absorption, and PL spectra. The quantum confinement effect of the Schiff base capped CdS NPs was confirmed by using UV-visible and PL spectrum analysis. The photocatalytic behaviour of CdS NPs was investigated using two different dyes, Rh6G and MB. We examined the antibacterial effect of this CdS NPs. These Schiff-base-coated CdS NPs were verified as luminescent probes in *in-vitro* fluorescence microscopy. In addition, an initial assessment of the biocompatibility of these NPs and capping agents was performed using an MTT cell viability assay. Biological applications of Schiff base capped CdS were compared with uncapped CdS. Significant amount of enhancement in fluorescence and biological activities are observed from this Schiff base capped CdS NPs. Furthermore, this is the first work which reports bioimaging and cytotoxicity studies of Schiff base-capped CdS NPs.

6.2 Materials and Methods

6.2.1 Materials and Reagents

All the chemicals, o-hydroxyacetophenone, acetylacetone, 1, 2-ethylenediamine, cadmium nitrate and sodium sulfide, solvents like DMSO, methanol, Rh6G and MBwere purchased from Sigma-Aldrich.

6.2.2 Synthesis of *3-((2-(-(1-(2-hydroxyphenyl) ethylidene) amino) ethyl) imino)-2-pentone* (L)

The detailed synthesis of **L** was described in chapter 5, materials and method section.

6.2.3 Synthesis of Schiff base capped CdS NPs (L-CdS)

In this procedure, 25 ml, 0.25 $x10^{-3}$ M cadmium nitrate ($CdNO_3$ ($6H_2O$)) and 25 ml 0.25 $x10^{-3}$ M sodium sulfide ($Na_2S.9H_2O$) were dissolved separately in ethanol. The solutions were stirred in an ultrasonicator for 30 minutes. Equimolar amount of the Schiff base, **L**, was used as capping agent dissolved in DMSO. This solution is added to the Cd^{2+} solution, which will prevent the agglomeration of CdS NPs. Stirring continued for 30 minutes. Sodium sulfide solution was added drop wise to the mixture under ultrasonic irradiation. The resulting greenish-yellow coloured precipitate, soluble in DMSO, was collected and filtered. The filtered CdS NPs were washed with distilled water and ethanol several times to remove the unreacted chemicals and dried in an oven at 50^0C for 2 hours. Figure.6.1 represents the possible reaction and reaction mechanism for the formation of L-CdS. A coordination bond between **L** and Cd^{2+} ion in the CdS NPs is formed here. The S^{2-} preferably makes ionic bond with Cd^{2+} and L-CdS is formed.

$$CdNO_3.6H_2O + \mathbf{L} \xrightarrow[Na_2S.9H_2O]{\text{Ultrasonication}} \text{L-CdS}$$

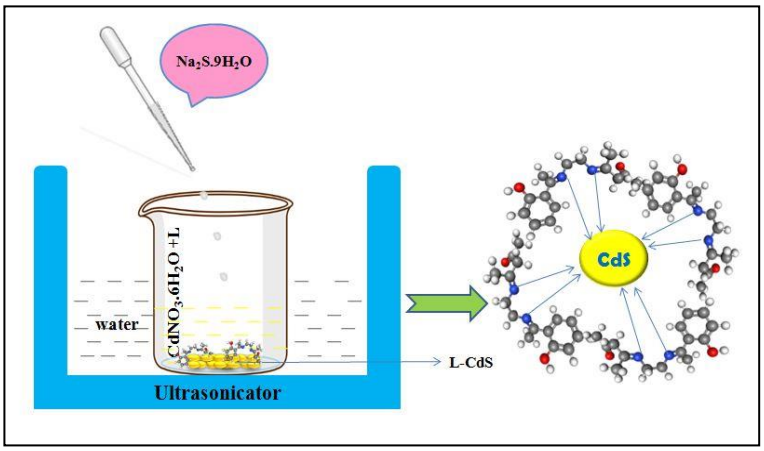

Figure.6.1 The possible formation mechanism of the L-CdS

6.2.4 Fabrication of L-CdS incorporated Rh6G-doped sol-gel glass

The L-CdS incorporated Rh6G doped sol-gel glasses were prepared as the procedure explained in the chapter 3. Here, L-CdS contains the presence of the Schiff base and it has a tendency to crystallize in the room temperature. This makes an uneven texture for the glass because ligand was crystallized unevenly throughout the glass. This glass cannot be used for any applications effectively.

6.2.5 Photocatalytic Activity

The photodegradation of organic dye solutions by L-CdS was studied. To do this, we chose two organic dyes; Rh6G and MB. The procedure is explained in the chapter 2.

6.2.6 Biological Applications

The antibacterial activity, cytotoxic studies, and bioimaging applications were done as the procedure explained in chapter 2. The antibacterials present in the samples can diffuse into the medium and interact in a plate freshly seeded with the test organisms. The resulting inhibition zones will be uniformly circular as there will be a confluent lawn of growth. Three microbes were taken in this procedure: two Gram-positive, *Staphylococcus aureus* and *Streptococcus mutans*, and one Gram-negative, *Pseudomonas aeruginosa* [32]. In this study, streptomycin was used as a standard antibacterial agent. For bioimaging studies, HeLa cells were used. A concentration of 2.5 and 5 μg/mL of L-CdS were added to the HeLa cells. Cells without drug were kept as control, and media without cells were kept blank. The plate was then incubated in a CO_2 incubator for 24 hours. After 24 hours of treatment, cells were viewed under a fluorescence microscope.

6.3 Results and discussions

6.3.1 Characterization of L-CdS

The formation of L-CdS was confirmed from their characterization data, including, UV-visible absorption, PL, XRD, SEM, and TEM imaging.

The UV–visible absorption spectra of uncapped CdS and L-CdS are shown in Figure.6.2. The absorption peak of both uncapped and L-CdS NPs were found in the visible range of wavelength. The bandgap energy (E_g) of CdS can be obtained by using the formula: $E_g=1240/\lambda$ (eV), where λ is the wavelength of the absorption edge. The L-CdS possesses an absorption wavelength peak at 474 nm and absorption edge is obtained at 500 nm. The calculated E_g using absorption edge wavelength is 2.5 eV. It may be due to the quantization effect of size. This blue shift is due to the grain size reduction, which leads to a wider energy gap [29]. The particle size R can be obtained from Brus formula [30]. The calculated particle size is around 2 nm.

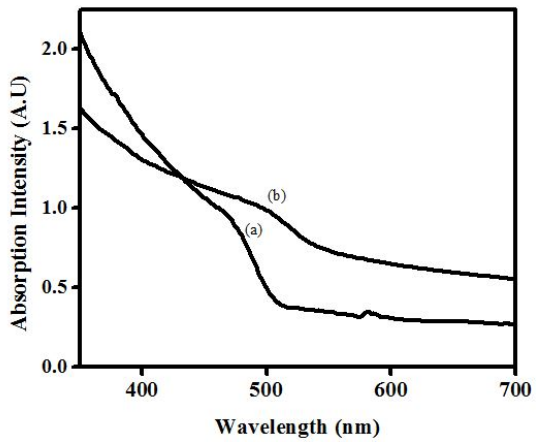

Figure.6.2 UV-visible absorption spectrum of (a) L- CdS and (b) uncapped CdS

The PL spectra of uncapped CdS and L-CdS are demonstrated in Figure.6.3 (a) and (b). The Figure.6.3 (a), shows two peaks in the range of 450 nm to 600 nm for an excitation wavelength of 400 nm. The first higher peak was centered at 487 nm and the second lower peak was centered at 541 nm. The peak at 487 nm is attributed to the emission from the absorption edge. The corresponding bandgap energy 2.5 eV, which is an increased value compared to the bandgap energy of bulk CdS (2.42 eV). This is due to the particle size reduction as a result of quantum confinement of the photo-generated electron-hole pairs [31]. The peak at 541 nm may be corresponds to emission due to surface states or traps associated crystalline defects. Here, in the CdS NPs, this emission is linked to cadmium and sulfur atom vacancies [32-34]. The uncapped CdS has also two peaks, one is at 491 nm and the second one is at 548 nm. The peaks of L-CdS are blue-shifted as compared to uncapped CdS. This blue shifting is due to the quantum confinement effect of L-CdS. A considerable amount of enhancement in the fluorescence intensity of L-CdS was noted. This may be due to the presence of Schiff base ligand which is highly fluorescent around the wavelength of 500 nm, which matches the emission wavelength of CdS NPs.

As the synthesized L-CdS possess emission wavelength in visible region and considering the biocompatibility, fluorescence cell imaging may be a key application. Also, due to the multiple emission wavelengths, L-CdS can be employed for the production of multicoloured light emitting diodes [23].

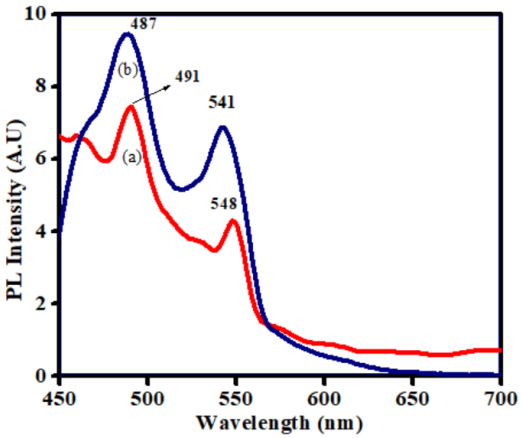

Figure.6.3 PL spectrum of (a) Uncapped CdS and (b) L-CdS

6.3.2 XRD

Figure.6.4 (a) and (b) show the powder XRD patterns of uncapped CdS and L-CdS respectively. Diffraction patterns were recorded at room temperature at 10-80 degrees. The average crystalline size of all samples can be found by using Debye-Scherrer's formula [35]. The uncapped CdS and L-CdS diffraction patterns show three peaks at 26.70, 43.80, and 51.50. These peaks can be indexed as (111), (220), and (311) crystallographic planes indicating that the prepared CdS NPs belong to the face-centered cubic phase, zinc blende structure (JCPDS no 75-1545). The widening of the XRD peak of L-CdS indicates the reduction in particle size. The crystalline size of uncapped and L-CdS was estimated at (111) peak and found respectively to be 25 nm and 5.7 nm. It was found that the crystalline size of L-CdS was reduced compared to uncapped CdS.

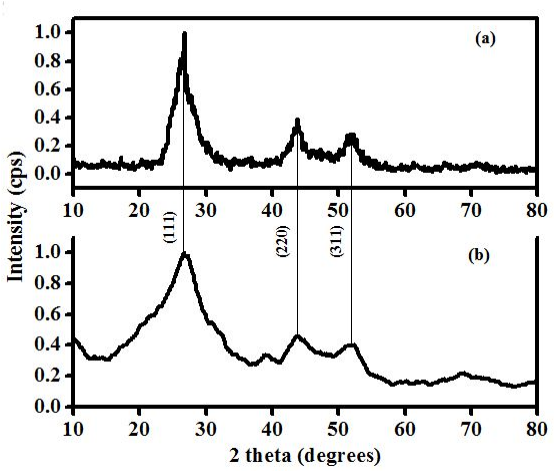

Figure.6.4 XRD image of (a) Uncapped CdS, (b) L-CdS

6.3.3 SEM

The SEM is a technique to investigate the surface morphology of materials. SEM image is recorded for L-CdS and is presented in Figure.6.5. The micrograph of L-CdS shows that the surface morphology has different spherical shapes. It is seen there is a size reduction in L-CdS is when compared to uncapped CdS.

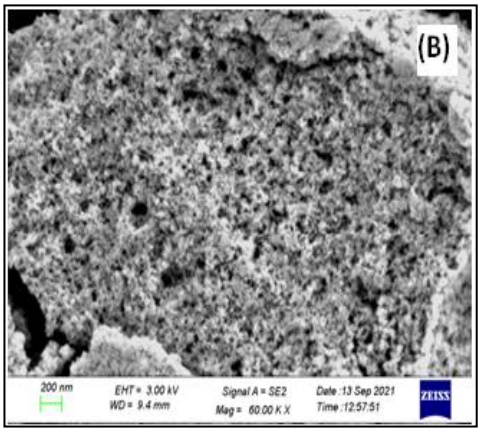

Figure.6.5 SEM image of L-CdS

6.3.4 TEM

The TEM image and SEAD pattern of L-CdS are shown in Figure.6.6. L-CdS exhibits monodispersed particles with an average size of 10 nm. The spherical shape of L-CdS is attributed to the interaction of donor atoms in **L** with the surface of the NPs. The interplanar spacing is observed to be 0.34 nm (Figure.6.6. (b)). The selected area electron diffraction pattern (Figure.6.6. (c)) visibly gives three diffraction rings of (111), (220) and (311) planes as shown, which recognizes the cubic phase. Some NPs get aggregated due to large specific surface area and high surface energy. The suggestion also indicates that the functional groups within the Schiff base readily bond with Cd^{2+}, serving as electron donors. This bonding reduces electrostatic repulsion, thereby promoting the stabilization of CdS nanocrystals into smaller and more compact dimensions.

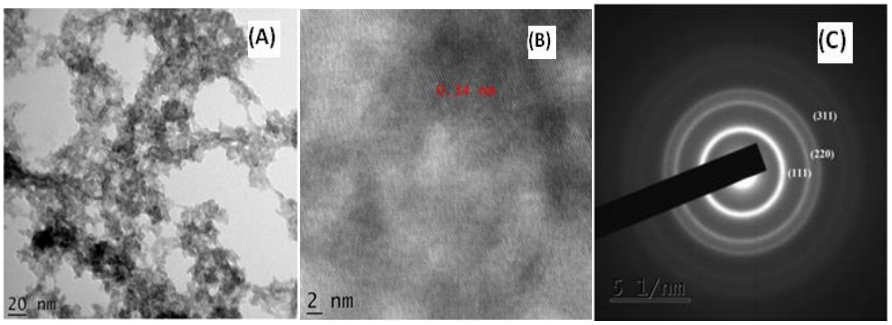

Figure.6.6 HRTEM images of (a) L-CdS (b) interplanar spacing (c) SAED pattern of L-CdS

6.3.5 Photocatalytic Activity of L-CdS

The photocatalytic degradation of Rh6G and MB was studied in the presence and absence of L-CdS under UV irradiation, for a period of 120 minutes. The absorption peak of Rh6G at 520 nm and absorption peak of MB at 665 nm were considered to determine the photocatalytic

activity. Figure.6.7 shows the absorption spectra of Rh6G in the presence L-CdS. The peak corresponding to 520 nm is due to the transition between S0 to S1 [36]. The intensity of absorption gradually deceases with time.

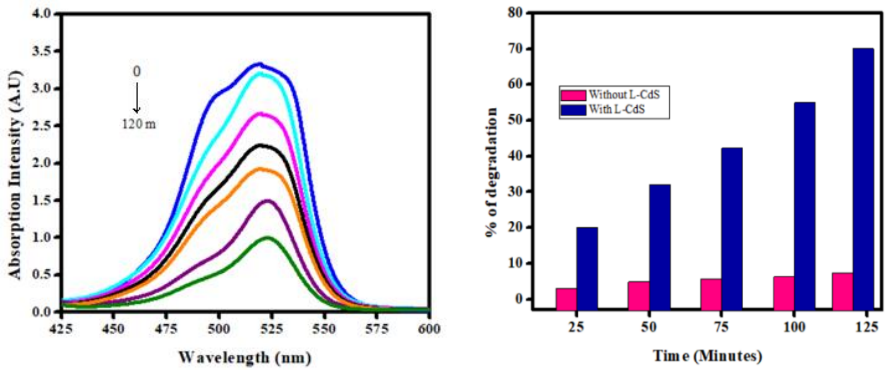

(a) (b)

Figure.6.7 (a) Photocatalytic degradations of Rh6G in the presence of L-CdS (b) percentage of degradation with and without catalyst

It was observed that the percentage of degradation (Figure.6.7 (b)) of Rh6G increased in the presence of the photocatalyst; 70% degradation occurred within 120 minutes. There is 10 times increment in the photodegradation in the presence of L-CdS.

Figure.6.8 (a) and (b) demonstrate the absorption spectra of MB in the presence of L-CdS. The maximum absorbance takes place in the range of 550 nm to 700 nm with a pair of characteristic peaks at 612 nm and 665 nm. The peak at 665 nm is due to π-π^* transition associated with the resonance of the π electrons from sulphur resonating with those from carbons in thiazinic center. The peak at 612 nm corresponds to π-π^* transition of benzene rings [37]. In the presence of the photocatalyst, within 120 minutes, 93 % of degradation occurred for the peak at 612 nm whereas, 98.9% degradation occurred for the peak at 665 nm.

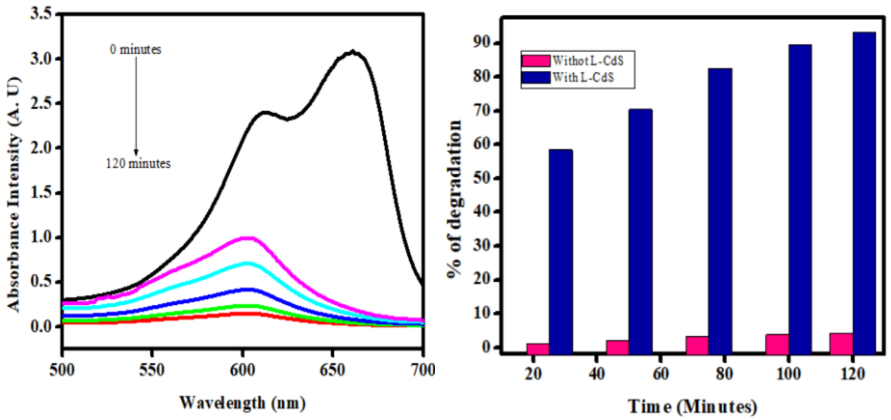

Figure.6.8 Photocatalytic degradation of MB in the (a) presence of catalyst under UV irradiation (b) percentage of degradation with and without catalyst

The L-CdS is found to be a potential photocatalyst for MB. The photodegradation of MB is greater than that of Rh6G, possibly due to Rh6G's higher photostability. Photocatalytic mechanism of L-CdS was instigated by irradiation by UV light. Excitation of electrons from the valence band to the conduction band of CdS, results in the production of electron-hole pairs [38-39]. In addition to longer charge carrier lifetimes, CdS NPs show better redox properties because the photo-generated electrons and holes are inhibited under UV irradiation. OH radicals are formed when the holes in CdS react with water molecules or hydroxide ions. The OH radicals are effective oxidizing agent, and it attacks organic pollutants present at the surface of CdS. The possible mechanism of photocatalytic reactions of Rh6G and MB are explained in chapter 3.

The percentage of degradation of methylene red (MR) dye by 10 mg of Schiff base capped CdS NPs reported to 65.61% [3]. Here, in this report, L-CdS shows about 70% degradation for Rh6G and 98% for

MB. This confirms that L-CdS is highly efficient photocatalyst than reported.

6.3.6 Antibacterial Activities

The experimental details for the antimicrobial studies were presented in the experimental section of chapter 2. The L-CdS is exhibiting inhibition to both Gram positive and Gram-negative pathogenic bacteria. The diameter of inhibition zone was measured for L-CdS for 1mg/ml concentration. Table.6.1 shows the inhibition zone diameter for the samples at 1 mg/ml concentration. All samples show better activity towards Gram-negative bacteria, Pseudomonas aeruginosa. L-CdS exhibited higher antibacterial activity than **L**. This can be explained as follows.

Increased lipophilicity facilitates permeation through the bacterium's membrane, making it more active. The chelation of metal ions with ligands can improve the biological activity of the parent organic compounds. According to Overtone's concept and Tweedy's chelation theory, metal complexes have higher biological activity than their ligands. When metal ions undergo chelation, their polarity is reduced due to the overlap of orbitals with the ligand and the partial sharing of positive charges with donor groups. Further, the delocalization of the π-electrons enhances the lipophilicity of the complex by increasing its density across the chelate sphere. Chelation makes the central metal atom more lipophilic, making it easier to penetrate the bacterial membrane's lipid layer. For the ligand **L** to enter the bacterial cell membrane, oxygen or nitrogen donor atoms must coordinate with lipopolysaccharide, damaging the outer cell membrane and inhibiting bacterial growth [1, 40].

Table.6. 1 Antibacterial activity of L-CdS

Species	Zone diameter (mm)	
	L-CdS (1 mg/ml)	**Standard (Streptomycin) (100 µg/ml)**
Pseudomonas aeruginosa	25	29
Staphylococcus aureus	21	27
Streptococcus mutans	17	25

6.3.7 Cytotoxicity analysis: MTT Assay

Cytotoxic effect of **L** and L-CdS against HeLa cell lines was examined within 24 hours. Figure.6.9 shows the MTT assay results with concentration versus cell survival rate. It was found that the Schiff base ligand, **L** shows 100% cell survival for different concentrations. Therefore, **L** is not toxic to HeLa cells. At the same time, L-CdS shows considerable toxicity towards HeLa cells. Figure.6.10 (b) implies that inhibition of HeLa cells is steadily enhanced with L-CdS concentration i.e, it showed a dose-dependent toxicity. At a concentration 2.5 µg/ml, it shows 82% cell viability and 62% viability 12.5µg/ml. The calculated LC_{50} value is equal to18.72 µg/ml.

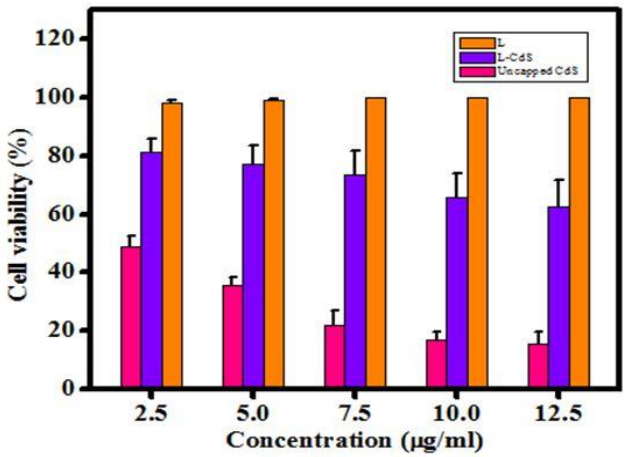

Figure.6.9 Histogram - cell viability of L and L- CdS

In Figure.6.10, the cell viabilities of the **L** and L-CdS for different concentrations are shown. The Schiff ligand, **L**, used here to cap CdS can improve biocompatibility by reducing the toxicity of unmodified CdS. Here the LC_{50} value is much greater than that of uncapped CdS, which indicates that toxicity reduced considerably for L-CdS. Toxicity and LC_{50} value are inversely proportional.

As CdS NPs possess photoluminescence in the visible range of wavelength, the biocompatible L-CdS can effectively be used as potential candidate for *in-vitro* cellular bioimaging.

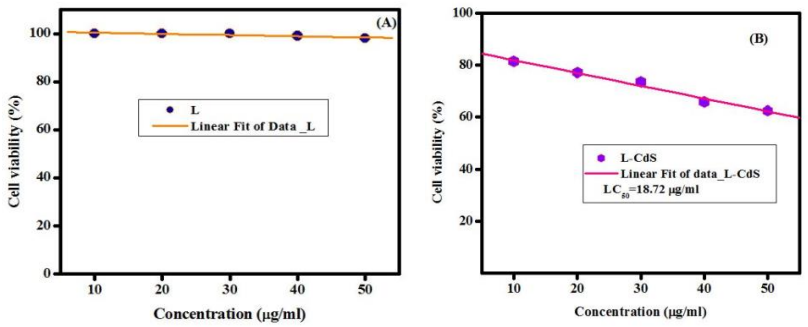

(a) (b)

Figure.6. 10 Cell viability and linear fit of (a) L (b) L-CdS

6.3.8 Bioimaging of L-CdS

The Cellular imaging of L-CdS is one of the vital features of this study. For this, HeLa cells were treated with L-CdS for 2.5 µg/ml and 5µg/ml, which is a less value than LC_{50} of L-CdS. After 24 hours of treatment, cells were viewed under a fluorescence microscope. The cell membrane, a double-layered lipid, detaches the cytoplasm from the surroundings. Figure.6.11 shows the bright field images of the HeLa cells treated with L-CdS (2.5µg/ml and 5µg/ml). The cells are clearly seen from the bright-field images. Cells with round shape represent cell death. It is obvious from the Figure.6.11, cells are destroyed in the

presence of L-CdS. Even though the cell death rate is lesser than that of uncapped CdS, cells are very clearly seen and not blurred in the presence of L-CdS. L-CdS were easily soluble in DMSO. It proves that L-CdS is a promising candidate for bioimaging. It is obvious from the Figure.6.11 (a) and (b) that; L-CdS shows a dose-dependent toxicity as seen from MTT assay. Higher number of cell death happened for a higher concentration. Figure.6.12 shows the fluorescent image of HeLa cells treated with L-CdS under green light. The cellular imaging capability of the biocompatible L-CdS is definitively proven by the bright green fluorescence.

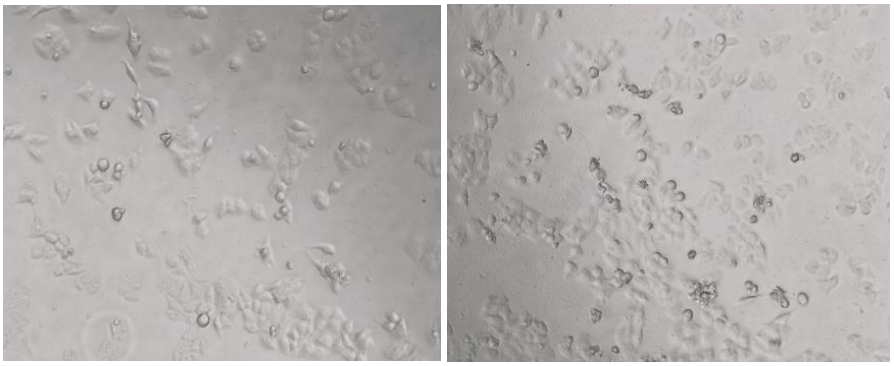

(a) (b)

Figure.6. 11 Bright-field images of HeLa cells in the presence of (a) L-CdS 2.5 and (b) 5µg/ml

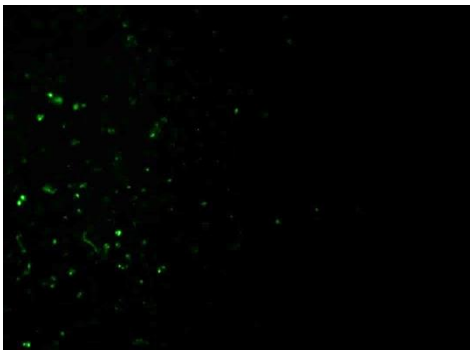

Figure.6. 12 Fluorescent image of the cells in the presence of L-CdS NPs showing green fluorescence

6.4 Conclusions

In this work, CdS NPs have been synthesized using sonochemical method with Schiff base (**L**) as a capping agent. By using this simple and effective method, toxic chemicals and time-consuming procedures can be avoided. This method provides a general approach for synthesizing metal sulfides with novel properties. From XRD and TEM data, the cubic phase and size of the prepared NPs were observed. The optical properties of CdS NPs were investigated by UV-visible and PL spectroscopy. The high photodegradation percentage of Rh6G (70%) and MB (98%) was observed in the presence of 10 mg of CdS NPs in 120 minutes of UV irradiation. The Schiff base and Schiff base capped CdS NPs were screened for their antibacterial activity and the results showed that they are biologically active. The cytotoxicity of the CdS NPs were assessed via the MTT assay, proved that the Schiff base capped CdS is less toxic than unmodified CdS. *In-vitro* cellular imaging applications of prepared L-CdS are also investigated and demonstrated.

References

[1] T Senasu and S Nanan, J. Mater. Sci.: Mater. Electron, 28(23) (2017) 17421.

[2] S A Osman et al., J. Serb. Chem. Soc., 79 (2014) 953.

[3] D Ayodhya et al., J. Fluoresc., 25(5) (2015) 1481.

[4] D Ayodhya et al., J. Materiomics, 5 (2019) 446.

[5] M S Omar et al., Synthesis, 11 (2020) 1309.

[6] A A Jimoh, J. Nanomater., 16 (1) (2015) 190

[7] M Masjedi, Superlattices Microstruct., 62 (2013) 30.

[8] B Nithyaja et al., J. App. Phy., 112 (2012) 064704.

[9] K R Kanude and Preeti Jain, Int. J. Sci. Res. Multidiscip. Stud., 3 (2017) 5.

[10] M N Borovaya et al., Nano. Res. Lett., 9 (2014) 1.

[11] A Kakanejadifard et al., Org. Chem. Res., 4 (2018) 210.

[12] T Ahamad et al., App. Phy. B, 122 (2016) 1.

[13] R Maity and K K Chattopadhyay, J. Nanopart. Res., 8 (2006) 125.

[14] Y C Zhang, G Y Wang and X Y Hu, J. Alloys Compd., 437 (2007) 47.

[15] X Ma et al., Mater. Res. Bull., 40 (2005) 2180.

[16] Y Wang et al., Mater. Lett., 60 (2006)1151.

[17] S Wang, et al., J. Am. Chem. Soc., 129 (2007) 3848.

[18] K W Böer et al., J. App. Phy., 107 (2010) 023701.

[19] J W Stouwdam and R A Janssen, Adv. Mater., 21(28) (2009) 2916.

[20] Z F Liu et al., J. Mater. Chem., 20(3) (2010) 492.

[21] R M Ma et al., Nanotechnology, 18 (2007) 205605.

[22] N Pradhan et al., Nano Lett., 14 (2008) 312.

[23] B Ghosh, M Das, P Banerjee and S Das, Sol. Energy Mater Sol. Cells., 92 (2008)1099.

[24] S Naranthatta et al., ACS omega, 6 (2021)8646.

[25] K Shivaji et al., ACS App. Nano Mater., 1 (2018)1683.

[26] Hong Liying et al., RSC adv., 7 (2017) 36819.

[27] D Xiang et al., Phys. E: Low-Dimens. Syst. Nanostructures., 44 (2011) 733.

[28] M Shakouri-Arani and M Salavati-Niasari, New J Chem., 38 (2014) 1179.

[29] V N Reena et al., Results Chem., 4 (2022) 100576.

[30] L E Brus, J. Chem. Phys., 80 (1984) 4403.

[31] V N Reena et al., AIP Adv., 12 (2022) 105217.

[32] López-Cabaña et al., Nano. Res. Lett., 6 (2011)1.

[33] H Cao et al., Inorg Chem., 45 (2006) 5103.

[34] J C Wu et al., J. Phys. Chem. C, 115 (2011) 5675.

[35] B D Cullity, Elements of Diffraction (Addison-Wesley, Philippines, 1978)

[36] J Guthmuller and B Champagne, The J. Phy. Chem., A112, (14) (2008) 3215.

[37] J P Tardivo et al., Photodiagn. Photodyn. Ther., 2 (2005) 175.

[38] A Khan et al., Inorg. Chem. Comm., 72 (2016) 33.

[39] D Ayodhya and G Veerabhadram, Mater. Sci. Eng. B Solid-State Mater. Adv. Technol., 225 (2017) 33.

[40] K Subin Kumar, J.Coord. Chem., 74 (2021) 2798.

Chapter 7

Chemical Sensors for Metal Ion Detection by Schiff Base Aiding Spectroscopic Techniques

In this chapter, various metal sensors are discussed, employing Schiff base ligands through four distinct techniques. The first approach utilizes an absorption spectra-based sensor for the detection of Fe^{3+} ions using Schiff base **L**. In the second method, a fluorescence spectrum-based sensing technique is employed to detect Ni^{2+} ions. Thirdly, the Raman spectra of thin films of different metal complexes are examined, revealing the capacity of Schiff base **L** to detect Fe^{3+}, and Cu^{2+} ions.

7.1 Introduction

In recent decades and ongoing today, a multitude of chemical sensors have been reported in scientific literature for detecting metal cations in aqueous or semi-aqueous environments, including within living cells. Metals are pivotal in the human body, playing essential roles in various biological processes. Some metals, such as sodium (Na), potassium (K), magnesium (Mg), calcium (Ca), vanadium (V), chromium (Cr), manganese (Mn), iron (Fe), cobalt (Co), nickel (Ni), copper (Cu), zinc (Zn), molybdenum (Mo), and cadmium (Cd), are indispensable for normal biological functions in humans. Notably, deficiencies in metals like Fe, Co, Ni, Ca, Cu, Zn, and Cr, which are typically found in ion form, can lead to a range of health issues. Food and water serve as essential sources of these vital metal ions, necessary for the survival of all organisms. However, an excess of these metals can become toxic. Inadequate levels of Co and Fe can result in anemia, Cu deficiency can lead to brain and heart diseases, as well as anemia. Zinc deficiency can cause growth retardation and skin changes, while Ca deficiency results in bone deterioration, and Cr deficiency reduces glucose tolerance. Consequently, the detection of metal ions within the human body is of paramount importance due to the significance of their permissible limits. There is a growing interest in designing and developing molecular sensors capable of detecting analytes even at exceedingly low concentrations.

Currently, a variety of methods, including flame atomic absorption spectroscopy, inductively coupled plasma optical emission spectroscopy, stripping voltammetry, X-ray fluorescence spectrometry, and inductively coupled plasma mass spectrometry, are utilized for the detection of metal ions. However, the majority of these techniques come with significant drawbacks, such as high costs, time-consuming sample preparation procedures, and limited sensitivity. To address these limitations, researchers

have turned to optical chemosensors for metal ion determination. Among these, Schiff base-based structures have demonstrated exceptional performance in the field of metal ion detection. Schiff base ligands have gained substantial attention due to their ease of synthesis and their ability to form complexes with a wide array of metals. Schiff bases serve as ligands in various metal complexes, and in chemical sensors, their role in positive ion detection is primarily associated with a fluorescent colour change when exposed to metal salts. Among the most notable sites for this purpose are Schiff base ligands. However, many other binding sites are employed in chemical sensors, including pyridine, anthracene, pyrene, quinoline, naphthalene, urea, phenolphthalein, rhodamine, and coumarin.

Schiff base ligands are organic chelating agents used in the synthesis of coordination complexes. They are derived from the condensation of diamines with carbonyl compounds, resulting in the formation of stable complexes with metal ions. Schiff bases can be synthesized with relative simplicity and provide an ideal electronic and geometrical framework for coordination with single metal ions or multiple metal ions simultaneously.

In light of these characteristics, Schiff base-based sensors have demonstrated outstanding performance when compared to various types of chemical optical sensors. While these Schiff base sensors are generally sensitive to a single metal ion in most cases, they stand out among organic molecules due to their promising optical response to metal ions, owing to their high chelating ability. The advantages of this class of compounds include ease of synthesis and relatively high yield [27].

Numerous imines-based optical probes have been documented in the literature. When these probes bind to a metal ion, their photophysical properties undergo changes, which can be monitored through the optical mechanisms mentioned earlier.

In 2007, another signaling mechanism involving the (-C=N-) isomerization in Schiff bases was reported, leading to the development of fluorogenic probes for metal ions. This -C=N isomerization dissipates the excited state energy of the molecule, resulting in non-radiative emission [27]. However, the introduction of a guest molecule, especially a metal ion, induces radiative emission through covalent binding with the (-C=N-) bond.

Additionally, Schiff bases exhibit a propensity for undergoing hydrolytic cleavage in the presence of various electrophilic catalysts, such as acids and metal ions. This hydrolytic cleavage of the imine bond by metal ions has been harnessed in the development of metal-based sensing systems, giving rise to numerous optical probes designed based on this strategy [27].

Schiff base-based sensors belong to the category of chemical sensors, which are designed as compact devices or materials capable of providing real-time and online information regarding the presence and concentration of specific compounds or ions in complex samples. These chemical sensors offer several advantages over traditional analytical instruments, as they are portable, straightforward to operate, and compact in size [3, 34].

Raman spectroscopy is a widely utilized molecular recognition technology, although its scattering cross-section is significantly smaller (10^{-6} and 10^{-14}) than that of infrared and fluorescence spectroscopies, respectively. This limitation has historically restricted its application in trace analysis and interface science. However, a crucial discovery by Fleischmann et al. in 1973 revealed that the Raman signal of pyridine molecules on the surface of a rough silver electrode was approximately 10^6 times stronger than in solution. This discovery gave birth to the surface-enhanced Raman phenomenon (SERS), marking a turning point in Raman spectroscopy.

Schiff base sensors, often utilized in Raman spectroscopy, are an interesting and effective approach for detecting various analytes, including metal ions, in a variety of samples. Schiff base ligands are designed to interact with specific metal ions or other analytes, leading to changes in their Raman spectra. These changes can be attributed to alterations in the vibrational modes of the molecule, which result from the formation of the Schiff base-analyte complex. By analyzing the Raman spectra before and after the interaction, it is possible to identify and quantify the analyte.

Schiff base sensors offer several advantages for Raman spectroscopy-based detection. Schiff base ligands can be tailored to selectively bind to specific metal ions or analytes, ensuring high selectivity in the detection process. The Raman signal changes induced by Schiff base-analyte interactions are often highly sensitive, allowing for the detection of even trace amounts of the target analyte. Schiff base sensors can be designed for various analytes and applications, from environmental monitoring to biomedical diagnostics.

Raman spectroscopy provides real-time information, making it suitable for continuous monitoring of analyte concentrations. Raman spectroscopy is a non-destructive technique, meaning that samples can be analyzed without altering their chemical composition.

This chapter discusses the development of a chemical sensor utilizing a Schiff base ligand, *3-((2-(-(1-(2-hydroxyphenyl) ethylidene) amino) ethyl) imino)-2-pentone*. The primary goal is to exploiting the absorption spectra and fluorescence spectra of the Schiff base for sensing applications. Furthermore, the chapter explores the fabrication of a thin film sensor device that incorporates the Schiff base for the purpose of detecting metal ions using Raman spectra.

7.2 Materials and Methods

All the chemicals, o-hydroxyacetophenone, acetylacetone, 1, 2 ethylenediamine, chloride or nitrate salts of different metals, solvents like DMSO, methanol, Rh6G and MB were purchased from Sigma-Aldrich. The solvents were received from the chemical suppliers and were used without further purification.

7.2.1 Preparation of the Schiff base ligand (L)

The preparation and characterization of the Schiff base ligand, **L**, is discussed in the experimental section of chapter 5. **L** is soluble only in DMSO or DMF

7.2.2 Sensing of metal ions by absorption spectrum

Methanolic solution of different metal ions (1 mM), Fe^{3+}, Cu^{2+}, Co^{2+}, Ni^{2+}, Al^{3+}, Cd^{2+}, Ba^{2+}, Ca^{2+}, Zn^{2+}, Mg^{2+}, were prepared and kept as stock solutions. From the stock solution 1 equivalent of each metal ion was mixed with 5 ml of 1 mM solution of **L.** UV-visible spectra of this mixture were recorded at room temperature by keeping the total concentration 1 mM and total volume 5 ml [27, 35].

7.2.3 Sensing of metal ions by fluorescence spectrum

Sensing metal ions through fluorescence spectra can be accomplished by following the procedure outlined in the previous section. Here we are measuring fluorescence response of **L** upon the addition of different metal ions as mentioned above [27].

7.2.4 Metal sensing by Raman spectrum-thin film method

In this procedure, a thin film of **L** was used to detect metal ions by employing their Raman spectra. The solution of ligand for coating was prepared by

taking 1 g of **L** in 20 ml DMSO. The complete dissolving was accomplished by heating the solution at 60^0C in an ultrasonicator. The solution was slightly viscous, easing the task of thin film fabrication. After the fabrication of **L**-film 1 drop of 1 mM metal ion solution (Fe^{3+}, Cu^{2+}, and $Ni2^{+}$) was spread over the surface of thin film. This was dried at 45^0C on a hot air oven.

The schematic figure shows (Figure.7.1) the fabrication of thin film used for metal ion detection. Figure 7.2 depicts the schematic representation of the L-film and the L-film after the spreading of metal ions, with the portion undergoing a colour change.

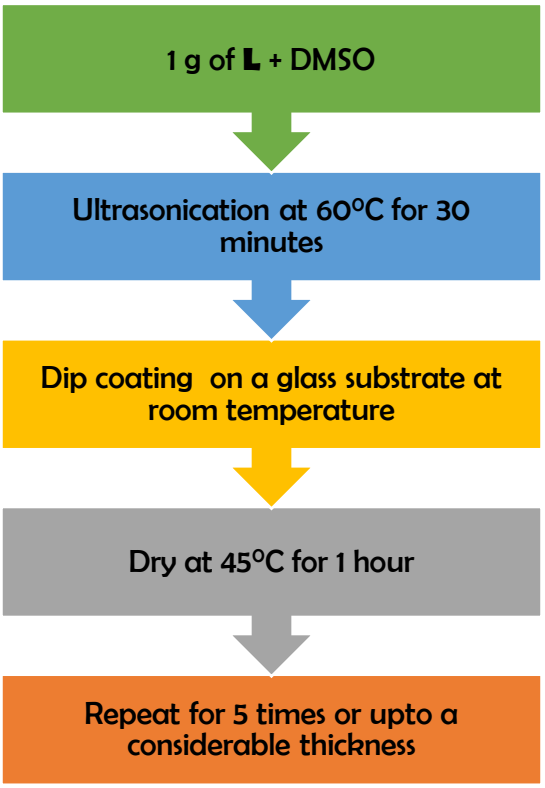

Figure.7.1 Schematic representation of fabrication of thin film of **L**

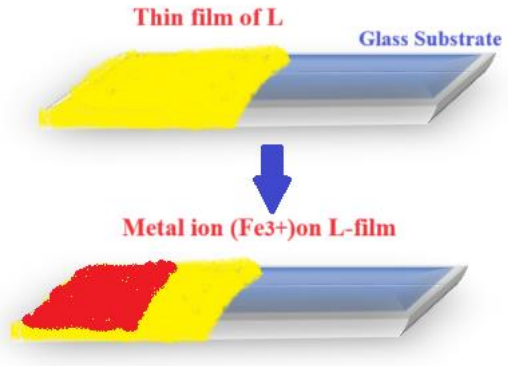

Figure.7.2 Schematic representation of Fe^{3+} on **L**-film

The Raman spectra of **L**-film and **L**-film with metal ion were measured and analysed.

7.3 Results and Discussions

7.3.1 Photo-physical investigations

The sensing capabilities of ligand **L** were assessed using the UV-visible spectra with various metal ions, including Ni^{2+}, Co^{2+}, Cu^{2+}, Zn^{2+}, Mg^{2+}, Fe^{3+}, Al^{3+}, Cd^{2+}, and Mn^{2+} in methanol. As depicted in Figure. 7.3, the free ligand **L** displayed two distinct absorption bands at 256 nm, and 396 nm. The peak at 315 nm may be due the presence of any impurities. Notably, the addition of solutions containing the above-mentioned metal ions, except for Fe^{3+}, to a solution of **L** in DMSO did not induce any changes in its spectrum.

However, when a methanol solution of Fe^{3+} was introduced, a noticeable alteration in the UV-visible spectrum was observed. In the case of Fe (III), a new peak emerged in the range of 450-500 nm. This phenomenon is likely attributed to a ligand-to-metal charge-transfer (LMCT) transition, signifying a unique response to the presence of Fe^{3+} ions.

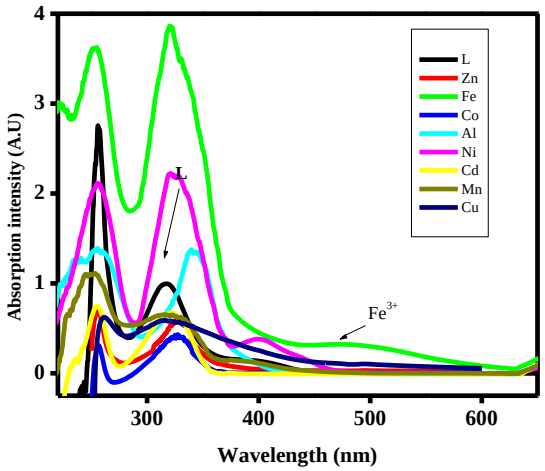

Figure.7.3 UV-visible absorption spectral changes of **L** upon the addition of different metal ions

According to the spectral data, a noticeable colour change was observed in the ligand **L**, shifting from yellow to red, upon the addition of a Fe^{3+} ion solution. This colour transformation indicates the formation of a complex between **L** and Fe^{3+}. This observation highlights the utility of **L** as a "naked-eye" sensor for detecting Fe^{3+} ions in methanol solutions.

To assess the sensitivity of **L** towards Fe^{3+} ions, different concentrations of Fe^{3+} (0.1 mM to 1 mM) were mixed with 1 mM ligand solution and observed their absorption spectra. The UV-visible titration of **L** in DMSO with Fe^{3+} in methanol was conducted and is depicted in Figure.7.4. With the gradual addition of 0 to 1 equivalent (0.1 mM to 1 mM) of Fe^{3+} to **L**, a new absorption peak emerged at 490 nm, distinct from the peak associated with **L** alone. Moreover, it was evident that the intensities of the absorption peaks increased with the rising concentration of Fe^{3+} from 0 to 1 equivalent. This effect was accompanied by a visible colour shift from yellow to red. The findings from this study indicate that the detection of Fe^{3+} ions can be

achieved with high sensitivity, down to a concentration as low as 0.1 mM [27].

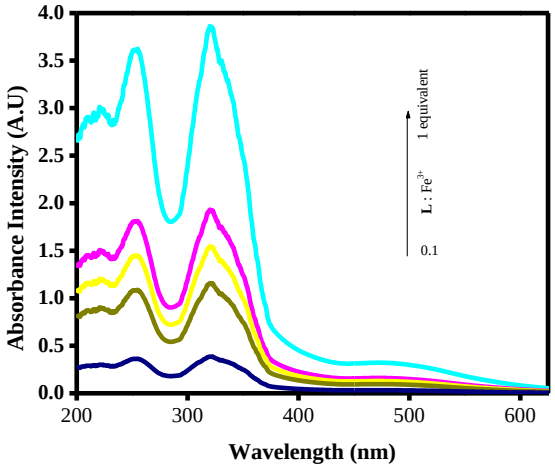

Figure.7.4 UV-visible absorption spectral change of **L** (1 mM) upon the addition of Fe^{3+} (0.1 to 1 mM)

7.3.2 Fluorescence emission spectra of L with Metal ions

The fluorescence behavior of ligand **L** was investigated following the addition of different methanolic metal solutions, including Ni^{2+}, Co^{2+}, Cu^{2+}, Zn^{2+}, Mg^{2+}, Fe^{3+}, Al^{3+}, Cd^{2+}, and Mn^{2+}. Specifically, one equivalent of each metal solution was added to 0.01 mmol of **L** in DMSO. The fluorescence spectra of all the samples were examined using an excitation wavelength of 350 nm, as depicted in Figure.7.5. Surprisingly, no notable changes in fluorescence were observed upon the addition of most metal ions, except for Ni^{2+}.

Ni^{2+} caused a notable increase in fluorescence intensity and a shift in peak wavelength from 500 nm to 466 nm in **L**, indicating its potential as a Ni^{2+} sensor in methanol. The nitrogen atom in the Schiff base likely facilitates

photo-induced electron transfer, resulting in over a tenfold increase in fluorescence emission compared to **L** alone.

Different concentrations of Ni^{2+} (0.1 to 1 millimole equivalent) were tested at a 350 nm excitation wavelength to detect the ligand's sensitivity. This emphasizes its potential as a highly sensitive Ni^{2+} sensor, even at low concentrations.

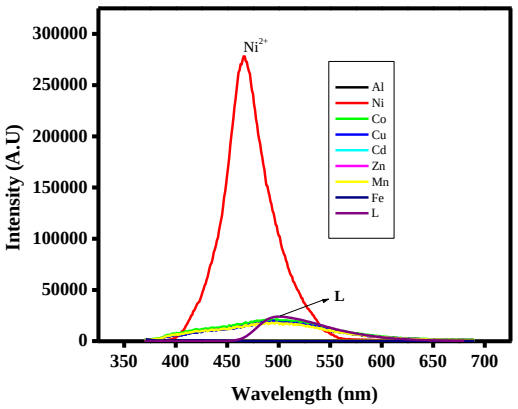

Figure.7.5 PL spectral change of **L** (1 mM) upon the addition of different metal ions

The fluorescence responses of ligand **L** towards the mentioned metal ions were also investigated. When excited at 350 nm, **L** displayed an emission peak at 500 nm. It's important to note that Schiff bases are typically weakly emissive due to the isomerization of unbridged (-C=N-) bonds, which dissipates the excited state energy. However, when Ni^{2+} ions were introduced, a remarkable change was observed in the emission spectrum. The emission intensity at 500 nm significantly increased, and a new emission peak emerged at 466 nm with an exceptionally high intensity (as illustrated in Figure.7.5). In contrast, the other metal ions did not induce this type of fluorescence response under similar conditions. This fluorescence turn-on behavior of **L** in the presence of Ni^{2+} is indicative of the formation of a stable chelate complex between **L** and Ni^{2+}. This complex rigidifies the molecule and effectively

suppresses the isomerization of (-C=N) bonds, thereby facilitating radiative emission and significantly enhancing the fluorescence intensity. [28].

Fluorescence spectrum monitoring of **L** was conducted with varying Ni^{2+} concentrations ranging from 0.01 to 0.1 mM. Figure.7.6 illustrates the increase in fluorescence intensity with higher Ni^{2+} concentrations. The lowest intensity was observed at 0.01 mM Ni^{2+}, indicating L's ability to detect Ni^{2+} down to 0.01 mM through fluorescence emission.

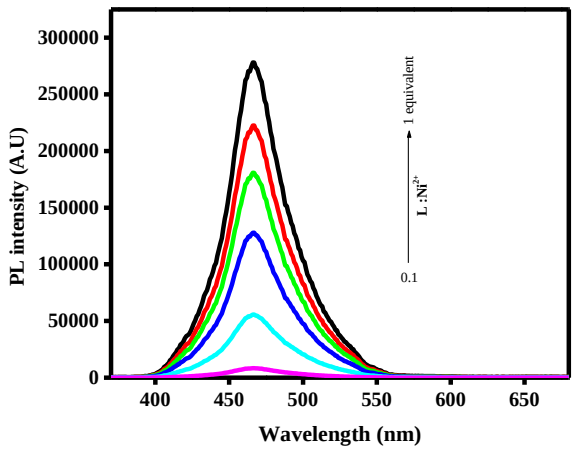

Figure.7.6 Fluorescence emission spectral variation of **L** and Ni^{2+} (0.1 to 1 equivalent).

7.3.3 Raman spectrum of L film with Metal ions

In this experimental investigation, the study focuses on assessing the sensing capabilities of a thin film ligand using Raman spectroscopy. The objective is to explore the film's potential in detecting specific metal ions. The Raman spectrum of the ligand thin film reveals distinctive bands associated with functional groups, such as $\upsilon_{-c=o}$, aromatic υ_{-CH2}, and phenolic υ_{-OH}. Notably, the absence of a phenolic band in metal complexes suggests a coordination change after deprotonation. By analyzing Raman bands below 500 cm^{-1}, insights into potential metal complex formations are gained. The results

indicate distinct bands in Cu^{2+} and Fe^{3+} complexes point towards the ligand's efficacy in selectively detecting these metal ions in a methanol environment. This investigation sheds light on the practical applications of the ligand thin film as a promising sensor for specific metal ions.

In the experimental line, the ligand is employed in a thin film form as part of an effort to fabricate a solid-state device capable of sensing metals. The inspiration behind using a thin film lies in the potential benefits for device fabrication, such as ease of integration and compatibility with certain sensing applications.

The thickness of the thin film is not measured in this stage of the investigation. Instead, the primary focus is on evaluating the ligand's ability to detect metals via Raman spectrum. The thin film's Raman spectrum serves as a vital tool for understanding the ligand's performance in metal detection. It provides valuable perceptions into the vibrational modes and structural characteristics of the thin film, offering information on how the ligand interacts with metal ions. The choice to highlight the detection ability rather than the thickness at this stage suggests a targeted investigation into the ligand's sensing capabilities. This experimental approach aims to pave the way for the development of a solid-state device that can effectively identify and analyze metal ions, along with the Raman spectrum of the thin film serving as a key indicator of the ligand's potential in this application. Further analyses and optimizations may be conducted to refine the device's performance for practical sensing applications in the future.

The Raman spectrum of the thin film of the ligand is presented in Figure. 7.7(a). It provides a detailed analysis of the molecular vibrations and interactions within the thin film. Raman spectra of the ligand **L** demonstrated a medium-intensity band at 1639 cm^{-1} is the characteristic band of $\upsilon_{-c=o}$. A band at 3135 cm^{-1} may be assigned to the aromatic υ_{-CH2} and another at 2905

cm^{-1} to the υ_{-CH} of the methyl group. Broad band at 3388 cm^{-1} may be assigned to the phenolic υ_{-OH} of the o-hydroxyacetophenone moiety. The band at 2995cm^{-1} may be attributed to the $-CH_3$ group present in the ligand.

When we consider the Raman spectra of metal complexes, broad band observed at 3445 cm^{-1} in the spectrum of ligand may be assigned to the phenolic υ_{-OH} of o-hydroxyacetophenone moiety, but this band is absent in the spectrum of all metal complexes indicating that the coordination of phenolicoxygen after deprotonation. If this ligand and metal ion form a metal complex, the Raman bands can be identified below 500 cm^{-1}. In the case of the copper ion on the thin film, as showed in Figure.7.7(b), Raman spectroscopy revealed characteristic bands at 400 cm^{-1} and 460 cm^{-1}, different from those attributed to the ligand alone. These distinctive bands are associated with the presence of Cu-N and Cu-O bonds, providing solid and precise identification of copper metal within the sample. The appearance of the peaks at 400 cm^{-1} and 460 cm^{-1} serves as robust evidence for the coordination of copper ions with nitrogen (Cu-N) and oxygen (Cu-O) within the ligand thin film. These findings highlight the sensitivity of the thin film of **L**, in selectively detecting Cu^{2+} ions in a methanol environment.

The identification of these precise Raman bands associated with copper-metal bonds strengthens the argument for the ligand's utility as a sensing material for copper ions. This observation is fundamental to the development of a metal detection device based on the ligand thin film, demonstrating its capability to discern and identify distinct metal ions within the tested environment. And in the case of Fe^{3+} complex (Figure.7.7(c)), two bands were observed below 500 cm^{-1} one is at 268cm^{-1} and the other is at 381cm^{-1}. The band at 286 cm^{-1} is due to the Fe-Cl_3 bond. This bond is also present in the complex, because Fe^{3+} needs three negative charges to neutralise. Therefore, along with Fe-N and Fe-O bonds there are another bond (Fe-Cl-)

is also present. Its presence was detected from the Raman spectra. Thus, the ligand, **L** can detect Fe^{3+} metal ion from methanol. The band at 381 cm^{-1} was either the bond corresponding to Fe-N or Fe-O [29-33].

When it considers the Raman spectrum of (Ni^{2+}-**L**) combination, (Figure.7.7(d)), almost all the peaks coincide with peaks of ligand. The merging of peaks suggests that the interaction between Ni^{2+} and the ligand is negligeable, reflecting a failure to establish a unique complex structure. Besides, the absence of any visible peaks below 500 cm^{-1} adds evidence, indicating a nonexistence of complexation. This spectral region is often revealing of vibrations associated with metal-ligand bonding, and the absence of such peaks underlines the non-formation or instability of a Ni^{2+} complex with the ligand in the solid-state configuration under consideration.

The detection method can be elaborated for sensing other heavy metal ions and ordinary essential metal ions. Other metal ions can also be detected using this technique.

We have successfully fabricated a solid-state metal sensor in thin film form employing Schiff base ligand with the aid of Raman spectroscopy. Modifications can be made to identify all metal ions by utilizing Schiff base thin film sensor via Raman spectroscopy. Schiff base ligand demonstrates a selective affinity for coordinating with specific metals. Hence, identifying suitable Schiff base for specific metals will constitute breakthrough in fabricating solid state, thin film metal sensor.

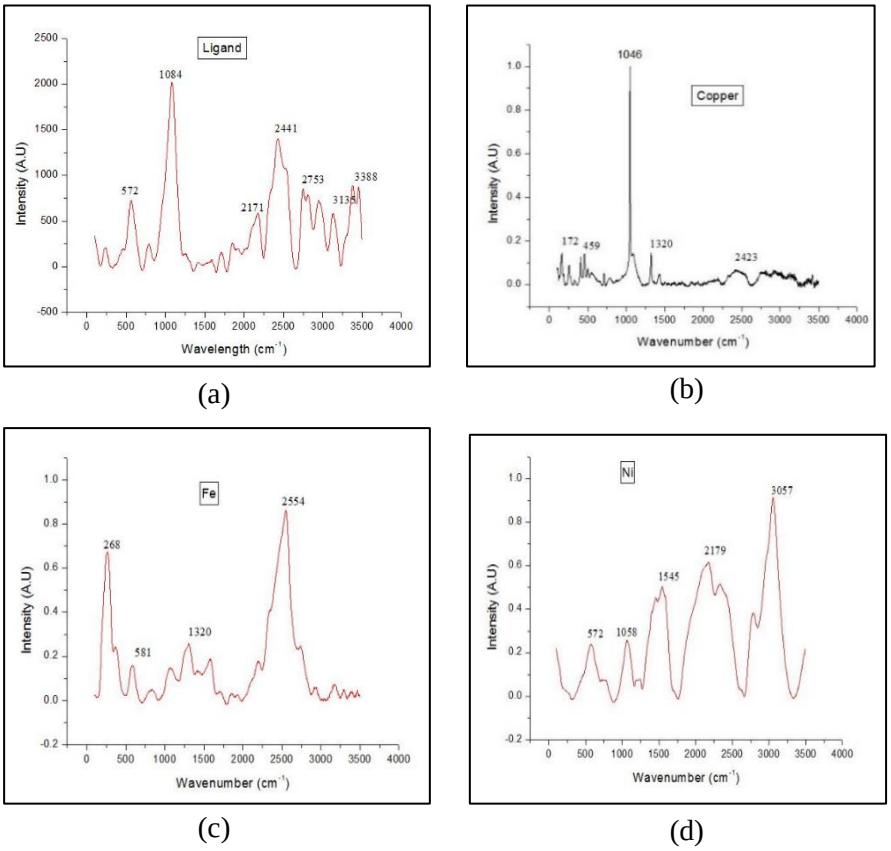

Figure.7.7 Raman spectra of thin film (a) ligand, **L** (b) **L**: Cu^{2+} (c) **L**: Fe^{3+} (d) **L**: Ni^{2+}

7.4 Conclusions

Different metal sensors with the aid of Schiff base ligand by utilizing three different spectroscopic techniques were discussed here. The absorption spectra-based sensor detected Fe^{3+} ion using the Schiff base **L**. Detection of Ni^{2+} ion was accomplished using fluorescence spectrum-based sensing method. Raman spectrum of different metal complexes in combination with **L** film was studied and investigated that **L** can detect Fe^{3+} and Cu^{2+} ions. The attempt to fabricate a solid-state metal sensor using Schiff base ligand via Raman spectroscopy is successful.

References

[1] S P Gupta, MOJ Bioorg. Org. Chem., 2 (2018) 221.

[2] K S Egorova and V P Ananikov Organometallics., 36(21) (2017) 4071.

[3] R H Holm, P Kennepohl and E I Solomon Chem. Rev., 96(7) (1996) 2239.

[4] G Hennrich et al., Inorg. Chem., 40 (2001) 641.

[5] Y Zheng et al., J. Am. Chem. Soc., 125 (2003) 2680.

[6] R Martinez et al., Organic Letters., 8 (2006) 3235.

[7] J Huang et al., Org. Biomol. Chem., 7 (2009)1299.

[8] N Singh, N et al., Tetrahedron Lett., 51 (2010) 3385.

[9] F A Abebe and E Sinn, Tetrahedron Lett., 52 (2011) 546.

[10] L Yang et al., Sens. Actuators B, 176 (2013)181.

[11] M Royzen et al., J. Am. Chem. Soc., 127 (2005)1612.

[12] K Subin Kumar and K K Aravindakshan, Results. Chem., 3 (2021) 100129.

[13] K B Kim et al., Dalton Trans., 42 (2013) 16569.

[14] J J Xiong et al., Sens. Actuators B, 226 (2016) 30.

[15] Y J Na, et al., Spectrochim. Acta A, 136 (2015) 1649.

[16] Y W Choi et al., Sens. Actuators B, 194 (2014) 343.

[17] V K Gupta, A K Singh, L K Kumawat, Sens. Actuators B, 195 (2014) 98.

[18] Y G Zhang, et al., Inorg. Chem. Commun., 39 (2014) 86.

[19] S Chall et al., Org. Biomol. Chem., 12 (2014) 6447.

[20] O G Beltran et al., Sensors, 14 (2014) 1358.

[21] M H Lee, et al., Chem. Commun., 46 (2010) 1407.

[22] L Wang, et al., Sens. Actuators B, 202 (2014) 949.

[23] Y J Na et al., New J. Chem., 38 (2014) 5769.

[24] L Fan et al., Spectrochim. Acta A Mol. Biomol. Spectrosc., 218, (2019) 342.

[25] A L Berhanu et al., TrAC Trends in Anal. Chem., 116, (2019) 74.

[26] S Guha et al., Talanta, 91, (2012) 18.

[27] P P Soufeena et al., Spectrochim. Acta A Mol. Biomol. Spectrosc., 223 (2019) 117201.

[28] M Z Alam eta l., J Fluoresc., 33(4) (2023) 1241.

[29] H Veisi et al., Catal Lett., 147 (2017) 976.

[30] G Xu, et al., J. Hazard. Mater., (2022) 424, 127303.

[31] Z Ge, et al., Anal. Chem., 65(17) (1993) 2335.

[32] A Ayman and A Aziz, J. Lumin., 143 (2013) 663.

[33] T Azargoshasb et al., ACS omega, 5(35) (2020) 22046.

[34] O S Wolfbeis, Angewandte Chemie International Edition, 52 (38) (2013) 9864.

[35] P P Soufeena and K K Aravindakshan, J. Lumin., 205 (2019) 400.

Chapter 8

General Conclusions

8.1 General Conclusions

The present investigation employs template synthesis for the preparation of NPs. The template synthesis of nanostructures is important because, it provides precise size, shape and composition of NPs. In this work, CdS NPs using DNA and a newly synthesized Schiff base ligand as templates were synthesized and characterized. Various photonic and biological applications of the CdS NPs were conducted, and similar applications were executed for DNA-capped Ag NPs.

The PL spectrum of D-CdS incorporated Rh6G-doped sol-gel glass was investigated. Here the concentration of Rh6G was set to 10^{-4} M. The results revealed a significant impact of CdS NPs on the emission of Rh6G, causing a shift from 586 nm to 572 nm. The annealing temperature also played a notable role in the PL of Rh6G-doped glasses, with variations observed from 573 nm to 584 nm. Additionally, the presence of CdS altered the CIE coordinates and enhanced the CCT values in chromaticity studies, categorizing the samples as warm light suitable for household lighting. The fluorescence lifetime decay of Rh6G remained largely unaffected by the addition of CdS. Furthermore, the study explored the potential of modifying the emission properties of Rh6G for use in designing solid-state lasers with wavelength tunability. This work also highlighted the efficient photodegradation (70% for R6G and 98% for MB) in the presence of 10 mg of CdS NPs during 120 minutes of UV irradiation. The antibacterial activity of these CdS NPs was demonstrated, indicating their biological efficacy. Cytotoxicity assessment via the MTT assay revealed that DNA capped CdS is less toxic than uncapped CdS. Furthermore, the *in vitro* cellular imaging applications of the prepared CdS were investigated, revealing its potential as an agent for bioimaging.

Various applications of DNA-capped Ag NPs were investigated in the preceding section. Notably, these NPs exhibit larvicidal as well as antibacterial activities. Their larvicidal properties are highlighted by the significant mortality observed in bioassays. In addition to their bioactivity, DNA-capped Ag NPs demonstrate versatility in enhancing fluorescence and tuning the emission wavelength in Rh6G doped sol-gel derived glasses. The investigation into their photocatalytic activity reveals a noticeable capacity, although it is established that they may not serve as optimal photocatalysts. Moreover, the cytotoxicity assessment places DNA-capped Ag NPs as suitable candidates for fluorescence imaging applications, exhibiting dose-dependent cell death toward HeLa cells. The multifaceted properties exhibited by DNA-capped Ag NPs highlight their potential in diverse fields, positioning them as promising materials for larvicidal, antibacterial, fluorescence enhancement, and bioimaging applications.

A novel Schiff base ligand, *3-((2-(-(1-(2-hydroxyphenyl) ethylidene) amino) ethyl) imino)-2-pentone* was synthesized and characterized. Schiff bases are conventionally used to coordinate metals to form metal complexes. Therefore, one complex, Ni (II) was synthesized and characterized. Based on the various analytical, spectral and magnetic moment data, Ni (II) complex is assigned to octahedral geometry. The bandgap energy calculation of ligand and Ni (II) complex propose that they can be considered as a semiconductor material. Based on the photoluminescence spectrum and chromaticity studies, it can be applied in green emitting organic light emitting diode. Both ligand and Ni (II) complex show biological activities like antibacterial, antioxidant and larvicidal activities. It is observed that Ni (II) complex shows better antibacterial, antioxidant and larvicidal activities than ligand. It is found that Schiff base ligand shows different biological activities and has less cytotoxicity.

Cadmium sulfide NPs have been successfully synthesized using Schiff base as a template. This method provides a general approach for synthesizing metal sulfides with novel properties. The high photodegradation percentage of Rh6G (70%) and MB (98%) was observed in the presence of CdS NPs for a period of 120 minutes UV irradiation. The Schiff base capped CdS NPs were screened for their antibacterial activity and the results showed that they are biologically active. The cytotoxicity of the CdS NPs were assessed via the MTT assay, proved that the Schiff base capped CdS is less toxic than unmodified CdS with a LC_{50} value of 18.72 µg/ml. The *In vitro* cellular imaging applications of prepared CdS are also investigated and demonstrated. This CdS NPs can effectively destroy HeLa cells and it shows a dose dependent property.

A chemical sensor with the aid of Schiff base ligand by utilizing three different techniques was also investigated in this work. The absorption spectra-based sensor could detect Fe^{3+} ion using the Schiff base. Also, Ni^{2+} ion was detected using fluorescence spectrum-based sensing method. The utilization of Raman spectroscopy for fabricating a solid-state metal sensor by incorporating Schiff base ligand is investigated. Raman spectrum of thin film of different metal complexes was studied and investigated that Schiff base can detect Fe^{3+} and Cu^{2+} ions. The attempt to fabricate a solid-state metal sensor using Schiff base ligand via Raman spectroscopy is succeeded.

The Table 8.1 gives the comparison study of different photonic and biological applications of DNA capped CdS, Schiff base capped CdS and DNA capped Ag NPs.

Table.8. 1 Comparison of different applications of CdS and Ag NPs

Sample	Photocatalytic activity (% of photodegradation)		Antibacterial effect (µL/ml)			Cytotoxicity LC_{50}
	Rh6G (λ_{abs}= 520 nm)	MB (λ_{abs}= 665 nm)	*Pseudomonas aeruginosa*	*Staphylococcus aureus*	*Streptococcus mutans*	
D-CdS	64%	98.9%	24	20	17	8 µg/ml
L-CdS	70%	98.9%	25	21	17	2.4 µg/ml
Ag NPs	<10%	34%	28	25	24	47 µL/ml

Upon observing the table above, the application of Schiff base capped CdS can vie with DNA capped CdS NPs. Observing into the cytotoxicity; L-CdS NPs shows enhanced toxicity than D-CdS NPs. Consequently, L-CdS can induce a greater number of deaths in HeLa cells than D-CdS. Both LC_{50} values represent concentrations deemed safe, as discussed in the respective chapters. The metal nanoparticle, Ag NP, shows less photocatalytic activity than CdS NPs. At the same time, antibacterial activity and cytotoxicity are higher than the CdS NPs.

In conclusion, this comprehensive study highlights the versatility and potential applications of CdS and Ag NPs. The synthesized materials demonstrated significant impacts in various domains, from influencing the photoluminescence of doped sol-gel glasses to exhibiting remarkable antibacterial properties and potential for bioimaging. The successful utilization of Schiff base ligands extends to the coordination of metals, demonstrated by the synthesized Ni (II) complex, showing enhanced biological activities. Moreover, the template synthesis approach employed for CdS NPs using Schiff base as a guide provides a promising technique for synthesizing CdS NPs with versatile applications. The exploration of these materials further extends to their application in chemical sensing, showcasing

the adaptability of Schiff base ligands across various sensing techniques. Altogether, this research contributes to the growing body of knowledge in nanomaterial synthesis, photonic applications, biological applications, and chemical sensing, opening new frontiers for potential advancements in materials science and interdisciplinary research.

Chapter 9

Future Prospects

The future scopes of this work are promising and offering numerous opportunities for further exploration and application. The results of the study, such as the tunability of emission properties in Rh6G-doped glasses and the efficient photodegradation capabilities of CdS and Ag NPs, suggest potential advancements in various fields. The categorization of the samples as warm light suitable for household lighting suggests potential applications in advanced lighting technologies. Further research could focus on optimizing these materials for energy-efficient lighting solutions. The demonstrated capability to modify the emission properties of Rh6G opens up opportunities for designing solid-state lasers with wavelength tunability. Future work could explore the development of compact and tunable lasers for specific applications in communications or medical devices. The efficient photodegradation observed in the presence of CdS NPs suggests potential applications in environmental remediation, such as water purification or wastewater treatment. Future studies could explore these NPs' effectiveness in large-scale applications.

Different biomedical applications done in this work are antibacterial activity, larvicidal activity, cytotoxicity, bioimaging of CdS, Ag NPs and Schiff base ligand and its Ni (II) complex.

The antibacterial activity of CdS, Ag and Ni (II) complex suggests potential biomedical applications, particularly in the development of antimicrobial agents or drug delivery systems. Additional research could focus on understanding the mechanisms and optimizing these materials for medical use. The assessment of cytotoxicity and the finding that capped CdS is less toxic than uncapped CdS are significant. Future research could investigate deeper into understanding the biocompatibility of these NPs, directing the way for potential applications in medicine and biotechnology. The investigation and demonstration of in vitro cellular imaging applications of

CdS and Ag NPs reveal possibilities for advancements in imaging technologies. Future work could concentrate on refining these applications for more sophisticated imaging techniques or targeted drug delivery.

A novel Schiff base with a biologically inspired structure has been synthesized and employed for the synthesis of CdS NPs. Extension can be done by synthesizing other NPs like ZnS, ZnO and CdSe. This method of synthesizing NPs is a novel technique and significant for different applications.

The future direction of bioimaging research and development encompasses several key directions; the expanded utilization of near-IR imaging, paving the way for the advancement of near-IR fluorophores, the adoption of a NPs approach for precise encapsulation also targeted delivery within an explicit biotic context, the exploration of *in-situ* initiation of fluorescent probes triggered by stimuli or drugs, the implementation of real-time, *in-vivo* imaging for monitoring dynamic biological activities, and the imaging microorganisms within their natural environments that are considerably smaller than the wavelength of light.

The successful application of Schiff base ligands in metal sensing, as discussed in this thesis, suggests promising future scopes in diverse fields. Future research could focus on enhancing the sensitivity and selectivity of the absorption spectra-based sensor for Fe^{3+} ions, potentially expanding its applicability to a wider range of metal ions. Further exploration of the fluorescence spectrum-based sensing method for Ni^{2+} detection may lead to advancements in real-time and selective metal monitoring. The study of Raman spectra in thin films opens up opportunities for developing novel solid-state metal sensors, with potential applications in areas such as environmental monitoring or industrial quality control.

The future prospects of chemical sensors utilizing Schiff base ligands appear promising, driven by ongoing research efforts to enhance their selectivity, sensitivity, and multifunctionality. Integration with nanomaterials, such as NPs, holds potential for improved performance. These sensors show significant promise in applications ranging from biological and environmental monitoring to biomedical diagnostics, with potential for *in vivo* use and early disease detection. Additionally, the integration of Schiff base ligand-based sensors with other analytical techniques and the exploration of flexible, wearable designs contribute to the evolving landscape of sensor technology. Continued interdisciplinary collaboration is expected to unlock the full potential of Schiff base ligand-based sensors in addressing complex challenges across various fields.